# Refining real site TKPH (tonne-kilometer-per-hour) of ultra-large off-the-road tires at mine sites

by

Shaosen Ma

A thesis submitted in partial fulfillment of the requirements for the degree of

Doctor of Philosophy

in

Mining Engineering

Department of Civil and Environmental Engineering
University of Alberta

**Abstract**

The objective of this PhD program is to refine the real site TKPH (tonne-kilometer-per-hour) of ultra-large off-the-road (OTR) tires at mine sites. To achieve this, a novel HLSRT model (a Hysteresis Loss model considering Strain levels, strain Rates, and rubber Temperatures) was first developed as per the experimental results from cyclic tensile tests; it was used to predict the hysteresis loss of OTR tire rubbers. Then this model was used to develop a mathematical equation that predicted the heat generation rates of OTR tire rubbers. Based on this mathematical equation, a new finite element OTR tire thermal (OTRTire-T) model was built to predict the temperatures in OTR tires. As per the results from the OTRTire-T model, the cycle length coefficient $K_1$ and the site ambient temperature coefficient $K_2$ in the real site TKPHs were refined under different site operating conditions (i.e., payloads, cycle speeds, ambient temperatures, and cycle lengths) and the effects of these site operating conditions on the real site TKPHs were investigated.

The results showed that the hysteresis loss of OTR tire rubbers was affected by strain levels, strain rates, and rubber temperatures. A large strain level (e.g., 100%) increased the hysteresis loss considerably. Rubber hysteresis loss increased with a rise in strain rates, and the increasing rates became greater at larger strain levels (e.g., 100%). In addition, a rise of rubber temperatures caused a decrease in hysteresis loss; however, the decrease became less significant when the rubber temperatures were above 10 ℃. The HLSRT model can predict the hysteresis loss of OTR tire rubbers with average mean absolute percent errors (MAPEs) of less than 13.6%. This model characterized the exponential increase of hysteresis loss at rising strain levels and identified the linear growth of hysteresis loss when the strain rate rose.

The OTRTire-T model predicted the temperatures of OTR tires that deviated by less than 8.63% from the on-site monitoring tire temperatures. The model results showed that the temperature in

OTR tires increased significantly when the tire was subjected to a large vertical load (e.g., 104 tonnes). The tire temperature increased with a rise in truck speeds, and the increase became more significant at these large vertical loads (e.g., 104 tonnes). Moreover, the model results showed that the tire temperature increased relatively rapidly at rising ambient temperatures from -30 to 40 °C.

As per the results from the OTRTire-T model, the cycle length coefficient $K_1$ and the site ambient temperature coefficient $K_2$ in the real site TKPH were refined. These refined coefficients provided insights into tire use at long cycle lengths and at cold ambient temperatures. For example, as per the refined $K_1$ coefficients, at an ambient temperature of 38 °C and an average cycle speed of 30 km/h, the real site TKPH increased from 2849 to 3049 tonne×km/h at rising cycle lengths from 10 to 20 km. Due to this increment in the real site TKPH, the truck payload was recommended to decrease by 31.8 tonnes when the cycle length was extended from 10 to 20 km.

At cold ambient temperatures of below 0 °C, as per the real site TKPH with refined site ambient temperature coefficient $K_2$, the loading capacity of the truck increased (compared with its rating payload of 363 tonnes) at mine sites. For example, at an ambient temperature of -5 °C and an average cycle speed of 38 km/h, the average vertical tire load was 89 tonnes, which indicates that the truck payload can be considered to be increased by 20.1% (i.e., having a recommended payload of 436 tonnes) during the haulage operations.

## Preface

This thesis is an original work by Shaosen Ma, which refined the real site TKPH (tonne-kilometer-per-hour) of ultra-large off-the-road (OTR) tires at mine sites. This thesis is based on five journal papers that have been published or submitted for consideration towards publication.

Chapter 2 of this thesis has been published as **S. Ma**, G. Huang, K. Obaia, S. W. Moon. W. V. Liu. Hysteresis loss of ultra-large off-the-road tire rubber compounds based on operating conditions at mine sites, *IMechE: Journal of Automobile Engineering*. © SAGE. (2022)

Chapter 3 of this thesis has been published as **S. Ma**, G. Huang, K. Obaia, S. W. Moon. W. V. Liu. A novel phenomenological model for predicting hysteresis loss of rubber compounds obtained from ultra-large off-the-road tires, *IMechE: Journal of Automobile Engineering*. © SAGE. (2022)

Chapter 4 has been submitted for peer review as **S. Ma**, Y. Guo, W. V. Liu. An analytical solution to predict temperatures of dumbbell-shaped rubber specimens under cyclic deformation, *Journal of Thermal Science and Engineering Applications*. © ASME Digital Collection. (2023)

Chapter 5 this thesis has been published as **S. Ma**, L. Wu, W. V. Liu. Numerical investigation of temperatures in ultra-large off-the-road tires under operating conditions at mine sites, *Journal of Thermal Science and Engineering Applications*. © ASME Digital Collection. (2023)

Chapter 6 has been submitted for peer review as **S. Ma**, C. Fan, W. V. Liu, Effects of site operating conditions on real site TKPH (tonne-kilometer-per-hour) of ultra-large off-the-road tires, *IMechE: Journal of Automobile Engineering*. © SAGE. (2023)

In this thesis, my work includes Conceptualization, Methodology, Validation, Formal analysis, Investigation, Data Curation, Writing, Review, and Editing. Dr. Wei Victor Liu was my academic supervisor, who contributed to Supervision, Resources, Review, and Editing in the thesis. Dr. Guangping Huang assisted in Review and Editing in Chapters 2 and 3. Mr. Yunting Guo, Dr. Linping Wu, and Mr. Chengkai Fan was involved in Review and Editing in Chapters 4, 5, and 6, respectively.

# DEDICATION

*This thesis is dedicated to my mother Xiurong Zhao and my wife Bingyu Xie.*

*I love you all dearly.*

me to go overseas to pursue my PhD degree and provides me valuable suggestions for my professional career.

Lastly, I would like to express my sincere gratitude to my mother Xiurong Zhao for her tremendous support, encouragement, and love. I extremely appreciate my wife Bingyu Xie for her dearly love.

# Table of contents

# List of tables

# List of figures

# Chapter 1. Introduction

## 1.1. Research background

Alberta's oil sands have the third-largest crude oil reserves worldwide, next to Venezuela and Saudi Arabia; oil sands mining is a key driver of Alberta's and Canada's economy (Stringham, 2012). During oil sands mining, truck haulage is the dominant bulk materials handling method that transports ores and overburdens (Sahoo et al., 2018). In truck haulage, ultra-large off-the-road (OTR) tires are the essential components of haul trucks. OTR tires refer to vehicle tires that use deep tread to provide traction on the unpaved haul roads covered by loose dirt, mud, sand, or gravel (Morton, 2017). Compared with highway-terrain (HT) tires, OTR tires contain deeper and wider grooves meant to help the tread sink into the haul road surfaces and tow the trucks under the operating conditions of high payload, low speed, and short-distance travel (Michelin, 2016). These OTR tires (e.g., Michelin XDR (Michelin, 2016) or Bridgestone VRDP (Bridgestone, 2020)) are expensive. For instance, one OTR tire for a 400-ton Caterpillar 797 truck costs about CA$ 60,000 (Oil Sands Discovery Center, 2016). However, the service life of OTR tires is short, lasting only 6 to 15 months (Oil Sands Discovery Center, 2016). This leads to high costs in tire repairs and replacements, which can account for over 25% of total operating costs and exceed the original purchase price of a truck over its lifetime (Carter, 2011). This also causes delays in production schedule and decreases in mine productivity.

The short service life of OTR tires is related to hysteresis loss and subsequent overheating in OTR tires (Li et al., 2012; Marais, 2017; Marais and Venter, 2018; Nyaaba, 2017). When a truck moves and its tires are subjected to cyclic deformations, the variation of strains in tires lags behind that of their stresses, accompanying by hysteresis loss (Hu et al., 2019). From hysteresis loss, heat

is generated and then trapped in tires, causing an internal heat build-up and a tire temperature rise (Marais, 2017). High tire temperatures of even up to 95 ℃ were reported under daily haulage operations at mine sites (Kerr, 2017; Meech and Parreira, 2013). These high tire temperatures can lead to a thermal weakening of tire rubbers, steel cords, and rubber-cord composites (Jamshidi et al., 2006; Z. P. Wang et al., 2013). The stiffness of tire rubbers and steel cords and the adhesion strength of rubber-cord composites tend to decrease as the tire temperature rises (Ramazani et al., 2011; Wu, 2009). In addition, a thermo-oxidation degradation of tire rubbers may occur at high tire temperatures (e.g., 95 ℃) (Benoit et al., 2009; Dolez et al., 2008). All of these may result in tire failures (Anzabi, 2015; Anzabi et al., 2012) and short service life of tires.

To reduce overheating and increase tire service life, mining companies use a TKPH (tonne-kilometer-per-hour) approach to managing OTR tires. The basis for this approach is that if mine operators ensure that the real site TKPH (Michelin, 2016) is kept smaller than the tire TKPH this will reduce tire failures. The tire TKPH is a rating of OTR tires; it is provided by tire manufacturers (e.g., Michelin, Bridgestone, Magna, Goodyear, and Continental) to characterize the working capacity of the tire (Caterpillar, 2018; Pascual et al., 2019). The real site TKPH is an index calculated from site operating conditions, including average vertical load per tire ($Q_m$) (having the conversion to payload), average cycle speed ($V_m$), cycle length (in relation to the cycle length coefficient $K_1$), and ambient temperature (related to the site ambient temperature coefficient $K_2$) (Michelin, 2016), and it is derived as

$$\text{Real site TKPH} = Q_m \times V_m \times K_1 \times K_2 \tag{1.1}$$

The TKPH approach (real site TKPH < tire TKPH) aims at reducing tire temperatures and increasing tire service life. However, this TKPH approach does not work well for OTR tires when

the tires are used at long cycle lengths. When the cycle length is longer than 10 km, unexpected high tire temperatures and short tire service life are frequently reported even if the TKPH approach has been applied to OTR tires. For example, one mine site tested a truck haulage having a cycle length of 12.8 km and using the Michelin 56/80R63 OTR tire (with the highest rating of tire TKPH of 2765). In this haulage, excessive tire temperatures (~90 °C) were recorded within the OTR tire (Syncrude, 2018). Also, tire deflation incidents occurred four times per week; tire suffered from various separations in liner, turn-up, bead, and sidewall—these are all signs of failures due to tire overheating. As a result, tire service life dropped from ~6000 hours (a normal average) to only 2800 hours (Syncrude, 2018). In addition to long cycle lengths, the current TKPH approach does not work well for OTR tires and it does not give any insights into tire temperatures when the tires are used at cold ambient temperatures (e.g., < 0 °C). In winter seasons, OTR tires can often carry a higher payload than the value estimated by the TKPH approach but the tire is not overheating (i.e., internal air temperatures are not exceeding 75 °C (Marais and Venter, 2018)) (Ta, 2018).

The TKPH approach does not work well at long cycle lengths (e.g., > 10 km) and at cold ambient temperatures (e.g., < 0 °C), which may be related to the lack of understanding in the cycle length coefficient $K_1$ and site ambient temperature coefficient $K_2$. As per in Equation (1.1), the Michelin's formula is too empirical regarding the determination of the $K_1$ and $K_2$ coefficients. For instance, the formula includes a set of $K_1$ coefficients ranging from 1.00 to 1.23 when the cycle length varies from 5 to 50 km and it selects the $K_2$ coefficients in the range of 0.635 to 1.016 as the ambient temperature is raised from 15 to 40 °C (Michelin, 2016). However, these $K_1$ and $K_2$ coefficients are only suggested in Michelin's handbook (Michelin, 2016), and they have not been validated by mining companies using real site operating conditions. It still remains unclear whether these coefficients can reflect the effects of site operating conditions on OTR tire temperatures and

guide the use of OTR tires at mine sites, especially at long cycle lengths (e.g., > 10 km) and at cold ambient temperatures (e.g., < 0 ℃).

For this, it is of great significance to understand the effects of site operating conditions on the $K_1$ and $K_2$ coefficients and refine these coefficients. Incorporating these refined $K_1$ and $K_2$ coefficients into the real site TKPHs may help utilize the TKPH approach for reducing overheating of OTR tires and prolonging tire service life, ultimately help mining companies save costs on OTR tires.

Despite its significance, a search of the literature over the past 20 years for relevant investigations yielded limited results. Thus, fundamental research is urgently needed to refine the cycle length coefficient $K_1$ and site ambient temperature coefficient $K_2$ and improve the real site TKPH under operating conditions at mine sites.

## 1.2. Research objectives

The overall objective of this thesis is to refine the real site TKPH (tonne-kilometer-per-hour) of ultra-large off-the-road (OTR) tires at mine sites. To achieve this overall objective, five sub-objectives are proposed as follows:

1.  To investigate the hysteresis loss of OTR tire rubbers experimentally;
2.  To develop a model for predicting the hysteresis loss of OTR tire rubbers;
3.  To evaluate the heat generation rate and temperatures of OTR tire rubbers;
4.  To predict the temperatures in OTR tires under site operating conditions, especially at long cycle lengths (e.g., > 10 km) and at cold ambient temperatures (e.g., < 0 ℃);
5.  To examine the effects of the long cycle lengths and cold ambient temperatures on real site TKPHs of OTR tires.
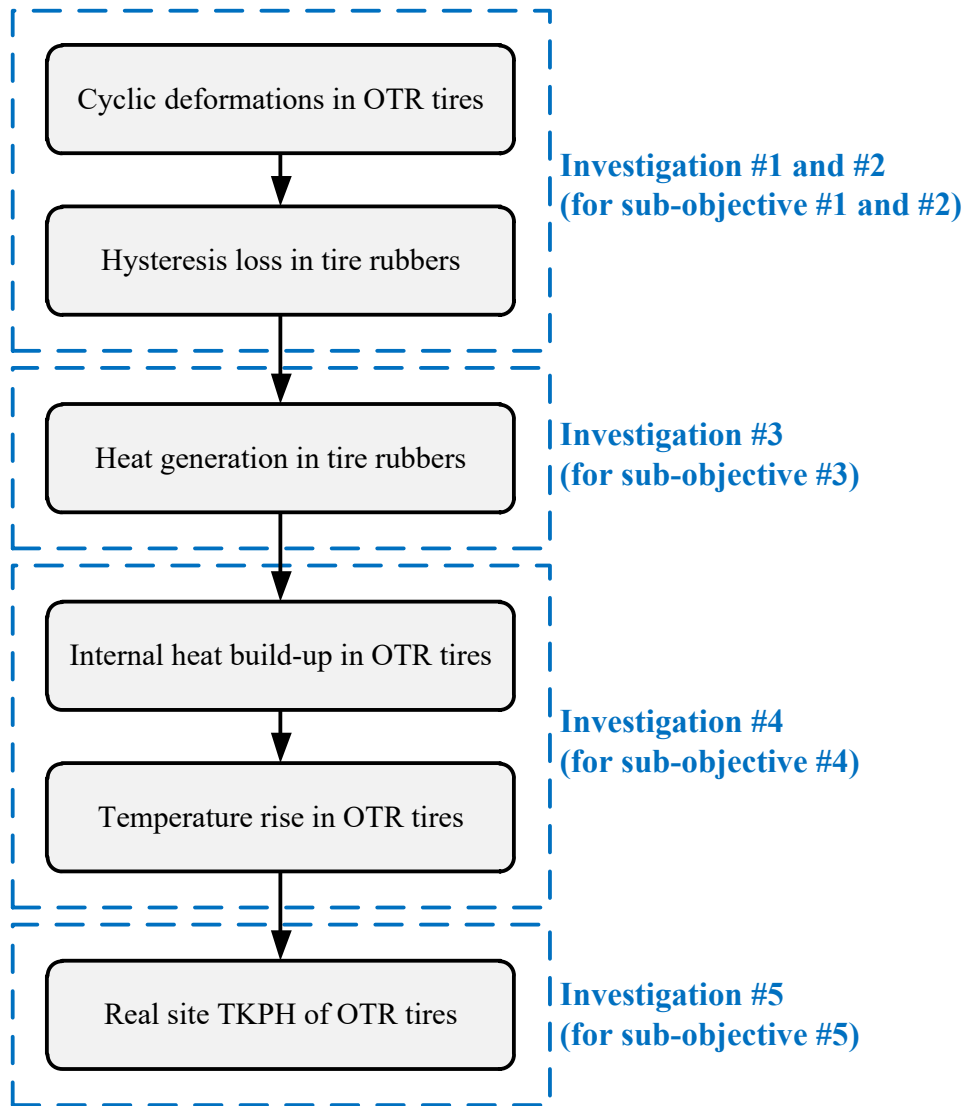
Figure 1.1. A flowchart showing the connection between the sub-objectives

The connection between these sub-objectives is presented in Figure . As shown in Figure , when a truck moves and its tires are subjected to cyclic deformations, the variation of strains in tires lags behind that of their stresses, accompanying by hysteresis loss (Hu et al., 2019). The hysteresis loss is of great interest since it is the source of the heat generated in OTR tire rubbers (Nyaaba, 2017). For this, Investigation #1 is conducted to experimentally examine the hysteresis loss of OTR tire rubbers. Based on the test results in Investigation #1, Investigation #2 is made to

develop a model for predicting the hysteresis loss based on operating conditions at mine sites. This model is then incorporated in Investigation #3 to evaluate the heat generation in OTR tire rubbers.

The heat generated in rubbers is trapped in OTR tires, causing an internal heat build-up and a tire temperature rise (Marais, 2017). This tire temperature rise is of interest because it may cause softening and thermal degradation of tire rubbers (Dolez et al., 2008) and result in short tire service life when the tire temperature increases up to high values (e.g., 95 °C). For this, Investigation #4 is conducted to predict the temperatures in OTR tires. These predictions are made under different operating conditions at mine sites, especially at long cycle lengths (e.g., > 10 km) and at cold ambient temperatures (e.g., < 0 °C).

As per the results derived from Investigation #4, Investigation #5 refined the cycle length coefficient $K_1$ and site ambient temperature coefficient $K_2$ by fundamentally investigating the effects of cycle lengths and ambient temperatures on tire temperatures at mine sites. Based on these coefficients, the real site TKPHs are calculated under different site operating conditions, especially at long cycle lengths (e.g., > 10 km) and at cold ambient temperatures (e.g., < 0 °C). It is of great significance to refine the real site TKPHs ($K_1$ and $K_2$ coefficients) because it can help utilize the TKPH approach for reducing overheating of OTR tires and prolonging tire service life.

## 1.3. Thesis statement and thesis outline

**Thesis statement:** Real site TKPHs are the key in utilizing the TKPH approach for reducing overheating of OTR tires and prolonging tire service life. The real site TKPHs can be refined by investigating the hysteresis loss, heat generation, and temperatures of OTR tires under operating conditions at mine sites.

As shown in Figure , this thesis includes seven chapters, presenting in a paper-based format. The summary of each chapter is listed as follows.

```
┌─────────────────────────────┐
│ Chapter 2:                  │
│ Hysteresis loss of OTR tire │
│ rubbers based on operating  │
│ conditions at mine sites    │
└─────────────────────────────┘

┌─────────────────────────────┐
│ Chapter 3:                  │
│ A novel phenomenological    │
│ model for predicting        │
│ hysteresis loss of OTR tire │
│ rubbers                     │
└─────────────────────────────┘

┌──────────────────┐   ┌─────────────────────────────┐   ┌──────────────────┐
│ Chapter 1:       │   │ Chapter 4:                  │   │ Chapter 7:       │
│ Research         │   │ An analytical solution to   │   │ Conclusions and  │
│ background,      │→  │ predict temperatures of     │ → │ contributions    │
│ literature       │   │ OTR tire rubbers under      │   │                  │
│ review, research │   │ cyclic deformation          │   └──────────────────┘
│ problems,        │   └─────────────────────────────┘
│ objective, and   │
│ thesis statement │   ┌─────────────────────────────┐
└──────────────────┘   │ Chapter 5:                  │
                       │ Numerical investigation of  │
                       │ temperatures in OTR tires   │
                       │ under operating conditions  │
                       │ at mine sites               │
                       └─────────────────────────────┘

                       ┌─────────────────────────────┐
                       │ Chapter 6:                  │
                       │ Effects of site operating   │
                       │ conditions on real site     │
                       │ TKPH of OTR tires           │
                       └─────────────────────────────┘
```

Figure 1.2. A flowchart showing the outline of this thesis.

**Chapter 1** introduces the research background regarding OTR tires and real site TKPH. This chapter points out the research problems, and also includes the research objectives and thesis statement.

**Chapter 2** aims to investigate the hysteresis loss of ultra-large OTR tire rubbers based on operating conditions at mine sites. Cyclic tensile tests were conducted on OTR tire rubbers at six strain levels ranging from 10% to 100%, eight strain rates from 10% to 500% s$^{-1}$, and fourteen rubber temperatures from -30 to 100 ℃. The test results showed that a large strain level (e.g., 100%) increased the hysteresis loss of tire rubbers considerably. Hysteresis loss of tire rubbers increased with a rise of strain rates, and the increasing rates became greater at large strain levels (e.g., 100%). Moreover, a rise of rubber temperatures caused a decrease in hysteresis loss; however, the decrease became less significant when the rubber temperatures were above 10 ℃. Compared with tread rubbers, sidewall rubbers showed greater hysteresis loss values and more rapid increases in hysteresis loss with the rising strain rates.

**Chapter 3** developed a novel phenomenological model that can predict the hysteresis loss of rubbers obtained from ultra-large OTR tires under typical operating conditions at mine sites. To achieve this, first, cyclic tensile tests were conducted on tire rubbers to derive the experimental results of hysteresis curves, peak stress, residual strain, and hysteresis loss at six strain levels, eight strain rates, and fourteen rubber temperatures. Then, referring to these experimental results, a phenomenological model was developed—the HLSRT model (a Hysteresis Loss model considering Strain levels, strain Rates, and rubber Temperatures). This HLSRT model was generated based on a novel strain energy function that was modified from the traditional Mooney-Rivlin (MR) function, and the model was used to predict the hysteresis loss of OTR tire rubbers. The prediction results showed that the HLSRT model estimated the hysteresis loss of tire rubbers with average and maximum mean absolute percent errors (MAPEs) of 11.2% and 18.6%, respectively, at strain levels ranging from 10% to 100%, strain rates from 10% to 500% s$^{-1}$, and rubber temperatures from -30 to 100 ℃. These MAPEs were relatively low when compared with

previous studies, showing that the HLSRT model has higher prediction accuracy. For the first time, the HLSRT model derived from this study has provided a new approach to predicting the hysteresis loss of OTR tire rubbers to guide the use of OTR tires in truck haulage at mine sites.

**Chapter 4** proposed an analytical solution that can predict temperatures of dumbbell-shaped rubber specimens under cyclic deformation. To achieve this, first, a new mathematical equation was developed based on a modified MR strain energy function, the pseudo-elasticity theory, and the inverse analysis method. This equation was used to determine the internal heat generation rates of tire rubbers. With heat generation rates, the governing equation of heat conduction and the mathematical expression of boundary conditions were further generated to describe the heat transfer in rubbers. Based on these equations, a novel analytical solution was developed—the RTDS solution (a solution to predict Rubber Temperatures in Dumbbell-shaped Specimens). This RTDS solution was used to predict rubber temperatures in dumbbell-shaped specimens under cyclic deformation. The results showed that the RTDS solution took 11.9 seconds to derive the rubber temperature results with an average MAPEs of 9.2% compared with lab recordings. The RTDS solution identified a logarithmic increase in rubber temperatures at rising strain levels, and it also identified an increase in rubber temperatures with the rising strain rates. Moreover, the RTDS solution characterized an inverse proportional relationship between the rubber temperature increments and the ambient temperatures.

**Chapter 5** aims to conduct a numerical investigation to examine the temperatures in OTR tires under operating conditions at mine sites. To achieve this, a new mathematical equation was developed based on a modified MR strain energy function, the pseudo-elasticity theory, and the inverse analysis method. This equation was used to determine the internal heat generation rates of tire rubbers. With heat generation rates, the governing equation of heat conduction and the

mathematical expression of boundary conditions were further generated to describe the heat transfer in tire rubbers. Based on these equations, a novel finite element (FE) OTR tire thermal (OTRTire-T) model was developed. This OTRTire-T model was used to numerically investigate the temperatures in OTR tires at vertical loads from 34 to 104 tonnes, truck speeds from 5 to 30 km/h, and ambient temperatures from -30 to 40 ℃. The results showed that a large vertical tire load (e.g., 104 tonnes) increased the tire rubber temperatures considerably. Tire rubber temperature also increased with a rise in truck speeds, and the increase became more significant at larger vertical loads (e.g., 104 tonnes). The OTRTire-T model identified an inverse proportional relationship between the rubber temperature increments and the ambient temperatures from -30 to 40 ℃. Nonetheless, the rubber temperature in the OTR tire increased relatively rapidly with a rise in ambient temperatures.

**Chapter 6** investigated the effects of site operating conditions on the real site TKPH (tonne-kilometer-per-hour) of ultra-large off-the-road (OTR) tires. To achieve this, a novel finite element OTR tire thermal (OTRTire-T) model was developed to predict the temperatures of OTR tires. As per the results from the OTRTire-T model, the cycle length coefficient $K_1$ and the site ambient temperature coefficient $K_2$ were refined and then compared with existing coefficients in the literature for cross-verification. After cross-verification, these $K_1$ and $K_2$ coefficients were used to calculate the real site TKPHs. The real site TKPHs were investigated under different site operating conditions (i.e., average vertical tire loads, average cycle speeds, ambient temperatures, and cycle lengths). The results showed that the real site TKPH increased with an increment in average cycle speeds from 10 to 45 km/h and a rise in ambient temperatures from -30 to 40 ℃. At cold ambient temperatures of below 0 ℃, as per the refined $K_2$ coefficients, the loading capacity of the truck increased (compared with its rating payload of 363 tonnes) at mine sites. In addition,

according to the refined $K_1$ coefficients, the real site TKPH increased as the cycle length extended, resulting in a decrease in the recommended truck payloads at rising cycle lengths from 10 to 20 km.

**Chapter 7** summarized the primary conclusions, contributions, limitations of this thesis. Recommendations for future research are also discussed.

# Chapter 2. Hysteresis loss of ultra-large off-the-road tire rubbers based on operating conditions at mine sites

## 2.1. Introduction

At mine sites, truck haulage is the dominant bulk material handling method that transports ores and overburdens (Sahoo et al., 2018). Haul trucks are equipped with ultra-large off-the-road (OTR) tires that are one of their most expensive parts. For instance, one OTR tire for a 400-ton Caterpillar 797 truck costs about CA$ 60,000 (Oil Sands Discovery Center, 2016). However, the service life of OTR tires is short, lasting only 6 to 15 months (Oil Sands Discovery Center, 2016). This leads to high costs in tire repairs and replacements, which can account for over 25% of total operating costs and exceed the original purchase price of a truck over its lifetime (Carter, 2011).

The short service life of OTR tires is believed to be related to hysteresis loss and subsequent overheating in OTR tire rubbers (Kerr, 2017; Li et al., 2012; Marais, 2017; Meech and Parreira, 2013; Nyaaba, 2017; Nyaaba et al., 2019b; Parreira, 2013). When a truck moves and its tires are subjected to cyclic deformations (Marais and Venter, 2018), the variation of strains in tire rubbers lags behind that of their stresses, accompanying by hysteresis loss (Hu et al., 2019). From hysteresis loss, heat is generated and then trapped in rubbers, causing an internal heat build-up and a rubber temperature rise (Marais, 2017). High rubber temperatures of even up to 95 ℃ were reported under daily haulage operations at mine sites (Kerr, 2017; Meech and Parreira, 2013). At the high rubber temperatures, the hysteresis loss of rubbers tends to decrease (He, 2005; He et al., 2006; Lv, 2005; Terrill et al., 2010), which mitigates the further heat build-up in rubbers. However, these high rubber temperatures are detrimental because high rubber temperatures may cause softening and thermal degradation of rubbers (Dolez et al., 2008), resulting in rubber failures (Anzabi, 2015; Anzabi et al., 2012; Lindeque, 2016; Zhou et al., 2008) and short service life of tires. This has raised much attention from mining researchers. Some research has started to

examine the hysteresis loss of OTR tire rubbers. For instance, the hysteresis loss of Bridgestone 24.00R35 OTR tire tread rubbers was studied by a hysteresis constant to estimate the rubber heat generation rates according to different truck speeds within 48 km/h (Li et al., 2012). These hysteresis loss-induced heat generation rates are the key parameters for modeling a rolling tire (Li et al., 2012), and the rates were applied by Marais and Venter (Marais and Venter, 2018) to create a thermal model for a 23.5R25 OTR tire and to predict the temperature rise in one of its cross-sections at the truck speeds of 15, 30 and 45 km/h. The results of tire thermal modeling showed that there were high temperatures (e.g., 80 °C) in rubbers located at both treads and sidewalls (Marais and Venter, 2018). A Michelin 56/80R63 OTR tire was numerically tested at the payloads of 101 tonnes and 115 tonnes and the truck speeds of 32 km/h and 48 km/h. The results indicated that tread and sidewall rubbers were susceptible to failures after certain deformation cycles (Nyaaba et al., 2019b). However, the abovementioned studies of OTR tire rubbers are still limited in that they focused on the application of hysteresis loss in rubber heat estimation and tire thermal modeling, but failed to investigate the hysteresis loss fundamentally and systematically.

Despite limited studies on OTR tire rubbers, there are more fundamental studies regarding the hysteresis loss of rubbers from highway-terrain (HT) tires under different testing conditions, including strain levels (Liu, 2007; Liu and Fatt, 2011), strain rates (Zhi et al., 2019, 2017) and rubber temperatures (He, 2005; He et al., 2006; Lv, 2005; Terrill et al., 2010). For example, hysteresis loss of rubbers obtained from a Bridgestone HT tire was examined at the strain rate of 1000% $s^{-1}$ and a rubber temperature of 20 °C (Liu, 2007). In this study, the hysteresis loss increased by 6 times when the strain level was raised from 10% to 40% (Liu, 2007). In addition, it was reported that the hysteresis loss of tread rubbers from a semi-steel radial tire at a high strain rate of 60% $s^{-1}$ was 21% greater than the hysteresis loss at 10% $s^{-1}$ (Zhi et al., 2017). Tire rubbers also

experienced over a 24% reduction in hysteresis loss when the rubbers were heated from 30 to 95 °C (Lv, 2005). However, the rubber recipes and operating conditions of OTR tires are different from those of HT tires. For instance, compared with a tread rubber of an Avon HT tire reported by Terrill et al. (Terrill et al., 2010), an OTR tire tread rubber contained 13.4% more polymer and 13% less carbon black (CB) (Joseph, 2014). Moreover, according to site data from an Athabasca oil sands mine (Ta, 2018), a Michelin 56/80R63 OTR tire carried a maximum payload of 104 tonnes at the truck speeds of 20 ~ 30 km/h on average, and these payloads and truck speeds are different from the operating conditions of HT tires on highways (e.g., a 195/60R14 HT tire rolls at the payload of 520 kg and the vehicle speed of 110 km/h on highways (Wu, 2009)). The differences in rubber recipes and operating conditions can result in the inability to reliably apply the results that are obtained from HT tire rubbers to OTR tire rubbers since rubber recipes and operating conditions can significantly affect the hysteresis loss of tire rubbers (El-Zomor, 2019; Narasimha Rao et al., 2006; Yoo et al., 2017). Based on this, it is found that there is a lack of fundamental research focusing on the hysteresis loss of real OTR tire rubbers based on operating conditions at mine sites. A comprehensive study is essential to investigate the effects of site operating conditions on the hysteresis loss of rubbers in real OTR tires.

To this end, this study aims to investigate the hysteresis loss of ultra-large OTR tire rubbers based on operating conditions at mine sites. Cyclic tensile tests were conducted on tread and sidewall rubbers since they often experience higher rubber temperatures (e.g., above 80 °C) at mine sites. The testing conditions covered six strain levels ranging from 10% to 100%, eight strain rates from 10% to 500% s$^{-1}$, and fourteen rubber temperatures from -30 to 100 °C.

## 2.2. Materials and Methods

### 2.2.1. Materials

The tread and sidewall rubbers were cut from a Michelin 56/80R63 E3 XDR S C4 OTR tire. This OTR tire is used for Caterpillar 797F trucks (Caterpillar, 2009) that are widely employed in oil sands mining.

According to ASTM D6370-99 (ASTM D6370-99, 2019), a compositional analysis by thermogravimetry (TG) was conducted to determine the amounts of organics (i.e., oil, polymer), CB and ash (e.g., Zinc Oxide and Silica) in tread and sidewall rubbers. The compositional results of tread and sidewall rubbers are listed in Table 2.1.

Table 2.1. Compositional results of tread and sidewall rubbers (% in weight)

| Rubber type | Organics (oil, polymer) | Carbon black | Ash (ZnO, Si) |
|---|---|---|---|
| Tread rubber | 67.55% | 23.23% | 9.22% |
| Sidewall rubber | 67.55% | 31.27% | 1.18% |

According to ASTM D412-16 (ASTM D412-16, 2016), the tread and sidewall rubbers were thinly sliced with a thickness of 2 mm each, using a rubber blade. Then, these slices were further cut into standard dumbbell-shaped specimens using a high-power laser cutter. The dimensions of the specimens are shown in Figure 2.1 in the units of mm. A series of calibrations were performed for the thickness of the dumbbell-shaped specimens. For each specimen, three measurements were made at three locations separately using a caliper, with one at the center and two at each end of the reduced section of the dumbbell. The specimens were saved when the difference between the maximum and minimum thicknesses was less than 0.08 mm.
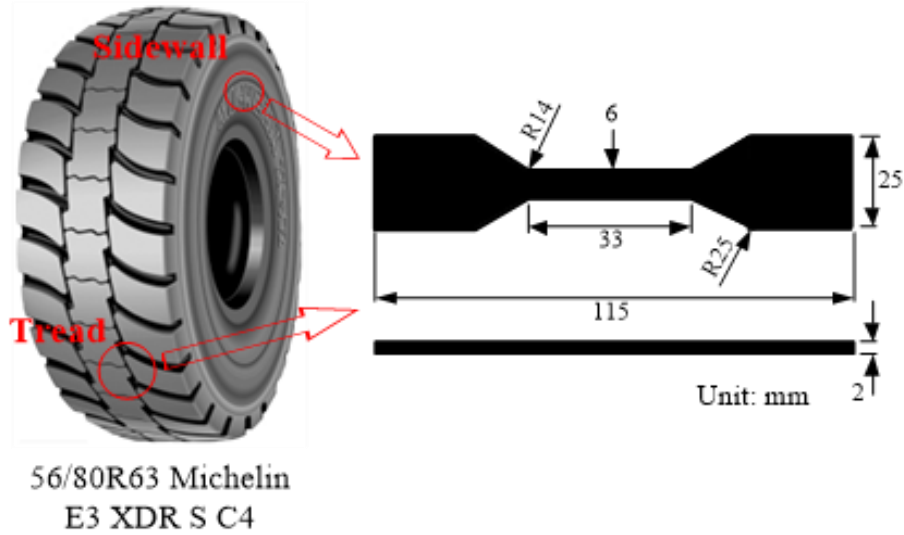
Figure 2.1. Source and dimensions of dumbbell-shaped tread and sidewall rubber specimens

## 2.2.2. Methods

To understand the effects of strain levels, strain rates and rubber temperatures on the hysteresis loss of tread and sidewall rubbers, cyclic tensile tests were conducted at six strain levels, eight strain rates, and fourteen rubber temperatures, as listed in Table 2.2. These testing conditions were obtained from the typical operating conditions on an Athabasca oil sands mine for a period of 365 days in 2018, as referred to in Appendix 2A. The schematic of the experimental setup is represented in Figure 2.2.

Table 2.2. Strain levels, strain rates and rubber temperatures in cyclic tensile tests

| Rubber type | Strain rate (s⁻¹) | Rubber temperature (°C) | Strain level (m/m) |
|---|---|---|---|
| Tread/Sidewall | 10%, 25%, 50%, 100%, 200%, 300%, 400%, and 500% | -30, -20, -10, 0, 10, 20, 30, 40, 50, 60, 70, 80, 90, and 100 | 10%, 20%, 40%, 60%, 80%, and 100% |
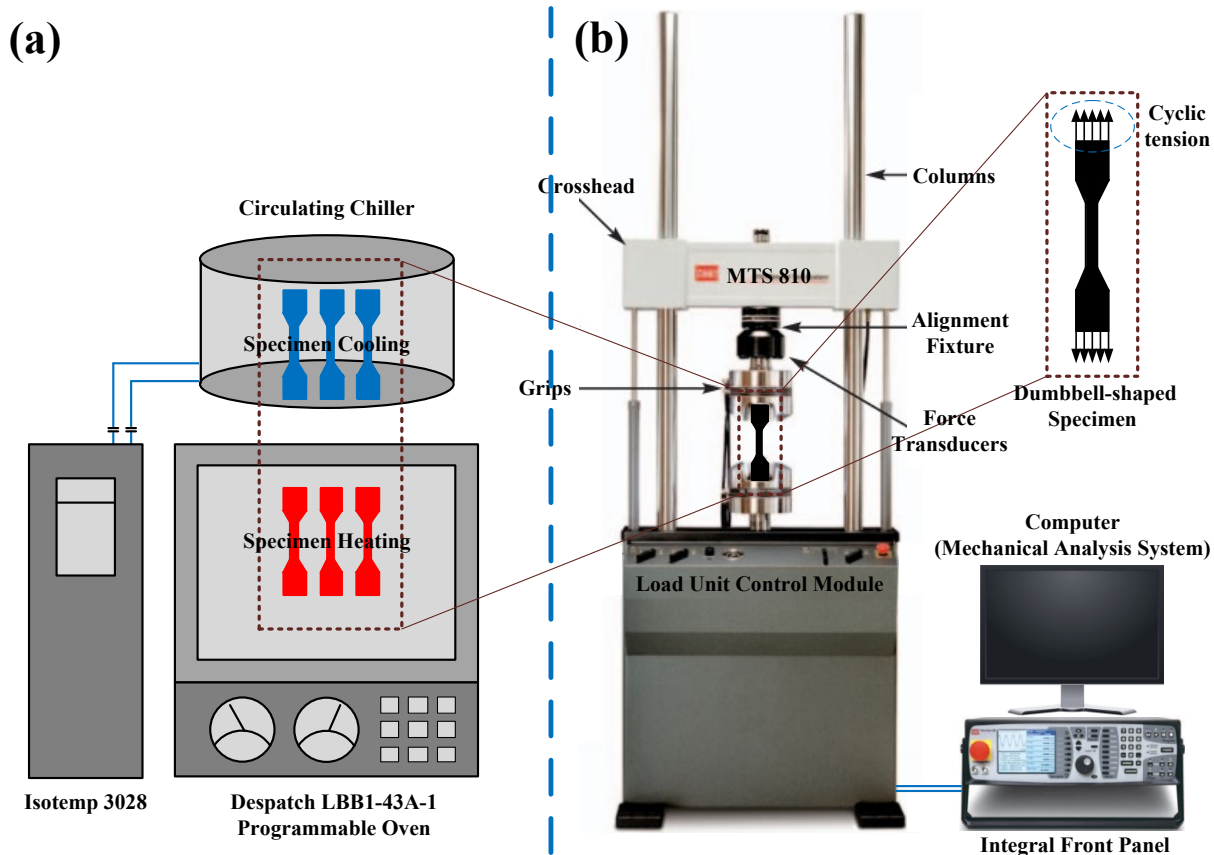
Figure 2.2. Schematic of the experimental setup: (a) programmable oven and circulating chiller;

(b) MTS 810 machine

### 2.2.2.1. Heating and cooling treatments

As shown in Figure 2.2(a), heating and cooling treatments were conducted on the dumbbell-shaped tread and sidewall rubber specimens. Eight groups of the specimens (with three specimens in each group) were heated with a Despatch LBB1-43A-1 programmable oven separately at the temperatures of 30, 40, 50, 60, 70, 80, 90 and 100 ℃. This oven has the capability of heating to 204 ℃ and control stability of ±0.5 ℃ (LBB, 2011). In addition, six other groups of specimens (again with three specimens in each group) were cooled with an Isotemp 3028 circulating chiller at the cold temperatures of -30, -20, -10, 0, 10 and 20 ℃, respectively. This

chiller can create a cold-temperature environment of lower than -30 ℃ with higher control stability of ±0.01 ℃ (Isotemp, 2005). Both the heating and cooling treatments lasted 24 hours to ensure a uniform rubber temperature in each specimen.

*2.2.2.2. Cyclic tensile tests*

Cyclic tensile tests were conducted on the heated (30 to 100 ℃) and cooled (-30 to 20 ℃) specimens using an MTS 810 servo-hydraulic machine (with a 25 kN load cell), as shown in Figure 2.2(b). The MTS 810 machine can stretch the specimens at a maximum stroke speed of 20000 mm/min, with an accuracy of 0.5% (MTS, 2006).

During cyclic tensile tests, multi-stage stretching-releasing operations (Krmela and Krmelová, 2017; Nyaaba et al., 2019a) were used to obtain the stress-strain curves of the specimens at six strain levels of 10%, 20%, 40%, 60%, 80%, and 100%. An example of a multi-stage stretching-releasing operation performed on a tread rubber specimen at 20 ℃ and 500% s$^{-1}$ can be described as follows: under a displacement-controlled mode, a tread rubber specimen was stretched uniaxially and reached a strain level of 10% before being released back to zero at a strain rate of 500% s$^{-1}$. This stretching-releasing operation was repeated five times at the 10% strain level since the stress-strain curves obtained from the first three cycles of stretching-releasing were unstable. Afterwards, the specimen was further stretched and released in the same manner at the 20%, 40%, 60%, 80%, and 100% strain levels successively until the stress-strain curves were created at all six strain levels. The stress-strain curves derived from this example of multi-stage stretching-releasing operation are represented in Figure 2.3.
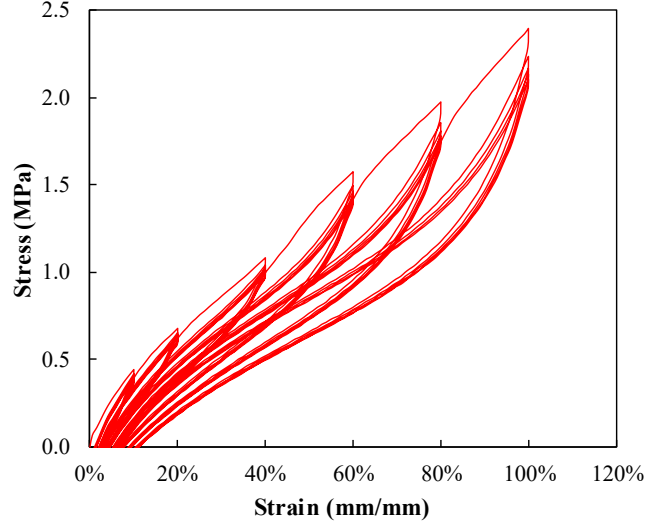
Figure 2.3. Stress-strain curves from an example of multi-stage stretching-releasing operation performed on a tread rubber specimen at 20 °C and 500% s[-1]

### 2.2.3. Calculation of hysteresis loss

As mentioned, the stress-strain curves obtained from the first three cycles of stretching-releasing at each strain level were unstable. Thus, in this study, the stable stress-strain curves from the last two cycles of stretching-releasing were used to calculate the hysteresis loss of tire rubbers at different strain levels.

The hysteresis loss was calculated following a method widely used in previous studies (Cho et al., 2013; Li et al., 2018, 2016; Luo et al., 2010). The hysteresis loss $H_\varepsilon$ (in kJ/m$^3$) of tire rubbers within one cycle of stretching-releasing operation was calculated as follows:

$$H_\varepsilon = W_{\varepsilon, \, load} - W_{\varepsilon, \, unload} = \int_0^\varepsilon \sigma_{load} \left( \varepsilon \right) d\varepsilon - \int_0^\varepsilon \sigma_{unload} \left( \varepsilon \right) d\varepsilon \qquad (2.1)$$

where $W_{\varepsilon, load}$ (in kJ/m³) and $W_{\varepsilon, unload}$ (in kJ/m³) are the strain energy per unit volume during stretching and releasing operations, respectively, and $\sigma_{load}(\varepsilon)$ (in MPa) and $\sigma_{unload}(\varepsilon)$ (in MPa) are the tensile stresses corresponding to a specific strain level $\varepsilon$ (in m/m) during stretching and releasing operations, respectively.

The hysteresis loss of tire rubbers within one cycle of stretching-releasing operation corresponds to the heat generation of tire rubbers during one revolution of the tire, as per other researchers (Maritz, 2015; Smith et al., 2012; Tang et al., 2014).

## 2.3. Results and discussion

Table 2.3 shows the hysteresis loss results of tread and sidewall rubbers under different testing conditions (i.e., strain levels, rubber temperatures, and strain rates). The strain levels changed from 10% to 100%, and the rubber temperatures varied from -30 to 100 ℃. The testing conditions also covered the strain rates ranging from 10% to 500% s$^{-1}$ and included a reference strain rate at 1% s$^{-1}$.

Table 2.3. Hysteresis loss results of tread and sidewall rubbers under different testing conditions

(in kJ/m$^3$)

| Tread | Strain rate: 1% s$^{-1}$ | | | Strain rate: 10% s$^{-1}$ | | | Strain rate: 100% s$^{-1}$ | | | Strain rate: 500% s$^{-1}$ | | |
|---|---|---|---|---|---|---|---|---|---|---|---|---|
| Strain level / Rubber temperature | 20% | 40% | 100% | 20% | 40% | 100% | 20% | 40% | 100% | 20% | 40% | 100% |
| -30 ℃ | 12.3 | 36.6 | 160.5 | 12.6 | 37.3 | 162.5 | 13.4 | 39.4 | 171.8 | 15.3 | 47.0 | 215.8 |
| -20 ℃ | 12.0 | 35.4 | 154.2 | 12.2 | 36.2 | 156.3 | 13.0 | 37.8 | 164.1 | 14.8 | 45.2 | 205.4 |
| -10 ℃ | 11.6 | 34.6 | 147.1 | 12.0 | 34.8 | 151.6 | 12.4 | 36.8 | 157.6 | 14.5 | 43.5 | 199.1 |
| 0 ℃ | 11.3 | 33.3 | 143.9 | 11.4 | 33.5 | 144.6 | 12.0 | 35.2 | 154.6 | 14.1 | 42.4 | 189.6 |
| 10 ℃ | 10.9 | 32.5 | 140.2 | 11.0 | 32.7 | 141.9 | 11.5 | 34.3 | 149.1 | 13.6 | 41.3 | 184.3 |
| 20 ℃ | 10.6 | 32.1 | 138.4 | 10.8 | 32.3 | 139.4 | 11.3 | 33.8 | 147.1 | 13.4 | 40.7 | 181.3 |
| 30 ℃ | 10.5 | 31.8 | 136.5 | 10.7 | 32.0 | 137.2 | 11.2 | 33.3 | 145.8 | 13.3 | 40.1 | 179.4 |
| 40 ℃ | 10.2 | 31.4 | 135.1 | 10.7 | 31.6 | 135.8 | 11.1 | 32.9 | 144.4 | 13.1 | 39.6 | 177.6 |
| 50 ℃ | 10.1 | 30.9 | 133.4 | 10.4 | 31.2 | 134.3 | 11.1 | 32.4 | 143.3 | 13.0 | 38.9 | 175.1 |
| 60 ℃ | 9.9 | 30.6 | 132.2 | 10.4 | 30.8 | 133.2 | 11.0 | 32.0 | 141.9 | 12.8 | 38.4 | 173.4 |
| 70 ℃ | 9.8 | 30.4 | 131.8 | 10.2 | 30.6 | 131.6 | 10.9 | 31.5 | 140.5 | 12.7 | 37.9 | 172.4 |
| 80 ℃ | 9.7 | 30.0 | 129.6 | 10.2 | 30.2 | 129.8 | 10.9 | 31.2 | 139.5 | 12.6 | 37.5 | 169.7 |
| 90 ℃ | 9.6 | 29.6 | 128.2 | 10.1 | 29.9 | 128.8 | 10.8 | 30.9 | 138.2 | 12.5 | 37.2 | 167.7 |
| 100 ℃ | 9.5 | 29.3 | 127.1 | 9.9 | 29.9 | 127.1 | 10.7 | 30.6 | 137.3 | 12.3 | 36.8 | 166.2 |
| **Sidewall** | **Strain rate: 1% s$^{-1}$** | | | **Strain rate: 10% s$^{-1}$** | | | **Strain rate: 100% s$^{-1}$** | | | **Strain rate: 500% s$^{-1}$** | | |
| Strain level / Rubber temperature | 20% | 40% | 100% | 20% | 40% | 100% | 20% | 40% | 100% | 20% | 40% | 100% |
| -30 ℃ | 14.3 | 43.3 | 188.1 | 15.1 | 44.5 | 189.4 | 15.6 | 45.4 | 196.8 | 18.2 | 56.9 | 254.1 |
| -20 ℃ | 13.7 | 41.6 | 180.2 | 14.1 | 42.4 | 179.5 | 14.5 | 43.5 | 190.4 | 17.5 | 54.3 | 240.6 |
| -10 ℃ | 13.2 | 39.7 | 174.2 | 13.4 | 39.6 | 173.1 | 14.0 | 42.1 | 180.6 | 16.9 | 51.1 | 232.2 |
| 0 ℃ | 12.8 | 37.7 | 164.6 | 12.8 | 37.8 | 165.4 | 13.3 | 40.4 | 174.4 | 16.1 | 49.7 | 221.6 |
| 10 ℃ | 12.2 | 36.8 | 157.5 | 12.2 | 36.8 | 159.6 | 12.8 | 38.9 | 168.8 | 15.6 | 47.8 | 213.5 |
| 20 ℃ | 11.9 | 35.8 | 154.1 | 12.0 | 36.1 | 155.3 | 12.6 | 38.1 | 165.4 | 15.3 | 46.5 | 209.6 |
| 30 ℃ | 11.7 | 35.1 | 152.3 | 11.8 | 35.7 | 152.8 | 12.5 | 37.7 | 162.5 | 15.0 | 45.3 | 206.1 |
| 40 ℃ | 11.5 | 34.8 | 147.8 | 11.7 | 34.9 | 150.1 | 12.4 | 37.2 | 158.8 | 14.7 | 44.8 | 203.4 |
| 50 ℃ | 11.4 | 34.0 | 144.5 | 11.5 | 34.4 | 147.2 | 12.2 | 36.5 | 155.2 | 14.5 | 44.0 | 199.6 |
| 60 ℃ | 11.3 | 33.2 | 142.1 | 11.3 | 33.7 | 144.2 | 12.0 | 35.7 | 152.1 | 14.2 | 43.2 | 197.7 |
| 70 ℃ | 11.0 | 32.7 | 139.8 | 11.1 | 33.3 | 143.3 | 12.0 | 35.2 | 150.6 | 13.9 | 42.9 | 194.2 |
| 80 ℃ | 10.9 | 32.2 | 136.8 | 10.9 | 32.8 | 139.9 | 11.8 | 34.2 | 146.2 | 13.7 | 42.0 | 190.2 |
| 90 ℃ | 10.7 | 31.9 | 133.4 | 10.8 | 32.3 | 138.0 | 11.7 | 33.9 | 144.9 | 13.5 | 41.3 | 187.8 |
| 100 ℃ | 10.4 | 31.0 | 131.6 | 10.6 | 31.9 | 136.9 | 11.6 | 33.3 | 143.4 | 13.4 | 40.6 | 182.9 |

Under different testing conditions, the hysteresis loss values of tire rubbers varied significantly, which is a result that is of great interest and has been rarely reported by current literature. For instance, at the strain rate of 500% s$^{-1}$ and a rubber temperature of 100 °C, the hysteresis loss of tread rubbers was 166.2 kJ/m$^3$ at the 100% strain level, which was about 13 times the result (12.3 kJ/m$^3$) at the 20% strain level. The hysteresis loss corresponds to the dissipated energy that is converted to heat (Cho et al., 2013; Lee et al., 2014; Tang et al., 2014; Van Blommestein, 2016). A large hysteresis loss is detrimental because it may lead to severe heat generation and subsequent overheating in OTR tire rubbers, as per other researchers (Li et al., 2012; Marais, 2017; Marais and Venter, 2018).

Cyclic tensile tests on the rubbers from the same model of OTR tires (Michelin 56/80R63) were conducted previously under the testing conditions of 1% s$^{-1}$, 20 °C and the 100% strain level, and these tests resulted in hysteresis loss of 134.1 kJ/m$^3$ (tread) and 150.6 kJ/m$^3$ (sidewall), respectively (Nyaaba, 2017; Nyaaba et al., 2019b). These values are similar to our test results (138.4 kJ/m$^3$ for tread; 154.1 kJ/m$^3$ for sidewall) in Table 2.3. In other words, our test results have been partially verified by values in the literature. Furthermore, it is of note that our test results were achieved under a broader range of testing conditions (i.e., strain rates of 10% ~ 500% s$^{-1}$ and rubber temperatures of -30 ~ 100 °C). For the first time, our test results correlated the hysteresis loss of OTR tire rubbers with the operating conditions at mine sites.

The hysteresis loss of rubbers from HT tires, in contrast to that of OTR tires, has been studied more extensively in current literature. For example, cyclic tensile tests were performed by Liu (Liu, 2007) on the rubbers obtained from a Bridgestone HT tire at the strain rates of 10% s$^{-1}$ and 100% s$^{-1}$. Under the same testing conditions of 20 °C and the 40% strain level, the reported hysteresis loss results were 39.7 kJ/m$^3$ at 10% s$^{-1}$ and 44.1 kJ/m$^3$ at 100% s$^{-1}$ (Liu, 2007). However,

these results are greater than those of tread (32.3 kJ/m$^3$ at 10% s$^{-1}$ and 33.8 kJ/m$^3$ at 100% s$^{-1}$) and sidewall rubbers (36.1 kJ/m$^3$ at 10% s$^{-1}$ and 38.1 kJ/m$^3$ at 100% s$^{-1}$) in Table 2.3. This proves that the hysteresis loss results derived from HT tire rubbers cannot be directly applied to OTR tire rubbers. In other words, the hysteresis loss of OTR tire rubbers should be studied based on the rubbers cut from real OTR tires.

Effects of strain levels on hysteresis loss of tread rubbers *错误!未找到引用源。* Figure 2.4 shows the relationship between hysteresis loss and strain levels for tread rubbers at 500% s$^{-1}$ and 20 °C. Herein, a strain level refers to the maximum tensile strain of tire rubbers within one stretching-releasing operation. According to Appendix 2A, the strain level of tire tread rubbers is approximately 40% when a truck is empty, and the rubber strain level reaches about 100% under a fully loaded condition (i.e., 363 tonnes).
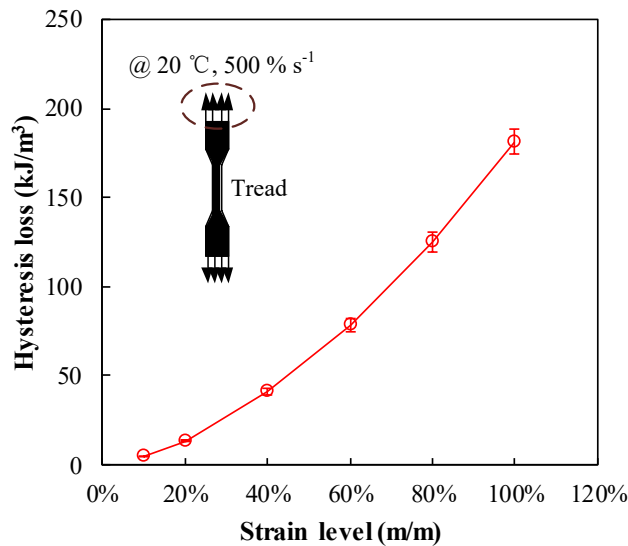


Figure 2.4. Relationship between hysteresis loss and strain levels for tread rubbers at 500% s$^{-1}$ and 20 °C

24

As shown in Table 2.3 and Figure 2.4, the hysteresis loss of tread rubbers increased with a rise of strain levels. At 500% s$^{-1}$ and 20 °C, as the strain level increased from 10% to 40%, the hysteresis loss of tread rubbers went up from 4.5 to 40.7 kJ/m$^3$, which shows a positive correlation between hysteresis loss and strain levels. A similar phenomenon was also observed in rubbers from HT tires. As reported by other researchers (Brancati et al., 2011; He, 2008; Krmela and Krmelová, 2017; Liu and Fatt, 2011), hysteresis loss correlated positively with strain levels in HT tire rubbers. For instance, cyclic tensile tests were conducted on the rubbers from a 12.00R20 HT tire at the strain rate of 33% s$^{-1}$ and a rubber temperature of around 23 °C. The results showed that the hysteresis loss of rubbers went up by 9 times when the strain level increased from 10% to 40% (He, 2008).

In Table 2.3 and Figure 2.4, it can be observed that a large strain level (e.g., 100%) increased the hysteresis loss of tread rubbers considerably. At 500% s$^{-1}$ and 20 °C, when the strain level was further raised from 40% to 100%, the hysteresis loss of tread rubbers increased from 40.7 to 181.3 kJ/m$^3$. This increment in hysteresis loss (140.6 kJ/m$^3$) was greater than that (36.2 kJ/m$^3$) from 10% to 40% strain level. This indicates that the effects of strain levels on the hysteresis loss became stronger as the strain levels reached large values (e.g., 100%). It is noted that these stronger effects of large strain levels on hysteresis loss are uncommon for the rubbers of HT tires. This is because the strain levels in HT tire rubbers are generally small. As indicated by other researchers (Li, 2012; Li et al., 2011; Xia et al., 2004), when used on highways, HT tire rubbers usually experience strain levels of less than 50%. Nevertheless, the strain levels of OTR tire rubbers are typically larger than this according to site operating conditions. At mine sites, OTR tire rubbers often show a strain level of 100%, which refers to the fully loaded condition. Moreover, it can be observed in Table 2.3 and Figure 2.4 that the hysteresis loss values of OTR

tire rubbers at large strain levels (e.g., 100%) were much greater than those subjected to small strain levels (e.g., within 50%). For example, as the strain level was raised up to 100%, the hysteresis loss of tread rubbers was 181.3 kJ/m$^3$, which was a result 4 times that (40.7 kJ/m$^3$) of tread rubbers at the 40% strain level. This indicates that during one revolution of the tire, heat generation of tread rubbers under the fully loaded condition could reach up to about 4 times that of when a truck is empty. The research on the influence of these large strain levels (e.g., 100%) on the hysteresis loss and heat generation of OTR tire rubbers is one of the highlights of this study.

**2.3.1. Effects of strain rates on hysteresis loss of tread rubbers**

Figure 2.5 illustrates the relationship between hysteresis loss and strain rates for tread rubbers at 20 °C. At the strain levels of 40% and 100%, the hysteresis loss of tread rubbers increased with a rise of strain rates generally, which was close to a linear trend. The strain rates were determined by the speeds of a truck following a similar procedure described by other researchers (Lin and Hwang, 2004; Maritz, 2015; Smith et al., 2012). For instance, for an empty truck, the strain rate of tire tread rubbers increases from 100% to 500% s$^{-1}$ when the truck speed is raised from 6 to 30 km/h. For a fully loaded truck, the tread strain rate goes up from 100% to 500% s$^{-1}$ when the truck speed increases from 4 to 20 km/h, as referred to in Appendix 2A.
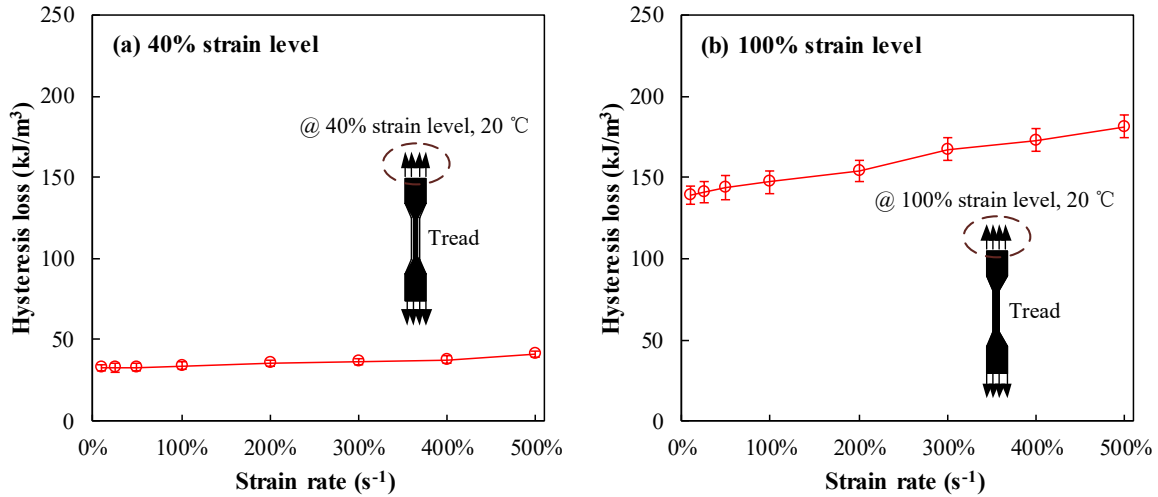
Figure 2.5. Relationship between hysteresis loss and strain rates for tread rubbers at 20 °C: (a) 40% strain level; (b) 100% strain level

As illustrated in Table 2.3 and Figure 2.5(a), the hysteresis loss of tread rubbers increased with the rising strain rates. At 20 °C and the 40% strain level, as the strain rate was raised from 100% to 500% s$^{-1}$, the hysteresis loss of tread rubbers increased from 33.8 to 40.7 kJ/m$^3$. This indicates that when a truck is empty, heat generation of tread rubbers during one revolution of the tire increases by 6.9 kJ/m$^3$ as the truck speed increases from 6 to 30 km/h. The increase of hysteresis loss with a rise of strain rates was known as strain-rate-dependent hysteresis loss in other studies (Azuma et al., 2007; Luo et al., 2010; Tomita et al., 2007). The strain-rate-dependent hysteresis loss was previously reported in HT tire rubbers by other researchers (Liu, 2007; Zhi et al., 2019). For example, according to Liu (Liu, 2007), the hysteresis loss of rubbers from a Bridgestone HT tire was studied at the same strain level of 40%, and a room temperature of 20 °C. The results showed that the hysteresis loss increased by 11% and 30% when the strain rate was raised from 10% to 100%, and then to 1000% s$^{-1}$, respectively.

Figure 2.5(b) presents the effects of strain rates on the hysteresis loss of tread rubbers at the 100% strain level. Compared with the increasing trend of hysteresis loss in Figure 2.5(a), the effects of strain rates became stronger: hysteresis loss increased with a rise of strain rates more rapidly at the 100% strain level than at the 40% strain level. As shown in Table 2.3 and Figure 2.5(b), at 20 ℃ and the 100% strain level, the hysteresis loss of tread rubbers grew from 147.1 to 181.3 kJ/m$^3$ when the strain rate increased from 100% to 500% s$^{-1}$. This indicates that under the fully loaded condition, heat generation of tread rubbers during one revolution of the tire went up by 34.2 kJ/m$^3$ when the truck speed was raised from 4 to 20 km/h. In addition, it is of note that the effects of strain rates on hysteresis loss were rarely examined in HT tire rubber rubbers at large strain levels (e.g., above 50%). This is because these large strain levels are not included in HT tire operating conditions on highways, as mentioned in Section 2.3.1.

**2.3.2. Effects of rubber temperatures on hysteresis loss of tread rubbers**

Figure 2.6 shows the variations of hysteresis loss with rubber temperatures in tread rubbers. At 500% s$^{-1}$ and the 100% strain level, the hysteresis loss of tread rubbers decreased from 215.8 to 166.2 kJ/m$^3$ when the rubber temperature was raised from -30 to 100 ℃.
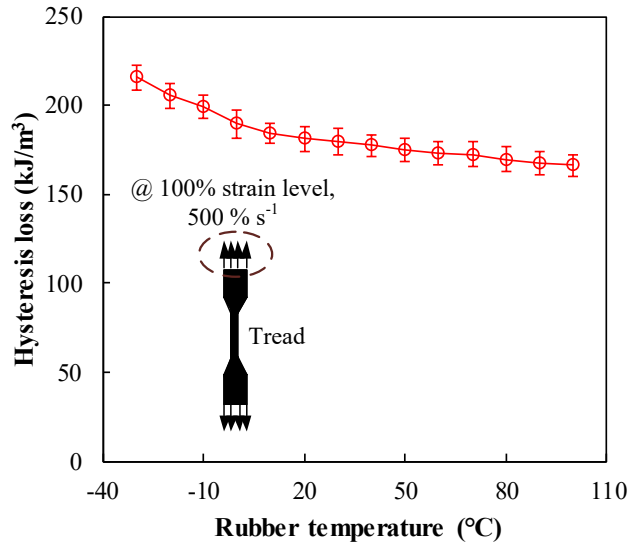
Figure 2.6. Relationship between hysteresis loss and rubber temperatures in tread rubbers at 500% s$^{-1}$ and 100% strain level

As shown in Table 2.3 and Figure 2.6, the hysteresis loss of tread rubbers decreased with a rise of rubber temperatures generally; however, the decrease in hysteresis loss became less significant when the rubber temperatures were above 10 °C. At 500% s$^{-1}$ and the 100% strain level, the hysteresis loss of tread rubbers reduced by approximately 15% as the rubber temperature was raised from -30 to 10 °C, yet it decreased by only 8% in total with further increases in rubber temperatures from 10 to 100 °C. The hysteresis loss decreased slightly when the rubbers were heated above 10 °C, which indicates that the rubber temperatures above 10 °C had less of a significant influence on the hysteresis loss of OTR tire rubbers. This observation is consistent with that of the hysteresis loss in rubbers from HT tires. For instance, at the strain rate of 600% s$^{-1}$, the hysteresis loss of tread rubbers from a 165/70R10 HT tire decreased from 38.8 to 13.6 kJ/m$^3$·when the rubber temperature was raised from -20 to 10 °C. However, the hysteresis loss only decreased

29

from 13.6 to 6.5 kJ/m$^3$·as the rubber temperature further increased from 10 to 100 ℃ (He, 2005; He et al., 2006).

It is noted that although a rise of rubber temperatures (e.g., from 10 to 100 ℃) affected slightly, or even mitigated, the hysteresis loss of tire rubbers to some extent (e.g., 8% on average), this temperature rise is detrimental because the tires lose strength when rubber temperature increases, as per other researchers (Feng, 2017; Jamshidi et al., 2005; Jamshidi and Taromi, 2007; Wu, 2009). For instance, a rise of rubber temperatures from 25 to 100 ℃ could cause over a 19% reduction in the adhesion strength of cord/rubber composites within a tire (Jamshidi et al., 2006). Besides, the rubber temperature rise can deteriorate the tensile performance (e.g., a reduction of tensile modulus) of tire rubbers and cords, which decreases tire stiffness and subsequently lowers the handling stability and ride comfort of vehicles (Wang et al., 2013; Xu, 2011). Based on this, the effects of rubber temperature rise on the strength of OTR tires should be further studied in the next phase.

### 2.3.3. Comparisons of hysteresis loss between tread and sidewall rubbers

Figure 2.7 presents the comparisons of hysteresis loss between tread and sidewall rubbers at 20 ℃ and the 100% strain level. As shown in Table 2.3 and Figure 2.7, the hysteresis loss values of sidewall rubbers were greater than those of tread rubbers under the same testing conditions. For instance, the hysteresis loss of sidewall rubbers was 155.3 kJ/m$^3$ at 10% s$^{-1}$, 20 ℃ and the 100% strain level, which was greater than the hysteresis loss (139.4 kJ/m$^3$) of tread rubbers under the same testing conditions. This is in accordance with the test results of Nyaaba et al. (Nyaaba et al., 2019b) that sidewall rubbers showed a hysteresis loss value that was about 12% greater than that of tread rubbers at 1% s$^{-1}$, 20 ℃ and the 100% strain level. Moreover, it can be observed in Table

2.3 and Figure 2.7 that sidewall rubbers showed a rapid increase of hysteresis loss with the rising strain rate. At 20 °C and the 100% strain level, as the strain rate was raised from 10% to 500% s$^{-1}$, the hysteresis loss of sidewall rubbers increased from 155.3 to 209.6 kJ/m$^3$, which was more rapid than the increment in hysteresis loss (from 139.4 to 181.3 kJ/m$^3$) of tread rubbers. To summarize, compared with tread rubbers, sidewall rubbers showed greater hysteresis loss values and more rapid increases in hysteresis loss with the rising strain rate. This can be partially explained by the larger amount of CB (31.27% in weight) in sidewall rubbers. A large amount of CB can cause large surface areas of CB, which results in extra frictional energy dissipation on the carbon black-polymer chain (CB-PC) interfaces as the sidewall rubbers are stretched at increased strain rates (Hu, 2013; Park et al., 2000; Raut et al., 2018).
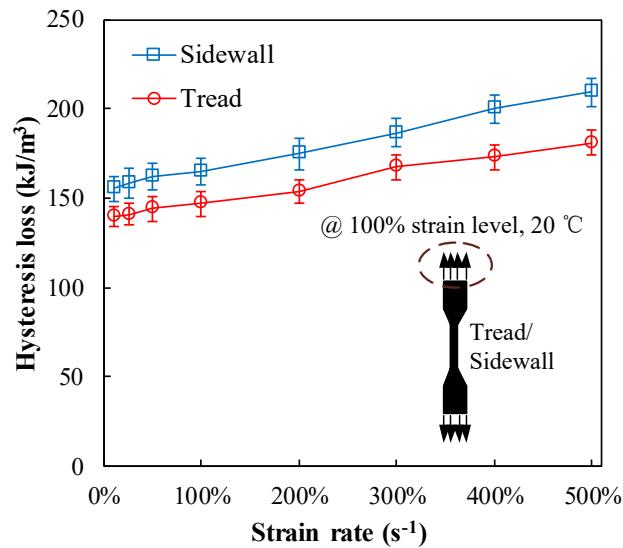


Figure 2.7. Comparisons of hysteresis loss between tread and sidewall rubbers at 20 °C and 100% strain level

Although sidewall rubbers showed greater hysteresis loss values than those in tread rubbers, site observations showed that tread rubbers of OTR tires experienced more failures than

those in tire sidewall rubbers at mine sites (Anzabi, 2015; Anzabi et al., 2012; Kerr, 2017; Zhou et al., 2008). According to Anzabi (Anzabi, 2015), 49% of tire failures were related to tread rubbers (e.g., tread cuts, separations), and the failures in tread rubbers were more than those (34% occupied) observed in sidewall rubbers. This may be related to the larger strain levels in tread rubbers (compared with sidewall rubbers) when an OTR tire is operated under a specific condition (i.e., payload, truck speed, and tire pressure). For instance, tread rubbers in a Michelin 56/80R63 OTR tire experienced strain levels reaching about 114% at a payload of 115 tonnes, a truck speed of 32 km/h and a tire pressure of 724 kPa, which were larger than the strain levels (e.g., within 30%) in sidewall rubbers (Nyaaba, 2017). These larger strain levels can cause greater hysteresis loss and, subsequently, severe heat generation and a higher rubber temperature, resulting in more failures in tread rubbers. Moreover, OTR tire tread rubbers are usually manufactured in the forms of thick tread blocks (Caterpillar, 2018; Michelin, 2016), which tends to retard the heat transfer from tread rubbers into the surrounding environment and further induce the rubber temperature rise and rubber failures in tread rubbers (He, 2005; Huang, 2016). In addition, tread rubbers of OTR tires contact with the haul road directly and can experience failures (i.e., rock cuts) when a truck drives over rugged rocks or sharp obstacles (Lindeque, 2016). For these reasons, compared with sidewall rubbers, tread rubbers of OTR tires are more susceptible to failures at mine sites.

## 2.4. Conclusion

This study investigated the hysteresis loss of ultra-large off-the-road (OTR) tire rubbers based on operating conditions at mine sites. Cyclic tensile tests were conducted on the tread and sidewall rubbers cut from a Michelin 56/80R63 OTR tire at six strain levels, eight strain rates, and fourteen rubber temperatures. The main conclusions are enumerated as follows:

1. Under the testing conditions of 100% s$^{-1}$, 20 °C, and the 40% strain level, the hysteresis loss values of tread and sidewall rubbers were 33.8 and 38.1 kJ/m$^3$, respectively, which are greatly different hysteresis loss results from those of highway-terrain (HT) tire rubbers. This proves that the hysteresis loss results derived from HT tire rubbers cannot be directly applied to OTR tire rubbers.

2. A large strain level (e.g., 100%) increased the hysteresis loss of tread rubbers considerably. Under the testing conditions of 500% s$^{-1}$ and 20 °C, the hysteresis loss increased from 40.7 to 181.3 kJ/m$^3$ as the strain level was raised from 40% to 100%, which indicates that during one revolution of the tire, heat generation of tread rubbers under the fully loaded condition could reach up to about 4 times that of when a truck is empty.

3. Hysteresis loss of tread rubbers increased with a rise of strain rates, and the increasing rates became greater at larger strain levels (e.g., 100%). At 20 °C and the 100% strain level, as the strain rate increased from 100% to 500% s$^{-1}$, the hysteresis loss grew from 147.1 to 181.3 kJ/m$^3$. This had quantitatively shown that under the fully loaded condition, heat generation of tread rubbers during one revolution of the tire went up by 34.2 kJ/m$^3$ when the truck speed was raised from 4 to 20 km/h.

4. A rise of rubber temperatures caused a decrease in hysteresis loss; however, the decrease became less significant when the rubber temperatures were above 10 °C. At 500% s$^{-1}$ and the 100% strain level, the hysteresis loss reduced by approximately 15% as the rubber temperature was raised from -30 to 10 °C, yet it decreased by only 8% in total with further increases in rubber temperatures from 10 to 100 °C.

5. Compared with tread rubbers, sidewall rubbers showed greater hysteresis loss values and

more rapid increases in hysteresis loss with the rising strain rate. At 10% s$^{-1}$, 20 °C, and the 100% strain level, the hysteresis loss of sidewall rubbers was 155.3 kJ/m$^3$, which was greater than that (139.4 kJ/m$^3$) of tread rubbers. Moreover, under the same testing conditions of 20 °C and the 100% strain level, as the strain rate was raised from 10% to 500% s$^{-1}$, the hysteresis loss of sidewall rubbers increased from 155.3 to 209.6 kJ/m$^3$, which was more rapid than the increment in hysteresis loss (from 139.4 to 181.3 kJ/m$^3$) of tread rubbers.

## Appendix 2A. Selection of strain levels, strain rates and rubber temperatures based on operating conditions at mine sites

A two-dimensional (2D) steady-state straight-line rolling tire model was established by Yang and Olatunbosun (Yang et al., 2013) to describe the relationship between motion and deformation on a rolling tire. In this study, this model was modified to determine the strain levels and strain rates of tire rubbers according to different payloads and truck speeds, as shown in Figure 2A.1.
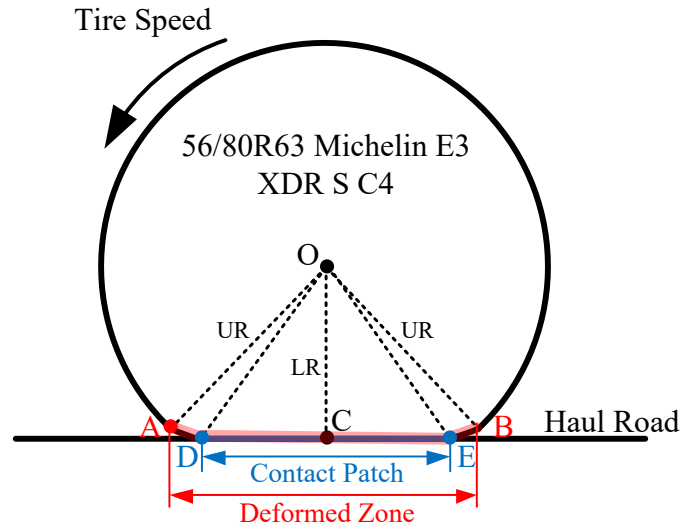
Figure 2A.1. Modified 2D steady-state straight-line rolling tire model (modified from the literature (Yang et al., 2013))

This modified model can be described as follows: a loaded Michelin 56/80R63 OTR tire rolls steadily on a smooth haul road, with no breaking, traction or steering force applied on it. The OTR tire undergoes a vertical deflection (VD) that can be obtained by determining the difference between loaded radius (LR) and unloaded radius (UR). The UR can be represented by OA or OB. O is the center of the tire; A and B are the two endpoints of the deformed zone.

To accommodate the VD, the rubbers within the contact patch (between Point D and Point E) are stretched at a specific strain rate, symmetrically with regard to the central Point C. Under stretching, the tensile strain occurs within the contact patch and peaks at Point C. When the OTR tire rolls with counter-clockwise direction, a specific rubber element close to tire surface experiences a strain increases from Point D to Point C and, subsequently, a strain decrease from Point C to Point E. In other words, this tire rubber element is applied by a stretching-releasing operation.

35

In this modified 2D tire model, the strain level of rubbers close to the tire surface has a linear relationship with the VD of the tire, as shown in Figure 2A.2. Moreover, according to Nyaaba (Nyaaba, 2017), the VD of a Michelin 56/80R63 OTR tire increased with a rise of vertical loads per tire, which was also close to a linear increasing trend, as shown in Figure 2A.3. Therefore, the correlations between rubber strain levels and vertical loads per tire can be obtained as follows: when a truck is fully loaded by 363 tonnes, the vertical load per tire reaches 104 tonnes, which indicates that the tire VD is 275 mm and the strain level of rubbers is 101%. On the other hand, for an OTR tire equipped on an empty truck, the vertical load per tire decreases to 43 tonnes, which corresponds to the tire VD of 115 mm and the rubber strain level of 42%.
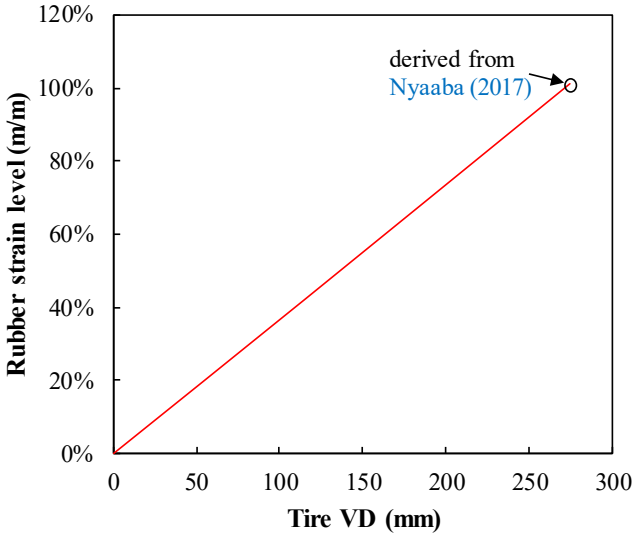


Figure 2A.2. Relationship between rubber strain level and tire VD
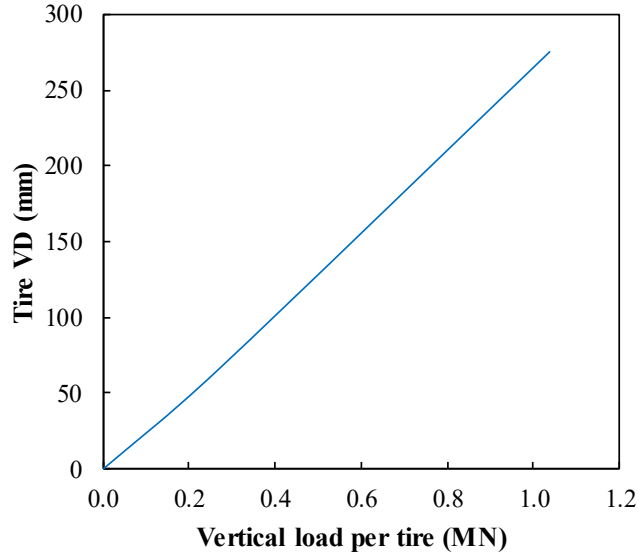
Figure 2A.3. Variation of tire VD with vertical load per tire based on a Michelin 56/80R63 OTR tire subjected to a tire pressure of 724 kPa (Nyaaba, 2017)

After the rubber strain levels were determined for the OTR tires on fully loaded and empty trucks, the strain rates of rubbers close to the tire surface were calculated according to different truck speeds. The truck speeds were obtained from Vital Information Management System (VIMS) data on an Athabasca oil sands mine site in 2018 (Ta, 2018). The VIMS data indicated that the average maximum truck speed was approximately 30 km/h for an empty truck, and about 20 km/h for a fully loaded truck.

The strain rates of tire rubbers can be calculated as follows

$$\dot{\varepsilon} = \frac{180 \cdot v \cdot SL}{\pi R \arccos\left(\dfrac{R-VD}{R}\right)} \qquad (2A.1)$$

37

where $\dot{\varepsilon}$ is the strain rate (in s$^{-1}$); $v$ is the truck speed (in m/s); $SL$ is the strain level (in m/m); $R$ is the radius of OTR tire (in m); $VD$ is the vertical deflection of OTR tire (in m).

As per Equation (2A.1), the strain rates of rubbers can be determined based on different rubber strain levels, truck speeds, tire radius, and VDs. For example, for an OTR tire (4 m in diameter) equipped on an empty truck, the VD of the tire is 115 mm, which corresponds to a rubber strain level of 42% and a contact patch that covers 39/360 of the tire circumference. When the truck moves at a truck speed of 30 km/h (8.33 m/s), this contact patch is passed through by a rubber element within 0.163 s. For this rubber element, to complete the variation of strain levels from 0 to 42%, and then back to 0 within 0.163 s, the rubber strain rate is required to reach 515% s$^{-1}$. Similarly, for an OTR tire under the fully loaded condition, a 275 mm-height VD corresponds to a rubber strain level of 101% and a contact patch covering 61/360 of the tire circumference. When the truck speed is 20 km/h (5.55 m/s), this contact patch is passed through by a rubber element within 0.384 s. To complete the variation of strain levels from 0 to 101%, and then back to 0 within 0.384 s, the strain rate of the rubber element is calculated as 526% s$^{-1}$. To summarize, the strain levels and strain rates of OTR tire rubbers are listed in Table 2A.1.

Table 2A.1. Strain levels and strain rates of OTR tire rubbers

| Payload condition | Gross vehicle weight (tonne) | Vertical load per tire (MN) | VD (mm) | Strain level (m/m) | Maximum truck speed (km/h) | Maximum strain rate (s$^{-1}$) |
|---|---|---|---|---|---|---|
| Empty | 260 | 0.43 | 115 | 42% | 30 | 515% |
| Fully loaded | 623 | 1.04 | 275 | 101% | 20 | 526% |

In addition, tire rubber temperatures in this study were selected based on Michelin Earthmover Management System (MEMS) data (Ta, 2018) and Alberta Weather Station (AWS) data (Alberta Agriculture and Forestry, 2018). The AWS data showed that the ambient

temperatures varied from -27 to 30 ℃; the MEMS data indicated that the internal tire temperatures ranged from -6 to 82 ℃. Additionally, according to Feng (Feng, 2017), internal tire temperatures can be 10 ~ 15 ℃ lower than peak rubber temperatures. For this reason, the testing temperatures in rubbers were raised up to 100 ℃ in this study.

To conclude, the test strain levels and strain rates were controlled within 100% and 500% s$^{-1}$, respectively. The test rubber temperatures ranged from -30 to 100 ℃.

# Chapter 3. A novel phenomenological model for predicting hysteresis loss of rubbers obtained from ultra-large off-the-road tires

This chapter has been published as **S. Ma**, G. Huang, K. Obaia, S. W. Moon. W. V. Liu. A novel phenomenological model for predicting hysteresis loss of rubber compounds obtained from ultra-large off-the-road tires, *IMechE: Journal of Automobile Engineering*. © SAGE. (2022)

## 3.1. Introduction

Ultra-large off-the-road (OTR) tires are widely used in truck haulage at mine sites (Marais, 2017; Marais and Venter, 2018). OTR tires have various rubbers, including inner filler, inner liner, soft apex, base, sidewall, and tread rubbers (Michelin, 2016). These rubbers are susceptible to failures during haulage operations, and these failures are related to hysteresis loss and subsequent overheating in rubbers (Anzabi, 2015; Anzabi et al., 2012; Kerr, 2017). The hysteresis loss is significantly affected by operating conditions (Li et al., 2012; Marais, 2017; Nyaaba, 2017). However, at mine sites, operating conditions vary dramatically. According to mine site data (Alberta Agriculture and Forestry, 2018; Ta, 2018) and conversion (in Appendix 3A), there are unique and large ranges of operating conditions: strain rates vary from 10% to 500% s$^{-1}$, rubber temperatures change from -30 to 100 °C, and strain levels range from 10% to 100%. Considering these operating conditions, the mining industry is of particular interest in predicting the hysteresis loss of rubbers in OTR tires. An accurate prediction of hysteresis loss can guide the use of OTR tires in truck haulage, thereby saving operating costs and improving productivity.

To predict hysteresis loss, there are many existing models in the literature; a majority of the models are phenomenological models, which are derived from direct observations and measurements of rubber mechanical responses associated with curve fitting of experimental data (Carleo et al., 2018; Liu, 2010). Phenomenological models usually contain a few model parameters but have the ability to predict hysteresis loss relatively accurately (Hu et al., 2019; Luo et al., 2010; Yu et al., 2017). For instance, a phenomenological model created by Hu et al. (Hu et al., 2019) included five model parameters but predicted the hysteresis loss of rubbers with an average mean absolute percent error (MAPE) of 10.6% (at strain rates from 2% to 100% s$^{-1}$, rubber temperatures

from -30 to 50 ℃, and strain levels from 0.2% to 10%). The model established by Luo et al. (Luo et al., 2010) contained four model parameters but estimated the rubber hysteresis loss with a MAPE of 13.7% (at strain rates from 4.8% to 1120% $s^{-1}$, a rubber temperature of 23 ℃, and strain levels from 0.8% to 8%). Also, the model developed by Yu et al. (Yu et al., 2017) included five model parameters but provided an estimation for rubber hysteresis loss with a MAPE of 7.7% (at a strain rate of 8% $s^{-1}$, a rubber temperature of 20 ℃, and strain levels from 30% to 90%). These previous models have proven that phenomenological models are appropriate to provide relatively accurate estimations for rubber hysteresis loss.

According to the literature, some phenomenological models are developed based on a rheological framework that is represented by various elastic and viscous elements combined in parallel and series connections (Carleo et al., 2018; Hurtado et al., 2013; Kießling et al., 2016). The rheological framework is split into an elastic component and a viscous component that involves operating variables such as strain rates (Amin et al., 2006; Liu, 2010), rubber temperatures (Besdo et al., 2010; Lion, 1997; Österlöf et al., 2015), and strain levels (Liu, 2007; Österlöf et al., 2016). The models based on rheological frameworks were previously used to predict the hysteresis loss of rubbers obtained from highway-terrain (HT) tires, as per other researchers (Liu, 2010, 2007; Liu and Fatt, 2011; Zhi et al., 2016). However, rubbers of OTR tires are different from those of HT tires. For instance, compared with the tread rubbers of an Avon HT tire reported by Terrill et al. (Terrill et al., 2010), tread rubbers obtained from a Michelin 56/80R63 OTR tire included 9.3% less carbon black (Ma et al., 2021a), and the OTR tire tread rubbers made by Joseph (Joseph, 2014) contained 13.4% more polymer and 13.0% less carbon black. These differences in tire rubbers make the models generated from rheological frameworks remain unknown if they can be applied to OTR tire rubbers to predict hysteresis loss.

In addition to models derived from rheological frameworks, models can also be generated based on a strain energy function that is typically expressed by three strain invariants (Beda, 2014; Kim et al., 2012). Strain energy functions have been widely used for OTR tire rubbers, according to many researchers (Li et al., 2012; Marais and Venter, 2018; Nyaaba et al., 2019b), and these functions can describe the hysteresis curves of rubbers at strain levels reaching 100%, which leads to the models achieving good results in estimating hysteresis loss when the strain levels vary within 100%. Some typical models are the Li model (Li et al., 2017), the Ogden model (Ogden and Roxburgh, 1999), the Dorfmann model (Dorfmann and Ogden, 2004), and the Wrubleski model (Wrubleski and Marczak, 2013). For example, the Li model (Li et al., 2017) predicted the hysteresis loss of rubbers with a MAPE of 8.2% at a strain rate of 1% $s^{-1}$ and a rubber temperature of 20 °C when the strain levels varied from 0 to 200%. The Dorfmann model (Dorfmann and Ogden, 2004) estimated the rubber hysteresis loss with a MAPE of 5.7% at 25 °C and a 2% $s^{-1}$ strain rate when the strain levels changed from 0 to 140%. However, traditional strain energy functions such as the Mooney-Rivlin (MR) (Mooney, 1940; Rivlin, 1948), Yeoh (Yeoh, 1993), Neo-Hookean (Wineman, 2005), and Marlow (Marlow, 2003) functions do not include operating variables such as strain rates and rubber temperatures. This makes the Li model (Li et al., 2017) derived from the Marlow function, and the Dorfmann model (Dorfmann and Ogden, 2004) and the Ogden model (Ogden and Roxburgh, 1999) based on the Neo-Hookean function unable to predict the variations of hysteresis loss values when the strain rates and rubber temperatures vary. This inability makes these models inapplicable to OTR tire rubbers used at mine sites. To summarize, there are existing models to predict the hysteresis loss of rubbers that are based on rheological frameworks or strain energy functions. The models derived from rheological frameworks can estimate the rubber hysteresis loss at different strain levels, strain rates, and rubber temperatures,

but it remains unknown if these models can be applied to OTR tire rubbers. Models based on traditional strain energy functions have been widely used for OTR tire rubbers, but they are restrained when the strain rates and rubber temperatures vary significantly at mine sites. Until now, according to the literature review, there has been a lack of a phenomenological model that can predict the hysteresis loss of rubbers from OTR tires under typical operating conditions at mine sites. This model is of great significance because it can guide the use of OTR tires in truck haulage and, ultimately, save operating costs and improve mine productivity.

To this end, the objective of this study is to develop a novel phenomenological model for predicting the hysteresis loss of OTR tire rubbers under typical operating conditions at mine sites. To achieve this, first, cyclic tensile tests were conducted on tire rubbers to derive the experimental results of hysteresis curves, hysteresis loss, peak stress, and residual strain at six strain levels, eight strain rates, and fourteen rubber temperatures. Then, referring to these experimental results, a phenomenological model was developed—the HLSRT model (a hysteresis loss model considering strain levels, strain rates, and rubber temperatures). This HLSRT model filled the research gap to predict the hysteresis loss of OTR tire rubbers. In addition, this HLSRT model was developed in novelty. The model was generated based on a new strain energy function that was modified the MR function by incorporating into it two new coefficients (i.e., a strain-rate-dependent coefficient and a rubber-temperature-dependent coefficient). The incorporation of these two coefficients is important because it caused that the HLSRT model further predicted the hysteresis loss of OTR tire rubbers at different strain rates and rubber temperatures in addition to different strain levels.

## 3.2. An overview of the methodology

A flowchart showing an overview of the methodology is represented in Figure 3.1.
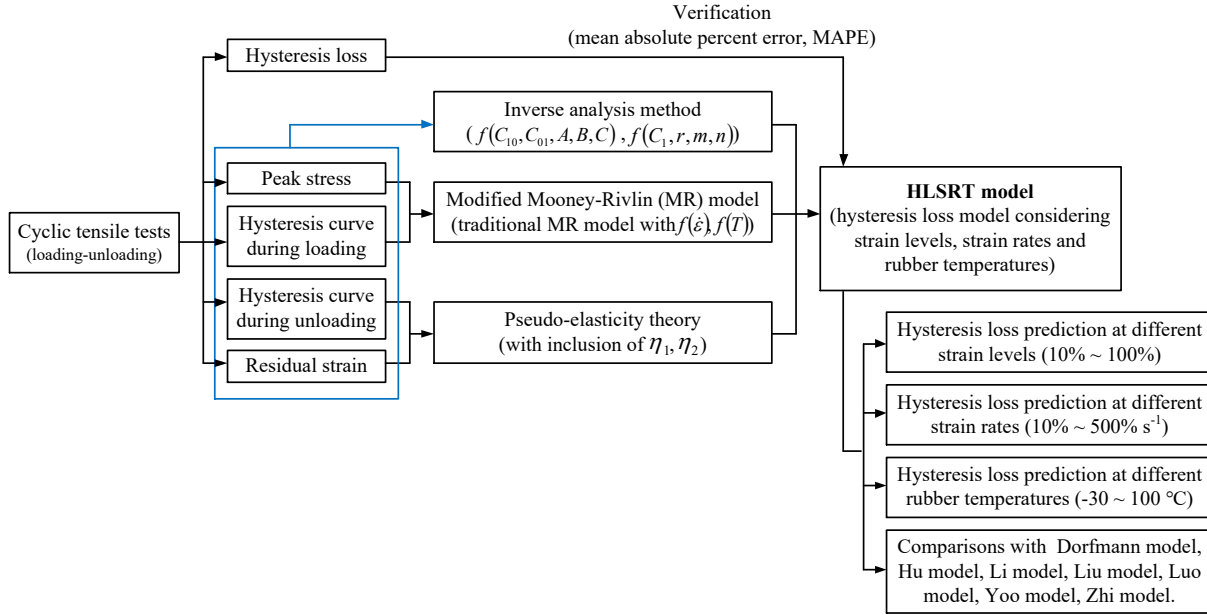
Figure 3.1. A flowchart showing an overview of the methodology

As shown in Figure 3.1, the development of the HLSRT model was derived from the experimental results from a series of cyclic tensile tests. First, cyclic tensile tests conducted the loading-unloading operations on tire tread rubbers to derive the results of hysteresis curves, peak stress, residual strain, and hysteresis loss at six strain levels, eight strain rates, and fourteen rubber temperatures. Then, the results of hysteresis curves and peak stress during loading motivated a modification of the traditional MR function (Mooney, 1940; Rivlin, 1948) by newly incorporating into it a strain-rate-dependent coefficient $f_1(\dot{\varepsilon})$ and a rubber-temperature-dependent coefficient $f_2(T)$. The results of hysteresis curves and residual strain during unloading inspired an application of the pseudo-elasticity theory (Ogden and Roxburgh, 1999). Based on this theory, the function of hysteresis curve during unloading was modified from the function of hysteresis curve during loading by adding two additional variables, denoted $\eta_1$ and $\eta_2$. Moreover, the experimental results of hysteresis curves, peak stress, and residual strain were also employed to determine the

material constants following the inverse analysis method (Fowles and Williams, 1970). In this method, the experimental results were used to establish an error function, i.e., $f\left(C_{10},C_{01},C_{1},r,m,n,A,B,C\right)$. The material constants $C_{10}$, $C_{01}$, $C_{1}$, $r$, $m$, $n$, $A$, $B$, and $C$ were then determined when the value of this error function were minimized. According to the modified MR function, the pseudo-elasticity theory, and the inverse analysis method, the HLSRT model was created to predict hysteresis loss.

After model development, the HLSRT model was verified by evaluating the deviations between the hysteresis loss results predicted from the HLSRT model and the hysteresis loss results derived from the cyclic tensile tests. These deviations were quantified using the MAPE, a well-known index in statistics. As per Beyer (Beyer, 1991), the expression of MAPE is given by

$$MAPE = \frac{1}{P}\sum_{k=1}^{P}\left|\frac{H_{experiment,k} - H_{prediction,k}}{H_{experiment,k}}\right| \qquad (3.1)$$

where $H_{prediction,k}$ (in kJ/m$^3$) and $H_{experiment,k}$ (in kJ/m$^3$) are the hysteresis loss results obtained from the model predictions and the experiments during one cycle of loading and unloading, respectively; $P$ is the number of data points.

The values of MAPE in other existing models (e.g., average MAPE of 13.7% (Luo et al., 2010); maximum MAPE of 28% (Liu, 2007)) were employed as the criteria to decide whether the hysteresis loss results estimated by the HLSRT model were in good agreement with the results measured by the tests. When the average MAPE is less than 13.7% and the maximum MAPE is not greater than 28%, the accuracy of a model is considered to be acceptable.

After model verification, the HLSRT model was used to predict the hysteresis loss of tire tread rubbers at strain levels ranging from 10% to 100%, strain rates from 10% to 500% s$^{-1}$, and rubber temperatures from -30 to 100 ℃. The predictive ability of the HLSRT model was further highlighted by comparing it with other existing models, such as the Dorfmann model (Dorfmann and Ogden, 2004), the Hu model (Hu et al., 2019), the Li model (Li et al., 2017), the Liu model (Liu and Fatt, 2011), the Luo model (Luo et al., 2010), the Yoo model (Yoo et al., 2016), and the Zhi model (Zhi et al., 2017).

## 3.3. Experiments

### 3.3.1. Experimental materials and methods

The tread rubbers were cut from a Michelin 56/80R63 OTR tire used at a local mine site. Then, the tread rubbers were cut into standard dumbbell-shaped specimens, as per ASTM D412-16 (ASTM D412-16, 2016). The dimensions of the dumbbell-shaped specimens are shown in Figure 3.2 in the units of mm.
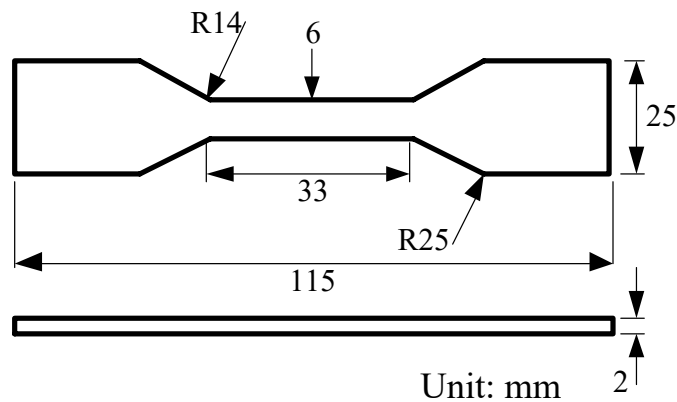


Figure 3.2. Dimensions of dumbbell-shaped specimen

Cyclic tensile tests were conducted at six strain levels, eight strain rates, and fourteen rubber temperatures, as listed in Table 3.1. The strain levels and strain rates were derived from the site data on an Athabasca oil sands mine in 2018, as referred to in Appendix 3A. The rubber temperatures were achieved by heating or cooling the tread rubber specimens at given temperatures for 24 hours.

Table 3.1. Strain levels, strain rates, and rubber temperatures in cyclic tensile tests

| Strain level (m/m) | 10%, 20%, 40%, 60%, 80%, and 100% |
|---|---|
| Strain rate ($s^{-1}$) | 10%, 25%, 50%, 100%, 200%, 300%, 400%, and 500% |
| Rubber temperature (℃) | -30, -20, -10, 0, 10, 20, 30, 40, 50, 60, 70, 80, 90, and 100 |

During cyclic tensile tests, uniaxial loading-unloading operations were used to obtain the hysteresis curves of tread rubber specimens. For instance, at 20 ℃ and a 500% $s^{-1}$ strain rate, a tread rubber specimen was loaded reaching a strain level of 100%, and then unloaded to zero, creating a closed hysteresis curve (i.e., also known as hysteresis loop, as per Le Cam (Le Cam, 2017)). This loading-unloading operation was repeated five times since the hysteresis curves derived from the first four cycles of loading and unloading were unstable. The hysteresis curves derived from the uniaxial loading-unloading operations at 20 ℃, a 500% $s^{-1}$ strain rate, and a 100% strain level are shown in Figure 3.3.
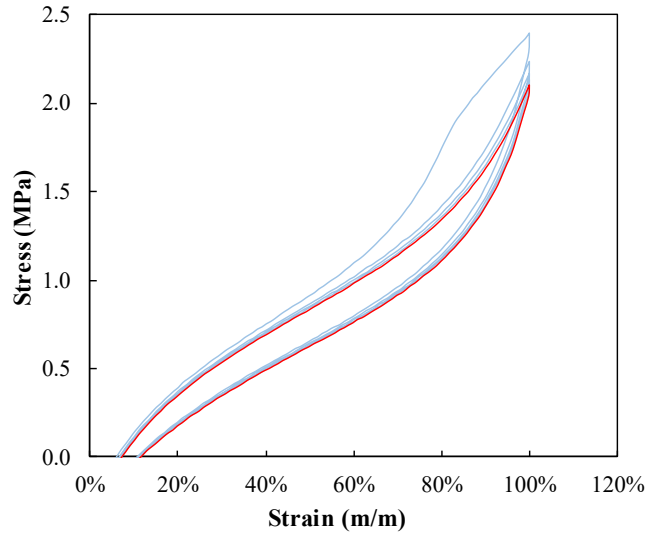
Figure 3.3. Hysteresis curves derived from the uniaxial loading-unloading operations at 20 °C, a 500% s$^{-1}$ strain rate, and a 100% strain level

The experimental results included the hysteresis loss, peak stress, and residual strain. According to other researchers (Cho et al., 2013; Luo et al., 2010), the hysteresis loss is represented by the integral area of the hysteresis loop, which corresponds to the dissipated energy that is converted to heat. The peak stress refers to the maximum stress within one loading-unloading cycle, and the residual strain is the strain that remains in rubbers after removal of stress (i.e., zero stress), as per Huang et al. (Huang et al., 2019). The results of peak stress and residual strain can help to describe the hysteresis curves in the next section of model development.

### 3.3.2. Experimental results and observations

Figure 3.4 shows the stable hysteresis curve of tread rubbers at 20 °C, a 500% s$^{-1}$ strain rate, and a 100% strain level. When the tread rubbers were loaded from 0 to 100% strain level, the stress on the loading path (Point A → Point B) of the hysteresis curve increased nonlinearly and reached a peak stress of 2.23 MPa at the 100% strain level. After reaching the peak stress, the tread

rubbers were unloaded to zero stress along the unloading path (Point B → Point C) of the hysteresis curve. On the unloading path, the stress at a given strain was smaller than that on the loading path (which was known as stress softening, as per other researchers (Dorfmann and Ogden, 2003; Harwood et al., 1965; Mullins, 1969)), and the zero stress corresponded to a residual strain of 11.5% (Point C → Point O). As calculated from the integral area of the hysteresis loop (Point A → Point B → Point C → Point A), the hysteresis loss of tread rubbers at 20 °C, a 500% s$^{-1}$ strain rate, and a 100% strain level was 181.3 kJ/m$^3$. To summarize, a stable hysteresis curve was characterized typically as a nonlinear stress-strain relationship on the loading path, stress softening and residual strains on the unloading path, and a hysteresis loop within one loading-unloading cycle.
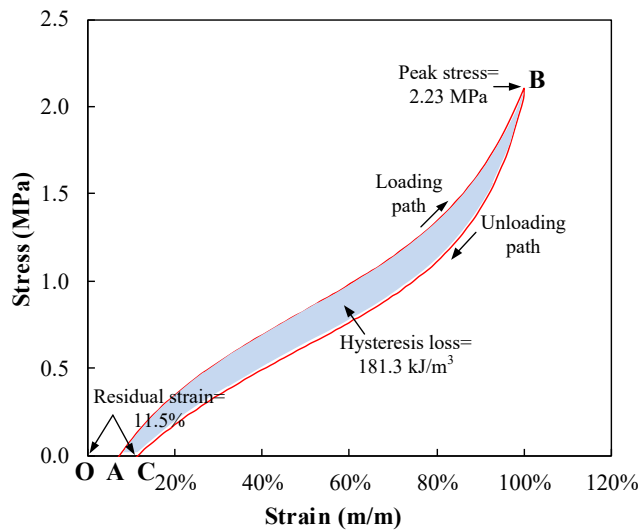


Figure 3.4. Stable hysteresis curve of tread rubbers at 20 °C, a 500% s$^{-1}$ strain rate, and a 100% strain level

Based on the stable hysteresis curves at different strain levels, strain rates, and rubber temperatures, the hysteresis loss, peak stresses, and residual strains were obtained under different

operating conditions, as listed in Table 3.2, Table 3.3, and Table 3.4, respectively. The operating conditions included three strain levels (from 10% to 100%), four strain rates (from 10% to 500% s$^{-1}$), and fourteen rubber temperatures (from -30 to 100 °C).

Table 3.2. Hysteresis loss of tread rubbers under different operating conditions (in kJ/m$^3$)

| Strain level Rubber temp. | Strain rate: 10% s$^{-1}$ | | | Strain rate: 100% s$^{-1}$ | | | Strain rate: 300% s$^{-1}$ | | | Strain rate: 500% s$^{-1}$ | | |
|---|---|---|---|---|---|---|---|---|---|---|---|---|
| | 20% | 40% | 100% | 20% | 40% | 100% | 20% | 40% | 100% | 20% | 40% | 100% |
| -30 °C | 12.6 | 37.3 | 162.5 | 13.4 | 39.4 | 171.8 | 14.4 | 43.2 | 193.4 | 15.3 | 47.0 | 215.8 |
| -20 °C | 12.2 | 36.2 | 156.3 | 13.0 | 37.8 | 164.1 | 13.9 | 41.1 | 184.8 | 14.8 | 45.2 | 205.4 |
| -10 °C | 12.0 | 34.8 | 151.6 | 12.4 | 36.8 | 157.6 | 13.3 | 40.2 | 178.4 | 14.5 | 43.5 | 199.1 |
| 0 °C | 11.4 | 33.5 | 144.6 | 12.0 | 35.2 | 154.6 | 13.1 | 38.8 | 170.8 | 14.1 | 42.4 | 189.6 |
| 10 °C | 11.0 | 32.7 | 141.9 | 11.5 | 34.3 | 149.1 | 12.9 | 37.1 | 166.7 | 13.6 | 41.3 | 184.3 |
| 20 °C | 10.8 | 32.3 | 139.4 | 11.3 | 33.8 | 147.1 | 12.4 | 37.3 | 164.2 | 13.4 | 40.7 | 181.3 |
| 30 °C | 10.7 | 32.0 | 137.2 | 11.2 | 33.3 | 145.8 | 12.2 | 37.0 | 162.6 | 13.3 | 40.1 | 179.4 |
| 40 °C | 10.7 | 31.6 | 135.8 | 11.1 | 32.9 | 144.4 | 12.0 | 36.3 | 159.0 | 13.1 | 39.6 | 177.6 |
| 50 °C | 10.4 | 31.2 | 134.3 | 11.1 | 32.4 | 143.3 | 12.0 | 35.7 | 159.2 | 13.0 | 38.9 | 175.1 |
| 60 °C | 10.4 | 30.8 | 133.2 | 11.0 | 32.0 | 141.9 | 11.7 | 35.8 | 158.6 | 12.8 | 38.4 | 173.4 |
| 70 °C | 10.2 | 30.6 | 131.6 | 10.9 | 31.5 | 140.5 | 11.8 | 34.7 | 156.5 | 12.7 | 37.9 | 172.4 |
| 80 °C | 10.2 | 30.2 | 129.8 | 10.9 | 31.2 | 139.5 | 11.7 | 34.4 | 155.7 | 12.6 | 37.5 | 169.7 |
| 90 °C | 10.1 | 29.9 | 128.8 | 10.8 | 30.9 | 138.2 | 11.6 | 34.7 | 153.0 | 12.5 | 37.2 | 167.7 |
| 100 °C | 9.9 | 29.9 | 127.1 | 10.7 | 30.6 | 137.3 | 11.5 | 33.7 | 151.8 | 12.3 | 36.8 | 166.2 |

Note: herein the hysteresis loss results at the strain rates of 10% s$^{-1}$, 100% s$^{-1}$, and 500% s$^{-1}$ were reported in our previous study (Ma et al., 2021a).

Table 3.3. Peak stresses of tread rubbers under different operating conditions (in MPa)

| Strain level<br>Rubber temp. | Strain rate: 10% s⁻¹ | | | Strain rate: 100% s⁻¹ | | | Strain rate: 300% s⁻¹ | | | Strain rate: 500% s⁻¹ | | |
|---|---|---|---|---|---|---|---|---|---|---|---|---|
| | 20% | 40% | 100% | 20% | 40% | 100% | 20% | 40% | 100% | 20% | 40% | 100% |
| **-30 °C** | 0.43 | 0.86 | 2.13 | 0.55 | 0.97 | 2.28 | 0.62 | 1.06 | 2.42 | 0.69 | 1.15 | 2.53 |
| **-20 °C** | 0.43 | 0.84 | 2.08 | 0.53 | 0.95 | 2.24 | 0.60 | 1.03 | 2.37 | 0.67 | 1.13 | 2.50 |
| **-10 °C** | 0.41 | 0.82 | 2.03 | 0.52 | 0.93 | 2.17 | 0.58 | 1.01 | 2.29 | 0.64 | 1.09 | 2.47 |
| **0 °C** | 0.41 | 0.80 | 1.99 | 0.50 | 0.92 | 2.10 | 0.56 | 0.98 | 2.25 | 0.63 | 1.07 | 2.33 |
| **10 °C** | 0.40 | 0.79 | 1.96 | 0.48 | 0.89 | 2.06 | 0.55 | 0.95 | 2.18 | 0.60 | 1.03 | 2.23 |
| **20 °C** | 0.39 | 0.77 | 1.91 | 0.48 | 0.87 | 2.04 | 0.53 | 0.93 | 2.14 | 0.58 | 1.00 | 2.23 |
| **30 °C** | 0.39 | 0.76 | 1.90 | 0.47 | 0.86 | 1.99 | 0.52 | 0.93 | 2.13 | 0.58 | 0.99 | 2.22 |
| **40 °C** | 0.38 | 0.75 | 1.88 | 0.47 | 0.86 | 1.98 | 0.51 | 0.92 | 2.10 | 0.57 | 0.98 | 2.20 |
| **50 °C** | 0.38 | 0.75 | 1.88 | 0.47 | 0.85 | 1.96 | 0.50 | 0.91 | 2.08 | 0.56 | 0.96 | 2.19 |
| **60 °C** | 0.38 | 0.75 | 1.87 | 0.46 | 0.85 | 1.96 | 0.50 | 0.90 | 2.05 | 0.55 | 0.96 | 2.16 |
| **70 °C** | 0.37 | 0.74 | 1.85 | 0.45 | 0.84 | 1.95 | 0.49 | 0.89 | 2.04 | 0.55 | 0.95 | 2.14 |
| **80 °C** | 0.37 | 0.74 | 1.83 | 0.44 | 0.83 | 1.94 | 0.49 | 0.88 | 2.02 | 0.55 | 0.94 | 2.12 |
| **90 °C** | 0.37 | 0.73 | 1.81 | 0.43 | 0.82 | 1.93 | 0.48 | 0.88 | 2.03 | 0.54 | 0.93 | 2.09 |
| **100 °C** | 0.37 | 0.72 | 1.80 | 0.42 | 0.80 | 1.91 | 0.48 | 0.87 | 2.00 | 0.54 | 0.92 | 2.08 |

Table 3.4. Residual strains of tread rubbers under different operating conditions (in %)

| Strain level<br>Rubber temp. | Strain rate: 10% s⁻¹ | | | Strain rate: 100% s⁻¹ | | | Strain rate: 300% s⁻¹ | | | Strain rate: 500% s⁻¹ | | |
|---|---|---|---|---|---|---|---|---|---|---|---|---|
| | 20% | 40% | 100% | 20% | 40% | 100% | 20% | 40% | 100% | 20% | 40% | 100% |
| **-30 °C** | 4.45 | 7.39 | 11.46 | 4.49 | 7.43 | 11.50 | 4.53 | 7.50 | 11.56 | 4.56 | 7.53 | 11.62 |
| **-20 °C** | 4.42 | 7.35 | 11.42 | 4.48 | 7.36 | 11.46 | 4.51 | 7.48 | 11.53 | 4.53 | 7.47 | 11.58 |
| **-10 °C** | 4.43 | 7.32 | 11.40 | 4.46 | 7.35 | 11.42 | 4.47 | 7.44 | 11.52 | 4.52 | 7.42 | 11.53 |
| **0 °C** | 4.39 | 7.29 | 11.37 | 4.45 | 7.31 | 11.39 | 4.46 | 7.40 | 11.49 | 4.49 | 7.38 | 11.49 |
| **10 °C** | 4.39 | 7.26 | 11.33 | 4.43 | 7.29 | 11.42 | 4.42 | 7.36 | 11.45 | 4.47 | 7.35 | 11.49 |
| **20 °C** | 4.37 | 7.24 | 11.34 | 4.43 | 7.28 | 11.39 | 4.41 | 7.35 | 11.41 | 4.46 | 7.32 | 11.46 |
| **30 °C** | 4.34 | 7.21 | 11.31 | 4.41 | 7.26 | 11.37 | 4.38 | 7.32 | 11.42 | 4.43 | 7.29 | 11.43 |
| **40 °C** | 4.33 | 7.19 | 11.28 | 4.38 | 7.24 | 11.35 | 4.35 | 7.33 | 11.39 | 4.41 | 7.28 | 11.40 |
| **50 °C** | 4.34 | 7.17 | 11.29 | 4.38 | 7.23 | 11.32 | 4.36 | 7.29 | 11.37 | 4.39 | 7.25 | 11.38 |
| **60 °C** | 4.29 | 7.15 | 11.25 | 4.36 | 7.24 | 11.33 | 4.31 | 7.28 | 11.35 | 4.38 | 7.21 | 11.36 |
| **70 °C** | 4.27 | 7.16 | 11.23 | 4.35 | 7.18 | 11.28 | 4.29 | 7.26 | 11.31 | 4.38 | 7.18 | 11.34 |
| **80 °C** | 4.25 | 7.14 | 11.21 | 4.33 | 7.14 | 11.25 | 4.30 | 7.21 | 11.28 | 4.32 | 7.21 | 11.33 |
| **90 °C** | 4.26 | 7.12 | 11.18 | 4.34 | 7.15 | 11.24 | 4.28 | 7.19 | 11.30 | 4.33 | 7.22 | 11.34 |
| **100 °C** | 4.23 | 7.09 | 11.18 | 4.29 | 7.12 | 11.22 | 4.27 | 7.20 | 11.28 | 4.30 | 7.18 | 11.30 |

The experimental results and observations in Table 3.2, Table 3.3, and Table 3.4, and in Figure 3.4 laid the basis for model development in the next section.

## 3.4. Phenomenological models for hysteresis loss

### 3.4.1. HLSRT model development

Referring to the experimental results and observations in Section 3.3.2, the HLSRT model was developed based on a modified MR function, the pseudo-elasticity theory, and the inverse analysis method.

#### 3.4.1.1. Hysteresis curve during loading

As observed from the experimental results in Table 3.3 and Figure 3.4, on the loading path of the hysteresis curve, the stress of rubbers showed a nonlinear relationship with strain, and the stress (e.g., peak stress) was also affected by both strain rates and rubber temperatures. The nonlinear relationship between the stress and strain was described by a two-parameter MR function (Mooney, 1940; Rivlin, 1948). This MR function has been widely used in previous studies (Kim et al., 2012; Kumar and Rao, 2016; Mohotti et al., 2014; Pang et al., 2011) and it can describe the nonlinear behaviors of rubber-like materials. In addition, to describe the effects of strain rates and rubber temperatures, the MR function was further modified by incorporating into it a new strain-rate-dependent coefficient and a new rubber-temperature-dependent coefficient. These two coefficients characterized the variations of hysteresis curves with strain rates and rubber temperatures, respectively.

According to the MR function (Mooney, 1940; Rivlin, 1948), the strain energy density $W$ (in kJ/m$^3$) is written as

$$W = C_{10}(I_1 - 3) + C_{01}(I_2 - 3) \tag{3.2}$$

where $C_{10}$ and $C_{01}$ are the material constants; $I_1$ and $I_2$ are the first and second principal strain invariants (in m/m).

It is assumed that rubbers are isotropic and incompressible elastomeric materials. According to Kumar and Rao (Kumar and Rao, 2016), $I_1$ and $I_2$ (in m/m) are written as

$$\begin{aligned} I_1 &= \lambda_1^2 + \lambda_2^2 + \lambda_3^2 \\ I_2 &= \lambda_1^2\lambda_2^2 + \lambda_2^2\lambda_3^2 + \lambda_3^2\lambda_1^2 \end{aligned} \tag{3.3}$$

where $\lambda_1$, $\lambda_2$, $\lambda_3$ are the principal stretch ratios oriented along three principal directions (in mm/mm).

Under the uniaxial tension, as per Kim et al. (Kim et al., 2012), $\lambda_1$, $\lambda_2$, $\lambda_3$ (in m/m) are

$$\begin{aligned} \lambda_1 &= \lambda_3 = \frac{1}{\sqrt{\lambda}} \\ \lambda_2 &= \lambda \end{aligned} \tag{3.4}$$

where $\lambda$ is the average stretch ratio (in m/m). As per Mohotti et al. (Mohotti et al., 2014), $\lambda$ is calculated by the strain $\varepsilon$ (in m/m):

$$\lambda = \varepsilon + 1 \tag{3.5}$$

Substituting Equations (3.3) ~ (3.5) to Equation (3.2), the strain energy density $W(\varepsilon)$ (in kJ/m³) at the strain of $\varepsilon$ (in m/m) can be rewritten as

$$W(\varepsilon) = C_{10}\left[(\varepsilon+1)^2 + 2(\varepsilon+1)^{-1} - 3\right] + C_{01}\left[(\varepsilon+1)^{-2} + 2(\varepsilon+1) - 3\right] \tag{3.6}$$

Then, the nonlinear relationship between the stress $\sigma(\varepsilon)$ (in MPa) and the strain $\varepsilon$ (in m/m) on the loading path of one hysteresis curve is derived as

$$\sigma(\varepsilon) = {dW(\varepsilon)}\Big/{d\varepsilon} = 2\left[1 - \frac{1}{(\varepsilon+1)^3}\right]\left[C_{10}(\varepsilon+1) + C_{01}\right] \tag{3.7}$$

The experimental results in Table 3.3 indicate that the stress on the loading path (e.g., peak stress) increased with the rising strain rate, which was close to a linear trend. Based on this, a strain-rate-dependent coefficient $f_1(\dot{\varepsilon})$ was introduced to describe the effect of strain rates on the hysteresis curves during loading, which is expressed as a linear function:

$$f_1(\dot{\varepsilon}) = {\sigma_{\dot{\varepsilon}}}\Big/{\sigma_{\dot{\varepsilon}_{ref}}} = A(\dot{\varepsilon} - 0.1) + 1 \tag{3.8}$$

where $A$ is the material constant; $\dot{\varepsilon}$ is the strain rate (in s$^{-1}$); $f_1(\dot{\varepsilon}) \geq 1$ since the strain rate of tire rubbers ranges from 10% to 500% s$^{-1}$. At the same strain, $\sigma_{\dot{\varepsilon}}$ (in MPa) and $\sigma_{\dot{\varepsilon}_{ref}}$ (in MPa) are the stresses under a certain strain rate and the reference strain rate (i.e., 10% s$^{-1}$), respectively.

As per Equation (3.8), the strain-rate-dependent coefficient is represented as a ratio of rubber stress at a given strain rate to the stress at the reference strain rate. From this, the coefficient is multiplied by Equation (3.7) to predict the rubber stresses on the loading path of the hysteresis curves at different strain rates.

Moreover, it is experimentally observed in Table 3.3 that the stress on the loading path (e.g., peak stress) also decreased with a rise of rubber temperatures, showing a manner of inverse proportional variation. From this, a rubber-temperature-dependent coefficient $f_2(T)$ was further developed. This coefficient is expressed as an inverse proportional function to describe the effect of rubber temperatures on the hysteresis curves during loading:

$$f_2(T) = \sigma_T \Big/ \sigma_{T_{ref}} = \frac{B}{T+50} + C \tag{3.9}$$

where $B$ and $C$ are the material constants; $T$ is the rubber temperature (in °C). At the same strain, $\sigma_T$ (in MPa) and $\sigma_{T_{ref}}$ (in MPa) are the stresses under a certain rubber temperature and the reference rubber temperature (i.e., -30 °C), respectively.

As per Equation (3.9), the rubber-temperature-dependent coefficient is represented as a ratio of rubber stress at a given rubber temperature to the stress at the reference rubber temperature. On the loading path of the hysteresis curves, this coefficient is multiplied by Equation (3.7) to derive the rubber stresses when rubber temperature varies.

By multiplying Equation (3.7) with the two coefficients, rubber stress $\sigma_l$ (in MPa) on the loading path of the hysteresis curve is obtained at varying strain rates and rubber temperatures:

$$\sigma_l = \sigma(\varepsilon) \cdot f_1(\dot{\varepsilon}) \cdot f_2(T) = 2\left[1 - \frac{1}{(\varepsilon+1)^3}\right]\left[C_{10}(\varepsilon+1) + C_{01}\right]\left[A(\dot{\varepsilon}-0.1)+1\right]\left[\frac{B}{T+50}+C\right] \tag{3.10}$$

In Equation (3.10), the strain-rate-dependent coefficient is presented as a factor that precedes the stress-strain formula $\sigma(\varepsilon)$. Based on this, the coefficient amplifies the stress in the

formula at each strain level. This coincides with the experimental results that rubber stress at each strain level increased with a rise of strain rates. For instance, in Table 3.3, when rubber temperature was 0 ℃, rubber stresses at each strain level (i.e., 20%, 40%, and 100%) increased by about 8.6% as strain rate was raised from 100% to 300% s$^{-1}$. Similarly, the rubber-temperature-dependent coefficient is presented as a pre-factor in Equation (3.10) to affect the rubber stress at each strain level when rubber temperature varies.

*3.4.1.2. Hysteresis curve during unloading*

The function to describe the hysteresis curve during unloading (as illustrated in Figure 3.4) was derived from the pseudo-elasticity theory developed by Ogden and Roxburgh (Ogden and Roxburgh, 1999). Based on this theory, the function of hysteresis curve during unloading was modified from the function of hysteresis curve during loading by adding two additional variables, denoted $\eta_1$ and $\eta_2$. These two variables were to describe the stress softening (Guo and Sluys, 2017; Suwannachit and Nackenhorst, 2010) and residual strains (Huang et al., 2019; Li et al., 2017) on the unloading path of the hysteresis curve, respectively.

Based on the pseudo-elasticity theory (Dorfmann and Ogden, 2004; Ogden and Roxburgh, 1999), the stress $\sigma_u$ (in MPa) on the unloading path of the hysteresis curve is derived as

$$\sigma_u = \eta_1 \cdot \frac{dW_l(\varepsilon)}{d\varepsilon} + (1 - \eta_2) \cdot \frac{dN(\varepsilon)}{d\varepsilon} \qquad (3.11)$$

where $\sigma_u$ (in MPa) is the stress on the unloading path of the hysteresis curve; $W_l(\varepsilon) = \int_0^\varepsilon \sigma_l d\varepsilon$ (in kJ/m$^3$); $N(\varepsilon)$ (in kJ/m$^3$) is expressed by the Neo-Hookean function (Wineman, 2005), and $dN(\varepsilon)/d\varepsilon$ is derived as

$$dN(\varepsilon)/d\varepsilon = C_1\left(2\varepsilon - \frac{2}{(\varepsilon+1)^2} - 1\right) \tag{3.12}$$

where $C_1$ is the material constant.

In Equation (3.11), the $\eta_1$ is referred to as a softening variable and is used to describe the stress softening on the unloading path of hysteresis curve. As per Dorfmann and Ogden (Dorfmann and Ogden, 2003), the variable $\eta_1$ is given by

$$\eta_1 = 1 - \frac{1}{r}\tanh\left[\frac{W_m - W_l(\varepsilon)}{m}\right] \tag{3.13}$$

where $0 < \eta_1 \leq 1$, with equality only at the beginning of the unloading path; $W_m$ (in kJ/m$^3$) is the maximum value of the strain energy achieved at the point where unloading begins; $r$ and $m$ are the material constants.

In Equation (3.11), the $\eta_2$ is a residual strain variable. Compared with $\eta_1$, this variable was less commonly used in the traditional models (Li et al., 2017; Ogden and Roxburgh, 1999). In this study, the introduction of $\eta_2$ was to describe the residual strains on the unloading path of hysteresis curve. This is important for OTR tire rubbers because residual strains of these rubbers

were relatively large (e.g., up to 11.6% as indicated in Table 3.4). The variable $\eta_2$ was first proposed by Dorfmann and Ogden (Dorfmann and Ogden, 2004), and it is given by

$$\eta_2 = \tanh\left[\left(\frac{W_l(\varepsilon)}{W_m}\right)^n\right] \bigg/ \tanh(1) \tag{3.14}$$

where $0 < \eta_2 \leq 1$, and $\eta_2 = 1$ when unloading begins; $n$ is the material constant.

By substituting Equations. (3.12) ~ (3.14) to Equation (3.11), the stress $\sigma_u$ (in MPa) on the unloading path of the hysteresis curve is written as

$$\sigma_u = 2\left[1 - \frac{1}{(\varepsilon+1)^3}\right]\left[C_{10}(\varepsilon+1) + C_{01}\right]\left[A(\dot{\varepsilon}-0.1)+1\right]\left[\frac{B}{T+50}+C\right]$$

$$\cdot\left(1 - \frac{1}{r}\tanh\left[\frac{W_m - W_l(\varepsilon)}{m}\right]\right) + C_1\left(1 - \tanh\left[\left(\frac{W_l(\varepsilon)}{W_m}\right)^n\right] \bigg/ \tanh(1)\right) \cdot \left(2\varepsilon - \frac{2}{(\varepsilon+1)^2} - 1\right)$$

(3.15)

Equation (3.15) is to predict the stress of tire rubbers on the unloading path of the hysteresis curve at different strain levels, strain rates, and rubber temperatures.

### 3.4.1.3. Hysteresis loss within one loading-unloading cycle

According to other researchers (Cho et al., 2013; Li et al., 2018, 2016; Luo et al., 2010), the hysteresis loss of rubbers is represented by the integral area of the hysteresis loop within one loading-unloading cycle. Based on this, the hysteresis loss $H$ (in kJ/m$^3$) of tire rubbers is calculated as follows

$$H = \int_0^{SL} \sigma_l \, d\varepsilon - \int_0^{SL} \sigma_u \, d\varepsilon \qquad (3.16)$$

where $\sigma_l$ and $\sigma_u$ are determined by Equation (3.10) and Equation (3.11), respectively; $SL$ is the value of the strain level (in m/m).

The hysteresis loss of tire rubbers within one cycle of loading and unloading corresponds to the heat generation of tire rubbers during one revolution of the tire, as per other researchers (Maritz, 2015; Smith et al., 2012; Tang et al., 2014). Equation (3.16) is the HLSRT model that has been developed in this study to estimate the hysteresis loss under the influences of strain levels, strain rates, and rubber temperatures.

*3.4.1.4. Determination of material constants*

The material constants in the HLSRT model were determined following an inverse analysis method widely used in previous studies (Ghoreishy, 2012; Jin and Cui, 2010; Lei and Szeri, 2007; Li et al., 2017). As per this method, an error function $f\left(C_{10}, C_{01}, C_1, r, m, n, A, B, C\right)$ was established based on the stresses on the hysteresis curve:

$$
\begin{aligned}
f\left(C_{10}, C_{01}, C_1, r, m, n, A, B, C\right) = & \sum_{i=1}^{M}\left[\sigma_{l-prediction,i}\left(\varepsilon\right) - \sigma_{l-\mathrm{experiment},i}\left(\varepsilon\right)\right]^2 \\
& + \sum_{j=1}^{N}\left[\sigma_{u-prediction,j}\left(\varepsilon\right) - \sigma_{u-\mathrm{experiment},j}\left(\varepsilon\right)\right]^2
\end{aligned}
\qquad (3.17)
$$

where $\sigma_{l-prediction,i}\left(\varepsilon\right)$ (in MPa) and $\sigma_{l-\mathrm{experiment},i}\left(\varepsilon\right)$ (in MPa) are the stresses derived from the model predictions and the experiments corresponding to the strain of $\varepsilon$ (in m/m) on the loading path of hysteresis curve, respectively; $\sigma_{u-prediction,j}\left(\varepsilon\right)$ (in MPa) and $\sigma_{u-\mathrm{experiment},j}\left(\varepsilon\right)$ (in MPa) are

the stresses obtained from the model predictions and the experiments at the strain of $\varepsilon$ (in m/m) during unloading, respectively; $M$ and $N$ are the numbers of data points.

As indicated by Equation (3.17), the smaller values of $f\left(C_{10}, C_{01}, C_1, r, m, n, A, B, C\right)$ indicate the smaller deviations between the stresses obtained from the model predictions and the experiments (in Table 3.2). Based on this, to minimize this deviation, the material constants causing the minimum value of $f\left(C_{10}, C_{01}, C_1, r, m, n, A, B, C\right)$ were determined, as shown in Table 3.5.

Table 3.5. Material constants in the HLSRT model for the given OTR tire tread rubber

| Rubber type | $C_{10}$ | $C_{01}$ | $C_1$ | $A$ | $B$ | $C$ | $r$ | $m$ | $n$ |
|---|---|---|---|---|---|---|---|---|---|
| Tread rubber | 1.21 | -0.58 | -0.26 | 0.04 | 2.84 | 0.55 | 0.57 | 1.55 | 1.97 |

In Table 3.5, the constants $C_{10}$, $C_{01}$, $C_1$, $r$, $m$, and $n$ determined the function that characterized the hysteresis curves of the tire rubber when strain level varied from 10% to 100%. The constants $A$, $B$, and $C$ determined the strain-rate-dependent and the rubber-temperature-dependent coefficients that described the variations of hysteresis curves at different strain rates ($10\% \sim 500\%$ s$^{-1}$) and rubber temperatures ($-30 \sim 100$ °C). As a result, one set of the nine constants fitted the different hysteresis curves of the given tire rubber at strain levels ranging from 10% to 100%, strain rates from 10% to 500% s$^{-1}$, and rubber temperatures from -30 to 100 °C.

Based on the nine material constants in Table 3.5, the HLSRT model for the given OTR tire rubber is obtained below

$$H = \int_0^{SL} \sigma_l d\varepsilon - \int_0^{SL} \left( 1 - \frac{1}{0.57} \tanh\left[ \frac{W_m - W_l(\varepsilon)}{1.55} \right] \right) \cdot \sigma_l d\varepsilon$$

$$+ 0.26 \int_0^{SL} \left( 1 - \tanh\left[ \left( \frac{W_l(\varepsilon)}{W_m} \right)^{1.97} \right] \middle/ \tanh(1) \right) \cdot \left( 2\varepsilon - \frac{2}{(\varepsilon+1)^2} - 1 \right) d\varepsilon$$

(3.18)

where,

$$\sigma_l = 2\left[ 1 - \frac{1}{(\varepsilon+1)^3} \right] \left[ 1.21(\varepsilon+1) - 0.58 \right] \left[ 0.04(\dot{\varepsilon}-0.1) + 1 \right] \left[ \frac{2.84}{T+50} + 0.55 \right]$$

(3.19)

In the HLSRT model, strain levels and strain rates of OTR tire rubbers are converted from payloads and speeds of haul trucks, respectively. Rubber temperatures are derived from tire temperatures at mine sites. Based on this, the HLSRT model has its engineering significance, and it is to predict the hysteresis loss of OTR tire rubbers under different operating conditions of payloads, truck speeds, and tire temperatures.

### 3.4.2. A brief review of phenomenological models

In addition to the HLSRT model, Table 3.6 has summarized seven other phenomenological models that exist in the literature, including the Dorfmann model (Dorfmann and Ogden, 2004), the Hu model (Hu et al., 2019), the Li model (Li et al., 2017), the Liu model (Liu and Fatt, 2011), the Luo model (Luo et al., 2010), the Yoo model (Yoo et al., 2016), and the Zhi model (Zhi et al., 2019). These seven models were selected from a collection of models in the last 20 years; they all achieved relatively good results in predicting hysteresis loss.

Table 3.6. A summary of selected phenomenological models for predicting hysteresis loss (in kJ/m$^3$)

| Name | Type | Equations | Variables and constants |
|---|---|---|---|
| Dorfmann model (Dorfmann and Ogden, 2004) | S | $H = \sum_{m=1}^{3} \mu_m \left( \lambda^{\alpha_m} + 2\lambda^{-\alpha_m/2} - 3 \right) / \alpha_m$ $- \int_{1}^{SL+1} \left[ \eta_1 \sum_{m=1}^{3} \mu_m \left( \lambda^{\alpha_m-1} - \lambda^{-\alpha_m/2-1} \right) \right] d\lambda$ $- \int_{1}^{SL+1} (1-\eta_2)\left(v_1\lambda - \bar{v}_2\lambda^{-2}\right) d\lambda$ | $H$ is the hysteresis loss (in kJ/m$^3$); $\lambda$ is the average stretch ratio (in m/m); $\eta_1$ and $\eta_2$ are the softening variable and residual strain variable, respectively; $SL$ is the value of strain level (in m/m); $\mu_m$, $\alpha_m$, $v_1$, and $\bar{v}_2$ are the material constants |
| Hu model (Hu et al., 2019) | R | $H = \pi\varepsilon^2 \dfrac{2a \cdot (\varepsilon/b)^c}{1+(\varepsilon/b)^{2c}} \times 10^{\frac{d\cdot(T-20)}{e+T-20}}$ | $H$ is the hysteresis loss (in kJ/m$^3$); $\varepsilon$ is the strain (in m/m); $T$ is the rubber temperature (in °C); $a$, $b$, $c$, $d$, and $e$ are the material constants |
| Li model (Li et al., 2017) | S | $H = \sum_{i=1}^{3} C_{i0}\left(\lambda^2 + 2\lambda^{-1} - 3\right)^i - 2C_{i0}$ $\cdot \int_{1}^{SL+1} \left[ \eta_1 \sum_{i=1}^{3} i\left(\lambda^2 + 2\lambda^{-1} - 3\right)^{i-1} \cdot \left(\lambda - \lambda^{-2}\right) \right] d\lambda$ | $H$ is the hysteresis loss (in kJ/m$^3$); $\lambda$ is the average stretch ratio (in m/m); $\eta_1$ is the softening variable; $SL$ is the value of strain level (in m/m); $C_{i0}$ is the material constant |
| Liu model (Liu and Fatt, 2011) | R | $H = 4\int_{1}^{SL+1} C_{10}^e\left(\lambda,\dot{\lambda}\right) \left( \lambda_e^2\left(\lambda,\dot{\lambda}\right) - \dfrac{1}{\lambda_e\left(\lambda,\dot{\lambda}\right)} \right) d\lambda$ where, $C_{10}^e\left(\lambda,\dot{\lambda}\right) = \dfrac{\sigma_A}{2}\left[ \left( \dfrac{\lambda}{e^{\alpha(\lambda,\dot{\lambda})\ln\frac{\lambda+1}{2}}} \right)^2 - \dfrac{e^{\alpha(\lambda,\dot{\lambda})\ln\frac{\lambda+1}{2}}}{\lambda} \right]^{-1}$ | $H$ is the hysteresis loss (in kJ/m$^3$); $\lambda$ is the average stretch ratio (in m/m); $SL$ is the value of strain level (in m/m); $\lambda_e\left(\lambda,\dot{\lambda}\right)$ is the stretch ratio associated with the intermediate spring (in m/m); $C_{10}^e\left(\lambda,\dot{\lambda}\right)$ and $\alpha\left(\lambda,\dot{\lambda}\right)$ are the constants that depend on the stretch ratio $\lambda$ (in m/m) and stretch ratio rate $\dot{\lambda}$ (in s$^{-1}$); $\sigma_A$ is the average stress in the hysteresis curve (in MPa) |

| Model | | Equation | Description |
|---|---|---|---|
| Luo model (Luo et al., 2010) | R | $$H = \pi\varepsilon^2 \frac{\left(a + \frac{b\dot{\varepsilon}}{2\varepsilon}\right)\cdot(\varepsilon/c)^d}{1+(\varepsilon/c)^{2d}}$$ | $H$ is the hysteresis loss (in kJ/m³); $\varepsilon$ is the strain (in m/m); $\dot{\varepsilon}$ is the strain rate (in s⁻¹); $a$, $b$, $c$, and $d$ are the material constants |
| Yoo model (Yoo et al., 2016) | R | $$H = 4\int_1^{SL+1}\left[\sum_{i=1}^{3}iC_i^e\left(\lambda_e^2 + 2\lambda_e^{-1} - 3\right)^{i-1}\right]$$ $$\cdot\left(\lambda_e^2 - \lambda_e^{-1}\right)d\lambda$$ where, $$\lambda_e = \lambda_e(\lambda,\dot{\lambda}), C_i^e = C_i^e(\lambda,\dot{\lambda})$$ $$2\sum_{i=1}^{3}iC_i^e\left(\lambda^2\lambda_\alpha^{-2} + 2\lambda^{-1}\lambda_\alpha - 3\right)^{i-1}$$ $$= \sigma_A\left(\lambda^2\lambda_\alpha^{-2} - \lambda^{-1}\lambda_\alpha\right)^{-1}$$ $$\ln\lambda_\alpha = \alpha(\lambda,\dot{\lambda})\ln\left[0.5(\lambda+1)\right]$$ | $H$ is the hysteresis loss (in kJ/m³); $\lambda$ is the average stretch ratio (in m/m); $SL$ is the value of strain level (in m/m); $\lambda_e(\lambda,\dot{\lambda})$ is the stretch ratio associated with the intermediate spring (in m/m); $C_i^e(\lambda,\dot{\lambda})$ and $\alpha(\lambda,\dot{\lambda})$ are the constants that depend on the stretch ratio $\lambda$ (in m/m) and stretch ratio rate $\dot{\lambda}$ (in s⁻¹); $\sigma_A$ is the average stress in the hysteresis curve (in MPa) |
| Zhi model (Zhi et al., 2019) | R | $$H = \int_0^{\frac{2\varepsilon}{\dot{\varepsilon}}}\sigma_a(\dot{\varepsilon},T)\sin\left(\frac{\pi\dot{\varepsilon}}{\varepsilon}t\right)$$ $$\cdot\frac{\varepsilon_a\sin\left(\frac{\pi\dot{\varepsilon}}{\varepsilon}t-\delta\right)}{dt}dt$$ | $H$ is the hysteresis loss (in kJ/m³); $\varepsilon$ and $\varepsilon_a$ are the strain (in m/m) and peak strain (in m/m); $\dot{\varepsilon}$ is the strain rate (in s⁻¹); $\sigma_a(\dot{\varepsilon},T)$ is the peak stress (in MPa) depending on the strain rate (in s⁻¹) and rubber temperature (in °C); $\delta$ is the phase angle (in rad); $t$ is the time (in s) |
| HLSRT model | S | $$H = \int_0^{SL}\sigma_l d\varepsilon - \int_0^{SL}\eta_1\sigma_l d\varepsilon -$$ $$C_1\int_0^{SL}(1-\eta_2)\cdot\left[2\varepsilon - 2(\varepsilon+1)^{-2} - 1\right]d\varepsilon$$ where, $$\sigma_l = 2\left[1-(\varepsilon+1)^{-3}\right]\left[C_{10}(\varepsilon+1)+C_{01}\right]$$ $$\left[A(\dot{\varepsilon}-0.1)+1\right]\left[B(T+50)^{-1}+C\right]$$ | $H$ is the hysteresis loss (in kJ/m³); $\varepsilon$ is the strain (in m/m); $\dot{\varepsilon}$ is the strain rate (in s⁻¹); $T$ is the rubber temperature (in °C); $\eta_1$ and $\eta_2$ are the softening variable and residual strain variable, respectively; $SL$ is the value of strain level (in m/m); $C_{10}$, $C_{01}$, $C_1$, $A$, $B$, and $C$ are the material constants |

Note: "R" and "S" represent that the model was generated based on a rheological framework and a strain energy function, respectively. The material constants in Table 6 were identified and summarized in Appendix 3B.

## 3.5. Discussions

### 3.5.1. Verification of the HLSRT model based on experimental results

To verify the HLSRT model, comparisons were conducted between the hysteresis loss results predicted from the HLSRT model and the hysteresis loss results measured from the experiments. In the comparisons, MAPE was employed to evaluate the deviations between these two groups of hysteresis loss results.

The MAPEs under different operating conditions are listed in Table 3.7. The operating conditions covered six strain rates (from 10% to 500% s$^{-1}$) and eight rubber temperatures (from -30 to 100 °C). Under each combination of strain rates and rubber temperatures, the MAPEs were calculated based on the predicted and experimentally measured hysteresis loss results at strain levels of 10%, 20%, 40%, 60%, 80%, and 100%.

Table 3.7. MAPEs under different operating conditions

| Strain rate / Rubber temp. | 10% s$^{-1}$ | 100% s$^{-1}$ | 200% s$^{-1}$ | 300% s$^{-1}$ | 400% s$^{-1}$ | 500% s$^{-1}$ |
|---|---|---|---|---|---|---|
| -30 °C | 12.3% | 13.3% | 12.5% | 9.8% | 8.8% | 12.2% |
| -10 °C | 9.3% | 12.4% | 13.3% | 10.9% | 9.8% | 11.4% |
| 0 °C | 12.2% | 18.6% | 12.9% | 13.4% | 13.5% | 13.6% |
| 20 °C | 11.7% | 11.4% | 11.8% | 9.8% | 9.4% | 9.4% |
| 40 °C | 12.4% | 9.6% | 10.9% | 12.6% | 10.8% | 11.6% |
| 60 °C | 12.7% | 10.3% | 9.0% | 11.6% | 10.8% | 9.7% |
| 80 °C | 9.5% | 11.7% | 7.0% | 10.4% | 9.6% | 10.4% |
| 100 °C | 11.2% | 10.4% | 7.8% | 11.5% | 12.7% | 10.9% |

In Table 3.7, the MAPEs varied from 7.0% to 18.6%, and the average MAPE was 11.2% at strain levels ranging from 10% to 100%, strain rates from 10% to 500% s$^{-1}$, and rubber temperatures from -30 to 100 °C. This indicates that the HLSRT model predicted the hysteresis loss of tread rubbers with an average MAPE of 11.2%, and the maximum MAPE from the model

predictions did not exceed 18.6% under any operating conditions (i.e., strain rates of 10% ~ 500% $s^{-1}$, rubber temperatures of -30 ~100 °C, and strain levels of 10% ~ 100%). As reported by other researchers (Liu, 2007; Luo et al., 2010), the prediction model with an average MAPE of 13.7% (Luo et al., 2010) and the model with a maximum MAPE of even up to 28% (Liu, 2007) were considered to be verified for estimating the hysteresis loss of rubbers obtained from highway-terrain (HT) tires. The average and maximum MAPEs from the HLSRT model were 11.2% and 18.6%, which are lower than 13.7% and 28%, respectively. Thus, the hysteresis loss results predicted by the HLSRT model were believed to be in good agreement with the results measured by the experiments. In other words, the HLSRT model can predict the hysteresis loss of tread rubbers with relatively high accuracy.

**3.5.2. Prediction of hysteresis loss under different operating conditions**

After verification, the HLSRT model was used to predict the hysteresis loss of tread rubbers under different operating conditions. These operating conditions included strain levels ranging from 10% to 100%, strain rates from 10% to 500% $s^{-1}$, and rubber temperatures from -30 to 100 °C.

*3.5.2.1. Prediction of hysteresis loss at different strain levels*

Figure 3.5 shows the prediction results of hysteresis loss for tread rubbers at strain levels from 10% to 100%. At a strain rate of 500% $s^{-1}$ and a rubber temperature of 20 °C, the HLSRT model identified an exponential increase of hysteresis loss at rising strain levels. This indicates that the hysteresis loss increased relatively slowly when the strain levels were small, but it increased rapidly with a further increase of strain levels. For instance, as the strain level was raised from 10% to 40%, the hysteresis loss grew from 2.5 to 37.4 kJ/m$^3$; when the strain level was further

raised from 40% to 100%, there was a rapid increase in hysteresis loss from 37.4 to 168.7 kJ/m$^3$. This predicted exponential increase of hysteresis loss coincided with the experimental results, showing an average MAPE of 9.4%.

The exponential increase of hysteresis loss indicated in the HLSRT model is also consistent with the predictions derived from other models shown in Figure 3.5, such as the Zhi model (Zhi et al., 2017), the Yoo model (Yoo et al., 2016), and the Liu model (Liu and Fatt, 2011). However, dissimilar to the HLSRT model, these three models cannot predict hysteresis loss accurately at large strain levels (e.g., above 40% or 60%). For instance, the Zhi model (Zhi et al., 2017) overestimated the hysteresis loss of tread rubbers at strain levels of over 60%, and the overestimation increased with a rise of strain levels and reached the maximum value of 16.1% at the 100% strain level. On the other hand, the Yoo model (Yoo et al., 2016) and the Liu model (Liu and Fatt, 2011) provided an underestimation for hysteresis loss values when the strain levels exceeded 40%, and this underestimation was magnified by 17.5% on average when the strain level was raised up to 100%. The Yoo model and the Liu model did not predict hysteresis loss accurately at large strain levels because these models were developed based on rheological frameworks that included linear elastic elements (Liu and Fatt, 2011; Yoo et al., 2016). These linear elastic elements cannot describe the nonlinear hysteresis curves precisely (Liu and Fatt, 2011). According to Figure 3.3, the hysteresis curves of OTR tire rubbers at strain levels exceeding 40% grew more nonlinearly compared with those at strain levels within 40%. This led to an inaccurate prediction for hysteresis loss at large strain levels (e.g., above 40%).

In Figure 3.5, there are four other models that precisely predicted the hysteresis loss at rising strain levels, including the Dorfmann model (Dorfmann and Ogden, 2004), the Hu model (Hu et al., 2019), the Li model (Li et al., 2017), and the Luo model (Luo et al., 2010). For example,

the Dorfmann model (Dorfmann and Ogden, 2004) estimated the hysteresis loss of tread rubbers with an average MAPE of 5.2%. The Hu model (Hu et al., 2019), the Li model (Li et al., 2017), and the Luo model (Luo et al., 2010) predicted the tread hysteresis loss with average MAPEs of 5.3%, 7.7%, and 4.7%, respectively. Note that these MAPEs are even lower than the MAPE (i.e., 9.4%) in the HLSRT model, which indicates that the Dorfmann model, the Hu model, the Li model, and the Luo model can predict the hysteresis loss at rising strain levels with higher accuracy. However, despite higher accuracy (e.g., 5.2%, 5.3%, 7.7%, and 4.7%), these four models are not considered to be superior to the HLSRT model because none of these models can identify the effects of strain rates and rubber temperatures on the hysteresis loss. The inability to predict the hysteresis loss at different strain rates and rubber temperatures makes these four models unsuitable for OTR tire rubbers. This is because, as mentioned, in OTR tire rubbers used at mine sites, the strain rates range from 10% to 500% s$^{-1}$, and the rubber temperatures fluctuate between -30 °C and 100 °C. These variable strain rates and rubber temperatures tend to cause different hysteresis loss values in tire rubbers, as per other researchers (Li et al., 2012; Marais and Venter, 2018; Nyaaba et al., 2019b).
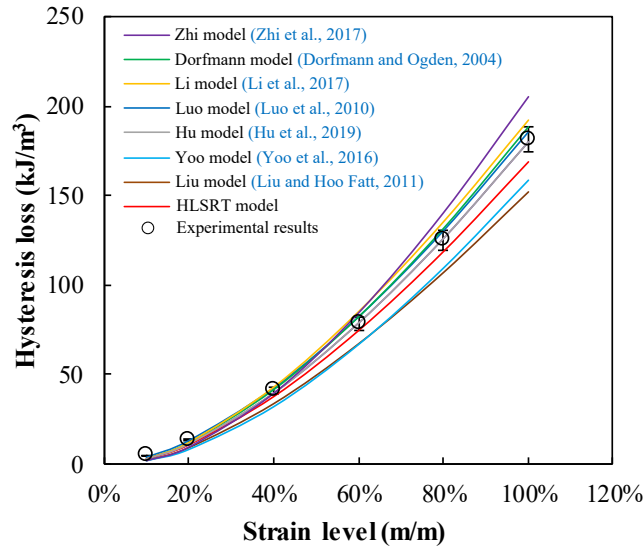
Figure 3.5. Prediction results of hysteresis loss for tread rubbers at 20 °C, a 500% s$^{-1}$ strain rate, and strain levels from 10% to 100%

### 3.5.2.2. Prediction of hysteresis loss at different strain rates

Figure 3.6 presents the prediction results of hysteresis loss for tread rubbers at strain rates from 10% to 500% s$^{-1}$. At 20 °C and the 100% strain level, the HLSRT model captured a linear increase of hysteresis loss at rising strain rates. For instance, the hysteresis loss grew uniformly from 141.3 to 170.1.3 kJ/m$^3$ as the strain rate was raised from 10% to 500% s$^{-1}$, which was close to a linear trend. This linear increasing trend of hysteresis loss overlapped with the experimental results, showing the deviations in hysteresis loss results with a MAPE of 10.4%.

The growth of hysteresis loss at rising strain rates can also be predicted by the Zhi model (Zhi et al., 2017), the Yoo model (Yoo et al., 2016), and the Liu model (Liu and Fatt, 2011). Nevertheless, the prediction accuracy of hysteresis loss in these models was not as high as that in the HLSRT model. For example, the Zhi model (Zhi et al., 2017) overestimated the hysteresis loss

at high strain rates (e.g., above 300% s$^{-1}$), and the Liu model (Liu and Fatt, 2011) provided an underestimation (i.e., 15.3% ~ 18.6%) for hysteresis loss values when the strain rates were greater than 100% s$^{-1}$. These overestimations or underestimations caused relatively high MAPEs in the Zhi model (i.e., 13.6%) and the Liu model (i.e., 15.3%), respectively, at rising strain rates from 10% s$^{-1}$ to 500% s$^{-1}$. These MAPEs are higher than that (i.e., 10.4%) in the HLSRT model, which indicates that these models predicted the hysteresis loss with prediction accuracy that was not as high as that in the HLSRT model. In addition, it is of note that despite higher accuracy (i.e., 10.4%), the HLSRT model still derived an underestimation for hysteresis loss values at high strain rates (e.g., above 200% s$^{-1}$). This underestimation increased with a rise of strain rates, which reached up to 13.6% at the strain rate of 500% s$^{-1}$.

In Figure 3.6, the prediction results of hysteresis loss from the Dorfmann model (Dorfmann and Ogden, 2004), the Hu model (Hu et al., 2019), and the Li model (Li et al., 2017) showed a set of flat lines at the rising strain rates. These flat lines indicate that these models failed to identify the growth of hysteresis loss as the strain rate increased. This can be explained by the absence of strain-rate-dependent coefficients in model development. Without the inclusion of strain-rate-dependent coefficients, these models cannot describe the variations of hysteresis loss at different strain rates, and the hysteresis loss values remained unchanged regardless of the rising strain rates. Due to their inability to characterize the variations of hysteresis loss with strain rates, the Dorfmann model, the Hu model, and the Li model are not suitable to predict the hysteresis loss of OTR tire rubbers at variable strain rates.
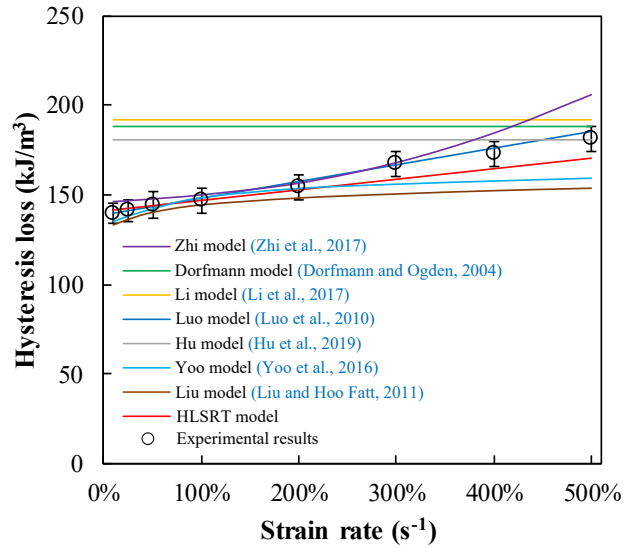
Figure 3.6. Prediction results of hysteresis loss for tread rubbers at 20 °C, a 100% strain level, and strain rates from 10% s$^{-1}$ to 500% s$^{-1}$

### 3.5.2.3. Prediction of hysteresis loss at different rubber temperatures

Figure 3.7 illustrates the prediction results of hysteresis loss for tread rubbers at rubber temperatures from -30 to 100 °C. At a 500% s$^{-1}$ strain rate and a 100% strain level, the HLSRT model characterized an inverse proportional variation of hysteresis loss with rubber temperatures. This indicates that the hysteresis loss reduced sharply at the beginning of the rubber temperature rise, yet it decreased slightly as the rubber temperature further increased. For instance, the hysteresis loss reduced by approximately 17% as the rubber temperature was raised from -30 to 10 °C; however, it decreased by only 7% in total with further increases in rubber temperatures from 10 to 100 °C. The inverse proportional variation of hysteresis loss was verified by the experimental results in this study. At a 500% s$^{-1}$ strain rate and a 100% strain level, the experimental results showed that the hysteresis loss decreased from 215.8·to 184.3, and then to

71

166.2 kJ/m$^3$ as the rubber temperature was raised from -30 to 10, and then to 100 ℃. This decreasing trend of hysteresis loss can be fitted with an inverse proportional function.

In Figure 3.7, it is observed that the inverse proportional relationship between hysteresis loss and rubber temperatures was not often well characterized in previous models, such as the Zhi model (Zhi et al., 2017). As predicted by the Zhi model, hysteresis loss reduced with a rise of rubber temperatures in a straight line, rather than in an inverse proportional variation. This is because the Zhi model did not contain a nonlinear rubber-temperature-dependent coefficient for modifying the hysteresis loss values under the influence of rubber temperatures. This makes the model not identify the nonlinear variations (i.e., inverse proportional) of hysteresis loss with rubber temperatures, causing discrepancies in predicting the hysteresis loss. The discrepancies herein included an overestimation for hysteresis loss values at relatively low rubber temperatures (e.g., below 60 ℃) and an underestimation for hysteresis loss values when rubbers were subjected to higher rubber temperatures (e.g., above 60 ℃). These discrepancies reached the maximum value of 15.2% at a rubber temperature of around 0 ℃.

In addition, it is of note that the variations of hysteresis loss with rubber temperatures were not identified by the Yoo model (Yoo et al., 2016), the Dorfmann model (Dorfmann and Ogden, 2004), the Li model (Li et al., 2017), the Luo model (Luo et al., 2010), or the Liu model (Liu and Fatt, 2011). In these five models, since there is no rubber-temperature-dependent coefficient, the effects of rubber temperatures on the hysteresis loss cannot be reflected. As a result, the predicted hysteresis loss values stayed the same at the rising rubber temperatures, which is not true. Thus, these five models cannot be used to predict the hysteresis loss of OTR tire rubbers at variable rubber temperatures.
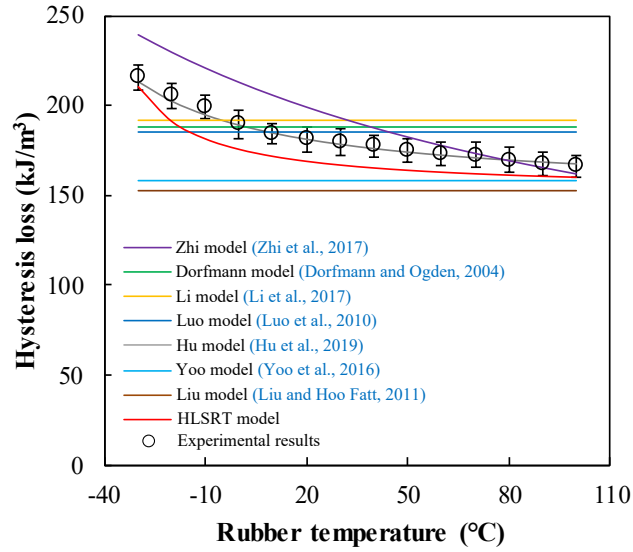
Figure 3.7. Prediction results of hysteresis loss for tread rubbers at a 500% s$^{-1}$ strain rate, a 100% strain level, and rubber temperatures from -30 ℃ to 100 ℃

### 3.5.2.4. Comparisons of the HLSRT model with existing phenomenological models

The comparisons of the HLSRT model with seven other existing phenomenological models listed in Table 3.6 are summarized in Table 3.8.

Table 3.8. Comparisons of the HLSRT model with existing phenomenological models

| Model name | Strain level (m/m) | Strain rate ($s^{-1}$) | Rubber temperature (℃) | Comments |
|---|---|---|---|---|
| Yoo model (Yoo et al., 2016) | Yes | Yes | No | Underestimations (13.3% ~ 16.4%) at large strain levels (> 40%) and at high strain rates (> 100% $s^{-1}$) |
| Dorfmann model (Dorfmann and Ogden, 2004) | Yes | No | No | |
| Li model (Li et al., 2017) | Yes | No | No | |
| Luo model (Luo et al., 2010) | Yes | Yes | No | |
| Hu model (Hu et al., 2019) | Yes | No | Yes | |
| Zhi model (Zhi et al., 2017) | Yes | Yes | Yes | Overestimations (14.1% ~ 16.1%) at large strain levels (> 60%) and at high strain rates (> 300% $s^{-1}$); Overestimations (~ 15.2%) at low rubber temperatures (< 60 ℃) |
| Liu model (Liu and Fatt, 2011) | Yes | Yes | No | Underestimations (15.3% ~ 18.6%) at large strain levels (> 40%) and at high strain rates (> 100% $s^{-1}$) |
| HLSRT model | Yes | Yes | Yes | Underestimations (7.0% ~ 13.6%) at large strain levels (> 60%) and at high strain rates (> 200% $s^{-1}$) |

In Table 3.8, eight phenomenological models were selected for comparisons regarding hysteresis loss prediction at strain levels ranging from 10% to 100%, strain rates from 10% to 500% $s^{-1}$, and rubber temperatures from -30 to 100 ℃. All eight models could predict hysteresis loss at rising strain levels although there were overestimations (e.g., 14.1% ~ 16.1%) from the Zhi model (Zhi et al., 2017) and underestimations (e.g., 13.3% ~ 18.6%) from the Yoo model (Yoo et al., 2016) and the Liu model (Liu and Fatt, 2011) at large strain levels (e.g., above 40% or 60%). Moreover, the Yoo model (Yoo et al., 2016), the Luo model (Luo et al., 2010), and the Liu model (Liu and Fatt, 2011) could predict the hysteresis loss of tread rubbers when the strain rate increased from 10% to 500% $s^{-1}$, and the Hu model (Hu et al., 2019) could estimate the tread hysteresis loss when the rubber temperature was raised from -30 to 100 ℃.

It is of note that only the Zhi model (Zhi et al., 2017) and the HLSRT model in this study could identify the variations of hysteresis loss under the influence of strain levels, strain rates, and

rubber temperatures. Nevertheless, the Zhi model (Zhi et al., 2017) showed deviations when estimating the hysteresis loss values. These deviations included overestimations (e.g., 14.1% ~ 16.1%) at large strain levels (e.g., above 60%) and at high strain rates (e.g., above 300% s$^{-1}$), and also included overestimations (e.g., 15.2%) at low rubber temperatures (e.g., below 60 °C). Compared with the Zhi model (Zhi et al., 2017), the HLSRT model can predict hysteresis loss with an average MAPE of 11.2%, showing relatively small deviations. Therefore, the HLSRT model was considered to be superior to estimate hysteresis loss at different strain levels, strain rates, and rubber temperatures based on typical operating conditions at mine sites.

## 3.6. Conclusion

This study proposed a novel phenomenological model—the HLSRT model (a hysteresis loss model considering strain levels, strain rates, and rubber temperatures). The HLSRT model was used to predict the hysteresis loss of rubbers obtained from ultra-large off-the-road (OTR) tires under typical operating conditions at mine sites. The main conclusions are enumerated as follows:

1. The HLSRT model predicted the hysteresis loss of tire tread rubbers with average and maximum mean absolute percent errors (MAPEs) of 11.2% and 18.6%, respectively, at strain levels ranging from 10% to 100%, strain rates from 10% to 500% s$^{-1}$, and rubber temperatures from -30 to 100 °C. These MAPEs were relatively low when compared with previous studies, showing that the HLSRT model has higher prediction accuracy.

2. The HLSRT model characterized the exponential increase of hysteresis loss at rising strain levels. This indicates that the hysteresis loss increased relatively slowly when the strain levels were small (e.g., within 40%), but it increased rapidly with a further increase of

strain levels (e.g., 40% ~ 100%).

3. The HLSRT model identified the linear growth of hysteresis loss as the strain rate increased. This shows that the hysteresis loss grew uniformly as the strain rate was raised from 10% to 500% s$^{-1}$.

4. The HLSRT model captured the inverse proportional variation of hysteresis loss with rubber temperatures. This indicates that the hysteresis loss reduced sharply at the beginning of the rubber temperature rise (e.g., -30 ~ 10 °C), but the hysteresis loss decreased slightly as the rubber temperature further increased (e.g., 10 ~ 100 °C).

5. The existing phenomenological models derived from rheological frameworks did not predict the hysteresis loss of OTR tire rubbers within acceptable MAPEs (e.g., an average MAPE of 13.7%) when the strain levels varied from 10% to 100%, when the strain rates changed from 10% to 500% s$^{-1}$, and when the rubber temperatures fluctuated between -30 °C and 100 °C. This proves that the existing models based on rheological frameworks cannot be applied to OTR tire rubbers to predict hysteresis loss.

## Appendix 3A. Conversion of operating conditions at mine sites

The strain levels of tire tread rubbers were derived from previous studies (Nyaaba, 2017; Nyaaba et al., 2019b). The strain rates of tire tread rubbers were calculated following a method previously used by Ma et al. (Ma et al., 2021a), which is given by

$$\dot{\varepsilon} = \frac{180 \cdot v \cdot SL}{\pi R \arccos\left(\dfrac{R - VD}{R}\right)} \tag{3A.1}$$

where $\dot{\varepsilon}$ is the strain rate (in s⁻¹); $v$ is the truck speed (in m/s); $SL$ is the strain level (in m/m); $R$ is the radius of the OTR tire (in m); $VD$ is the vertical deflection of the OTR tire (in m) that correlates with payloads, as per Nyaaba (Nyaaba, 2017). Herein, the values of $VD$ are 275 mm and 115 mm under the laden (i.e., 363-tonne payload) and unladen (i.e., zero payload) conditions, respectively.

According to Equation (3A.1), the strain levels and strain rates of OTR tread rubbers can be converted from truck speeds and payloads, as listed in Table 3A.1 and Table 3A.2. The truck speeds were derived from Vital Information Management System (VIMS) data at a local mine site (Ta, 2018). The VIMS data indicated that the average maximum truck speed was approximately 20 km/h for a laden truck and about 30 km/h for an unladen truck.

Table 3A.1. Conversion from truck speeds and payloads to strain levels and strain rates of OTR tread rubbers under the laden condition (i.e., 363-tonne payload)

| Truck speed (km/h) | Payload (tonne) | Strain levels (m/m) | Strain rate (s⁻¹) |
|---|---|---|---|
| 0.4 | 363 | 101% | 11% |
| 1 | 363 | 101% | 27% |
| 2 | 363 | 101% | 53% |
| 4 | 363 | 101% | 105% |
| 8 | 363 | 101% | 210% |
| 12 | 363 | 101% | 315% |
| 16 | 363 | 101% | 420% |
| 20 | 363 | 101% | 526% |

Table 3A.2. Conversion from truck speeds and payloads to strain levels and strain rates of OTR

tread rubbers under the unladen condition (i.e., zero payload)

| Truck speed (km/h) | Payload (tonne) | Strain levels (m/m) | Strain rate (s$^{-1}$) |
|---|---|---|---|
| 0.6 | 0 | 42% | 10% |
| 1.5 | 0 | 42% | 26% |
| 3 | 0 | 42% | 52% |
| 6 | 0 | 42% | 103% |
| 12 | 0 | 42% | 206% |
| 18 | 0 | 42% | 309% |
| 24 | 0 | 42% | 412% |
| 30 | 0 | 42% | 515% |

Rubber temperatures in OTR tread rubbers were derived from Michelin Earthmover

Management System (MEMS) data (Ta, 2018) and Alberta Weather Station (AWS) data (Alberta

Agriculture and Forestry, 2018) at the mine site. The MEMS data indicated that the tire internal

temperatures varied from -6 ℃ to 82 ℃, and the AWS data showed that the ambient temperatures

changed from -27 ℃ to 30 ℃. Based on this, the rubber temperatures were selected ranging from

-30 to 100 ℃.

## Appendix 3B. Identification of material constants in the models

The material constants in the models were determined following an inverse analysis

method widely used in previous studies (Ghoreishy, 2012; Jin and Cui, 2010; Lei and Szeri, 2007;

Li et al., 2017). As per this method, first, an error function $f_{error}$ containing the material constants

was developed based on the results of hysteresis loss or the stresses on the hysteresis curves. Then

the material constants were determined when these constants minimize the value of $f_{error}$.

For the Hu model (Hu et al., 2019) or the Luo model (Luo et al., 2010), an error function

was developed according to the results of hysteresis loss, and this function is given by

$$f_{error} = \sum_{i=1}^{P} \left[ H_{prediction,i}\left(\varepsilon\right) - H_{experiment,i}\left(\varepsilon\right) \right]^2 \qquad (3B.1)$$

where $H_{prediction,i}\left(\varepsilon\right)$ (in kJ/m$^3$) and $H_{experiment,i}\left(\varepsilon\right)$ (in kJ/m$^3$) are the hysteresis loss derived from

the model predictions and the experiments corresponding to the strain of $\varepsilon$ (in m/m), respectively;

$P$ is the number of data points.

Then the material constants in the two models were determined when the values of $f_{error}$

were minimized, respectively, as summarized in Table 3B.1.

Table 3B.1. Material constants in the Hu model and the Luo model

| Model | *a* | *b* | *c* | *d* | *e* |
|---|---|---|---|---|---|
| Hu model | 148.14 | 0.19 | 0.61 | 0.03 | 4.58 |
| Luo model | 108.46 | 12.25 | 0.25 | -0.46 | / |

On the other hand, for other models such as the Dorfmann model (Dorfmann and Ogden,

2004), the Li model (Li et al., 2017), the Liu model (Liu and Fatt, 2011), and the Yoo model (Yoo

et al., 2016), error functions were established according to the results of the stresses on the

hysteresis curves, as follows:

$$f_{error} = \sum_{i=1}^{M} \left[ \sigma_{l-prediction,i}\left(\varepsilon\right) - \sigma_{l-experiment,i}\left(\varepsilon\right) \right]^2 + \sum_{j=1}^{N} \left[ \sigma_{u-prediction,j}\left(\varepsilon\right) - \sigma_{u-experiment,j}\left(\varepsilon\right) \right]^2 \qquad (3B.2)$$

where $\sigma_{l-prediction,i}\left(\varepsilon\right)$ (in MPa) and $\sigma_{l-experiment,i}\left(\varepsilon\right)$ (in MPa) are the stresses derived from the

model predictions and the experiments corresponding to the strain of $\varepsilon$ (in m/m) on the loading

path of hysteresis curve, respectively; $\sigma_{u-prediction,j}\left(\varepsilon\right)$ (in MPa) and $\sigma_{u-experiment,j}\left(\varepsilon\right)$ (in MPa) are

the stresses obtained from the model predictions and the experiments at the strain of $\varepsilon$ (in m/m) during unloading, respectively; $M$ and $N$ are the numbers of data points.

Then the material constants causing the minimum values of $f_{error}$ were identified in each model, as shown in Table 3B.2, 3B.3, and 3B.4.

Table 3B.2. Material constants in the Dorfmann model and the Li model

| Model | Material constants |
|---|---|
| Dorfmann model | $\mu_1 = -1.49$, $\mu_2 = 0.21$, $\mu_3 = -0.001$, $\alpha_1 = -0.98$, $\alpha_2 = 4.13$, $\alpha_3 = -4.32$, $V_1 = 1.61$, $\bar{V}_2 = -0.63$ |
| Li model | $C_{10} = 1.05$, $C_{20} = 0.42$, $C_{30} = 0.15$ |

Table 3B.3. Material constants in the Liu model

| Strain rate / Strain level | 100% s⁻¹ | 200% s⁻¹ | 300% s⁻¹ | 400% s⁻¹ | 500% s⁻¹ |
|---|---|---|---|---|---|
| 20% | $C_{10} = 1.47$ $\alpha = 0.25$ | $C_{10} = 1.52$ $\alpha = 0.26$ | $C_{10} = 1.55$ $\alpha = 0.27$ | $C_{10} = 1.59$ $\alpha = 0.29$ | $C_{10} = 1.66$ $\alpha = 0.31$ |
| 40% | $C_{10} = 1.24$ $\alpha = 0.19$ | $C_{10} = 1.27$ $\alpha = 0.20$ | $C_{10} = 1.32$ $\alpha = 0.22$ | $C_{10} = 1.36$ $\alpha = 0.23$ | $C_{10} = 1.43$ $\alpha = 0.25$ |
| 100% | $C_{10} = 0.92$ $\alpha = 0.15$ | $C_{10} = 0.94$ $\alpha = 0.16$ | $C_{10} = 0.98$ $\alpha = 0.17$ | $C_{10} = 1.03$ $\alpha = 0.19$ | $C_{10} = 1.10$ $\alpha = 0.20$ |

Table 3B.4. Material constants in the Yoo model

| Strain rate / Strain level | 100% s⁻¹ | 200% s⁻¹ | 300% s⁻¹ | 400% s⁻¹ | 500% s⁻¹ |
|---|---|---|---|---|---|
| 20% | $C_1 = 2.32$ <br> $C_2 = -0.94$ <br> $\alpha = 1.98$ | $C_1 = 2.35$ <br> $C_2 = -0.92$ <br> $\alpha = 1.94$ | $C_1 = 2.37$ <br> $C_2 = -0.91$ <br> $\alpha = 1.91$ | $C_1 = 2.40$ <br> $C_2 = -0.90$ <br> $\alpha = 1.88$ | $C_1 = 2.43$ <br> $C_2 = -0.88$ <br> $\alpha = 1.85$ |
| 40% | $C_1 = 1.72$ <br> $C_2 = -0.51$ <br> $\alpha = 1.67$ | $C_1 = 1.75$ <br> $C_2 = -0.50$ <br> $\alpha = 1.64$ | $C_1 = 1.76$ <br> $C_2 = -0.49$ <br> $\alpha = 1.62$ | $C_1 = 1.79$ <br> $C_2 = -0.46$ <br> $\alpha = 1.62$ | $C_1 = 1.82$ <br> $C_2 = -0.46$ <br> $\alpha = 1.60$ |
| 100% | $C_1 = 1.31$ <br> $C_2 = -0.38$ <br> $\alpha = 1.52$ | $C_1 = 1.33$ <br> $C_2 = -0.37$ <br> $\alpha = 1.50$ | $C_1 = 1.36$ <br> $C_2 = -0.34$ <br> $\alpha = 1.49$ | $C_1 = 1.39$ <br> $C_2 = -0.32$ <br> $\alpha = 1.48$ | $C_1 = 1.41$ <br> $C_2 = -0.30$ <br> $\alpha = 1.45$ |

# Chapter 4. An analytical solution to predict temperatures of dumbbell-shaped rubber specimens under cyclic deformation

Chapter 4 has been submitted for peer review as **S. Ma**, Y. Guo, W. V. Liu. An analytical solution to predict temperatures of dumbbell-shaped rubber specimens under cyclic deformation, *Journal of Thermal Science and Engineering Applications*. © ASME Digital Collection. (2023)

## 4.1. Introduction

Pneumatic tires are widely used in automotive engineering (Duffy and Wright, 2015; Gent and Walter, 2006); they have various rubbers, including inner filler, inner liner, soft apex, base, sidewall, and tread rubbers (Michelin, 2016). When a vehicle moves, tire rubbers are subjected to cyclic deformation (Marais and Venter, 2018). Under cyclic deformation, the variation of strains in rubbers lags behind that of their stresses, accompanying with hysteresis loss (Hu et al., 2019). From hysteresis loss, heat is generated and then trapped in rubbers, causing an internal heat build-up and a rubber temperature rise (Marais, 2017; Nyaaba, 2017). This rubber temperature rise has attracted much attention from tire researchers because it may affect the mechanical behaviors (e.g., it may reduce the tensile modulus (Yang et al., 2014)) and shorten the fatigue life (Luo et al., 2020, 2019; Zhang et al., 2018) of tire rubbers.

The mechanical behaviors and fatigue life of tire rubbers have been extensively studied based on dumbbell-shaped rubber specimens under uniaxial cyclic loading in many laboratories (Brieu et al., 2010; Ghoreishy et al., 2013; Kocjan et al., 2022; Rangarajan and Ramarathnam, 2021). Due to the influence of rising temperatures on rubber mechanical behaviors and fatigue life, researchers (Behnke et al., 2016; Zhang et al., 2018) are interested in measuring the rubber temperatures in specimens. According to the literature (Guo et al., 2018; Rodas et al., 2016; Schieppati et al., 2019), traditional thermal couples were rarely used to measure rubber temperatures. Inserting thermal couples into specimens may weaken the original structure of the specimens and reduce their tensile modulus (Benkahla et al., 2013) and fatigue life (Zine et al., 2011). Compared with thermal couples, infrared (IR) cameras were more widely used to measure the rubber temperatures in specimens (Rodas et al., 2016; Schieppati et al., 2019). IR cameras can measure rubber temperatures without coming into contact with specimens (Guo et al., 2018),

which ensures that rubber mechanical behaviors are not disturbed by the measurements. In the literature, IR cameras were used to measure rubber temperatures under different testing conditions of strain levels (Guo et al., 2018; Martinez et al., 2013), strain rates (Rodas et al., 2016; Wang et al., 2013), and ambient temperatures (Schieppati et al., 2019). For instance, Martinez et al. (Martinez et al., 2013) used a camera measurement to evaluate the rubber temperatures on the surface of a dumbbell-shaped specimen under cyclic deformation. The results showed that at a strain level of 650%, the surface temperature increased by 7.8 °C when the specimen was cyclically deformed at a strain rate of 50% s$^{-1}$. In addition, Wang et al. (Wang et al., 2013) employed an IR camera to measure the surface temperatures of a dumbbell-shaped rubber specimen at an ambient temperature of 25 °C. The results indicated that the surface temperature increased by 10.3 °C when the strain level was 300% and the strain rate was 23% s$^{-1}$. However, an IR camera can only measure the surface temperatures; it cannot detect the internal temperatures of rubber specimens. Nonetheless, the internal temperatures are significant because they are related to the occurrence of microcracks inside the rubber specimens in fatigue tests (Weng et al., 2011). These microcracks may result in rubber fatigue failures, as per other researchers (Mars and Fatemi, 2003, 2002).

Apart from direct measurements, numerical models and analytical solutions can be used to predict both surface and internal temperatures of rubber specimens. Until now, there have been some numerical models in the literature (Guo et al., 2018; Rodas et al., 2016). For example, Rodas et al. (Rodas et al., 2016) developed a numerical model for a dumbbell-shaped rubber specimen. This model predicted rubber temperatures with relatively high accuracy. At a strain level of 25% and a strain rate of 150% s$^{-1}$, the model predicted the surface temperatures of the specimen with a mean absolute percent error (MAPE) of 11.9% compared with lab recordings. In addition, under cyclic deformation, this model predicted that the internal temperature at the center of the specimen

84

increased by 36.7% at an ambient temperature of 15 °C, which is much greater than the increase (23.9%) in surface temperatures. Another numerical model developed by Guo et al. (Guo et al., 2018) estimated the surface temperatures of a dumbbell-shaped rubber specimen with an MAPE of 12.8% at a strain rate of 100% s$^{-1}$ and strain levels from 10% to 40%. This model also predicted the internal temperature at the center of the specimen, and the temperature went up by 7.1% when the specimen was deformed at an ambient temperature of 23 °C. Compared with numerical models, analytical solutions are usually more time-efficient at predicting temperatures in solids. For instance, as per a study by Fernandes et al. (Fernandes et al., 2010), an analytical solution and a 3D finite element (FE) model were used to predict temperatures in a cast iron sample with a thickness of 65 mm and lateral dimensions of 80.5 × 80 mm. The results indicated that the analytical solution took 306 s to obtain the sample temperatures, which saved 98.7% of the computational time (23,040 s) used in the 3D FE model. Flint et al. (Flint et al., 2018) found that to predict temperatures in a steel cuboid (85 × 30 × 300 mm) under welding, the computational time (2 min) of an analytical solution was 99.9% less than that (7200 min) of a 3D FE model. A search of the literature over the past 20 years for analytical solutions to predict rubber temperatures in dumbbell-shaped specimens yielded no results. Such a solution is necessary because it can efficiently predict both surface and internal temperatures in rubber specimens. As mentioned, rubber temperatures (especially internal temperatures in rubbers) are important since they can help explain the mechanical behaviors and fatigue life of rubber specimens under cyclic deformation.

The objective of this study is to propose an analytical solution to predict temperatures of dumbbell-shaped rubber specimens under cyclic deformation. To achieve this, an analytical solution was developed—the RTDS solution (a solution to predict Rubber Temperatures in Dumbbell-shaped Specimens). This RTDS solution filled the research gap to efficiently predict

both surface and internal temperatures in rubber specimens under different testing conditions (i.e., strain levels, strain rates, and ambient temperatures) in a laboratory. In addition, this RTDS solution was developed in novelty. It included a novel mathematical equation that determined the internal heat generation rates of rubbers. This equation was originally developed based on a modified Mooney-Rivlin (MR) strain energy function, the pseudo-elasticity theory, and the inverse analysis method.

## 4.2. Methodology

### 4.2.1. An overview of the methodology

A flowchart showing an overview of the methodology is represented as in Figure 4.1.
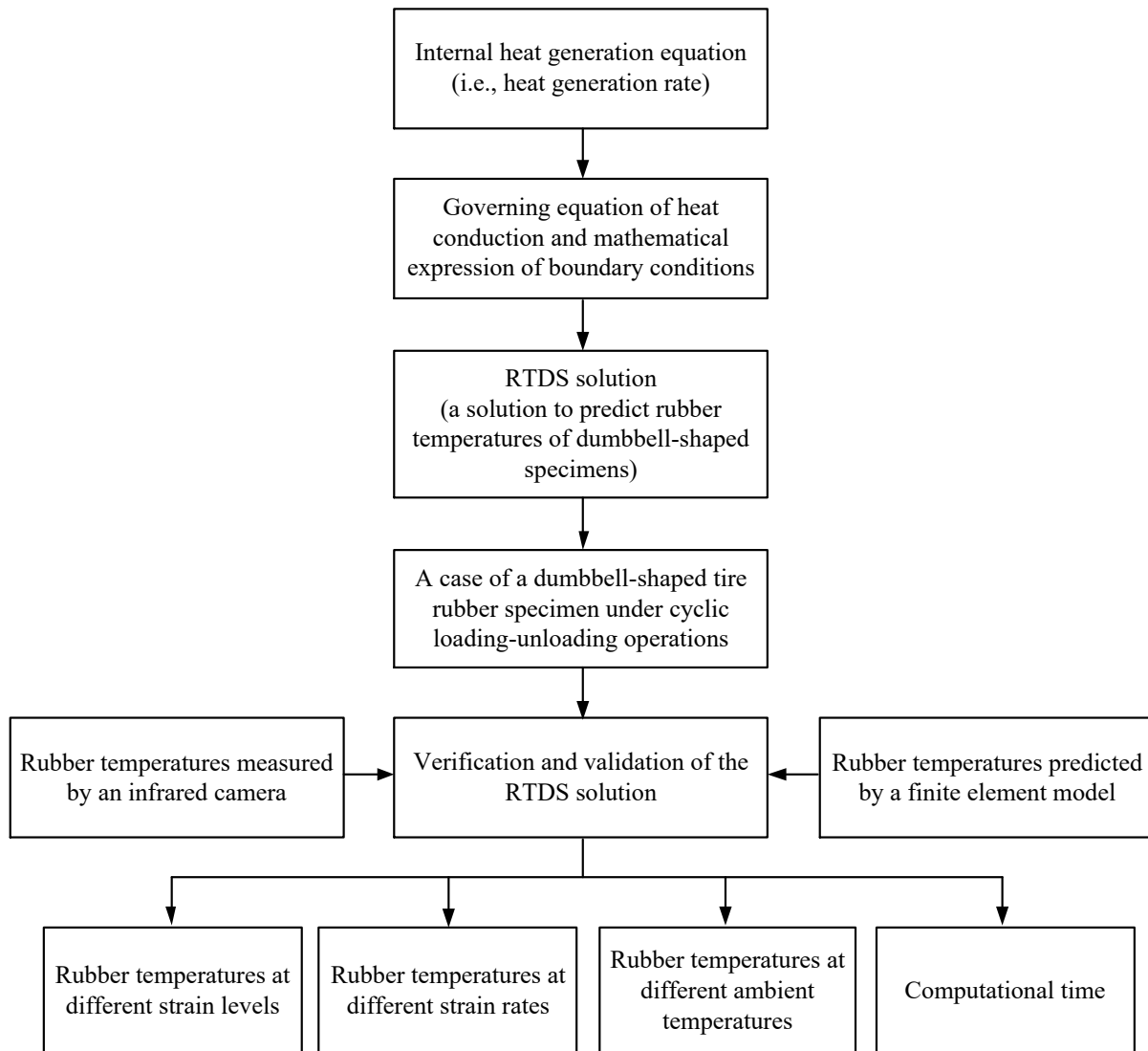
Figure 4.1. A flowchart showing an overview of the methodology

As shown in Figure 4.1, a new mathematical equation was developed to determine the internal heat generation rates of rubbers. With heat generation rates, the governing equation of heat conduction and the mathematical expression of boundary conditions were further generated to describe the heat transfer in rubbers. Based on these equations, the RTDS solution was developed. The RTDS solution was used to predict rubber temperatures in a case scenario of a dumbbell-shaped tire rubber specimen under cyclic loading-unloading operations. These predictions were

conducted under different testing conditions of strain levels, strain rates, and ambient temperatures, as listed in Table 4.1. These testing conditions were converted from typical operating conditions of tires, as referred to Ma et al. (Ma et al., 2022b).

Table 4.1. Strain levels, strain rates, and ambient temperatures used in the operations

| Strain level (m/m) | Strain rate (s$^{-1}$) | Ambient temperature (℃) |
|---|---|---|
| 10%, 20%, 40%, 60%, 80%, and 100% | 10%, 25%, 50%, 100%, 200%, 300%, 400%, and 500% | -30, -20, -10, 0, 10, 20, and 30 |

In the case scenario, the dumbbell-shaped rubber specimen was derived from a Michelin 56/80R63 tire. The specimen was prepared following ASTM D412-16 (ASTM D412-16, 2016), as shown in Figure 4.2(a) and 4.2(b) in units of mm. The rubber specimen was first exposed to a specific ambient temperature that ranged from -30 to 30 °C. This exposure lasted eight hours to ensure that the initial rubber temperature reached the ambient temperature uniformly. Then the rubber specimen was applied by cyclic loading-unloading operations. Under a displacement-controlled mode, the rubber specimen was loaded uniaxially reaching a strain level (i.e., 10%, 20%, 40%, 60%, 80%, or 100%) and then unloaded back to zero at a certain strain rate within the range of 10% to 500% s$^{-1}$. This loading-unloading operation was repeated for 1000 seconds until the rubber temperature became stable. During the operations, the rubber temperatures on a cross section of the rubber specimen were predicted by the RTDS solution, including the rubber temperatures at Point A ($x=3$, $y=2$), Point B ($x=3$, $y=1.5$), and Point C ($x=3$, $y=1$), as shown in Figure 4.2(c).
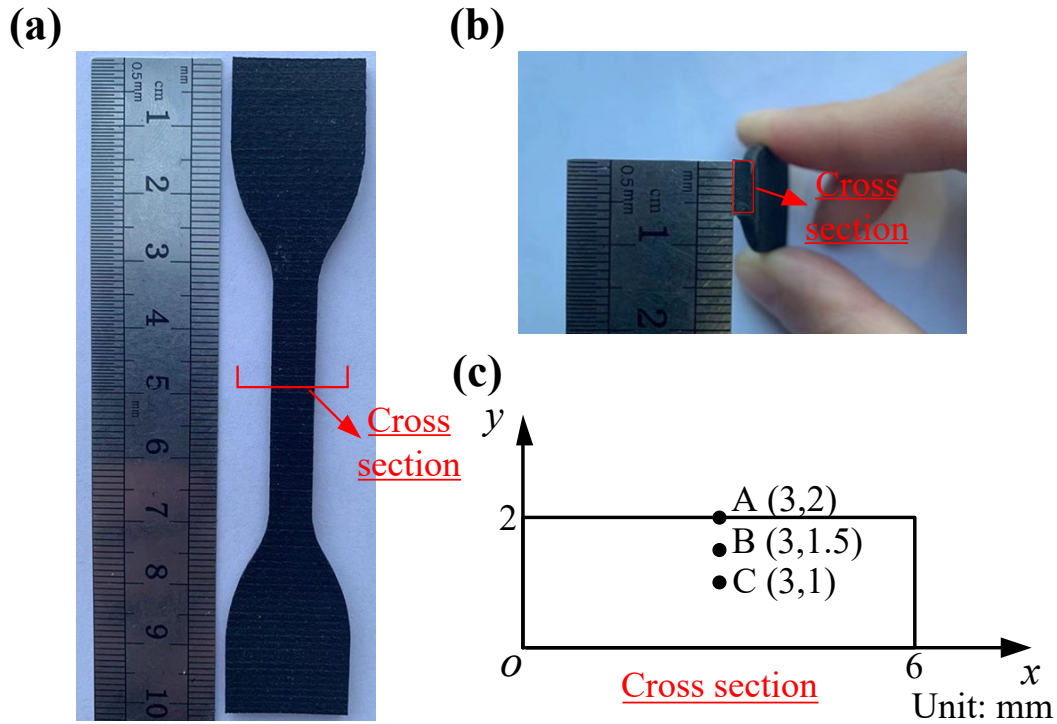
Figure 4.2. Dumbbell-shaped tire rubber specimen: (a) geometry and dimension; (b) cross section; (c) observation points of rubber temperatures

The RTDS solution was executed with a MATLAB code. To verify the code, a finite element (FE) model was developed to predict the rubber temperatures in specimens. At Points A, B, and C, the rubber temperatures derived from this FE model were compared with the rubber temperatures from the RTDS solution code. The deviation in results was evaluated using a statistical index of MAPE. The MAPE is a well-known and commonly accepted index that evaluates the average difference between the forecasted values and the reference values (Dodge, 2008; Zwillinger, 2018). In the code verification, the forecasted values refer to the rubber temperatures derived from the RTDS solution code; the reference values are the rubber temperatures predicted by the FE model. As per Zwillinger (Zwillinger, 2018), the MAPE is given as

$$MAPE = \frac{1}{M} \sum_{i=1}^{M} \left| \frac{T_{FE\,model,i} - T_{RTDScode,i}}{T_{FE\,model,i}} \right| \tag{4.1}$$

where $T_{RTDScode,i}$ (in °C) and $T_{FE\,model,i}$ (in °C) are the rubber temperatures derived from the RTDS solution code and the FE model, respectively; $M$ is the number of data points.

The MAPE calculated from Equation (4.1) was compared with the MAPEs derived from code verifications of other temperature solutions in solids, such as the code verification in a study by Minaei and Safikhani (Minaei and Safikhani, 2021). When the MAPE from Equation (4.1) was not greater than the MAPE in the study, the RTDS solution code was considered to be verified numerically by the FE model.

Apart from the verification, a validation was made for the RTDS solution to ensure that the predicted rubber temperatures were in accordance with physical phenomena. To achieve this, the rubber temperatures on the surface of the specimen were measured in the laboratory. At Point A, the measured rubber temperatures were compared with the rubber temperatures predicted by the RTDS solution, and their deviation was evaluated using the index of MAPE. This MAPE was calculated as in Equation (4.2).

$$MAPE = \frac{1}{N} \sum_{i=1}^{N} \left| \frac{T_{measurement,i} - T_{RTDS,i}}{T_{measurement,i}} \right| \tag{4.2}$$

where $T_{RTDS,i}$ (in °C) and $T_{measurement,i}$ (in °C) are the rubber temperatures derived from the RTDS solution and the laboratory measurements, respectively; $N$ is the number of data points.

The MAPE calculated from Equation (4.2) was compared with the MAPEs derived from other analytical solutions that predict rubber temperatures in cylindrical specimens under cyclic deformation, such as the Luo solution (Luo et al., 2018). When the MAPE from Equation (4.2) was not greater than the MAPEs in the Luo solution, the predicted rubber temperatures were believed to be in good agreement with the measured rubber temperatures, and the RTDS solution was experimentally validated.

After verification and validation, the RTDS solution was used to predict rubber temperatures (e.g., surface temperatures and internal temperatures) in dumbbell-shaped specimens under different testing conditions of strain levels (10% ~ 100%), strain rates (10% ~ 500% s$^{-1}$), and ambient temperatures (-30 ~ 30 °C). In addition, the computational time of the RTDS solution was compared with that of the FE model to highlight the efficiency of the RTDS solution.

## 4.2.2. The RTDS solution

### 4.2.2.1. Internal heat generation equation

A new mathematical equation was developed to determine the internal heat generation rates of rubbers. The heat generation rate is the amount of the heat generated in rubbers per unit volume and unit time on the cross section of the specimen (in Figure 4.2(c)). The heat generation rate $\dot{Q}$ (in W/m$^3$) was calculated following a method widely used in previous studies (Cho et al., 2013; Li et al., 2018; Tang et al., 2014), and is expressed as

$$\dot{Q} = H \cdot f = \left( \int_0^\varepsilon \sigma_l d\varepsilon - \int_0^\varepsilon \sigma_u d\varepsilon \right) \cdot f \tag{4.3}$$

where $H$ (in kJ/m$^3$) is the hysteresis loss, which occurs due to the viscoelasticity of rubbers (Banić et al., 2012); $\sigma_l$ (in MPa) and $\sigma_u$ (in MPa) are the tensile stresses during loading and unloading, respectively; $\varepsilon$ (in m/m) is the tensile strain ranging from 0 to a certain strain level (i.e., 10%, 20%, 40%, 60%, 80%, or 100%); $f$ (in Hz) is the frequency of the strain, which can be calculated by the strain rate $\dot{\varepsilon}$ (in s$^{-1}$) of rubbers:

$$f = \frac{\dot{\varepsilon}}{2\varepsilon} \tag{4.4}$$

The stress $\sigma_l$ (in MPa) during loading was derived based on a two-parameter Mooney-Rivlin (MR) function (Mooney, 1940; Rivlin, 1948) that has been widely used in previous studies (Kim et al., 2012; Kumar and Rao, 2016; Pang et al., 2011) to characterize the stress-strain curves of rubber-like materials. To consider the effects of strain rates and rubber temperatures, the MR function was modified by newly incorporating into it a strain-rate-dependent coefficient $f_1(\dot{\varepsilon})$ and a rubber-temperature-dependent coefficient $f_2(T)$, following a procedure used in our previous study (Ma et al., 2021b). According to this modified MR function, the stress $\sigma_l$ (in MPa) at different strain rates and rubber temperatures is derived as

$$\sigma_l = 2\left[1 - \frac{1}{(\varepsilon+1)^3}\right]\left[C_{10}(\varepsilon+1) + C_{01}\right] \cdot f_1(\dot{\varepsilon}) \cdot f_2(T) \tag{4.5}$$

where $C_{10}$ and $C_{01}$ are the material constants; $f_1(\dot{\varepsilon}) = A(\dot{\varepsilon} - 0.1) + 1$; $f_2(T) = B/(T+50) + C$; $T$ (in °C) is the rubber temperature; $A$, $B$, and $C$ are the material constants. Equation (4.5) is a

one-dimensional (1D) solution of the stress-strain relationship, which fits the loading mode in the uniaxial cyclic tests.

Then the stress $\sigma_u$ (in MPa) during unloading was derived from the pseudo-elasticity theory developed by Ogden and Roxburgh (Ogden and Roxburgh, 1999). Based on this theory, the formula of the stress-strain relationship during unloading was modified from the formula of the stress-strain relationship during loading by adding two additional variables, denoted as $\eta_1$ (Huang et al., 2019) and $\eta_2$ (Dorfmann and Ogden, 2004). Then the stress $\sigma_u$ (in MPa) is derived as

$$\sigma_u = \eta_1 \cdot \sigma_l + (1-\eta_2) \cdot \frac{dN(\varepsilon)}{d\varepsilon} \tag{4.6}$$

where $N(\varepsilon)$ (in J/m$^3$) is expressed by the Neo-Hookean function (Wineman, 2005), and $\frac{dN(\varepsilon)}{d\varepsilon}$ is given by

$$\frac{dN(\varepsilon)}{d\varepsilon} = C_1 \left( 2\varepsilon - \frac{2}{(\varepsilon+1)^2} - 1 \right) \tag{4.7}$$

where $C_1$ is the material constant.

As per Dorfmann and Ogden (Dorfmann and Ogden, 2004), the variables $\eta_1$ and $\eta_2$ are written as

$$\eta_1 = 1 - \frac{1}{r} \tanh \left[ \frac{W_m - W_l(\varepsilon)}{m} \right]$$

$$\eta_2 = \tanh \left[ \left( \frac{W_l(\varepsilon)}{W_m} \right)^n \right] \Big/ \tanh(1)$$

(4.8)

where $W_l(\varepsilon)$ (in J/m$^3$) is the strain energy density during loading corresponding to a strain $\varepsilon$ (in m/m), and $W_l(\varepsilon) = \int_0^\varepsilon \sigma_l d\varepsilon$; $W_m$ (in J/m$^3$) is the maximum value of the strain energy density achieved at the point where unloading begins; $0 < \eta_1 \le 1$, $0 < \eta_2 \le 1$, and $\eta_1 = \eta_2 = 1$ at the beginning of the unloading; $r$, $m$, and $n$ are the material constants.

By substituting Equations (4.4) ~ (4.8) into Equation (4.3), the internal heat generation rates of rubbers were predicted at different strain levels, strain rates, and rubber temperatures. The material constants $C_{10}$, $C_{01}$, $A$, $B$, $C$, $C_1$, $r$, $m$, and $n$ were determined following an inverse analysis method widely used in previous studies (Jin and Cui, 2010; Lei and Szeri, 2007; Li et al., 2017). As per this method, an error function $f_{error}(C_{10}, C_{01}, A, B, C, C_1, r, m, n)$ was established based on the heat generation rates $\dot{Q}$ (in W/m$^3$), as follows:

$$f_{error}(C_{10}, C_{01}, A, B, C, C_1, r, m, n) = \sum_{i=1}^{P} \left[ \dot{Q}_{experimental,i}(\varepsilon, \dot{\varepsilon}, T) - \dot{Q}_{analytical,i}(\varepsilon, \dot{\varepsilon}, T) \right]^2$$

(4.9)

where $\dot{Q}_{analytical,i}(\varepsilon, \dot{\varepsilon}, T)$ (in W/m$^3$) and $\dot{Q}_{experimental,i}(\varepsilon, \dot{\varepsilon}, T)$ (in W/m$^3$) are the heat generation rates derived from the RTDS solution and the laboratory measurement (as listed in Table 4A.1 in Appendix 4A), respectively; and $P$ is the number of data points.

From Equation (4.9), the smaller values of $f_{error}\left(C_{10}, C_{01}, A, B, C, C_1, r, m, n\right)$ indicate the smaller deviations between the heat generation rates derived from the RTDS solution and the laboratory measurement. Based on this, to minimize this deviation, the material constants causing the minimum value of $f_{error}\left(C_{10}, C_{01}, A, B, C, C_1, r, m, n\right)$ were determined, as shown in Table 4.2.

Table 4.2. Material constants for the given tire rubber

| $C_{10}$ | $C_{01}$ | $C_1$ | $A$ | $B$ | $C$ | $r$ | $m$ | $n$ |
|---|---|---|---|---|---|---|---|---|
| 1.21 | -0.58 | -0.26 | 0.04 | 2.84 | 0.55 | 0.57 | 1.55 | 1.97 |

*4.2.2.2. Governing equation of heat conduction and mathematical expression of boundary conditions*

Under cyclic deformation, the heat generated in rubbers is conducted on the cross section of the specimen (in Figure 4.2(c)). As per Bergman et al. (Bergman et al., 2011), the governing equation of the heat conduction is given by

$$\rho c \frac{\partial T(x,y,t)}{\partial t} = k\left(\frac{\partial^2 T(x,y,t)}{\partial x^2} + \frac{\partial^2 T(x,y,t)}{\partial y^2}\right) + \dot{Q}\left(\varepsilon, \dot{\varepsilon}, T_0\right) \tag{4.10}$$

where $T(x,y,t)$ (in °C) is the rubber temperature at the time $t$ (in s) and the point $(x,y)$ (in m) on the cross section of the specimen; $T_0$ (in °C) is the initial rubber temperature; $k$ (in W/(m·°C)) is the thermal conductivity of rubbers; $\rho$ (in kg/m$^3$) is the rubber density; $c$ (in J/(kg·°C)) is the specific heat capacity. In Equation (4.10), it is assumed that rubbers are homogenous and isotropic materials. The density, thermal conductivity, specific heat capacity, and heat generation rate do not vary with a rise of rubber temperatures. Equation (4.10) is simplified as in a two-dimensional (2D) depiction. This takes into account that each cross section of the specimen has the same initial

rubber temperatures, heat generation rates, and heat boundary condition. The profile of rubber temperatures on the cross sections can be extremely close to each other and the heat conduction between the sections can be negligible.

As stretched in Figure 4.2(c), the boundary of the cross section is in contact with the ambient environment. Through the boundary, the heat generated and conducted on the cross section is further transferred into the ambient environment. This process of heat transfer is typically in the form of heat convection (Bengtson, 2010; Jiji, 2009). To describe this, the mathematical expression of the boundary conditions related to heat convection (Cebeci and Bradshaw, 2012; Jiji, 2009) is written as

$$
\begin{aligned}
&T(x,y,t_0) = T_0 \\
&k\frac{\partial T(x,y,t)}{\partial x} + h\big(T(x,y,t)-T_\infty\big) = 0 \text{ at } x = 0; \\
&k\frac{\partial T(x,y,t)}{\partial x} - h\big(T(x,y,t)-T_\infty\big) = 0 \text{ at } x = 3L; \\
&k\frac{\partial T(x,y,t)}{\partial y} + h\big(T(x,y,t)-T_\infty\big) = 0 \text{ at } y = 0; \\
&k\frac{\partial T(x,y,t)}{\partial y} - h\big(T(x,y,t)-T_\infty\big) = 0 \text{ at } y = L
\end{aligned}
\tag{4.11}
$$

where $t \geq 0$; $0 \leq x \leq 3L$, $0 \leq y \leq L$, and $L = 0.002 \text{ m}$; $T_\infty$ (in °C) is the ambient temperature; $h$ (in W/(m$^2$·°C)) is the convective heat transfer coefficient. As per Bengtson et al. (Bengtson, 2010), when the movement of fluid (i.e., airflow) is parallel with a flat plate (i.e., the surface of the specimen), $h$ (in W/(m$^2$·°C)) is written as

$$
h = 0.664 \times \frac{\lambda}{L_r} \times \left(\frac{u \cdot L_r}{v}\right)^{1/2} \times P_r^{1/3}
\tag{4.12}
$$

where $\lambda$ (in W/(m·°C)), $v$ (in m²/s), and $P_r$ are the thermal conductivity, kinematic viscosity, and Prandtl number of the airflow; $u$ (in m/s) is the relative speed between the specimen and the airflow, and $u = L_r \cdot \dot{\varepsilon}$; $L_r$ (in m) is the length of the reduced section of the dumbbell-shaped specimen, which is equal to 0.033 m.

Then Equations (4.10) ~ (4.12) were solved using a method of the Green's function (GF) (Greenberg, 2015), as shown in Equation (4.13). This GF is efficient in application for deriving temperature results using only a few terms of series (Cole et al., 2010). It has been widely used to derive the solution of various partial differential equations in other studies (Cole et al., 2010; Duffy, 2015).

$$
\begin{aligned}
T(x,y,t) = T(x,y,t_0) &+ \frac{\alpha \cdot \dot{Q}}{k} \int_{\tau=0}^{t} d\tau \iint_{x'y'} G_{xy}(x,y,t|x',y',\tau) dx'dy' \\
&+ \frac{\alpha \cdot hT_\infty}{k} \int_{\tau=0}^{t} d\tau \Big[ \int_{x'=0}^{3L} G_x(x,t|x',\tau) dx' \cdot \big( G_y(y,t|L,\tau) - G_y(y,t|0,\tau) \big) \\
&+ \int_{y'=0}^{L} G_y(y,t|y',\tau) dy' \cdot \big( G_x(x,t|3L,\tau) - G_x(x,t|0,\tau) \big) \Big]
\end{aligned}
\tag{4.13}
$$

where $T(x,y,t_0)$ (in °C) is the initial rubber temperature at the point $(x,y)$ (in m) on the cross section of the specimen when $t = 0$ s; $\alpha$ (in m²/s) is the thermal diffusivity of rubbers, and $\alpha = k/\rho c$; $G_{xy}(x,y,t|x',y',\tau) = G_x(x,t|x',\tau) \cdot G_y(y,t|y',\tau)$; $G_x(x,t|x',\tau)$ (in m⁻¹) is the GF related to the $x$ (in m), $t$ (in s) of observation points, and the $x'$ (in m), $\tau$ (in s) of heat source points; $G_y(y,t|y',\tau)$ (in m⁻¹) is the GF related to the $y$ (in m), $t$ (in s) of observation points, and the $y'$ (in m), $\tau$ (in s) of heat source points.

As per a study by Cole et al. (Cole et al., 2010), $G_x\left(x,t|x',\tau\right)$ and $G_y\left(y,t|y',\tau\right)$ are written

as

$$G_x\left(x,t|x',\tau\right)=\frac{2}{3L}\sum_{m=1}^{\infty}e^{-\beta_{m1}^2\alpha(t-\tau)/(3L)^2}\left[\beta_{m1}\cos\left(\beta_{m1}x/3L\right)+3B_i\sin\left(\beta_{m1}x/3L\right)\right]$$
$$\times\frac{\left[\beta_{m1}\cos\left(\beta_{m1}x'/3L\right)+3B_i\sin\left(\beta_{m1}x'/3L\right)\right]}{\left(\beta_{m1}^2+9B_i^2\right)\cdot\left[1+3B_i/\left(\beta_{m1}^2+9B_i^2\right)\right]+3B_i}$$
$$G_y\left(y,t|y',\tau\right)=\frac{2}{L}\sum_{m=1}^{\infty}e^{-\beta_{m2}^2\alpha(t-\tau)/L^2}\left[\beta_{m2}\cos\left(\beta_{m2}y/L\right)+B_i\sin\left(\beta_{m2}y/L\right)\right]$$
$$\times\frac{\left[\beta_{m2}\cos\left(\beta_{m2}y'/L\right)+B_i\sin\left(\beta_{m2}y'/L\right)\right]}{\left(\beta_{m2}^2+B_i^2\right)\cdot\left[1+B_i/\left(\beta_{m2}^2+B_i^2\right)\right]+B_i}$$

(4.14)

where the values of $\beta_{m1}$ and $\beta_{m2}$ are the positive eigenvalues (arranged in increasing order) of

$$\tan\beta_{m1}=\frac{6\beta_{m1}B_i}{\beta_{m1}^2-9B_i^2}$$

$$\tan\beta_{m2}=\frac{2\beta_{m2}B_i}{\beta_{m2}^2-B_i^2}$$

(4.15)

where $B_i$ is the Biot number, and $B_i=hL/k$.

In Equations (4.10) ~ (4.15), the thermal conductivity $k$ (in W/(m·°C)) and the thermal diffusivity $\alpha$ (in m²/s) were determined experimentally using a Hot Disk TPS 500 thermal constants analyzer (Disk, 2018). This analyzer was used because according to other researchers (Cheheb et al., 2012; Gschwandl et al., 2019) it can measure the thermal parameters (e.g., thermal conductivity, thermal diffusivity, and heat capacity) of a wide range of materials including rubbers.

These measurements were conducted at temperatures ranging from -30 to 30 ℃. The results are shown in Figure 4A.1 in Appendix 4A.

### 4.2.2.3. Expression of the RTDS solution

Based on the internal heat generation equation (in Section 4.2.2.1) and the governing equation of heat conduction and the mathematical expression of boundary conditions (in Section 4.2.2.2), the RTDS solution was developed as in Equation (4.16). This RTDS solution was designed to predict rubber temperatures in the dumbbell-shaped specimen at different strain levels, strain rates, and ambient temperatures.

$$T(x,y,t) = T(x,y,t_0) + \frac{\alpha \cdot \dot{Q}}{k} \int_{\tau=0}^{t} d\tau \iint_{x'y'} \left( G_x(x,t|x',\tau) \cdot G_y(y,t|y',\tau) \right) dx' dy'$$

$$+ \frac{\alpha \cdot hT_\infty}{k} \int_{\tau=0}^{t} d\tau \left[ \int_{x'=0}^{3L} G_x(x,t|x',\tau) dx' \cdot \left( G_y(y,t|L,\tau) - G_y(y,t|0,\tau) \right) \right.$$

$$\left. + \int_{y'=0}^{L} G_y(y,t|y',\tau) dy' \cdot \left( G_x(x,t|3L,\tau) - G_x(x,t|0,\tau) \right) \right]$$

where

$$G_x(x,t|x',\tau) = \frac{2}{3L} \sum_{m=1}^{\infty} e^{-\beta_{m1}^2 \alpha(t-\tau)/(3L)^2} \left[ \beta_{m1} \cos(\beta_{m1}x/3L) + 3B_i \sin(\beta_{m1}x/3L) \right]$$

$$\times \frac{\left[ \beta_{m1} \cos(\beta_{m1}x'/3L) + 3B_i \sin(\beta_{m1}x'/3L) \right]}{\left( \beta_{m1}^2 + 9B_i^2 \right) \cdot \left[ 1 + 3B_i / \left( \beta_{m1}^2 + 9B_i^2 \right) \right] + 3B_i}$$

$$G_y(y,t|y',\tau) = \frac{2}{L} \sum_{m=1}^{\infty} e^{-\beta_{m2}^2 \alpha(t-\tau)/L^2} \left[ \beta_{m2} \cos(\beta_{m2}y/L) + B_i \sin(\beta_{m2}y/L) \right]$$

$$\times \frac{\left[ \beta_{m2} \cos(\beta_{m2}y'/L) + B_i \sin(\beta_{m2}y'/L) \right]}{\left( \beta_{m2}^2 + B_i^2 \right) \cdot \left[ 1 + B_i / \left( \beta_{m2}^2 + B_i^2 \right) \right] + B_i}$$

$$\dot{Q} = \left[ \int_0^\varepsilon \sigma_l d\varepsilon - \int_0^\varepsilon \left( 1 - \frac{1}{r} \tanh\left( \frac{W_m - W_l(\varepsilon)}{m} \right) \right) \cdot \sigma_l d\varepsilon \right. \tag{4.16}$$

$$\left. + C_1 \int_0^\varepsilon \left( 1 - \tanh\left( \frac{W_l(\varepsilon)}{W_m} \right)^n \Big/ \tanh(1) \right) \cdot \left( 2\varepsilon - \frac{2}{(\varepsilon+1)^2} - 1 \right) d\varepsilon \right] \cdot \frac{\dot{\varepsilon}}{2\varepsilon}$$

$$\sigma_l = 2 \left[ 1 - \frac{1}{(\varepsilon+1)^3} \right] \left[ C_{10}(\varepsilon+1) + C_{01} \right] \left[ A(\dot{\varepsilon} - 0.1) + 1 \right] \left[ \frac{B}{T+50} + C \right]$$

where the material constants $C_{10}$, $C_{01}$, $A$, $B$, $C$, $C_1$, $r$, $m$, and $n$ are determined based on the experimental results of heat generation rates (as listed in Table 4A.1 in Appendix 4A); the thermal conductivity $k$ (in W/(m·°C)) and the thermal diffusivity $\alpha$ (in m²/s) are measured at different temperatures from -30 to 30 °C (as shown in Figure 4A.1 in Appendix 4A).

## 4.2.3. Laboratory measurements for surface temperatures of rubber specimens

Laboratory measurements were conducted to monitor the surface temperatures of rubber specimens to validate the RTDS solution experimentally. The schematic of the experimental setup is shown in Figure 4.3.
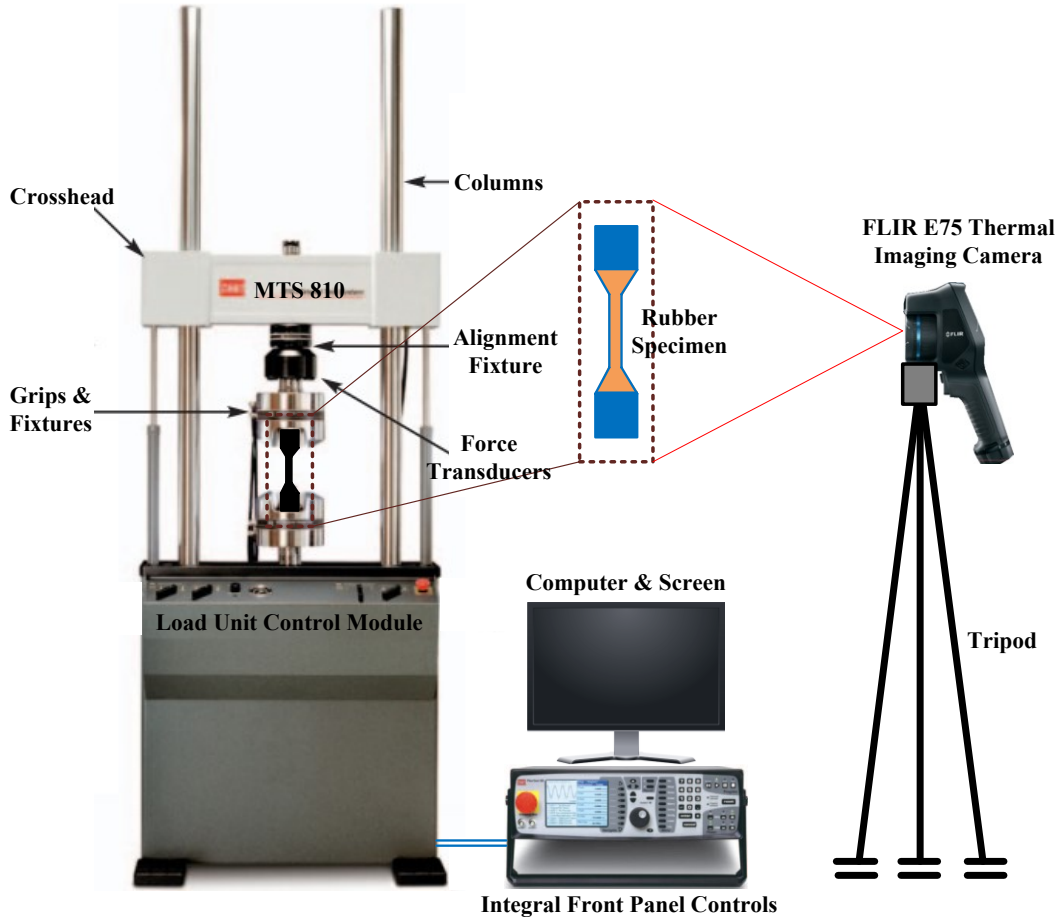


Figure 4.3. Schematic of the experimental setup

As shown in Figure 4.3, the rubber specimen was mounted on an MTS 810 machine that can stretch the specimen at a maximum stroke speed of 20,000 mm/min with an accuracy of 0.5% (MTS, 2006). This MTS 810 machine performed cyclic loading-unloading operations on the rubber specimen at different strain levels (10% ~ 500%) and strain rates (10% ~ 500% $\text{s}^{-1}$). During

the operations, an infrared (IR) camera was placed one meter away from the specimen to measure the rubber temperatures on the surface of the specimen, including the rubber temperatures at Point A (in Figure 4.2(c)). This measurement lasted 1000 seconds, and the IR camera captured 1000 data points of rubber temperatures at Point A at a rate of one data point per second. These data points were used to derive the variation of rubber temperatures at Point A. In the laboratory, the ambient temperature was 20 ℃. The camera and the specimens were brought into the laboratory eight hours prior to the measurements to ensure that their initial temperatures were consistent with the room temperature (i.e., 20 ℃).

In the measurements, the IR camera was used because the camera can monitor the surface temperatures of an object including a rubber specimen (Luo et al., 2018; Wang and Wang, 2021). In our case, an FLIR E75 IR camera was used to measure rubber temperatures; this camera has a thermal sensitivity of < 0.03 ℃ and a graphic resolution of 320 × 240 pixels (FLIR, 2018).

**4.2.4. Finite element modelling of rubber temperatures in specimens**

A finite element (FE) model was developed to predict rubber temperatures in specimens to numerically verify the RTDS solution. This FE model was built using ABAQUS software that has been widely used in other studies (Tang et al., 2014; Zhi et al., 2019) to solve heat transfer problems in rubbers. The representation of this FE model is shown in Figure 4.4.
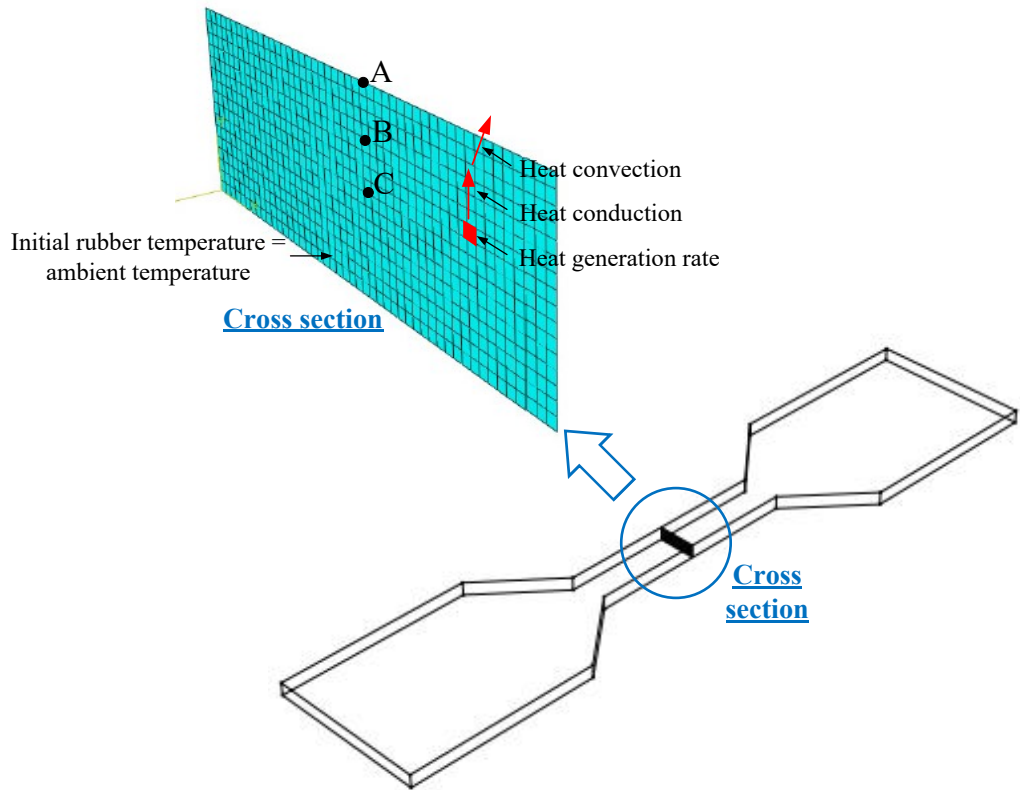
Figure 4.4. Representation of the finite element model

As shown in Figure 4.4, the FE model was developed as per one cross section of the dumbbell-shaped rubber specimen. This cross section was meshed into 768 elements that were $0.125 \times 0.125$ mm each. This number of elements was determined from mesh independence tests. The test results showed that when the number of elements was further increased from 768, the variation in the predicted rubber temperatures did not exceed 1%. This 1% variation in results was widely accepted in mesh independence tests for numerical models that predicted temperatures in solids (Rodrigues et al., 2015; Tye-Gingras and Gosselin, 2014). In addition, the element type of DC2D8 was used in the FE model. The DC2D8 elements were widely employed in previous studies (Cho et al., 2013; Su et al., 2015) to simulate the heat transfer in rubbers.

In Figure 4.4, before deformation, an initial rubber temperature was given to each element. This temperature was consistent with the ambient temperature (-30 ~ 30 ℃). When the specimen was deformed cyclically, the heat generation rate calculated by Equation (4.3) was further applied to each element. During cyclic deformation, the heat conduction on the cross section was evaluated based on the thermal conductivity, specific heat capacity, and density of rubbers (as indicated in Figure 4A.1). The heat transfer through the boundary of the cross section was described by a convective heat transfer coefficient derived from Equation (4.12). To obtain the variation of rubber temperatures with time, the FE model was solved in the module of transient heat transfer analysis in ABAQUS software. The cyclic deformation lasted 1000 seconds, and the model captured 1000 data points of rubber temperatures at the observation points (i.e., Points A, B, and C) at a rate of one data point per second, respectively. In addition, the computational time of this FE model was recorded. This time was compared with that of the RTDS solution to highlight the computational efficiency of the solution.

## 4.3. Results and discussions

### 4.3.1. Verification and validation of the RTDS solution

To verify the RTDS solution code, comparisons were made between the rubber temperatures derived from the code and the rubber temperatures from the FE model. These comparisons were conducted based on the surface temperatures at Point A, and the internal temperatures at Points B and C. Some results of the comparisons are shown in Figure 4.5.
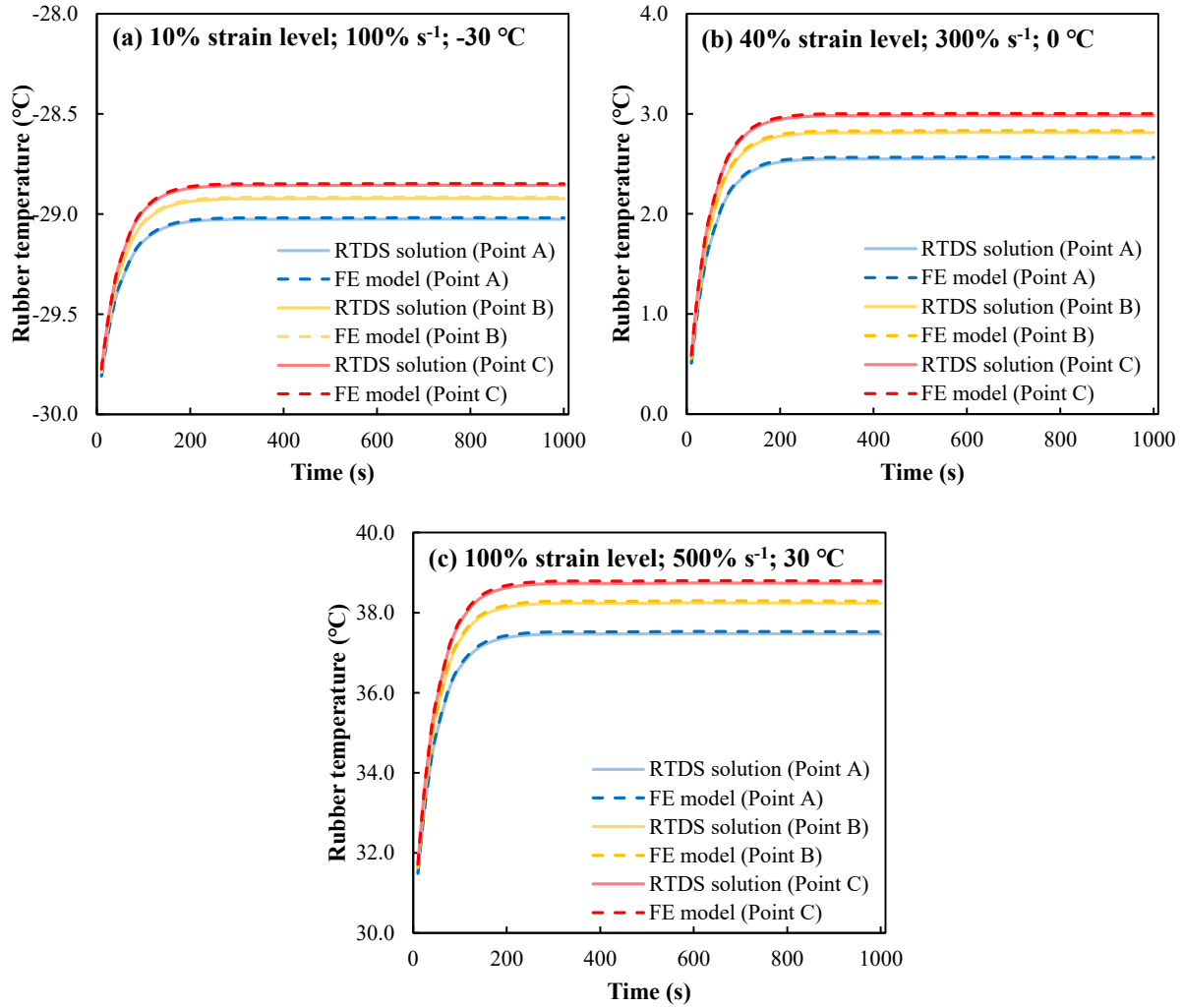
Figure 4.5. Comparisons in rubber temperature results between the RTDS solution code and the FE model: (a) at the 10% strain level, the 100% s$^{-1}$ strain rate, and -30 °C ambient temperature; (b) at the 40% strain level, the 300% s$^{-1}$ strain rate, and 0 °C ambient temperature; (c) at the 100% strain level, the 500% s$^{-1}$ strain rate, and 30 °C ambient temperature

As per the comparisons in Figure 4.5, the rubber temperatures predicted by the RTDS solution code matched well with the rubber temperatures derived from the FE model. At Points A, B, and C, the average MAPE was calculated as 0.56% at strain levels ranging from 10% to 100%, strain rates from 100% to 500% s$^{-1}$, and ambient temperature from -30 to 30 °C. This MAPE was

considered to be acceptable for numerically verifying the RTDS solution. This is because 0.56% is less than the MAPEs accepted for verifications in many previous studies (Minaei and Safikhani, 2021; Yu et al., 2019, 2018). For instance, as per a study by Minaei and Safikhani (Minaei and Safikhani, 2021), an analytical solution code with a MAPE of 1.72% (compared with 3D FE model results) was numerically verified to predict fluid temperatures in an earth-to-air heat exchanger.

Apart from verification, to validate the RTDS solution, comparisons were made between the rubber temperatures predicted by the RTDS solution and the rubber temperatures derived from laboratory measurements at Point A. The comparisons were conducted at six strain levels (10% ~ 100%), eight strain rates (10% ~ 500% $s^{-1}$), and an ambient temperature of 20 °C. In each comparison, the MAPE was calculated based on the predicted and measured rubber temperatures, as listed in Table 4.3.

Table 4.3. MAPEs from the comparisons between the RTDS solution and the laboratory measurements (%)

| Strain rate / Strain level | 10% $s^{-1}$ | 25% $s^{-1}$ | 50% $s^{-1}$ | 100% $s^{-1}$ | 200% $s^{-1}$ | 300% $s^{-1}$ | 400% $s^{-1}$ | 500% $s^{-1}$ |
|---|---|---|---|---|---|---|---|---|
| 10% | 5.3 | 6.5 | 7.2 | 7.6 | 8.6 | 8.1 | 8.8 | 9.2 |
| 20% | 6.1 | 6.9 | 7.6 | 7.9 | 8.2 | 9.9 | 10.8 | 10.1 |
| 40% | 7.8 | 7.6 | 6.9 | 8.6 | 9.2 | 10.4 | 10.5 | 12.6 |
| 60% | 6.4 | 8.2 | 7.4 | 8.1 | 9.9 | 9.1 | 11.6 | 12.8 |
| 80% | 8.4 | 9.7 | 7.9 | 8.8 | 9.4 | 9.9 | 11.8 | 13.4 |
| 100% | 9.6 | 9.6 | 9.9 | 10.8 | 10.6 | 11.4 | 12.7 | 12.4 |

In Table 4.3, the MAPE varied from 5.3% to 13.4%, and the average MAPE was 9.2% at strain levels from 10% to 100% and strain rates from 10% to 500% $s^{-1}$. As per a study by Luo et al. (Luo et al., 2018), the analytical solution with an average MAPE of 11.3% (compared with lab

recordings) was considered to be validated for predicting rubber temperatures in cylindrical specimens under cyclic deformation. The average MAPE from the RTDS solution was 9.2%, which is smaller than the average MAPE of 11.3%. Thus, the rubber temperatures predicted by the RTDS solution were believed to be in good agreement with the measured rubber temperatures. In other words, the RTDS solution predicted rubber temperatures with relatively high accuracy, and the RTDS solution was experimentally validated.

### 4.3.2. Computational time

Table 4.4 shows the comparison of the computational time in the RTDS solution and the FE model. In this study, computational time refers to the total amount of time required to derive rubber temperature results from the RTDS solution or the FE model. To compare it can help evaluate the computational efficiency of the RTDS solution.

Table 4.4. Comparison of the computational time in the RTDS solution and the FE model

|  | RTDS solution | FE model |
|---|---|---|
| Computational time | 11.9 s | 175.2 s |

Note: herein the RTDS solution and the FE model were performed on an Intel(R) Core (TM) i7-3770 3.40 GHz processor with 16 GB RAM.

In Table 4.4, the computational time of the RTDS solution was 11.9 s, which is about 93.2% less than the time (175.2 s) used in the FE model. This indicates that compared with the FE model, the RTDS solution has higher efficiency to predict rubber temperatures in specimens. Similar comparison results were also found in previous studies (Fernandes et al., 2010; Flint et al., 2018; Haghpanahi et al., 2013) when solving heat transfer problems and predicting temperatures in solids. For example, as per Fernandes et al. (Fernandes et al., 2010), an analytical solution and

a 3D FE model were used to solve the same heat transfer problem in a cast iron sample with a thickness of 65 mm and lateral dimensions of 80.5 × 80 mm. The results indicated that the analytical solution took 306 s to obtain the sample temperatures, which is 98.7% less than the amount of time (23,040 s) required in the 3D FE model.

### 4.3.3. Prediction of rubber temperatures under different testing conditions

After verification, the RTDS solution was used to predict rubber temperatures in dumbbell-shaped specimens under different testing conditions. These testing conditions included strain levels ranging from 10% to 100%, strain rates from 10% to 500% s$^{-1}$, and ambient temperatures from -30 to 30 °C. These testing conditions reflected typical operating conditions at mine sites in Alberta, Canada (Ma et al., 2022b).

*4.3.3.1. Rubber temperatures at different strain levels*

Figure 4.6 shows the prediction results of tire rubber temperatures at a strain rate of 500% s$^{-1}$, an ambient temperature of 20 °C, and strain levels from 10% to 100%. At Point A on the surface of the specimen, the RTDS solution identified a logarithmic increase in the rubber temperatures at rising strain levels. This indicates that the temperature increased relatively rapidly when the strain levels were small, but went up slowly with a further increase in strain levels. For instance, as the strain level was raised from 10% to 40%, the rubber temperature grew from 21.9 to 24.4 °C; however, when the strain level was further raised from 40% to 100%, there was relatively slow growth in the temperature, from 24.4 to 27.9 °C. This logarithmic increase in temperature overlapped with the prediction from the FE model (as represented by dashed lines), and it also coincided with experimental measurements, showing an average MAPE of 11.7%.

At Points B and C within the specimen, the RTDS solution predicted that the rubber temperature increased with a rise of strain levels in a similar logarithmic manner. However, the increases in temperatures at Points B and C were more significant than that at Point A. For example, as the strain level was raised from 10% to 100%, the rubber temperature at Point B increased from 22.1 to 28.8 ℃ and the rubber temperature at Point C grew from 22.3 to 29.3 ℃. The increments in rubber temperatures at both Point B (6.7 ℃) and Point C (7.0 ℃) were greater than that (6.0 ℃) at Point A. This indicates that compared with surface temperatures, the internal temperature increased more significantly under cyclic deformation. A similar phenomenon was also observed in other numerical investigations in previous studies (Bazkiaei et al., 2021; Guo et al., 2018; Luo et al., 2018; Rodas et al., 2016). As per Rodas et al. (Rodas et al., 2016), a numerical investigation was conducted for a dumbbell-shaped rubber specimen under cyclic deformation at a strain rate of 150% s$^{-1}$, an ambient temperature of 15 ℃, and a strain level of 25%. The results showed that the increase in the internal temperatures at the center of the specimen was 1.9 ℃ higher than the increase in surface temperatures.
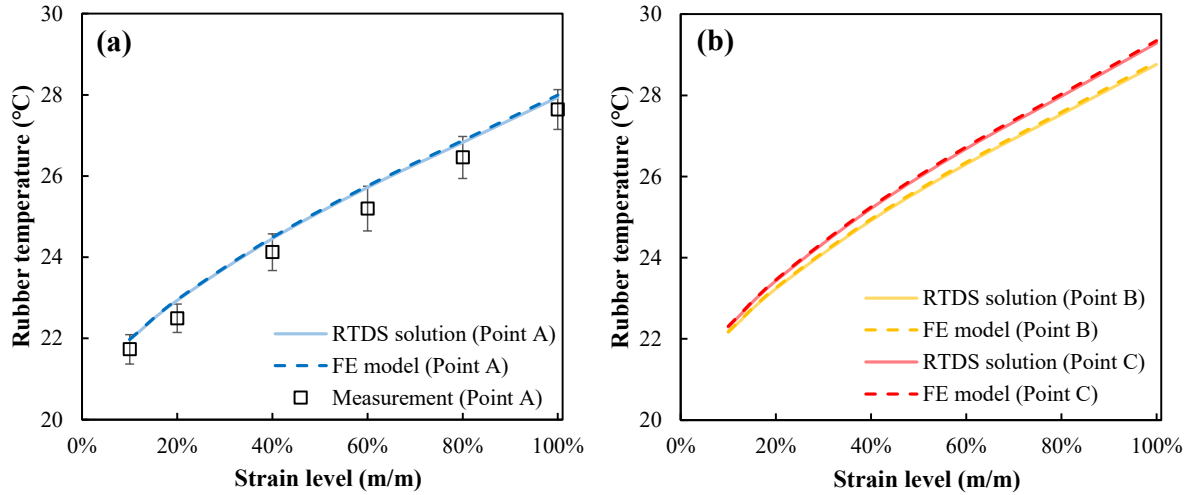
Figure 4.6. Prediction results of rubber temperatures at 20 °C, a strain rate of 500% s$^{-1}$, and strain levels from 10% to 100%: (a) Point A on the surface of the specimen; (b) Point B and Point C within the specimen

In Figure 4.6, the predicted increases of rubber temperatures at rising strain levels from 10% to 40% are consistent with the temperature predictions for rubbers from other numerical solutions in previous studies (Guo et al., 2018; Luo et al., 2018; Rodas et al., 2016). For instance, as per Guo et al. (Guo et al., 2018), the surface temperatures of a dumbbell-shaped rubber specimen were numerically studied at a strain rate of 100% s$^{-1}$ and an ambient temperature of 23 °C. The results indicated that the surface temperature increased by 0.6 °C when the strain level was raised from 10% to 40%. The numerical solution created by Rodas et al. (Rodas et al., 2016) estimated that the temperature on the surface of a cylindrical rubber specimen increased from 19.6 to 21.0 °C at a strain rate of 200% s$^{-1}$, an ambient temperature of 15 °C, and rising strain levels from 25% to 50%. However, dissimilar to the numerical solutions that only predicted rubber temperatures at the strain levels within 40%, the RTDS solution conducted the predictions for rubber temperatures when the strain level was further raised from 40% to 100%. For tire rubbers, the increase in rubber

110

temperatures at large strain levels (e.g., above 40%) is of great interest. Large strain levels from 40% to 100% are typical operating conditions for off-the-road (OTR) tire rubbers used at construction and mine sites (Ma et al., 2022b; Nyaaba, 2017; Nyaaba et al., 2019a). For instance, the rubbers of a Michelin 56/80R63 OTR tire are subjected to strain levels reaching 101% under fully loaded conditions (i.e., 363 tonnes) (Ma et al., 2022b). In addition, at large strain levels exceeding 40%, the rubber temperature still increased significantly. As shown in Figure 6, the increase in rubber temperatures at a large strain level of 100% reached 7.0 °C at Point C, which is 2.4 times that (2.9 °C) of when the strain level was 40%. One of the highlights of the RTDS solution in this study is that it can predict the temperatures of tire rubbers at large strain levels (i.e., 40% ~ 100%).

### 4.3.3.2. Rubber temperatures at various strain rates

Figure 4.7 illustrates the prediction results of tire rubber temperatures at an ambient temperature of 20 °C and strain rates from 10% to 500% s$^{-1}$. At the strain level of 40%, the RTDS solution identified an increase in rubber temperatures with the rising strain rates. For instance, at Point A on the surface of the specimen, the rubber temperature increased from 20.1 to 24.2 °C when the strain rate was raised from 10% to 500% s$^{-1}$. At Points B and C within the specimen, the rubber temperature increased relatively dramatically with rising strain rates. For example, as the strain rate was raised from 10% to 500% s$^{-1}$, the rubber temperature at Point B grew from 20.0 to 24.7 °C, and there was a temperature increase from 20.1 to 25.1 °C at Point C. These predicted increases in rubber temperatures matched well with the prediction from the FE model (as plotted by dashed lines), and their MAPE was calculated as only 0.64%. In addition, these predicted increases were also consistent with the temperature predictions for tire rubbers from other numerical solutions in previous studies (Marais, 2017; Van Blommestein, 2016; Zhi et al., 2019).

As per Zhi et al. (Zhi et al., 2019), at a strain level of 0.6% and an ambient temperature of 0 °C, a numerical solution was developed to predict the temperatures of a cylindrical tire rubber specimen under cyclic deformation. The results showed that the rubber temperatures at the center of the specimen increased by 2.3 and 2.4 °C when the strain rate was raised from 24% to 48% s$^{-1}$, and then from 48% to 72% s$^{-1}$, respectively.
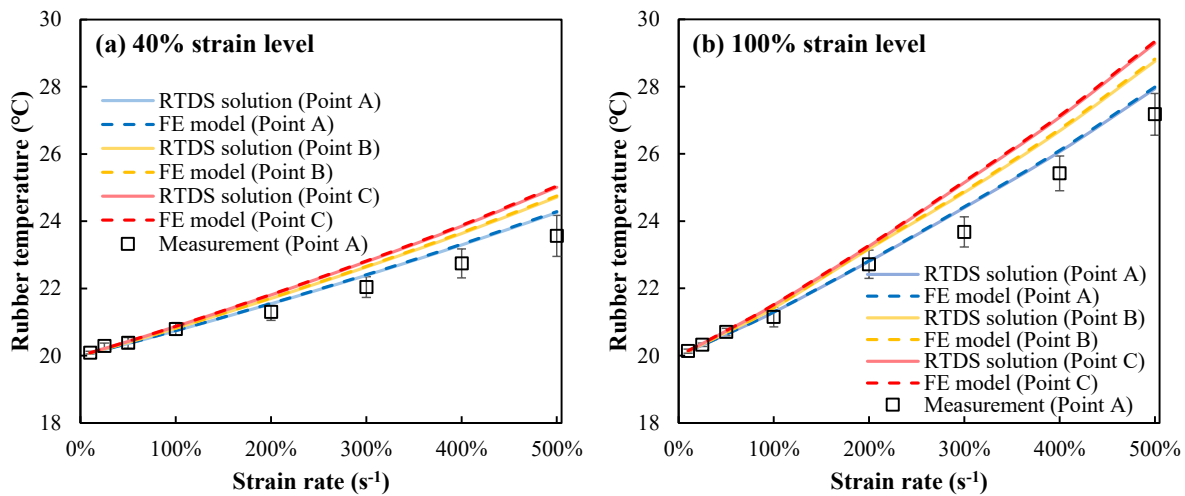


Figure 4.7. Prediction results of rubber temperatures at 20 °C and strain rates from 10% to 500% s$^{-1}$: (a) 40% strain level; (b) 100% strain level

In Figure 4.7, as predicted by the RTDS solution, the increase of rubber temperatures induced by the rising strain rates became more significant at a larger strain level: the rubber temperature increased with the rising strain rates more rapidly at the 100% strain level than at the 40% strain level. For instance, at Point A, when the strain rate was raised from 10% to 500% s$^{-1}$, the rubber temperature increased from 20.1 to 27.9 °C at the 100% strain level. This increment in rubber temperatures (7.8 °C) is greater than that (4.1 °C) at the 40% strain level. Moreover, at Point C, the rubber temperature increased with the rising strain rates (from 10% to 500% s$^{-1}$) by 9.2 °C

when the strain level was 100%, which is 1.8 times that (5.0 °C) of when the strain level was 40%.

The increase of rubber temperatures induced by the rising strain rates (from 10% to 500% s$^{-1}$) at

large strain levels (e.g., 40% ~ 100%) is of great interest since these strain rates and strain levels

are included in the operating conditions of tire rubbers. For example, as per Ma et al. (Ma et al.,

2022b), the rubbers of a Michelin 56/80R63 tire are subjected to strain rates from 11% to 526% s$^{-}$

$^{1}$ and strain levels up to 101% during daily operations.

As shown in Figure 4.7, at Point A, there were deviations between the rubber temperatures

predicted by the RTDS solution and the measured rubber temperatures with an average MAPE of

9.4%. These deviations were mainly derived from the differences between the predicted rubber

temperatures and the measured rubber temperatures at high strain rates from 100% to 500% s$^{-1}$.

For instance, at an ambient temperature of 20 °C and a strain level of 100%, the predicted rubber

temperatures at Point A matched well with the measured rubber temperatures when the strain rates

were small (i.e., within 100% s$^{-1}$); however, the predicted rubber temperatures became slightly

higher than the measured rubber temperatures (with deviations from 0.4 to 0.8 °C) with a further

increase in strain rates from 100% to 500% s$^{-1}$. These deviations at high strain rates are related to

the variations of thermal conductivity and thermal diffusivity, according to previous studies

(Goyanes et al., 2008; Huang, 2016; Mu et al., 2007). When the strain rate increased above 100%

s$^{-1}$, there were relatively high temperatures in rubbers. For example, at 20 °C and a strain level of

100%, the rubber temperature at Point A increased from 21.3 to 27.9 °C when the strain rate was

raised from 100% to 500% s$^{-1}$. As the rubber temperature increased, the thermal conductivity and

diffusivity of rubbers tended to change. As shown in Figure A1, when the rubber temperature was

raised from 21.3 to 27.9 °C, the thermal conductivity increased by 1.2%; the thermal diffusivity

decreased by 2.4%. As per other researchers (Kerschbaumer et al., 2019; Wang et al., 2017), the

increasing thermal conductivity and decreasing thermal diffusivity can retard a further rise in rubber temperatures and decrease peak values at rising strain rates. However, these variations in thermal conductivity and diffusivity were not considered in the RTDS solution. This caused that the rubber temperatures predicted by the RTDS solution were higher than the measured rubber temperatures, especially at high strain rates (e.g., above 100% s$^{-1}$). In the next phase of research, it would be useful to focus on developing a modified RTDS solution that can consider the variations of thermal conductivity and diffusivity at high strain rates.

### *4.3.3.3. Effects of ambient temperatures on rubber temperatures*

Figure 4.8 shows the prediction results of tire rubber temperatures from two different aspects at ambient temperatures from -30 to 30 ℃. At a strain level of 100% and a strain rate of 500% s$^{-1}$, Figure 4.8(a) illustrates the rubber temperature increment at increasing ambient temperatures from -30 to 30 ℃; Figure 4.8(b) presents the rubber temperatures when the ambient temperature was raised from -30 to 30 ℃. This range of ambient temperatures can cover the average temperatures in most regions of North America in all seasons (Alberta Agriculture and Forestry, 2018).
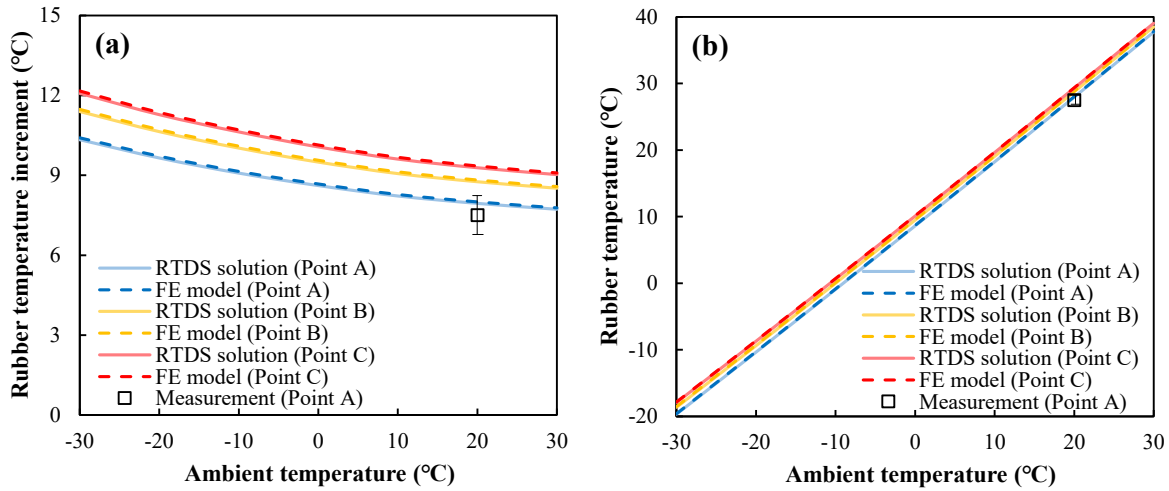
Figure 4.8. Prediction results of rubber temperatures at a strain level of 100%, a strain rate of

500% s$^{-1}$, and ambient temperatures from -30 to 30 °C: (a) rubber temperature increment; (b)

rubber temperature

As shown in Figure 4.8(a), at Point A on the surface of the specimen and at Points B and

C within the specimen, the RTDS solution characterized an inverse proportional relationship

between the rubber temperature increments and the ambient temperatures from -30 to 30 °C. This

indicates that the rubber temperature increment reduced relatively sharply at low ambient

temperatures from -30 to 0 °C, but decreased slightly as the ambient temperature increased above

0 °C. For instance, at a strain level of 100% and a strain rate of 500% s$^{-1}$, the rubber temperature

increment at Point A reduced by 16.7% as the ambient temperature was raised from -30 to 0 °C;

however, it decreased by only 8.6% with further increases in ambient temperatures from 0 to 30

°C. Similarly, the rubber temperature increment at Point C decreased from 11.5 to 9.7, and then to

9.2 °C when the ambient temperature increased from -30 to 0, and then to 30 °C, respectively. The

decreasing trend of rubber temperature increments can be partially explained by the decline of heat

generation rates at high ambient temperatures. From Table A1, as the ambient temperature was

115

raised from -30 to 30 °C, the heat generation rate decreased from 539.5 to 448.5 kW/m$^3$ at a strain level of 100% and a strain rate of 500% s$^{-1}$. As per other researchers (He, 2005; He et al., 2006), the decreased heat generation rates may reduce the heat build-up and mitigate the temperature rise in tire rubbers. In addition, thermal conductivity and thermal diffusivity of rubbers tended to change at rising ambient temperatures. In Figure A1, the thermal conductivity increased from 0.299 to 0.333 W/(m·°C), and the thermal diffusivity decreased from 0.234 to 0.201 mm$^2$/s when the ambient temperature was raised from -30 to 30 °C. The increasing thermal conductivity and decreasing thermal diffusivity may further lead to a reduction in rubber temperature increments, according to previous studies (Kerschbaumer et al., 2019; Wang et al., 2017).

As observed in Figure 4.8(b), despite the decreasing trend in rubber temperature increments, the rubber temperature increased relatively rapidly with a rise of ambient temperatures. For example, at a strain level of 100% and a strain rate of 500% s$^{-1}$, the rubber temperature at Point A grew from -20.4 to 37.9 °C at increasing ambient temperatures from -30 to 30 °C. Similarly, there were increases in rubber temperatures at Point B (58.2 °C) and Point C (58.1 °C) when the ambient temperature was raised from -30 to 30 °C. This phenomenon is consistent with the observations of tire rubber temperatures in previous studies (Li et al., 2012; Sokolov, 2009; Zhao et al., 2001). For instance, Li et al. (Li et al., 2012) found that the maximum rubber temperature in a Bridgestone 24.00R35 tire increased by 20.4% when the ambient temperature was raised by 20 °C. At rising ambient temperatures, predicting the increase in rubber temperatures is of great interest since it may affect the mechanical behaviors and shorten the fatigue life of tire rubbers. The RTDS solution is the first to predict the increase of rubber temperatures at rising ambient temperatures efficiently using an analytical method.

## 4.4. Conclusion

For the first time, this study successfully developed a novel analytical solution—the RTDS solution (a solution to predict Rubber Temperatures in Dumbbell-shaped Specimens). This RTDS solution was used to predict the surface and internal temperatures of dumbbell-shaped rubber specimens under different testing conditions of strain levels, strain rates, and ambient temperatures. The main conclusions are as follows:

1. The RTDS solution predicted the temperatures of dumbbell-shaped tire rubber specimens at strain levels from 10% to 100%, strain rates from 10% to 500% $s^{-1}$, and ambient temperatures from -30 to 30 °C. The average mean absolute percent error (MAPE) between the rubber temperatures predicted by the RTDS solution and the temperatures derived from laboratory measurements was 9.2%. This MAPE was relatively low when compared with previous studies, showing that the RTDS solution has higher prediction accuracy.

2. To derive rubber temperature results, the computational time of the RTDS solution was 11.9 seconds, which is about 93.2% less than the time (175.2 seconds) used in a finite element (FE) model. This indicates that compared with the FE model, the RTDS solution has higher efficiency to predict rubber temperatures in specimens.

3. The RTDS solution identified a logarithmic increase in rubber temperatures at rising strain levels. This indicates that the rubber temperature increased relatively rapidly when the strain levels were small (e.g., 10% ~ 40%), but went up slowly with a further increase in strain levels (e.g., 40% ~ 100%).

4. The RTDS solution identified an increase in rubber temperatures with the rising strain rates, and this increase became more significant at larger strain levels (e.g., 100%). When the strain rate was raised from 10% to 500% $s^{-1}$, the rubber temperature increased from

20.1 to 27.9 °C at the 100% strain level. This increment in rubber temperatures (7.8 °C) is greater than that (4.1 °C) at the 40% strain level.

5. The RTDS solution characterized an inverse proportional relationship between the rubber temperature increments and the ambient temperatures from -30 to 30 °C. This indicates that the rubber temperature increment reduced relatively sharply at low ambient temperatures from -30 to 0 °C, but decreased slightly as the ambient temperature increased above 0 °C.

## Appendix 4A. Experimental results of heat generation rates and thermal parameters

The experimental results of heat generation rates of rubbers are listed in Table 4A.1. In Table 4A.1, the strain rate varied from 10% to 500% s$^{-1}$, which corresponded to the strain frequencies ranging from 0.05 to 2.5 Hz. The heat generation rates in this range of strain frequencies were evaluated by conducting the traditional cyclic loading tests on rubbers via an MTS 810 servo-hydraulic machine. Note that there is no need to conduct the Dynamic Mechanical Analysis (DMA) tests that have been widely used to evaluate rubber heat generation rates at high strain frequencies from 5 to 50 Hz (Cho et al., 2013; Smith et al., 2012).

Table 4A.1. Experimental results of heat generation rates of rubbers (in kW/m$^3$)

| Strain level / Rubber temp. | Strain rate: 10% s$^{-1}$ | | | Strain rate: 100% s$^{-1}$ | | | Strain rate: 300% s$^{-1}$ | | | Strain rate: 500% s$^{-1}$ | | |
|---|---|---|---|---|---|---|---|---|---|---|---|---|
| | 20% | 40% | 100% | 20% | 40% | 100% | 20% | 40% | 100% | 20% | 40% | 100% |
| -30 °C | 3.2 | 4.7 | 8.1 | 33.5 | 49.3 | 85.9 | 108.0 | 162.0 | 290.1 | 191.3 | 293.8 | 539.5 |
| -20 °C | 3.1 | 4.5 | 7.8 | 32.5 | 47.3 | 82.1 | 104.3 | 154.1 | 277.2 | 185.0 | 282.5 | 513.5 |
| -10 °C | 3.0 | 4.4 | 7.6 | 31.0 | 46.0 | 78.8 | 99.8 | 150.8 | 267.6 | 181.3 | 271.9 | 497.8 |
| 0 °C | 2.9 | 4.2 | 7.2 | 30.0 | 44.0 | 77.3 | 98.3 | 145.5 | 256.2 | 176.3 | 265.0 | 474.0 |
| 10 °C | 2.8 | 4.1 | 7.1 | 28.8 | 42.9 | 74.6 | 96.8 | 139.1 | 250.1 | 170.0 | 258.1 | 460.8 |
| 20 °C | 2.7 | 4.0 | 7.0 | 28.3 | 42.3 | 73.6 | 93.0 | 139.9 | 246.3 | 167.5 | 254.4 | 453.3 |
| 30 °C | 2.7 | 4.0 | 6.9 | 28.0 | 41.6 | 72.9 | 91.5 | 138.8 | 243.9 | 166.3 | 250.6 | 448.5 |
| 40 °C | 2.7 | 4.0 | 6.8 | 27.8 | 41.1 | 72.2 | 90.0 | 136.1 | 238.5 | 163.8 | 247.5 | 444.0 |
| 50 °C | 2.6 | 3.9 | 6.7 | 27.8 | 40.5 | 71.7 | 90.0 | 133.9 | 238.8 | 162.5 | 243.1 | 437.8 |
| 60 °C | 2.6 | 3.9 | 6.7 | 27.5 | 40.0 | 71.0 | 87.8 | 134.3 | 237.9 | 160.0 | 240.0 | 433.5 |
| 70 °C | 2.6 | 3.8 | 6.6 | 27.3 | 39.4 | 70.3 | 88.5 | 130.1 | 234.8 | 158.8 | 236.9 | 431.0 |
| 80 °C | 2.6 | 3.8 | 6.5 | 27.3 | 39.0 | 69.8 | 87.8 | 129.0 | 233.6 | 157.5 | 234.4 | 424.3 |
| 90 °C | 2.5 | 3.7 | 6.4 | 27.0 | 38.6 | 69.1 | 87.0 | 130.1 | 229.5 | 156.3 | 232.5 | 419.3 |
| 100 °C | 2.5 | 3.7 | 6.4 | 26.8 | 38.3 | 68.7 | 86.3 | 126.4 | 227.7 | 153.8 | 230.0 | 415.5 |

Note: herein the rubber temperature is equal to the ambient temperature before the loading-unloading operations (as mentioned in Section 4.2.1).

The experimental results of thermal parameters for tire rubbers are shown in Figure 4A.1. The thermal conductivity $k$ and thermal diffusivity $\alpha$ were determined using a Hot Disk TPS 500 thermal constants analyzer (Disk, 2018). The density $\rho$ was measured at different rubber temperatures (i.e., -30 ~ 30 °C) in the laboratory. The specific heat capacity $c$ was calculated as per the equation $c = k/\rho\alpha$ in the textbook (Bergman et al., 2011).
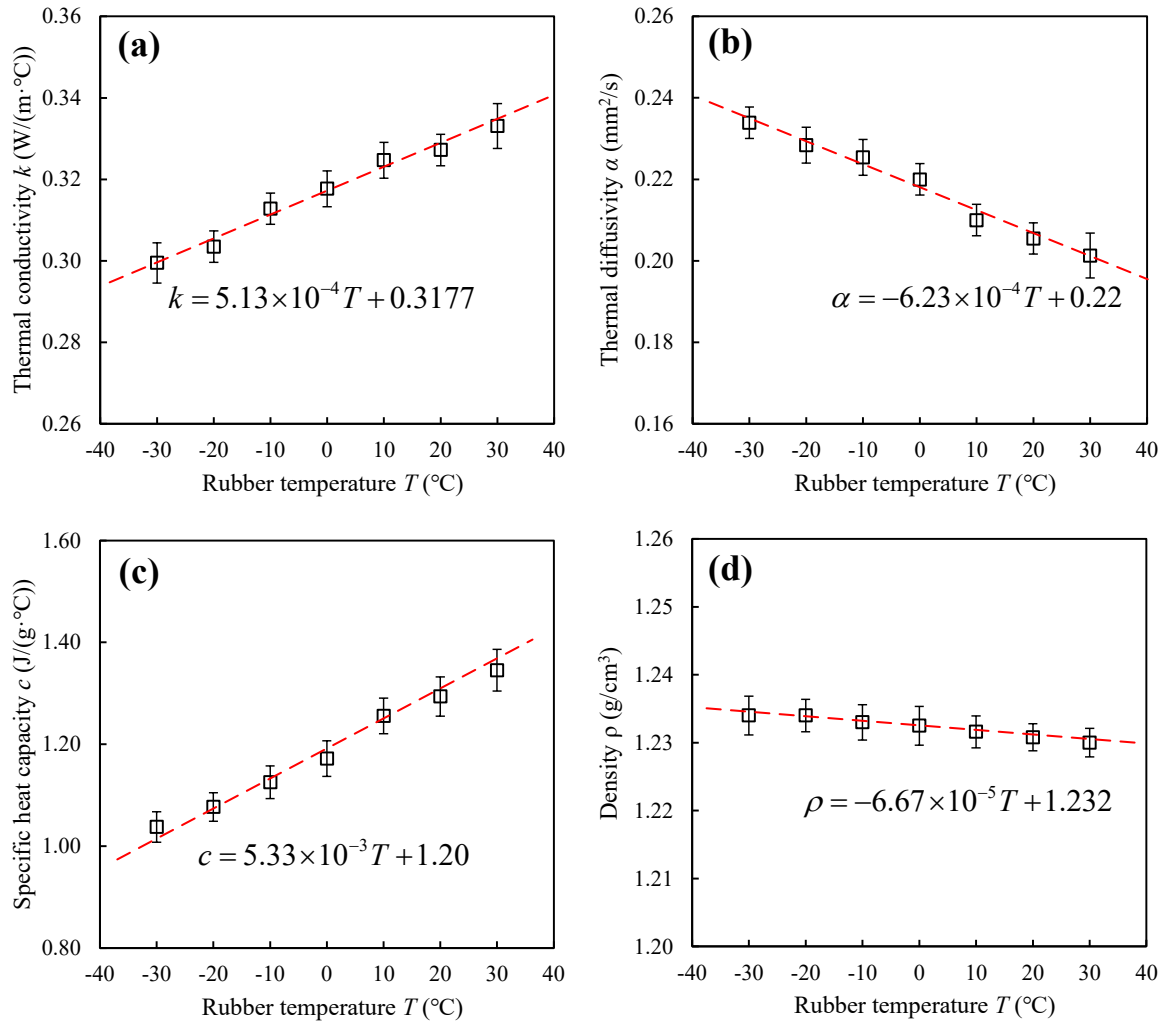
Figure 4A.1. Experimental results of thermal parameters: (a) thermal conductivity; (b) thermal diffusivity; (c) specific heat capacity; (d) density

## Appendix 4B. Characteristics of stress-strain relationship

An example of the stress-strain relationship at 20 °C and a strain rate of 100% s$^{-1}$ is plotted as in Figure 4B.1. In Figure 4B.1, when the rubber specimen was loaded from 0 to a strain level of 100%, the stress increased nonlinearly along the loading path and reached a peak stress of 2.34 MPa at the 100% strain level. After reaching the peak stress, the rubber specimen was unloaded to

zero stress along the unloading path. On the unloading path, the stress at a given strain was smaller than that on the loading path (which was known as stress softening, as per other researchers (Dorfmann and Ogden, 2003; Harwood et al., 1965)), and the zero stress corresponded to a residual strain of 8.1%.
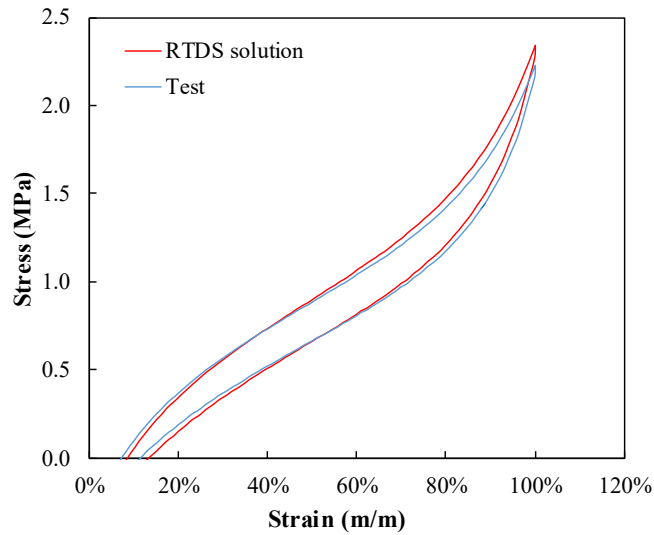


Figure 4B.1. An example of the stress-strain relationship at 20 °C and a strain rate of 100% s$^{-1}$

In Figure 4B.1, the stress-strain curve predicted by the RTDS solution was consistent with the curve derived from the tests, showing the deviation with an average MAPE of only 6.4%. The consistency in the curves caused that there were consistent results of hysteresis loss and heat generation rates output from the solution and the tests, which provided the foundation to further verify the rubber temperatures.

# Chapter 5. Numerical investigation of temperatures in ultra-large off-the-road tires under operating conditions at mine sites

Chapter 5 this thesis has been published as **S. Ma**, L. Wu, W. V. Liu. Numerical investigation of temperatures in ultra-large off-the-road tires under operating conditions at mine sites, *Journal of Thermal Science and Engineering Applications*. © ASME Digital Collection. (2023)

## 5.1. Introduction

Ultra-large off-the-road (OTR) tires are one of the most expensive components of haul trucks. For instance, one Michelin 56/80R63 OTR tire used for a Caterpillar 797 truck costs about CA $60,000 (Oil Sands Discovery Center, 2016). However, the service life of OTR tires is short, lasting only between 6-15 months (Oil Sands Discovery Center, 2016). The short service life of OTR tires is believed to be related to high temperatures within the tires (Meech and Parreira, 2013; Parreira, 2013). According to previous studies (Kerr, 2017; Li et al., 2012; Nyaaba, 2017), tire temperatures are significantly affected by operating conditions. At mine sites, operating conditions vary dramatically. As per mine site data (Alberta Agriculture and Forestry, 2018; Ta, 2018) and conversion (in Appendix 5A), there are a unique and large range of operating conditions: vertical loads vary from 0.34 to 1.04 MN, truck speeds change from 5 to 30 km/h, and ambient temperatures range from -30 to 40 °C. Because of these variable operating conditions, the mining industry is of particular interest when investigating the temperatures in OTR tires.

Currently, there are several methods to measure the temperatures in OTR tires. Using thermal couples has been a traditional method for temperature measurement (He, 2005). However, inserting thermal couples into tires may weaken the original structure of the tires and reduce their strengths (Anzabi, 2015; Anzabi et al., 2012). Infrared (IR) cameras can measure tire temperatures without making contact (Allouis et al., 2016; Farroni et al., 2017), which ensures that the tire strengths are not disturbed by the measurements. But IR cameras can only measure the surface temperatures of the tires; they cannot detect their internal temperatures (Wu, 2017). The internal temperatures are important because they are related to the occurrence of internal microcracks that may result in failures inside the tires (Nyaaba et al., 2019a, 2019b). To measure the internal temperatures in OTR tires, Michelin Earthmover Management Systems (MEMSs) are widely used

at mine sites (Michelin, 2016). The MEMS is mounted on the inner layer of the tire's lower sidewall, and its sensor is exposed to the air inflated within the tire to monitor temperatures (Michelin, 2016). However, the temperatures of the inflated air are usually different from the temperatures of tire rubbers (Golbakhshi et al., 2014; Li et al., 2012). As reported by Golbakhshi et al. (Golbakhshi et al., 2014), at a truck speed of 60 km/h and an ambient temperature of 40 °C, the temperature of the inflated air in a 115/60R13 tire was 73.6 °C, which was lower than the temperature in the casing rubbers (79.6 °C) and higher than the temperature in the tread rubbers (66.2 °C). This may cause that the results from the MEMS cannot be used to determine the temperatures within OTR tire rubbers. Determining rubber temperatures is significant since it can help explain the large amount of failures that occur in tire rubbers. As per site observations by Anzabi (2015), the failures in tread and sidewall rubbers accounted for over 80% of the tire failures at mine sites.

Apart from direct measurements, numerical methods can be used to investigate both surface and internal temperatures in OTR tires. The internal temperatures include rubber temperatures and air temperatures within the tires. There have been some numerical studies (Li et al., 2012; Marais and Venter, 2018; Nyaaba, 2017) that focused on the temperatures in OTR tires under operating conditions at mine sites. For instance, Li et al. (2012) conducted a 2D finite element (FE) modeling to examine the temperature distribution in a Bridgestone OTR tire when the ambient temperature was in the range of -40 to 40 °C. In this model, the heat generation rates and thermal parameters (e.g., thermal conductivity and heat capacity) were determined based on various OTR tire rubbers, such as tread, casing, and sidewall rubbers. However, these rates and parameters were obtained at 23 °C—their variations at different rubber temperatures were not considered in the model. As per a study by Ma et al. (2022a), the heat generation rates in tire

rubbers decreased by 23.0% at rising rubber temperatures from -30 to 100 °C. Ma et al. (2022a) also reported that the thermal conductivity and heat capacity increased by 48 mW/(m·°C) and 466 mJ/(g·°C), respectively, when the rubber temperature was raised from -40 to 40 °C. Ignoring these variations of heat generation rates and thermal parameters may result in inaccurate model results since the rates and parameters significantly affect the rubber temperatures in tires (He, 2005; Wu, 2017). This issue also existed in the study conducted by Marais and Venter (2018) when they numerically studied the temperatures in a 23.5R25 OTR tire. In addition to the studies by Li et al. (2012) and Marais and Venter (2018), Nyaaba (2017) built a 3D FE model for a Michelin 56/80R63 OTR tire. In this model, varying heat generation rates and thermal parameters were considered at different rubber temperatures from 23 to 121 °C. Nonetheless, this 3D FE model was still problematic when it was used to investigate tire temperatures. This model calculated the heat generation rates of tire rubbers based on a parallel rheological framework (PRF) function built in ABAQUS software (Nyaaba, 2017). This function was previously used for highway-terrain (HT) tire rubbers (Liu, 2010; Liu and Fatt, 2011; Zhi et al., 2016); however, it has never been proven to be used for OTR tire rubbers—OTR tire rubbers have unique recipes in comparison to HT tire rubbers (Ma et al., 2022b). Using this unproven function to calculate rubber heat generation rates makes the model questionable for predicting the temperatures in OTR tires. In addition, as per Nyaaba (2017), the 3D FE model predicted the tire temperatures at a vertical load of 1.15 MN and truck speeds up to 48 km/h. However, these vertical loads and truck speeds did not simulate the operating conditions at mine sites. As per mine site data (Ta, 2018), tire vertical loads are usually no more than 1.04 MN and truck speeds typically vary from 5 to 30 km/h. By failing to simulate these operating conditions, the model results cannot reflect the OTR tire temperatures at mine sites since operating conditions can significantly affect the tire temperatures (Kerr, 2017; Marais, 2017).

Until now, there has been a lack of a numerical investigation that can predict the temperatures in OTR tires under operating conditions at mine sites. This numerical investigation on OTR tire temperatures is of great significance because it can help explain the failures and short service life of tires.

The objective of this study is to conduct a numerical investigation to predict the temperatures in OTR tires under operating conditions at mine sites. This study focused on a Michelin 56/80R63 OTR tire since it is widely used at oil sands mine sites (Kerr, 2017). Tire temperatures were investigated based on a novel FE OTR tire thermal (OTRTire-T) model. For the first time, this OTRTire-T model used a new mathematical equation to calculate the internal heat generation rates of OTR tire rubbers. This OTRTire-T model is also the first model in the literature that was validated by on-site monitoring data to predict temperatures in OTR tires at mine sites.

## 5.2. Methodology

### 5.2.1. An overview of the methodology

A flowchart showing an overview of the methodology is represented in Figure 5.1.

```
┌─────────────────┐
│ 3D finite element│
│ (FE) OTR tire    │
│ simulation       │
└─────────────────┘
         │
         ▼
┌─────────────────┐   ┌──────────────────┐   ┌──────────────────┐
│                 │   │ Internal heat    │   │ Governing equation│
│                 │   │ generation       │   │ of heat conduction│
│ Stresses and    │   │ equations (i.e., │   │ and mathematical  │
│ strains         │   │ heat generation  │   │ expression of     │
│                 │   │ rates)           │   │ boundary conditions│
└─────────────────┘   └──────────────────┘   └──────────────────┘
         │                     │                      │
         └─────────────────────┼──────────────────────┘
                               ▼
                    ┌──────────────────┐
                    │ Development of the│
                    │ OTRTire-T model  │
                    └──────────────────┘
                               │
                               ▼
                    ┌──────────────────┐     ┌──────────────────┐
                    │ Validation of the│◄────│ Temperature      │
                    │ OTRTire-T model  │     │ observation in   │
                    │                  │     │ the OTR tire at  │
                    │                  │     │ mine sites       │
                    └──────────────────┘     └──────────────────┘
              │              │              │
              ▼              ▼              ▼
┌──────────────┐  ┌──────────────┐  ┌──────────────┐
│ Tire         │  │ Tire         │  │ Tire         │
│ temperature  │  │ temperature  │  │ temperature  │
│ investigations│ │ investigations│ │ investigations│
│ at different │  │ at different │  │ at different │
│ vertical loads│ │ truck speeds │  │ ambient      │
│              │  │              │  │ temperatures │
└──────────────┘  └──────────────┘  └──────────────┘
```

Figure 5.1. A flowchart showing an overview of the methodology

As shown in Figure 5.1, first, a 3D FE simulation was made on a rolling OTR tire on a haul road. In this simulation, the OTR tire contained structural components and various tire rubbers. The structural components included a casing ply, a transition belt, a penetration protection belt, and working belts. The tire rubbers varied according to locations such as inner liner, apex, casing, sidewall, and tread. These structural components and tire rubbers were built according to the geometry and construction of a Michelin 56/80R63 OTR tire. The tire was then inflated and was

127

applied by a vertical load. At this vertical load, the tire rolled on a smooth haul road. During the rolling, the stresses and strains in tire rubbers were studied and output.

As per stresses and strains, a new mathematical equation was developed to determine the internal heat generation rates of tire rubbers. With heat generation rates, the governing equation of heat conduction and the mathematical expression of boundary conditions were generated to describe the heat transfer in tire rubbers. Based on these equations, an FE OTRTire-T model was developed. This model was used to predict temperatures in the OTR tire at different vertical loads. These vertical loads were converted from the payloads on a truck following the procedure shown in Appendix A. In addition, the OTRTire-T model predicted the tire temperatures under different operating conditions of truck speeds and ambient temperatures at mine sites.

After model development, the OTRTire-T model was validated by evaluating the deviations between the temperature results derived from the model and the temperature results monitored from mine sites. These deviations were quantified using the mean absolute percentage error (MAPE). The MAPE is a well-known and commonly accepted index that evaluates the average difference between the forecasted values and the reference values (Dodge, 2008; Zwillinger, 2018). In the model validation, the forecasted values refer to the predicted temperatures in the OTRTire-T model; the reference values are the on-site monitoring temperatures. As per Zwillinger (2018), the MAPE is given as

$$MAPE = \frac{1}{M} \sum_{i=1}^{M} \left| \frac{T_{monitoring,i} - T_{OTRTire-T,i}}{T_{monitoring,i}} \right| \tag{5.1}$$

where $T_{OTRTire-T,i}$ (in °C) and $T_{monitoring,i}$ (in °C) are the temperatures derived from the OTRTire-T model and the on-site monitoring, respectively; $M$ is the number of data points.

The MAPE calculated from Equation (5.1) was compared with the MAPEs derived from the validations of other FE thermal models that predicted temperatures in HT tires, such as the models in studies by Wu (2017) and He (2005). When the MAPE from Equation (5.1) was not greater than the MAPE in these studies (He, 2005; Wu, 2017), the predicted temperatures were believed to be in good agreement with the on-site monitoring temperatures, and the OTRTire-T model was validated.

After model validation, the OTRTire-T model was used to predict temperatures in the OTR tire under different conditions of vertical loads, truck speeds, and ambient temperatures as listed in Table 5.1. These conditions were derived from the typical operating conditions on an Alberta oil sands mine for a period of 365 days in 2018 (Ta, 2018), as referred to in Appendix 5A.

Table 5.1. Vertical loads, truck speeds, and ambient temperatures in the modeling

| Vertical load (MN) | Truck speed (km/h) | Ambient temperature (°C) |
|---|---|---|
| 0.34, 0.54, 0.74, 0.94, 1.04 | 5, 10, 15, 20, 25, 30 | -30, -20, -10, 0, 10, 20, 30, 40 |

### 5.2.2. Simulation of a rolling OTR tire

A 3D FE simulation was made to predict the rubber stresses and strains in a Michelin 56/80R63 OTR tire. The geometry and construction of the tire is represented in Figure 5.2. This OTR tire simulation was conducted using ABAQUS software that has been widely used to solve

the nonlinear deformation (Nyaaba, 2017; Xia, 2011) and heat transfer problems (Smith et al., 2012; Tang et al., 2014) in tires.
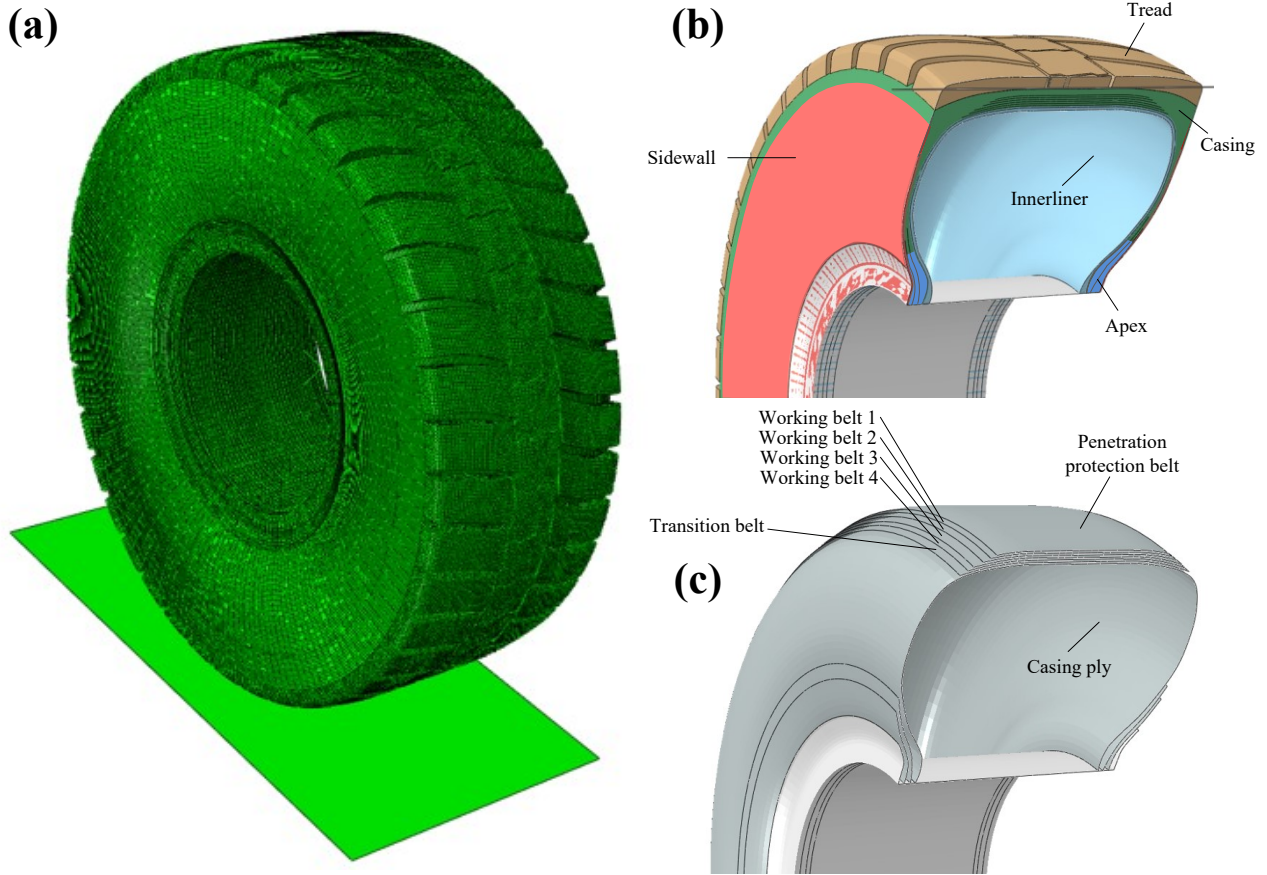


Figure 5.2. Geometry and construction of a Michelin 56/80R63 OTR tire: (a) overall; (b) tire rubbers (c) structural components

As shown in Figure 5.2, the OTR tire contained various tire rubbers, including inner liner, apex, casing, sidewall, and tread rubbers. These rubbers were described by the Mooney-Rivlin (MR) functions that have been widely used in previous studies (Kim et al., 2012; Kumar and Rao, 2016) to characterize the constitutive stress-strain relationship of rubber-like materials. For each kind of rubbers in the OTR tire, their material constants in the MR function were identified based on tensile test results from real tire rubber samples in the laboratory, as referred to in Appendix

5B. The structural components (i.e., belts and ply) in the OTR tire were assumed to be isotropic elastic materials. The elastic parameters (i.e., density, elastic modulus, and Poisson's ratio) of these belts and ply were previously studied in a research by Nyaaba (2017). These parameters are summarized in Table 5B.2. Apart from tire rubbers and structural components, the air inflated in the OTR tire was also simulated. This simulation was not common in tires as per previous studies (Cho et al., 2013; Marais, 2017; Tang et al., 2014). The inflated air was simulated to help develop the novel OTRTire-T model in Section 5.2.3 to predict temperatures inside the OTR tire in addition to tire rubber temperatures.

In Figure 5.2, the tire rubbers were meshed into hexahedral C3D8R elements. The C3D8R element has been widely used in other studies (Liang et al., 2019; Neves et al., 2010) to simulate the deformations in tire rubbers. The elements meshed in the tire belts and casing ply were quadrilateral SFM3D4R elements. These elements were proven to be able to mimic the distortions and twists in membrane structures in tires such as belts and plies, as per previous studies (W. Wang et al., 2013; Zhou et al., 2015). In addition, the inflated air inside the tire was meshed into hexahedral AC3D8R elements that deform in coordination with the deformations of C3D8R elements in tire rubbers (Hu et al., 2021). After the determination of element types in meshing, the number of elements were further determined based on mesh independence tests, as referred to in Appendix C. To save computational time without compromising simulation accuracy, the number of elements in the tire rubbers, tire belts/ply, and inflated air were selected as 389734, 43327, and 649516, respectively.

After meshing, the OTR tire rolled on a rigid haul road under a vertical load ranging from 0.34 to 1.04 MN. During rolling, the six components of stresses (S11, S22, S33, S13, S23, and S33

131

(in MPa)) and the six components of strains (LE11, LE22, LE33, LE13, LE23, and LE33 (in m/m)) were obtained and output from each tire rubber element.

### 5.2.3. The OTRTire-T model

*5.2.3.1. Internal heat generation equation*

A new mathematical equation was developed to determine the internal heat generation rates of rubbers in OTR tires. The heat generation rate is the amount of heat generated in tire rubbers per unit volume and unit time (Lin and Hwang, 2004; Tang et al., 2014). For each rubber element, the total heat generation rate $\dot{Q}$ (in W/m$^3$) can be calculated as the sum of the heat generation rates $\dot{Q}_{ij}$ (in W/m$^3$) derived as per the six components of stresses and strains (Wu, 2017), as follows:

$$\dot{Q} = \sum_{i=j=1}^{3} \dot{Q}_{ij} + \sum_{\substack{i=1, j=1 \\ i \neq j}}^{3} \dot{Q}_{ij} \qquad (5.2)$$

where $\dot{Q}_{ij}$ (in W/m$^3$) is the heat generation rate determined as per the stresses and strains on the $ij$ component (Li et al., 2018; Tang et al., 2014), and is written as

$$\dot{Q}_{ij} = \left( \int_{0}^{LE_{ij}} \sigma_{ij,l} d\varepsilon_{ij} - \int_{0}^{LE_{ij}} \sigma_{ij,u} d\varepsilon_{ij} \right) \cdot f \qquad (5.3)$$

where $\sigma_{ij,l}$ (in MPa) and $\sigma_{ij,u}$ (in MPa) are the stresses on the $ij$ component during loading and unloading, respectively; $0 \leq \sigma_{ij,l} \leq S_{ij}$, $0 \leq \sigma_{ij,u} \leq S_{ij}$; $\varepsilon_{ij}$ (in m/m) is the strain on the $ij$ component ranging from 0 to the output strain $LE_{ij}$ (in m/m); $f$ (in Hz) is the frequency of the

strain $\varepsilon_{ij}$ (in m/m), which is derived as $f = \dot{\varepsilon}_{ij}/2\varepsilon_{ij}$ ; $\dot{\varepsilon}_{ij}$ (in s$^{-1}$) is the strain rate of tire rubbers on the $ij$ component.

In previous studies (Li et al., 2012; Nyaaba, 2017), there were some issues when determining the heat generation rate $\dot{Q}_{ij}$ (in W/m$^3$) of OTR tire rubbers. For instance, Nyaaba (Nyaaba, 2017) calculated the heat generation rates of OTR tire rubbers based on the PRF function built in ABAQUS software. The PRF function was previously used for HT tire rubbers (Liu, 2010; Liu and Fatt, 2011; Zhi et al., 2016), but it remains unclear whether this function can be applied to OTR tire rubbers since OTR tire rubbers differ from HT tire rubbers in their recipes (e.g., in the amounts of CB and polymers). As per the study by Li et al. (2012), the heat generation rates of OTR tire rubbers were determined based on a traditional MR function (Mooney, 1940; Rivlin, 1948). This traditional MR function has been proven to be used for OTR tire rubbers (Marais and Venter, 2018), but it does not include operating variables such as strain rates and rubber temperatures. This makes the function unable to predict the variations of heat generation rates when the strain rates and rubber temperatures vary in OTR tires. To avoid these issues, the heat generation rate $\dot{Q}_{ij}$ (in W/m3) of OTR tire rubbers in this study was calculated as per a modified MR function. The MR function was modified by newly incorporating into it a strain-rate-independent coefficient $f_1(\dot{\varepsilon})$ and a rubber-temperature-dependent $f_2(T)$ following a procedure used in our previous study (Ma et al., 2021b). According to this modified MR function, the stress $\sigma_{ij,l}$ (in MPa) at different strain rates and rubber temperatures is derived as

$$\sigma_{ij,l} = 2\left[1 - \frac{1}{\left(\varepsilon_{ij}+1\right)^3}\right]\left[C_{10}\left(\varepsilon_{ij}+1\right)+C_{01}\right]\cdot f_1\left(\dot{\varepsilon}_{ij}\right)\cdot f_2\left(T\right) \tag{5.4}$$

where $C_{10}$ (in MPa) and $C_{01}$ (in MPa) are the material constants; $f_1(\dot{\varepsilon}_{ij}) = A(\dot{\varepsilon}_{ij} - 0.1) + 1$,

$f_2(T) = B/(T+50) + C$, $A$, $B$, and $C$ are the material constants. $T$ (in °C) is the rubber temperature that is equal to the ambient temperature (i.e., -30 to 30 °C) when the OTR tire starts to roll. The strain rate $\dot{\varepsilon}_{ij}$ (in s$^{-1}$) was calculated as per different truck speeds during the tire rolling:

$$\dot{\varepsilon}_{ij} = \frac{180 \cdot v \cdot LE_{ij}}{3.6 \cdot \pi R \arccos\left(\dfrac{R-VD}{R}\right)} \tag{5.5}$$

where $v$ (in km/h) is the truck speed (i.e., 5 to 30 km/h); $R$ (in m) is the radius of the OTR tire; $VD$ (in m) is the vertical deflection of the OTR tire that output from the simulation in Section 2.2. Equation (5.5) was introduced in our previous study (Ma et al., 2021b) to obtain the strain rates of OTR tire rubbers from truck speeds at mine sites.

The stress $\sigma_{ij,u}$ (in MPa) in Equation (5.3) was derived from the pseudo-elasticity theory developed by Ogden and Roxburgh (1999). Based on this theory, the formula of the stress-strain relationship during unloading was modified from the formula of the stress-strain relationship during loading by adding two additional variables, denoted as $\eta_1$ (Huang et al., 2019) and $\eta_2$ (Dorfmann and Ogden, 2004). Then the stress $\sigma_{ij,u}$ (in MPa) is derived as

$$\sigma_{ij,u} = \eta_1 \cdot \sigma_{ij,l} + (1-\eta_2) \cdot dN(\varepsilon_{ij})/d\varepsilon_{ij} \tag{5.6}$$

where $N(\varepsilon_{ij})$ (in J/m$^3$) is expressed by the Neo-Hookean function (Wineman, 2005), and $dN(\varepsilon_{ij})/d\varepsilon_{ij}$ is given by

$$dN\left(\varepsilon_{ij}\right)/d\varepsilon_{ij} = C_1\left(2\varepsilon_{ij} - \frac{2}{\left(\varepsilon_{ij}+1\right)^2} - 1\right) \qquad (5.7)$$

where $C_1$ is the material constant.

As per Dorfmann and Ogden (2004), the variables $\eta_1$ and $\eta_2$ are written as

$$\eta_1 = 1 - \frac{1}{r}\tanh\left[\frac{W_m - W_l\left(\varepsilon_{ij}\right)}{m}\right]$$

$$\eta_2 = \tanh\left[\left(\frac{W_l\left(\varepsilon_{ij}\right)}{W_m}\right)^n\right]\Big/\tanh(1) \qquad (5.8)$$

where $W_l\left(\varepsilon_{ij}\right)$ (in J/m³) is the strain energy density during loading corresponding to a strain $\varepsilon_{ij}$ (in m/m), and $W_l\left(\varepsilon_{ij}\right) = \int_0^{LE_{ij}}\sigma_{ij,l}d\varepsilon_{ij}$ ; $W_m$ (in J/m³) is the maximum value of the strain energy density achieved at the point where unloading begins; $0 < \eta_1 \leq 1$, $0 < \eta_2 \leq 1$, and $\eta_1 = \eta_2 = 1$ at the beginning of the unloading; $r$, $m$, and $n$ are the material constants.

By substituting Equations (5.3) ~ (5.8) into Equation (5.2), the internal heat generation rates of OTR tire rubbers were predicted at different strains, strain rates, and rubber temperatures. The material constants were identified based on cyclic tensile test results from real tire rubber samples in the laboratory, as referred to in Appendix 5B.

During the tire rolling, the heat generated in tire rubbers is conducted in the OTR tire, as is shown stretched in Figure 5.3.
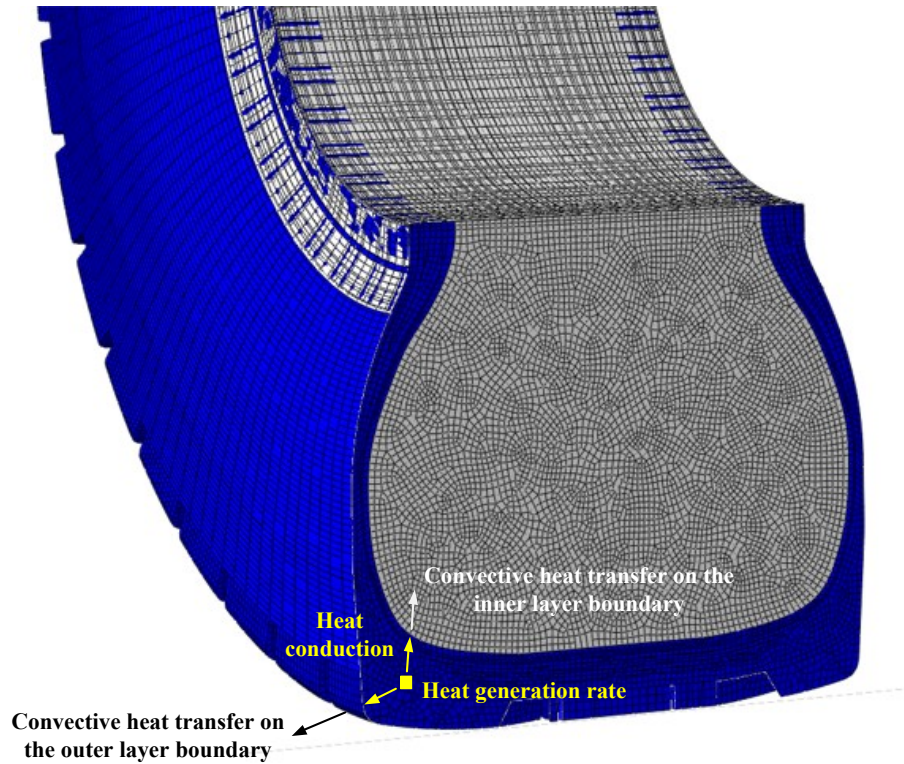


Figure 5.3. Schematic of heat conduction and convection in the OTR tire

It is assumed that tire rubbers are homogenous and isotropic materials. As per Bergman et al. (2011), the governing equation of the heat conduction is given by

$$\rho c \frac{\partial T(x,y,z,t)}{\partial t} = k\left(\frac{\partial^2 T(x,y,z,t)}{\partial x^2} + \frac{\partial^2 T(x,y,z,t)}{\partial y^2} + \frac{\partial^2 T(x,y,z,t)}{\partial z^2}\right) + \dot{Q} \tag{5.9}$$

where $T(x,y,z,t)$ (in °C) is the rubber temperature at the time (in s) and the point $(x,y,z)$ (in m) in the OTR tire; $\rho$ (in kg/m³) is the rubber density; $k$ (in W/(m·°C)) is the thermal conductivity of the tire rubbers; $c$ (in J/(kg·°C)) is the specific heat capacity. The thermal conductivity and specific heat capacity were experimentally measured at different rubber temperatures using a Hot Disk TPS 500 thermal constants analyzer (Disk, 2018). The results are shown in Table 5B.6 in Appendix 5B.

As shown stretched in Figure 5.3, the outer layer boundary of the OTR tire is in contact with the ambient environment. Through this boundary, the heat generated and conducted within the OTR tire is transferred into the ambient environment. To describe this, the mathematical expression of the boundary condition related to convective heat transfer (Cebeci and Bradshaw, 2012; Jiji, 2009) is written as

$$k \frac{\partial T(x,y,z,t)}{\partial S_{outer}} = h_{outer} \left( T(x,y,z,t) - T_\infty \right) \tag{5.10}$$

where $S_{outer}$ represents the outer layer boundary of the OTR tire; $T_\infty$ (in °C) is the ambient temperature; $h_{outer}$ (in W/(m2·°C)) is the convective heat transfer coefficient on the tire outer layer boundary. As per a study by Nyaaba et al. (2019b), $h_{outer}$ (in W/(m2·°C)) is a variable related to the truck speeds $v$ (in km/h), and it can be written as

$$h_{outer} = 5.9 + 1.03v \tag{5.11}$$

In addition, there is convective heat transfer on the inner layer boundary where the OTR tire rubbers contacts the inflated air within the tire. Similar to Equation (5.10), the mathematical expression of the boundary condition on the tire's inner layer is derived as

$$k \frac{\partial T(x,y,z,t)}{\partial S_{inner}} = h_{inner} \left( T(x,y,z,t) - T_{in} \right) \tag{5.12}$$

where $S_{inner}$ represents the inner layer boundary of the OTR tire; $h_{inner}$ (in W/(m²·°C)) is the convective heat transfer coefficient on the tire inner layer boundary, which was selected as 3.0 W/(m²·°C) (Nyaaba, 2017); $T_{in}$ (in °C) is the temperature of the inflated air, which varies with tire rubber temperatures during the tire rolling.

*5.2.3.3. Model development for predicting tire temperatures*

Based on the internal heat generation equation (in Section 5.2.3.1) and the governing equation of heat conduction and the mathematical expression of boundary conditions (in Section 5.2.3.2), the OTRTire-T model was developed to predict the temperatures in the OTR tire. This OTRTire-T model predicted the temperature variations and distribution in the OTR tire within 3600 seconds until the tire temperatures became stable. These temperature predictions were conducted based on different operating conditions of payloads, truck speeds, and ambient temperatures at mine sites.

As shown in Figure 5.4, the rubber temperatures in the regions of tread, sidewall, and shoulder of the OTR tire were focused on because it has been reported that over 83% of tire failures at mine sites are related to these regions (Anzabi, 2015). In addition, the temperatures at Point A were also predicted. Point A is located at the inflated air inside the OTR tire close to the inner layer

of the lower sidewall. At Point A, the predicted temperatures were used for comparison with the temperatures observed from mine sites to validate the OTRTire-T model.
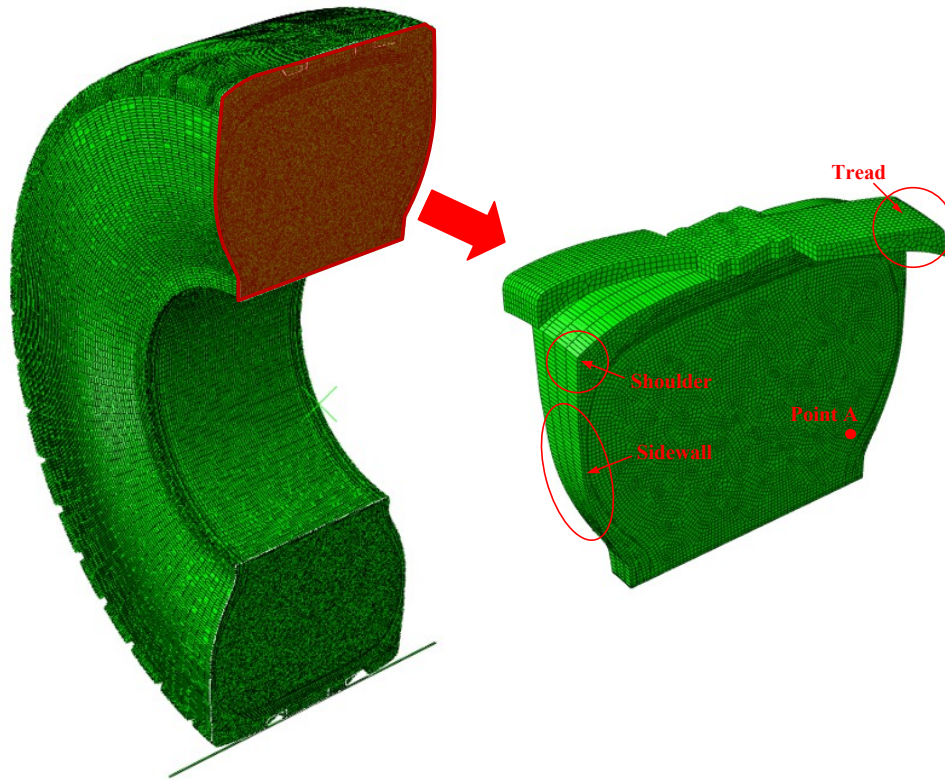


Figure 5.4. Key regions for temperature prediction in the OTR tire

*5.5.3.4. Temperature observation in the OTR tire at mine sites*

At mine sites, the temperatures of the inflated air at Point A were observed to validate the OTRTire-T model. These air temperatures were monitored by a Michelin Earthmover Management System (MEMS) (Michelin, 2016) installed inside the OTR tire, as shown in Figure 5.5. The MEMS is the latest tire management system released by Michelin that has been widely used at mine sites to monitor and record real-time temperatures in OTR tires (Baker et al., 2018; Carter, 2020).

The MEMS sensor: to monitor the air temperature at a location overlapping with Point A
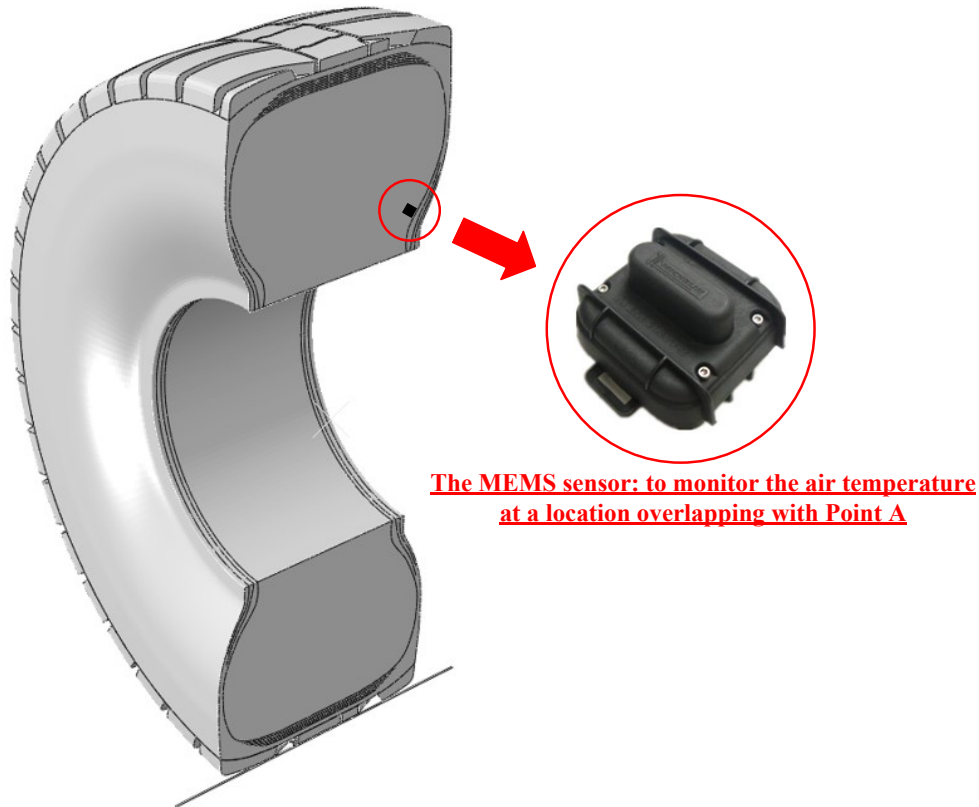
Figure 5.5. Schematic of the MEMS installation

As shown in Figure 5.5, the MEMS was mounted on the inner layer of the tire's lower sidewall; its sensor was exposed to the inflated air within the OTR tire and used to monitor the air temperatures at a location overlapping with Point A in Figure 5.4. The MEMS recorded these air temperatures in real time, collecting one data point every five minutes under different operating conditions at mine sites (Ta, 2018). These operating conditions included real-time payloads and truck speeds recorded by the Vital Information Management System (VIMS) (Caterpillar, 2018) and the real-time ambient temperatures derived from Alberta Climate Information Service (ACIS) (Alberta Agriculture and Forestry, 2018).

At an Alberta oil sands mine site, the MEMS in each OTR tire received in total 105120 data points of temperatures in a period of 365 days in 2018 as per a report by Ta (2018). In our study, 12 of the 105120 data points were used for model validation under their corresponding operating conditions. These 12 data points were randomly selected from each month of the year from January to December, respectively.

## 5.3. Results and discussions

### 5.3.1. Validation of the OTRTire-T model

To validate the OTRTire-T model, comparisons were made between the air temperatures predicted by the OTRTire-T model and the air temperatures derived from on-site observation at Point A. The comparisons were conducted at 12 vertical loads (1.00~1.05 MN), 12 truck speeds (24.3~27.5 km/h), and 12 ambient temperatures (-10.7~23.9 °C). In each comparison, the MAPE was calculated based on the predicted and observed air temperatures, as listed in Table 5.2.

Table 5.2. MAPEs from the comparisons between the OTRTire-T model and the on-site observation

| Group # | Truck speed (km/h) | Payload (tonne) | Ambient temperature (°C) | Vertical load per tire (MN) | Observed air temperature at Point A (°C) | Simulated air temperature at Point A (°C) | Deviation (%) |
|---|---|---|---|---|---|---|---|
| 1 | 24.3 | 370 | -10.7 | 1.05 | 46.0 | 52.0 | 12.97 |
| 2 | 26.2 | 348 | -2.0 | 1.01 | 53.9 | 59.9 | 11.09 |
| 3 | 26.8 | 356 | -5.3 | 1.03 | 52.0 | 58.1 | 11.65 |
| 4 | 27.5 | 358 | 13.9 | 1.03 | 67.3 | 73.8 | 9.65 |
| 5 | 26.5 | 364 | 22.1 | 1.04 | 79.0 | 83.0 | 5.04 |
| 6 | 27.4 | 355 | 23.9 | 1.03 | 82.0 | 84.9 | 3.52 |
| 7 | 26.4 | 343 | 19.7 | 1.01 | 73.2 | 79.8 | 9.01 |
| 8 | 26.4 | 358 | 21.0 | 1.03 | 79.0 | 83.0 | 5.03 |
| 9 | 25.8 | 340 | 11.6 | 1.00 | 66.0 | 72.5 | 9.83 |
| 10 | 25.9 | 359 | 5.7 | 1.03 | 61.2 | 66.8 | 9.12 |
| 11 | 26.7 | 365 | -8.5 | 1.04 | 51.9 | 57.1 | 10.09 |
| 12 | 24.9 | 359 | -4.6 | 1.03 | 57.0 | 60.7 | 6.56 |

In Table 5.2, the MAPE varied from 3.52% to 12.97%, and the average MAPE was 8.63% at vertical loads ranging from 1.00 to 1.05 MN, truck speeds from 24.3 to 27.5 km/h, and ambient temperatures from -10.7 to 23.9 °C. This indicates that the OTRTire-T model predicted the temperatures of the inflated air at Point A with an average MAPE of 8.63%, and the maximum MAPE from the model predictions did not exceed 12.97% under any operating conditions (i.e., payloads of 340 to 370 tonnes, truck speeds of 24.3 to 27.5 km/h, and ambient temperatures of -10.7 to 23.9 °C) at mine sites. As per the studies by Wu (2017) and He (2005), FE thermal models with average MAPEs of 11.4% (Wu, 2017) and 10.9% (He, 2005) were considered to be validated for predicting the temperatures in HT tires. The average MAPE from the OTRTire-T model was

8.63%, which is lower than 11.4% and 10.9%. Thus, the temperatures predicted by the OTRTire-T model were believed to be in good agreement with the observed temperatures from mine sites. In other words, the OTRTire-T model predicted temperatures in the OTR tire with relatively high accuracy, and the model was validated.

### 5.3.2. Effects of vertical loads on tire rubber temperatures

Figure 5.6 shows the effects of vertical loads on maximum rubber temperatures at a truck speed of 30 km/h and an ambient temperature of 20 °C. The vertical load refers to the load vertically applied to one OTR tire. According to Appendix A, the vertical load on an OTR tire is approximately 0.34 MN when a truck is empty, and it reaches about 1.04 MN under the fully loaded condition (i.e., 363 tonnes).
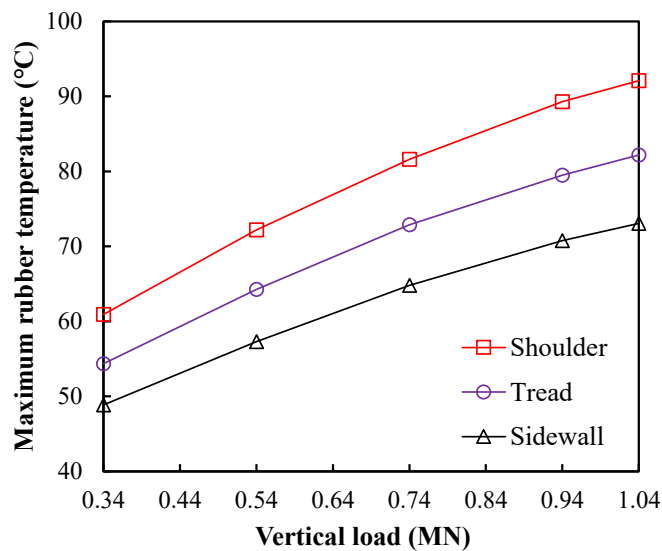


Figure 5.6. Effects of vertical loads on tire rubber temperatures at 30 km/h and 20 °C

In Figure 5.6, in the sidewall region, the maximum rubber temperature increased logarithmically at rising vertical loads. This indicates that the rubber temperature increased

relatively rapidly when the vertical loads were small but went up slowly with a further increase in vertical loads. For instance, as the vertical load was raised from 0.34 to 0.54 MN, the rubber temperature increased from 48.9 to 57.3 ℃; however, when the vertical load was further raised from 0.54 to 1.04 MN, there was relatively slow growth in the rubber temperature, from 57.3 to 73.1 ℃. In the tread and shoulder regions, the maximum rubber temperature increased with a rise in vertical loads in a similar logarithmic manner. However, the increases in rubber temperatures in the tread and shoulder regions were more significant than that in the sidewall region. For example, as the vertical load was raised from 0.34 to 1.04 MN, the maximum rubber temperature in the tread region increased from 54.4 to 82.2 ℃ and the maximum rubber temperature in the shoulder region grew from 60.9 to 92.1 ℃. These increments in the maximum rubber temperatures in both the tread (27.8 ℃) and shoulder (31.2 ℃) regions were greater than that (24.2 ℃) in the sidewall region. A similar phenomenon was also observed in HT tires, as per other studies (Cho et al., 2013; Tang et al., 2014; Wu, 2017). Compared with the sidewall region, the rubber temperatures in the tread and shoulder regions in HT tires increased more significantly (Cho et al., 2013; Tang et al., 2014; Wu, 2017). For instance, Wu (2017) examined the rubber temperatures in a 235/60R18 HT tire at a truck speed of 80 km/h and an ambient temperature of 26 ℃. The results showed that rubber temperatures in the shoulder and tread regions went up by 31.5% and 25.8%, respectively, when the vertical load was raised from 1.5 to 4.5 kN. These temperature increments were greater than that (23.3%) observed in sidewall rubbers in the HT tire.

In Figure 5.6, the increases in tire rubber temperatures were investigated at large vertical loads from 0.34 to 1.04 MN. This is uncommon for investigations into HT tires because the vertical loads on an HT tire are generally small. As indicated by other researchers (Li, 2012; Li et al., 2011; Xia et al., 2004), when used on highways, HT tires usually carry vertical loads of less than 50 kN.

However, the increase in rubber temperatures at large vertical loads (e.g., above 0.34 MN) is of great interest for OTR tires. Large vertical loads from 0.34 to 1.04 MN are typical operating conditions for OTR tires used at mine sites. For instance, an OTR tire often carries a vertical load up to 1.04 MN under the fully loaded condition. In addition, at large vertical loads exceeding 0.34 MN, the tire rubber temperature still increased significantly. As observed in in Figure 5.6, when the vertical load was raised to 1.04 MN, the maximum rubber temperature in the tread region was 82.2 °C, which was 27.8 °C higher than that (54.4 °C) at the vertical load of 0.34 MN. This indicates that at 30 km/h and 20 °C, the tread rubber temperatures in the OTR tire under the fully loaded condition could be 27.8 °C higher than they are when the truck is empty. One of the highlights of this study is predicting the rubber temperatures in OTR tires at large vertical loads (e.g., 0.34~1.04 MN).

### 5.3.3. Relationship between tire rubber temperatures and truck speeds

Figure 5.7 shows the relationships between maximum rubber temperatures and truck speeds at an ambient temperature of 20 °C and vertical loads of 0.34 MN and 1.04 MN. As per the Appendix A, a tire vertical load of 1.04 MN refers to the fully loaded condition of a truck (i.e., 363 tonnes); the vertical load is 0.34 MN when the truck is empty.
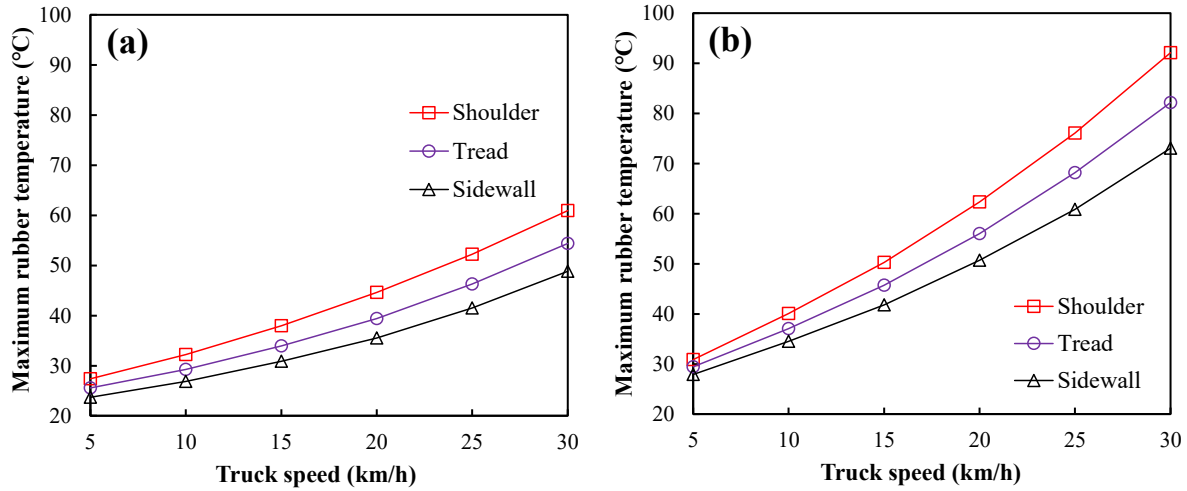
Figure 5.7. Relationship between maximum rubber temperatures and truck speeds at 20 °C (a) when the vertical load is 0.34 MN; (b) when the vertical load is 1.04 MN

In Figure 5.7(a), at 20 °C and a vertical load of 0.34 MN, rubber temperatures increased with rising truck speeds. For instance, in the sidewall region, the maximum rubber temperature increased from 23.7 to 48.9 °C with a rise in truck speed from 5 to 30 km/h. In the tread and shoulder regions, the rubber temperature increased relatively dramatically with rising truck speeds. For example, when the truck speed was raised from 5 to 30 km/h, the maximum rubber temperature in the tread region grew from 25.6 to 54.4 °C, and there was an increase in the maximum rubber temperatures from 27.4 to 60.9 °C in the shoulder region. A similar phenomenon was also observed in HT tires in previous studies (Lin and Hwang, 2004; Narasimha Rao et al., 2006; Sokolov, 2009). As per Narasimha et al. (2006), at a vertical load of 6 kN and an ambient temperature of 30 °C, an FE thermal model was developed to predict the rubber temperatures in a 235/75R15 HT tire. The results showed that the rubber temperature at the shoulder of the tire increased from 87.3 to 105.1 °C with a rise in truck speed from 40 to 60 km/h.

In Figure 5.7(b), as predicted by the OTRTire-T model, the increase in rubber temperatures induced by rising truck speeds became more significant at a larger vertical load: the rubber temperature increased with the truck speeds more rapidly at a vertical load of 1.04 MN than at a vertical load of 0.34 MN. For instance, in the sidewall region, when the truck speed was raised from 5 to 30 km/h, the maximum rubber temperature increased from 27.9 to 73.1 °C at the vertical load of 1.04 MN. This increment in rubber temperatures (45.2 °C) was greater than that (25.2 °C) when the vertical load was 0.34 MN. Moreover, in the shoulder region, the maximum rubber temperature increased with the rising truck speeds (from 5 to 30 km/h) by 61.2 °C when the vertical load was 1.04 MN, which was 27.7 °C higher than that (33.5 °C) when the vertical load was 0.34 MN. The increase in rubber temperatures induced by rising truck speeds at large vertical loads (e.g., 1.04 MN) has rarely been examined in HT tires. This is because these large vertical loads are not included in HT tire operating conditions on highways, as mentioned in Section 5.3.2. However, large vertical loads (e.g., 1.04 MN) are typical for OTR tires. According to Appendix 5A, a tire vertical load of 1.04 MN refers to the fully loaded condition of a truck (i.e., 363 tonnes). In Figure 5.7(b), at a vertical load of 1.04 MN, the maximum rubber temperature in the tread region increased from 29.5 to 82.2 °C with a rise in truck speeds from 5 to 30 km/h. This indicates that at 20 °C, when the truck speed increased from 5 to 30 km/h, the tread rubber temperature went up by 52.7 °C in an OTR tire under the fully loaded condition of the truck. Another highlight of this study is the investigation of the effects of truck speeds on rubber temperatures in OTR tires at larger vertical loads (e.g., 1.04 MN).

### 5.3.4. Tire rubber temperatures at various ambient temperatures

Figure 5.8 shows two different aspects of tire rubber temperatures at ambient temperatures from -30 to 40 °C. At a vertical load of 1.04 MN and a truck speed of 30 km/h, Figure 5.8(a)

illustrates the rubber temperature increment at increasing ambient temperatures from -30 to 40 °C; Figure 5.8(b) presents the rubber temperatures when the ambient temperature was raised from -30 to 40 °C. This range of ambient temperatures can cover the average temperatures in most regions of North America in all seasons (Alberta Agriculture and Forestry, 2018).
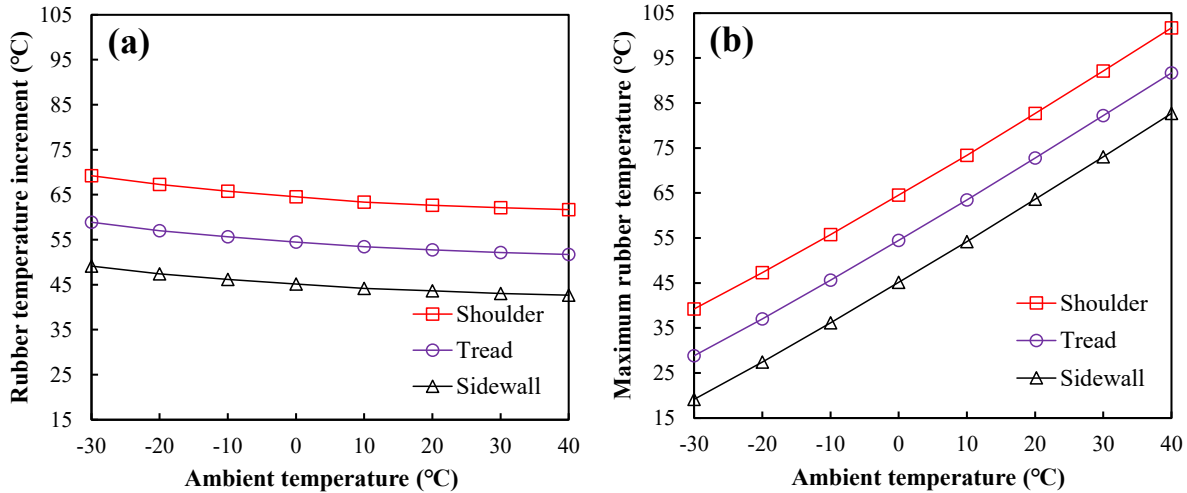


Figure 5.8. Tire rubber temperatures at a vertical load of 1.04 MN, a truck speed of 30 km/h, and ambient temperatures from -30 to 40 °C: (a) rubber temperature increment; (b) maximum rubber temperature

As shown in Figure 5.8(a), for OTR tire rubbers in multiple regions of sidewall, tread, and shoulder, there were inverse proportional relationships between the rubber temperature increments and the ambient temperatures from -30 to 40 °C. This indicates that the rubber temperature increment reduced relatively sharply at low ambient temperatures from -30 to 0 °C but decreased slightly as the ambient temperature increased above 0 °C. For instance, at a vertical load of 1.04 MN and a truck speed of 30 km/h, the rubber temperature increment in the sidewall region reduced by 8.2% as the ambient temperature increased from -30 to 0 °C; however, it decreased by only

4.8% with further increases in ambient temperatures from 0 to 40 ℃. Similarly, the rubber temperature increment in the tread region decreased from 58.9 to 54.5, and then to 51.7 ℃ when the ambient temperature increased from -30 to 0, and then to 40 ℃, respectively. The decreasing trend of rubber temperature increments in the tread region can be partially explained by the decline of heat generation rates of tread rubbers at high ambient temperatures. From Table 5B.3, as the ambient temperature was raised from -30 to 40 ℃, the heat generation rate of tread rubbers decreased from 539.5 to 444.0 kW/m$^3$. According to other researchers (He, 2005; He et al., 2006), the decreased heat generation rates may reduce the heat build-up and mitigate the temperature rise in the tread rubbers. In addition, the thermal conductivity and thermal diffusivity of the tread rubbers tend to change at rising ambient temperatures. In Tables 5B.6 and 5B.7, the thermal conductivity increased from 299 to 333 mW/(m·℃), and the thermal diffusivity decreased from 0.234 to 0.201 mm$^2$/s when the ambient temperature was raised from -30 to 40 ℃. The increasing thermal conductivity and decreasing thermal diffusivity may further lead to a reduction in rubber temperature increments, according to previous studies (Kerschbaumer et al., 2019; Wang et al., 2017).

As observed in Figure 5.8(b), despite the decreasing trend in rubber temperature increments, the rubber temperature increased relatively rapidly with a rise in ambient temperature. For example, at a vertical load of 1.04 MN and a truck speed of 30 km/h. the maximum rubber temperature in the sidewall region grew from 19.2 to 82.7 ℃ at increasing ambient temperatures from -30 to 40 ℃. Similarly, there were increases in the maximum rubber temperature in the tread region (62.8 ℃) and the shoulder region (62.5 ℃) when the ambient temperature rose from -30 to 40 ℃. This phenomenon is consistent with the observations of HT tires in previous studies (Golbakhshi and Namjoo, 2014; Narasimha Rao et al., 2006). For instance, Golbakhshi and

149

Namjoo (2014) found that the maximum rubber temperature in a 185/60R15 HT tire increased by 49.7 °C at rising ambient temperatures from -10 to 40 °C, when the vertical load was 3 kN and the vehicle speed was 80 km/h. At rising ambient temperatures, predicting the increase in rubber temperatures is of great interest since it may lead to tire failures and short service life (Anzabi, 2015; Anzabi et al., 2012; Lindeque, 2016). The OTRTire-T model is the first model to predict the increase of tire rubber temperatures at rising ambient temperatures based on a 3D FE OTR tire simulation.

## 5.4. Conclusion

This study conducted a numerical investigation to examine the temperatures in off-the-road (OTR) tires under operating conditions at mine sites. The main conclusions are enumerated as follows:

1. A novel finite element (FE) OTR tire thermal (OTRTire-T) model was developed to predict the temperatures in OTR tires at vertical loads from 0.34 to 1.04 MN, truck speeds from 5 to 30 km/h, and ambient temperatures from -30 to 40 °C. The average mean absolute percent error (MAPE) between the temperatures predicted by the OTRTire-T model and the temperatures derived from on-site observation was 8.63%. This MAPE was relatively low when compared with previous studies, showing that the OTRTire-T model has higher prediction accuracy.

2. A large vertical load (e.g., 1.04 MN) increased the tire rubber temperatures considerably. At 30 km/h and 20 °C, when the vertical load increased from 0.34 to 1.04 MN, the rubber temperature in the tread region increased from 54.4 to 82.2 °C. This indicates that the tread rubber temperature in an OTR tire under the fully loaded condition could be 27.8 °C higher

150

than it is when the truck is empty.

3. The tire rubber temperature increased with a rise in truck speeds, and the increase became more significant at larger vertical loads (e.g., 1.04 MN). At 20 °C and a vertical load of 1.04 MN, the maximum rubber temperature in the tread region increased from 29.5 to 82.2 °C with a rise in truck speeds from 5 to 30 km/h. This has quantitatively shown that in a truck under the fully loaded condition, the tread rubber temperature went up by 52.7 °C in an OTR tire.

4. The OTRTire-T model identified an inverse proportional relationship between the rubber temperature increments and the ambient temperatures from -30 to 40 °C. This indicates that the rubber temperature increment reduced relatively sharply at low ambient temperatures from -30 to 0 °C but decreased slightly as the ambient temperature increased above 0 °C.

5. Despite the decreasing trend in rubber temperature increments, the rubber temperature in the OTR tire increased relatively rapidly with a rise of ambient temperatures. For example, at a vertical load of 1.04 MN and a truck speed of 30 km/h. the maximum rubber temperature in the sidewall region grew from 19.2 to 82.7 °C at increasing ambient temperatures from -30 to 40 °C.

## Appendix 5A. Conversion of operating conditions at mine sites

The vertical load on an OTR tire was converted from the payload of a truck, as listed in Table 5A.1. As per a study by Kerr (Kerr, 2017), a rear OTR tire bears 13% of the load from gross vehicle weight (GVW) when a truck is empty. This rear OTR tire carries 16.7% of the GVW load when the truck is under the fully loaded condition. In this study, the GVW includes the truck

weight (i.e., 260 tonnes) (Caterpillar, 2018) and the payloads. The payloads were derived from the VIMS database on an Alberta oil sands mine for a period of 365 days in 2018 (Ta, 2018).

Table 5A.1. Conversion from truck payloads to tire vertical loads

| Payload condition | Gross vehicle weight (tonne) | Vertical load on a rear OTR tire (MN) |
|---|---|---|
| Empty | 260 | 0.34 |
| Fully loaded | 623 | 1.04 |

## Appendix 5B. Mechanical and thermal properties of OTR tire rubbers

Tensile tests on tire rubbers and structural components (i.e., belts and ply) were previously performed in a study by Nyaaba (Nyaaba, 2017). These tensile tests were conducted based on real rubber, belt, and ply samples derived from a Michelin 56/80R63 OTR tire. The material constants are listed in Table 5B.1 and 5B.2.

Table 5B.1. Material constants in OTR tire rubbers

| Rubber type | C10 (MPa) | C01 (MPa) |
|---|---|---|
| Sidewall | 0.38 | 0.12 |
| Casing | 0.44 | 0.13 |
| Tread | 0.47 | 0.12 |
| Apex | 1.00 | 0.42 |
| Innerliner | 0.17 | 0.07 |

Table 5B.2. Material constants in structural components (belts and ply)

| | Density (kg/m$^3$) | Elastic modulus (GPa) | Poisson's ratio |
|---|---|---|---|
| Transition belt; working belts 1, 2, 3, and 4; penetration protection belt; casing ply | 7800 | 100 | 0.3 |

Cyclic tensile tests were conducted on tread and sidewall rubbers at different strain levels from 20% to 100%, strain rates from 10% to 500% s-1, and rubber temperatures from -30 to 100 °C. The test results of heat generation rates are listed in Table 5B.3 and 5B.4. In addition, as per a study by Nyaaba (Nyaaba, 2017), under the same testing conditions, the heat generation rate of apex rubbers and innerliner rubbers were 7% and 11% higher than that of tread rubbers; the heat generation rate of casing rubber is about 4% lower than that of sidewall rubbers.

Table 5B.3. Experimental results of heat generation rates of tread rubbers (in kW/m$^3$)

| Strain level / Rubber temp. | Strain rate: 10% s$^{-1}$ | | | Strain rate: 100% s$^{-1}$ | | | Strain rate: 300% s$^{-1}$ | | | Strain rate: 500% s$^{-1}$ | | |
|---|---|---|---|---|---|---|---|---|---|---|---|---|
| | 20% | 40% | 100% | 20% | 40% | 100% | 20% | 40% | 100% | 20% | 40% | 100% |
| -30 °C | 3.2 | 4.7 | 8.1 | 33.5 | 49.3 | 85.9 | 108.0 | 162.0 | 290.1 | 191.3 | 293.8 | 539.5 |
| -20 °C | 3.1 | 4.5 | 7.8 | 32.5 | 47.3 | 82.1 | 104.3 | 154.1 | 277.2 | 185.0 | 282.5 | 513.5 |
| -10 °C | 3.0 | 4.4 | 7.6 | 31.0 | 46.0 | 78.8 | 99.8 | 150.8 | 267.6 | 181.3 | 271.9 | 497.8 |
| 0 °C | 2.9 | 4.2 | 7.2 | 30.0 | 44.0 | 77.3 | 98.3 | 145.5 | 256.2 | 176.3 | 265.0 | 474.0 |
| 10 °C | 2.8 | 4.1 | 7.1 | 28.8 | 42.9 | 74.6 | 96.8 | 139.1 | 250.1 | 170.0 | 258.1 | 460.8 |
| 20 °C | 2.7 | 4.0 | 7.0 | 28.3 | 42.3 | 73.6 | 93.0 | 139.9 | 246.3 | 167.5 | 254.4 | 453.3 |
| 30 °C | 2.7 | 4.0 | 6.9 | 28.0 | 41.6 | 72.9 | 91.5 | 138.8 | 243.9 | 166.3 | 250.6 | 448.5 |
| 40 °C | 2.7 | 4.0 | 6.8 | 27.8 | 41.1 | 72.2 | 90.0 | 136.1 | 238.5 | 163.8 | 247.5 | 444.0 |
| 50 °C | 2.6 | 3.9 | 6.7 | 27.8 | 40.5 | 71.7 | 90.0 | 133.9 | 238.8 | 162.5 | 243.1 | 437.8 |
| 60 °C | 2.6 | 3.9 | 6.7 | 27.5 | 40.0 | 71.0 | 87.8 | 134.3 | 237.9 | 160.0 | 240.0 | 433.5 |
| 70 °C | 2.6 | 3.8 | 6.6 | 27.3 | 39.4 | 70.3 | 88.5 | 130.1 | 234.8 | 158.8 | 236.9 | 431.0 |
| 80 °C | 2.6 | 3.8 | 6.5 | 27.3 | 39.0 | 69.8 | 87.8 | 129.0 | 233.6 | 157.5 | 234.4 | 424.3 |
| 90 °C | 2.5 | 3.7 | 6.4 | 27.0 | 38.6 | 69.1 | 87.0 | 130.1 | 229.5 | 156.3 | 232.5 | 419.3 |
| 100 °C | 2.5 | 3.7 | 6.4 | 26.8 | 38.3 | 68.7 | 86.3 | 126.4 | 227.7 | 153.8 | 230.0 | 415.5 |

Table 5B.4. Experimental results of heat generation rates of sidewall rubbers (in kW/m$^3$)

| Strain level / Rubber temp. | Strain rate: 10% s$^{-1}$ | | | Strain rate: 100% s$^{-1}$ | | | Strain rate: 300% s$^{-1}$ | | | Strain rate: 500% s$^{-1}$ | | |
|---|---|---|---|---|---|---|---|---|---|---|---|---|
| | 20% | 40% | 100% | 20% | 40% | 100% | 20% | 40% | 100% | 20% | 40% | 100% |
| -30 ℃ | 3.8 | 5.6 | 9.5 | 39.0 | 56.8 | 98.4 | 124.2 | 186.3 | 333.6 | 227.5 | 355.6 | 635.3 |
| -20 ℃ | 3.5 | 5.3 | 9.0 | 36.3 | 54.4 | 95.2 | 119.9 | 177.2 | 318.8 | 218.8 | 339.4 | 601.5 |
| -10 ℃ | 3.4 | 5.0 | 8.7 | 35.0 | 52.6 | 90.3 | 114.8 | 173.4 | 307.7 | 211.3 | 319.4 | 580.5 |
| 0 ℃ | 3.2 | 4.7 | 8.3 | 33.3 | 50.5 | 87.2 | 113.0 | 167.3 | 294.6 | 201.3 | 310.6 | 554.0 |
| 10 ℃ | 3.1 | 4.6 | 8.0 | 32.0 | 48.6 | 84.4 | 111.3 | 160.0 | 287.6 | 195.0 | 298.8 | 533.8 |
| 20 ℃ | 3.0 | 4.5 | 7.8 | 31.5 | 47.6 | 82.7 | 107.0 | 160.9 | 283.2 | 191.3 | 290.6 | 524.0 |
| 30 ℃ | 3.0 | 4.5 | 7.6 | 31.3 | 47.1 | 81.3 | 105.2 | 159.6 | 280.5 | 187.5 | 283.1 | 515.3 |
| 40 ℃ | 2.9 | 4.4 | 7.5 | 31.0 | 46.5 | 79.4 | 103.5 | 156.5 | 274.3 | 183.8 | 280.0 | 508.5 |
| 50 ℃ | 2.9 | 4.3 | 7.4 | 30.5 | 45.6 | 77.6 | 103.5 | 154.0 | 274.6 | 181.3 | 275.0 | 499.0 |
| 60 ℃ | 2.8 | 4.2 | 7.2 | 30.0 | 44.6 | 76.1 | 101.0 | 154.4 | 273.6 | 177.5 | 270.0 | 494.3 |
| 70 ℃ | 2.8 | 4.2 | 7.2 | 30.0 | 44.0 | 75.3 | 101.8 | 149.6 | 270.0 | 173.8 | 268.1 | 485.5 |
| 80 ℃ | 2.7 | 4.1 | 7.0 | 29.5 | 42.8 | 73.1 | 101.0 | 148.4 | 268.6 | 171.3 | 262.5 | 475.5 |
| 90 ℃ | 2.7 | 4.0 | 6.9 | 29.3 | 42.4 | 72.5 | 100.1 | 149.6 | 263.9 | 168.8 | 258.1 | 469.5 |
| 100 ℃ | 2.7 | 4.0 | 6.8 | 29.0 | 41.6 | 71.7 | 99.2 | 145.4 | 261.9 | 167.5 | 253.8 | 457.3 |

In the OTRTire-T model, the material constants $C_{10}$, $C_{01}$, $A$, $B$, $C$, $C_1$, $r$, $m$, and $n$ were determined following an inverse analysis method widely used in previous studies (Jin and Cui, 2010; Lei and Szeri, 2007). As per this method, an error function $f_{error}\left(C_{10}, C_{01}, A, B, C, C_1, r, m, n\right)$ was established based on the heat generation rates $\dot{Q}$ (in W/m$^3$), as follows:

$$f_{error}\left(C_{10}, C_{01}, A, B, C, C_1, r, m, n\right) = \sum_{i=1}^{P} \left[\dot{Q}_{experimental,i}\left(\varepsilon, \dot{\varepsilon}, T\right) - \dot{Q}_{analytical,i}\left(\varepsilon, \dot{\varepsilon}, T\right)\right]^2 \qquad (5B.1)$$

where $\dot{Q}_{analytical,i}\left(\varepsilon,\dot{\varepsilon},T\right)$ (in W/m³) and $\dot{Q}_{experimental,i}\left(\varepsilon,\dot{\varepsilon},T\right)$ (in W/m³) are the heat generation rates derived from the OTRTire-T model and the cyclic tensile tests (as listed in Tables 5B.3 and 5B.4), respectively; and $P$ is the number of data points.

From Equation (5B.1), the smaller values of $f_{error}\left(C_{10},C_{01},A,B,C,C_{1},r,m,n\right)$ indicate the smaller deviations between the heat generation rates derived from the OTRTire-T model and the cyclic tensile tests. Based on this, to minimize this deviation, the material constants causing the minimum value of $f_{error}\left(C_{10},C_{01},A,B,C,C_{1},r,m,n\right)$ were determined, as shown in Table 5B.5.

Table 5B.5. Material constants in the OTRTire-T model for different tire rubbers

| Rubber type | $C_{10}$ | $C_{01}$ | $C_{1}$ | $A$ | $B$ | $C$ | $r$ | $m$ | $n$ |
|---|---|---|---|---|---|---|---|---|---|
| Sidewall | 1.03 | -0.71 | -0.15 | 0.05 | 2.85 | 0.48 | 0.67 | 2.35 | 1.89 |
| Casing | 1.28 | -0.35 | -0.18 | 0.04 | 3.14 | 0.97 | 0.39 | 1.42 | 1.67 |
| Tread | 1.21 | -0.58 | -0.26 | 0.04 | 3.84 | 0.55 | 0.57 | 1.55 | 1.97 |
| Apex | 1.36 | -0.61 | -0.31 | 0.06 | 2.52 | 0.61 | 0.64 | 1.28 | 2.15 |
| Innerliner | 1.31 | -0.85 | -0.24 | 0.05 | 1.34 | 0.84 | 0.91 | 1.72 | 2.39 |

After determination of heat generation rates, the thermal conductivity and diffusivity of the tire rubbers were experimentally determined using a Hot Disk TPS 500 thermal constants analyzer (Disk, 2018). The results are listed in Tables 5B.6 and 5B.7.

Table 5B.6. Thermal conductivity of different tire rubbers (W/(m·°C))

| Rubber type | -30 °C | -10 °C | 0 °C | 20 °C | 40 °C | 60 °C | 80 °C | 100 °C |
|---|---|---|---|---|---|---|---|---|
| Sidewall | 0.279 | 0.287 | 0.296 | 0.301 | 0.315 | 0.325 | 0.336 | 0.342 |
| Casing | 0.241 | 0.253 | 0.267 | 0.275 | 0.279 | 0.283 | 0.288 | 0.296 |
| Tread | 0.299 | 0.310 | 0.315 | 0.320 | 0.333 | 0.351 | 0.364 | 0.376 |
| Apex | 0.311 | 0.321 | 0.335 | 0.338 | 0.351 | 0.371 | 0.386 | 0.392 |
| Innerliner | 0.256 | 0.263 | 0.275 | 0.281 | 0.284 | 0.293 | 0.299 | 0.305 |

Table 5B.7. Thermal diffusivity of different tire rubbers ($mm^2$/s)

| Rubber type | -30 °C | -10 °C | 0 °C | 20 °C | 40 °C | 60 °C | 80 °C | 100 °C |
|---|---|---|---|---|---|---|---|---|
| Sidewall | 0.254 | 0.251 | 0.247 | 0.242 | 0.238 | 0.234 | 0.228 | 0.219 |
| Casing | 0.278 | 0.269 | 0.259 | 0.245 | 0.237 | 0.231 | 0.224 | 0.209 |
| Tread | 0.234 | 0.224 | 0.217 | 0.209 | 0.201 | 1.996 | 1.994 | 1.987 |
| Apex | 0.299 | 0.286 | 0.275 | 0.269 | 0.254 | 0.246 | 0.239 | 0.231 |
| Innerliner | 0.312 | 0.301 | 0.294 | 0.286 | 0.281 | 0.274 | 0.269 | 0.257 |

## Appendix 5C. Mesh independence test

A mesh independence test was conducted to determine the number of elements in the 3D FE OTR tire model. As shown in Table 5C.1, the peak strain in OTR tire rubbers was 56.1% when the number of elements in tire rubbers, belts/ply, and inflated air were selected as 389734, 43327, and 649516, respectively. Further refining the mesh had almost no influence on the peak strain, while it significantly increased the computational time. For example, when the meshes were refined from Mesh #4 to Mesh #5, the peak strain remained stable at 56.1%; however, the computational time was extended from 23.2 to 52.3 h since the number of meshes increased about two times. To save computational time without compromising simulation accuracy, the number of

elements in tire rubbers, tire belts/ply, and inflated air were selected as 389734, 43327, and 649516, respectively.

Table 5C.1. Mesh independence test

| | Number of elements | | | Peak strain | Computational time |
|---|---|---|---|---|---|
| | Rubbers | Belts/ply | Inflated air | (%) | (h) |
| Mesh #1 | 7794 | 867 | 12991 | 54.8 | 0.38 |
| Mesh #2 | 15589 | 1733 | 25981 | 55.1 | 1.03 |
| Mesh #3 | 103932 | 11556 | 173208 | 55.6 | 6.60 |
| Mesh #4 | 389734 | 43327 | 649516 | 56.1 | 23.2 |
| Mesh #5 | 779468 | 86654 | 1299032 | 56.1 | 52.3 |

# Chapter 6. Effects of site operating conditions on real site TKPH (tonne-kilometer-per-hour) of ultra-large off-the-road tires

## 6.1. Introduction

Ultra-large off-the-road (OTR) tires are one of the most expensive components of haul trucks. For instance, one Michelin 56/80R63 OTR tire that is used for a Caterpillar 797 truck costs about CA\$ 60,000 (Oil Sands Discovery Center, 2016). However, the service life of OTR tires is short, at between 6 to 15 months (Oil Sands Discovery Center, 2016). The short service life of OTR tires is believed to be related to high tire temperatures (Meech and Parreira, 2013; Parreira, 2013). For example, the tire temperature can reach up to 92.1 °C in the shoulder region of a 56/80R63 OTR tire (Ma et al., 2022d). According to previous studies (Kerr, 2017; Li et al., 2012; Nyaaba, 2017), tire temperatures are significantly affected by site operating conditions. At mine sites, operating conditions vary dramatically. As per mine site data (Alberta Agriculture and Forestry, 2018; Ta, 2018) and conversion (as referred to in Ma et al. (Ma et al., 2022d)), there is a unique and large range of operating conditions: average vertical loads (per tire) vary from 34 to 83 tonnes, average cycle speeds usually change from 10 to 45 km/h, ambient temperatures range from -30 to 40 °C, and cycle lengths differ from 5 to 50 km. Considering these site operating conditions, the mining industry has a particular interest in controlling tire temperatures, and thereby prolonging tire service life.

Currently, the TKPH (tonne-kilometer-per-hour) approach has been widely used to control tire temperatures at mine sites (Carter, 2016; Kagogo, 2014). In this approach, tire temperatures are controlled by keeping the real site TKPH smaller than the tire TKPH (Caterpillar, 2018; Michelin, 2016). The tire TKPH is a rating of OTR tires; it is provided by tire manufacturers (e.g., Michelin, Magna, and Bridgestone) to characterize the working capacity of the tire (Caterpillar, 2018; Pascual et al., 2019). The real site TKPH is an index calculated from site operating

160

conditions, including average vertical load per tire ($Q_m$) (having the conversion from payload), average cycle speed ($V_m$), ambient temperature, and cycle length (Michelin, 2016), and it is derived as

$$\text{Real site TKPH} = Q_m \times V_m \times K_1 \times K_2 \qquad (6.1)$$

According to Equation (6.1), the real site TKPH includes a cycle length coefficient $K_1$ that quantifies the effects of cycle lengths on the real site TKPH and a site ambient temperature coefficient $K_2$ which is used to evaluate the influence of ambient temperatures on the real site TKPH (Michelin, 2016). The cycle length coefficient $K_1$ is included because the temperatures within the OTR tire (i.e., tire temperature and air temperature inside the tire) vary with cycle lengths at mine sites, which ultimately affects the real site TKPH. As per previous studies (Meech and Parreira, 2013; Parreira, 2013), the tire temperature and internal air temperature increased with a rise in cycle lengths. For instance, at an average vertical tire load of 48 tonnes and an average cycle speed of 16 km/h, the internal air temperature in a Bridgestone 40.00R57 OTR tire increased from 75.6 to 78.0 °C at rising cycle lengths from 8 to 10 km when the ambient temperature was 35 °C (Meech and Parreira, 2013). In addition to cycle length, the site ambient temperature also influences the real site TKPH (Caterpillar, 2018). At rising ambient temperatures from 20 to 40 °C, the tread temperature in a Bridgestone 24.00R35 tire increased from 54.1 to 69.1 °C (Li et al., 2012), leading to a rise in the real site TKPH by 10.8%. Thus, the site ambient temperature coefficient $K_2$ is used so that the influence of ambient temperatures is taken into consideration.

Up to now, OTR tire manufacturers have provided real site TKPHs, including the values of the $K_1$ and $K_2$ coefficients. For instance, Michelin (Michelin, 2016) and Magna (Magna, 2014)

161

provide their real site TKPHs containing a set of $K_1$ in the same values ranging from 1.00 to 1.23 when the cycle length changes from 5 to 50 km. Michelin and Magna also select the same $K_2$ values in the range of 0.635 to 1.016 as the ambient temperature is raised from 15 to 40 °C (Magna, 2014; Michelin, 2016). In addition, Bridgestone (Bridgestone, 2020) delivers the real site TKPHs with similar $K_2$ coefficients in values of 0.813~1.020 at rising ambient temperatures from 15 to 40 °C. However, unexpected high tire temperatures and short service life are frequently reported even if these real site TKPHs are applied to ultra-large OTR tires under operating conditions at mine sites. For instance, according to Bridgestone OTR tires Data Book (Bridgestone, 2020), the real site TKPH of a Bridgestone 40.00R57 OTR tire was considered as 745 when the tire was used at an average vertical load of 48 tonnes, an average cycle speed of 16 km/h, an ambient temperature of 35 °C, and a cycle length of 10 km. This real site TKPH was smaller than the tire TKPH (773 (Bridgestone, 2020)), but the tire still suffered from overheating—its internal air temperature reached up to 78.0 °C (Parreira, 2013) and exceeded the rating temperature of the tire (i.e., 75 °C (Marais, 2017)). In addition, Nyaaba (Nyaaba, 2017) reported that there were high tire temperatures of up to 95 °C in a Michelin 56/80R63 OTR tire even if the tire was working under a Michelin real site TKPH (2528) that was smaller than its tire TKPH rating (2765) (Michelin, 2016). The tire service life also dropped from a normal value of ~6000 hours (Kerr, 2017) to only 3442 hours (Nyaaba, 2017). From these studies and observations, it is noted that relevant research is scarce about the real site TKPH of ultra-large OTR tires under real site operating conditions. It is of great significance to understand the effects of site operating conditions on the real site TKPH of ultra-large OTR tires because it can help utilize the TKPH approach to reduce the overheating of OTR tires and prolong tire service life.

The objective of this study is to investigate the effects of site operating conditions on the real site TKPH of ultra-large OTR tires. In this study, the real site TKPHs were derived based on two sets of refined cycle length coefficients $K_1$ and site ambient temperature coefficients $K_2$. For the first time, these $K_1$ and $K_2$ coefficients were investigated fundamentally as to the effects of cycle lengths and ambient temperatures on OTR tire temperatures. The OTR tire temperatures were predicted using a novel finite element OTR tire thermal (OTRTire-T) model that was originally developed by the current authors. This OTRTire-T model is the first model in the literature that has been validated to be able to predict the temperatures in OTR tires at mine sites.

## 6.2. Methodology

### 6.2.1. An overview of the methodology

A flowchart showing an overview of the methodology is represented in Figure 6.1.
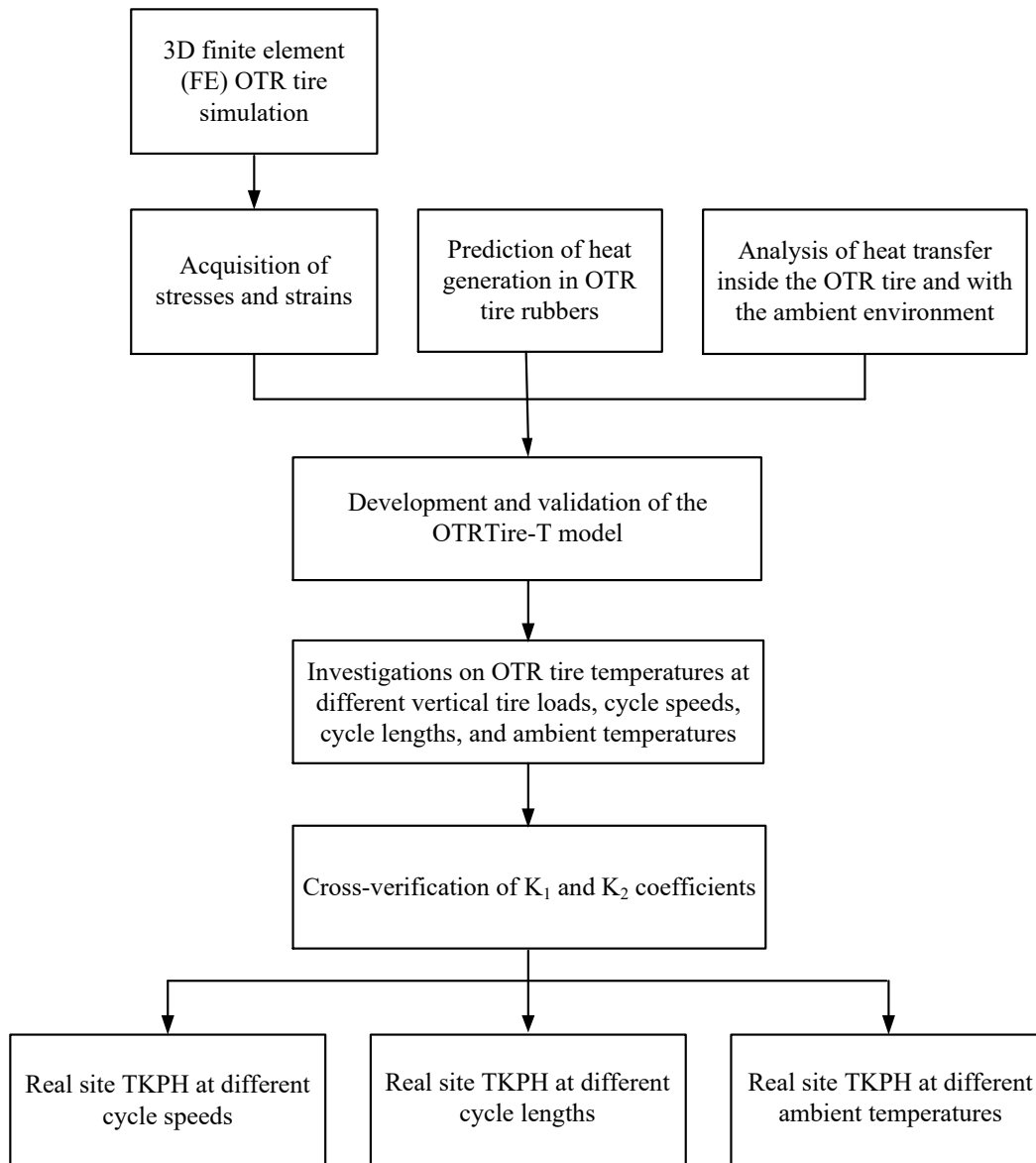
Figure 6.1. Flowchart showing an overview of the methodology

As shown in Figure 6.1, first, a 3D finite element (FE) simulation was made on a rolling

OTR tire on a haul road. In this simulation, the OTR tire was constructed with structural

components and various tire rubbers. The structural components included working belts and a

casing ply. The tire rubbers varied according to location, such as inner liner, apex, casing, sidewall,

and tread. These structural components and tire rubbers were assembled in accordance with the

geometry and construction of a Michelin 56/80R63 OTR tire. The Michelin 56/80R63 OTR tire was selected since it has been widely used at local mine sites in Alberta (Kerr, 2017). In this simulation, after been assembled, the tire was inflated and rolled on the haul road at a specific vertical tire load and truck speed. During the rolling, the stresses and strains in the tire rubbers were examined and output.

Based on the simulated OTR tire and output stresses and strains, an FE OTR tire thermal (OTRTire-T) model was developed following the procedure originally introduced in our previous study (Ma et al., 2022d). This OTRTire-T model contained a new mathematical equation that had been proven to determine the internal heat generation rates of OTR tire rubbers. In addition, the model described the heat conduction inside the OTR tire and the heat transfer between the tire and the ambient environment (Ma et al., 2022d). In this study, the OTRTire-T model was used to predict the temperatures in the OTR tire at various average vertical tire loads. These vertical tire loads were converted from the payloads on a truck following the method shown in Ma et al. (Ma et al., 2022d). The model also predicted tire temperature results under different operating conditions of average cycle speeds, cycle lengths, and ambient temperatures.

According to the results from the OTRTire-T model, the cycle length coefficient $K_1$ and the site ambient temperature coefficient $K_2$ in the real site TKPH were refined by fundamentally investigating the effects of cycle lengths and ambient temperatures on tire temperatures. For the first time, the detailed procedures for finding these $K_1$ and $K_2$ coefficients were developed, and have been summarized in Appendix 6A. These procedures had never before been found in the literature, and they are the highlights of this study. Then the $K_1$ and $K_2$ coefficients were compared with the coefficients provided by other OTR tire manufacturers (i.e., Michelin, Bridgestone, and Magna) for cross-verification. These manufacturers were selected because their OTR tire products

have been widely used at mine sites (Kerr, 2017; Li et al., 2012). After cross-verification, the $K_1$ and $K_2$ coefficients were used to calculate the real site TKPHs as per Equation (6.1). The real site TKPHs were then investigated under different site operating conditions of average vertical tire loads, average cycle speeds, ambient temperatures, and cycle lengths in the values listed in Table 6.1. These values were derived from the real operating conditions in Alberta's mine sites (Alberta Agriculture and Forestry, 2018; Ta, 2018).

Table 6.1. Site operating conditions in investigating the real site TKPHs

| Payload (tonne) | Average vertical tire load (tonne) | Average cycle speed (km/h) | Cycle length (km) | Ambient temperature (°C) |
|---|---|---|---|---|
| 0~363 | 34~83 | 10~45 | 5~50 | -30~40 |

### 6.2.2. Simulation of the Michelin 56/80R63 OTR tire

A 3D FE simulation was made to predict the rubber stresses ($S_{ij}$) and strains ($LE_{ij}$) in a Michelin 56/80R63 OTR tire. This simulation was conducted using ABAQUS software that has been widely used in tire engineering to solve the problems relating to nonlinear deformation (Cho et al., 2013; Xia, 2011) and heat transfer (Smith et al., 2012; Tang et al., 2014). The geometry and construction of the tire is represented in Figure 6.2.
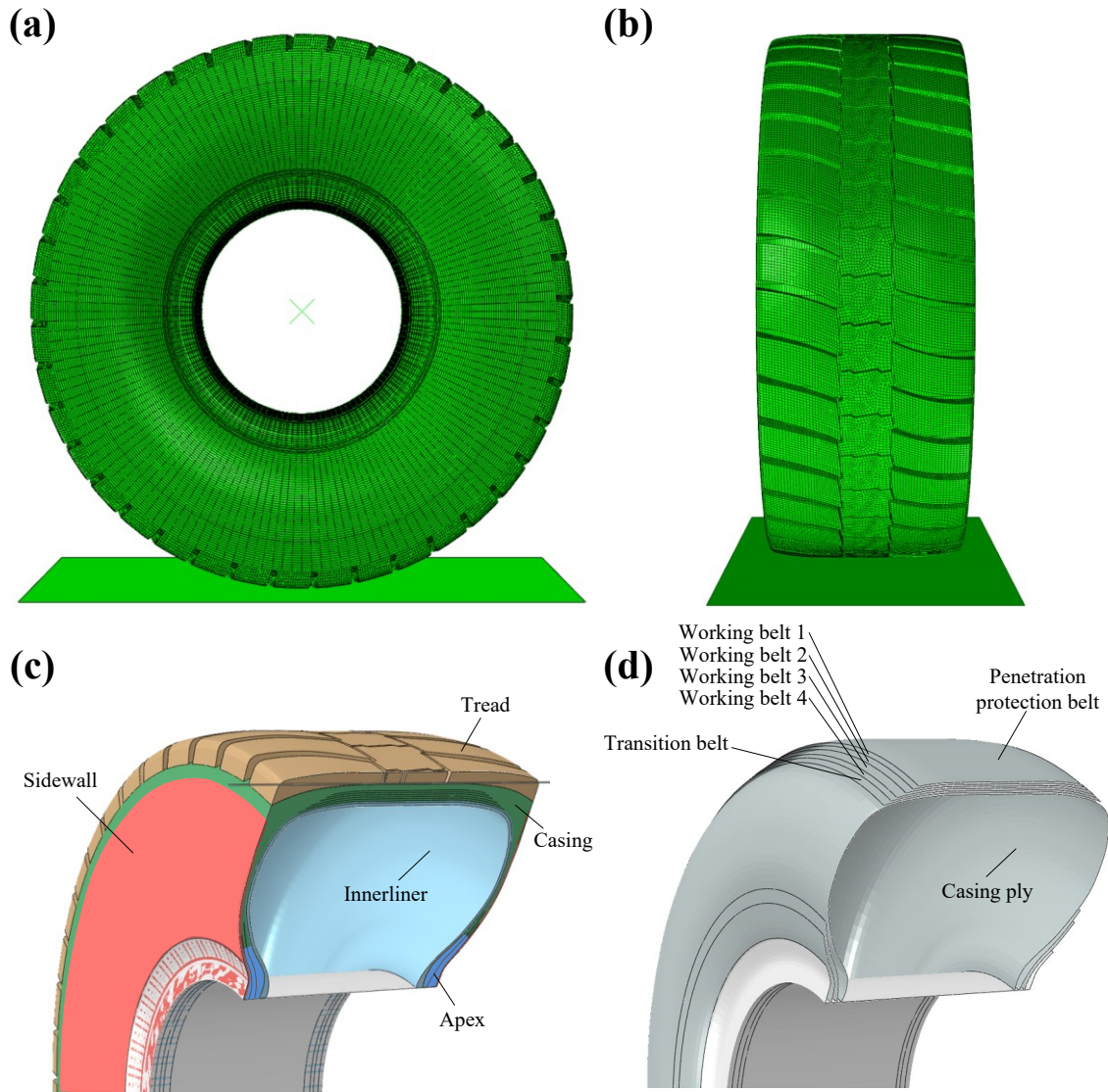
Figure 6.2. Geometry and construction of a Michelin 56/80R63 OTR tire: (a) front view; (b) side view; (c) tire rubbers; (d) structural components (Figure 6.2(c) and (d) were retrieved from Ma et al. (Ma et al., 2022d))

As shown in Figure 6.2, the OTR tire was constructed with various tire rubbers including inner liner, apex, casing, sidewall, and tread rubbers. These rubbers were described by the Mooney-Rivlin (MR) functions that have been widely used in other studies (Kim et al., 2012; Kumar and Rao, 2016) to characterize rubber-like materials. For each kind of rubber, the material

constants in the MR function were identified based on tensile test results of real tire rubbers in the laboratory, as referred to in the methods in the study by Nyaaba (Nyaaba, 2017). In addition, the structural components (i.e., belts and ply) were considered to be isotropic elastic materials. Their elastic parameters such as density, elastic modulus, and Poisson's ratio can be found in our previous study (Ma et al., 2022d). In the OTR tire, the tire rubbers and tire belts/ply were meshed into 389734 C3D8R elements and 43327 SFM3D4R elements, respectively. The C3D8R elements have been widely used in other studies (Liang et al., 2019; Neves et al., 2010) to simulate the deformations in tire rubbers. The SFM3D4R elements had been proven by other researchers to be able to mimic the distortions and twists in membrane structures such as tire belts and plies (W. Wang et al., 2013; Zhou et al., 2015). The number of these elements was determined by the mesh independence tests that were made in our previous study (Ma et al., 2022d). Apart from tire rubbers and structural components, the air inflated into the OTR tire was also simulated. This is not a common practice in other research (Cho et al., 2013; Marais, 2017; Tang et al., 2014), and is one of the highlights of this study. The inflated air is key to helping develop the OTRTire-T model in Section 2.3 to predict the air temperatures inside the OTR tire as well as the tire rubber temperatures. In this simulation, the inflated air was meshed into hexahedral 649516 AC3D8R elements that deform in coordination with the deformations of C3D8R elements in tire rubbers (Hu et al., 2021).

### 6.2.3. The OTRTire-T model

The OTRTire-T model was developed to detect the temperatures in the OTR tire at different average vertical tire loads, average cycle speeds, cycle lengths, and ambient temperatures. The OTRTire-T model is considered to be better at detecting tire temperatures when compared with other temperature measurement methods. These methods include the use of thermal couples,

infrared (IR) cameras, and Michelin Earthmover Management Systems (MEMSs). Using thermal couples is a traditional method for measuring temperatures (He, 2005). However, inserting thermal couples into tires may weaken the original structure of the tires and reduce their strength (Anzabi, 2015; Anzabi et al., 2012). IR cameras can measure tire temperatures without making contact (Allouis et al., 2016; Farroni et al., 2017), which ensures that the tire strength is not disturbed by the measurements. But IR cameras can only measure the surface temperatures of the tires; they cannot detect their internal temperatures (Wu, 2017). MEMSs can monitor the air temperatures inside the tire but are unable to measure the temperatures within the tire rubbers (Michelin, 2016). On the contrary, the OTRTire-T model provides for the measurement of both surface and internal temperatures in OTR tires. The internal temperatures include rubber temperatures and air temperatures inside the tire.

*6.2.3.1. Mathematical equation for predicting heat generation rates*

The heat generation rate is the amount of heat generated in tire rubbers per unit volume and unit time (Lin and Hwang, 2004; Tang et al., 2014). In the OTRTire-T model, a mathematical equation was developed to predict rubber heat generation rates following the method originally used in our study (Ma et al., 2022d), and is written as

$$\dot{Q} = \sum_{i=j=1}^{3} \dot{Q}_{ij} + \sum_{\substack{i=1, j=1 \\ i \neq j}}^{3} \dot{Q}_{ij}$$

where

$$\dot{Q}_{ij} = \left[ \int_0^{LE_{ij}} \sigma_{ij} d\varepsilon_{ij} - \int_0^{LE_{ij}} \eta_1 \sigma_{ij} d\varepsilon_{ij} + C_1 \int_0^{LE_{ij}} (1-\eta_2) \cdot \left( 2\varepsilon_{ij} - \frac{2}{(\varepsilon_{ij}+1)^2} - 1 \right) d\varepsilon_{ij} \right] \cdot \frac{\dot{\varepsilon}_{ij}}{2\varepsilon_{ij}} \tag{6.2}$$

$$\sigma_{ij} = 2 \left[ 1 - \frac{1}{(\varepsilon_{ij}+1)^3} \right] \left[ C_{10}(\varepsilon_{ij}+1) + C_{01} \right] \left[ A(\dot{\varepsilon}_{ij} - 0.1) + 1 \right] \left[ \frac{B}{T+50} + C \right]$$

$$\dot{\varepsilon}_{ij} = \frac{180 \cdot v \cdot LE_{ij}}{3.6 \cdot \pi R \arccos\left( \frac{R-VD}{R} \right)}$$

where $\dot{Q}$ (in W/m³) is the total heat generation rate in the rubber element, and $\dot{Q}_{ij}$ (in W/m³) is

the heat generation rate determined as per the stresses and strains on the $ij$ component. $\sigma_{ij}$ (in

MPa) is the stress, and $0 \leq \sigma_{ij} \leq S_{ij}$; $\varepsilon_{ij}$ (in m/m) is the strain ranging from 0 to the output strain $LE_{ij}$

(in m/m). $\dot{\varepsilon}_{ij}$ (in s⁻¹) is the rubber strain rate; $T$ (in °C) is the rubber temperature that is equal to

the ambient temperature (i.e., -30 to 40 °C) when the OTR tire starts to roll. $v$ (in km/h) is the

truck speed; $R$ (in m) is the radius of the OTR tire; $VD$ (in m) is the vertical deflection of the

tire output from the simulation in Section 2.2. In addition, $\eta_1$ and $\eta_2$ are the softening variable

and residual strain variable, respectively; their values have been provided in our study (Ma et al.,

2022c). $A$, $B$, $C$, $C_{10}$, $C_{01}$, and $C_1$ are the material constants. The material constants of the

tire rubbers (i.e., inner liner, apex, casing, sidewall, and tread) were determined based on the

experimental results of rubber heat generation rates that were derived in our previous study (Ma

et al., 2022b).

The mathematical equation in Equation (6.2) has been proven to be the first equation in the literature that can determine the internal heat generation rates in OTR tire rubbers (Ma et al., 2022d). Rubber heat generation rates are the foundation on which temperatures can be predicted in OTR tires in Section 6.2.3.2.

*6.2.3.2. Temperature prediction in the OTR tire*

The OTRTire-T model predicted the temperatures in the OTR tire based on the internal heat generation equation in Section 6.2.3.1 and the following Equation (6.3). Equation (6.3) includes the governing equation of heat conduction (Bergman et al., 2011) and the mathematical expression of the convective heat transfer (Cebeci and Bradshaw, 2012; Jiji, 2009). The convective heat transfer occurs on the OTR tire's outer layer boundary (which is in contact with the ambient environment) and the inner layer boundary (which contacts the inflated air).

$$\rho c \frac{\partial T(x,y,z,t)}{\partial t} = k \left( \frac{\partial^2 T(x,y,z,t)}{\partial x^2} + \frac{\partial^2 T(x,y,z,t)}{\partial y^2} + \frac{\partial^2 T(x,y,z,t)}{\partial z^2} \right) + \dot{Q}$$

where

$$t = \frac{CL \cdot 3600}{v}$$

$$k \frac{\partial T(x,y,z,t)}{\partial S_{outer}} = h_{outer} \left( T(x,y,z,t) - T_\infty \right)$$

$$k \frac{\partial T(x,y,z,t)}{\partial S_{inner}} = h_{inner} \left( T(x,y,z,t) - T_{in} \right)$$

$$h_{outer} = 5.9 + 1.03v$$

(6.3)

where $T(x,y,z,t)$ (in °C) is the temperatures at the time $t$ (in s) and at the point $(x,y,z)$ (in m) in the OTR tire. $CL$ (in km) is the cycle length, and $v$ (in km/h) is the truck speed. $\rho$ (in kg/m³) is the rubber density; $k$ (in W/(m·°C)) is the thermal conductivity of tire rubbers, and $c$ (in J/(kg·°C)) is the specific heat capacity. The density, thermal conductivity, and heat capacity had been

measured experimentally in our study (Ma et al., 2022a). These measurements were made at different temperatures (i.e., -30 ~ 40 °C) using a Hot Disk TPS 500 thermal constants analyzer (Disk, 2018). In addition, $S_{outer}$ represents the outer layer boundary of the OTR tire; $T_\infty$ (in °C) is the ambient temperature; $h_{outer}$ (in W/(m²·°C)) is the convective heat transfer coefficient at the boundary of tire outer layer, which is related to the truck speed $v$ (in km/h). $S_{inner}$ denotes the tire inner layer boundary; $T_{in}$ (in °C) is the temperature of the inflated air inside the tire; it varies with tire rubber temperatures during the rolling. $h_{inner}$ (in W/(m²·°C)) is the convective heat transfer coefficient on the tire's inner layer, which was selected as 3.0 W/(m²·°C) (Nyaaba, 2017).

The OTRTire-T model is the first model in the literature that has been validated to predict the temperatures in the OTR tire (Ma et al., 2022d). This validation was made based on the on-site monitoring data of the air temperatures inside the tire. At an Alberta oil sands mine site, a MEMS temperature sensor received a total of 105120 data points of the air temperatures in an OTR tire for 365 days in 2018 as per a report by Ta (Ta, 2018).

*6.2.3.3. Simulation of site operating conditions in the OTRTire-T model*

The OTRTire-T model simulated the operating conditions of the OTR tire within a complete cycle of a hauling trip and a return trip at mine sites. These site operating conditions included average vertical tire loads from 34 to 83 tonnes, average cycle speeds from 10 to 45 km/h, ambient temperature from -30 to 40 °C, and cycle lengths from 5 to 50 km.

As shown in Figure 6.3, below is an example for the simulation scenario at an ambient temperature of 15 °C, an average vertical tire load of 83 tonnes (corresponding to a vertical tire

load of 104 tonnes during the hauling trip), an average cycle speed of 30 km/h, and a cycle length of 20 km.
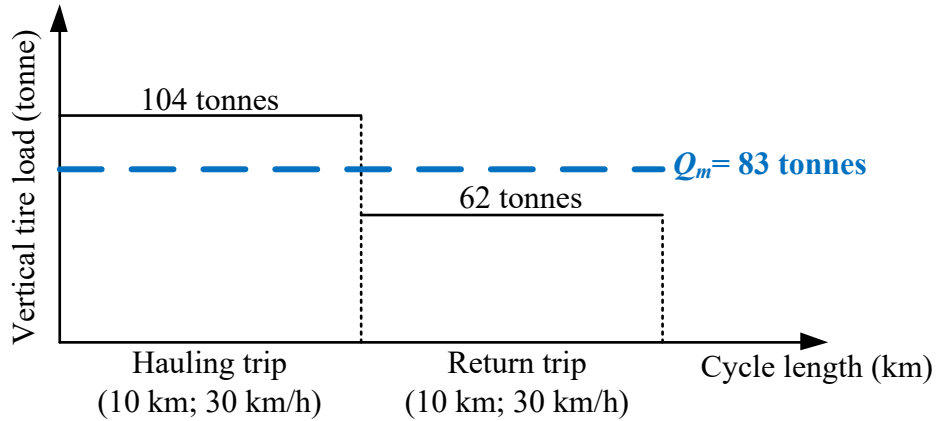


Figure 6.3. A simulation example of site operating conditions at an ambient temperature of 15 °C, an average cycle speed of 30 km/h, an average vertical tire load of 83 tonnes, and a cycle length of 20 km

As shown in Figure 6.3, at 15 °C, the OTRTire-T model first simulated the tire rolling a distance of 10 km during the hauling trip (half of the cycle length). In this trip, the tire rolled at a hauling speed of 30 km/h and a vertical tire load of 104 tonnes. This vertical tire load corresponded to the fully loaded condition of a haul truck when the payload was 363 tonnes. Then the tire was simulated to roll another 10 km, covering the remaining distance in the return trip. During this return trip, the truck was running empty (i.e., under a payload of zero) and as a result the vertical load on the truck's front tire decreased to 62 tonnes. The speed of the tire in the return trip was kept at 30 km/h to ensure an average cycle speed of 30 km/h in the simulation.

## 6.3. Results and discussions

### 6.3.1. Cross-verification of the $K_1$ and $K_2$ coefficients

To cross-verify the $K_1$ and $K_2$ coefficients, comparisons were made between the coefficients derived from the OTRTire-T model and the coefficients provided by other tire manufacturers such as Michelin (Michelin, 2016), Magna (Magna, 2014), and Bridgestone (Bridgestone, 2020). These manufacturers were selected because their OTR tire products have been widely used at Alberta's mine sites (Kerr, 2017; Li et al., 2012) and they have disclosed their $K_1$ and $K_2$ coefficients in the real site TKPH. The comparisons were conducted at average cycle speeds ranging from 10 to 45 km/h, ambient temperatures from -30 to 40 °C, and cycle lengths from 5 to 50 km. These operating conditions were derived from real mine sites in Alberta (Alberta Agriculture and Forestry, 2018; Ta, 2018). Some results of the comparisons are shown in Figure 6.4.
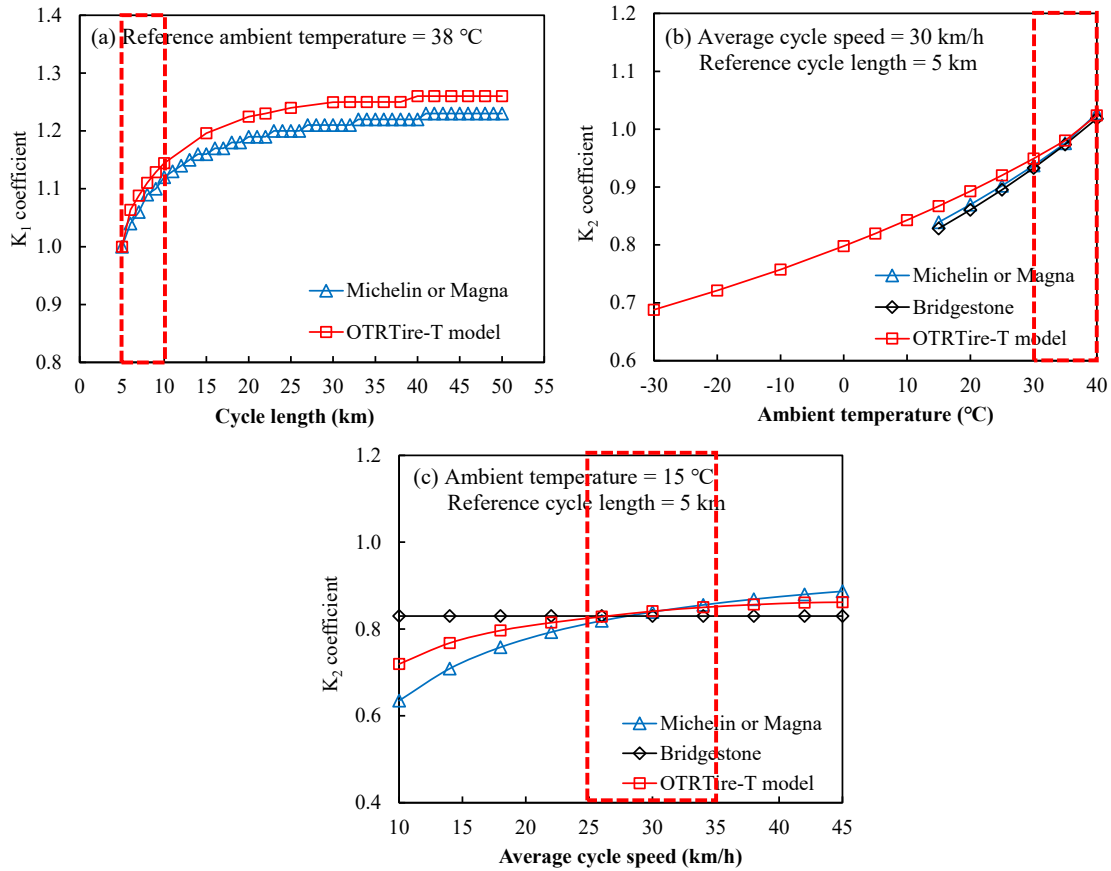
Figure 6.4. Comparisons of the $K_1$ and $K_2$ coefficients: (a) the $K_1$ coefficients at cycle lengths ranging from 5 to 50 km; (b) the $K_2$ coefficients at increasing ambient temperatures from -30 to 40 °C; (c) the $K_2$ coefficients with a rise of average cycle speeds from 10 to 45 km/h.

In Figure 6.4, the $K_1$ and $K_2$ coefficients derived from the OTRTire-T model have similar values with many of the coefficients provided by the tire manufacturers Michelin, Magna, and Bridgestone. These similar values occur at cycle lengths ranging from 5 to 10 km, ambient temperatures from 30 to 40 °C, and average cycle speeds of 25 to 35 km/h (highlighted with the red boxes). For instance, at the cycle lengths ranging from 5 to 10 km (the most common cycle lengths at mine sites (Meech and Parreira, 2013)), the $K_1$ coefficient derived from the OTRTire-T model increased from 1.00 to 1.14; these values were consistent with the ones (1.00 to 1.12) in the

Michelin $K_1$ coefficients, with a deviation of only 2.1%. In addition, when the ambient temperature rose from 30 to 40 °C and the average cycle speed increased from 25 to 35 km/h, the OTRTire-T model-based $K_2$ coefficients matched well with the Michelin (or Magna) $K_2$ coefficients and the Bridgestone $K_2$ coefficients, showing a deviation in values with an average mean absolute percentage error (MAPE) of 0.7% and 1.1%, respectively. Based on this, the $K_1$ and $K_2$ coefficients derived from the OTRTire-T model were considered to be cross-verified by the existing coefficients at cycle lengths ranging from 5 to 10 km, ambient temperatures from 30 to 40 °C, and average cycle speeds of 25 to 35 km/h. Beyond these operating conditions, the $K_1$ and $K_2$ coefficients at cycle lengths ranging from 10 to 50 km, ambient temperatures from -30 to 30 °C, and average cycle speeds of 10~25 km/h and of 35~45 km/h are not well understood. They are further discussed below based on the results from the OTRTire-T model.

### 6.3.2. Real site TKPHs at different ambient temperatures

Figure 6.5 shows the variations of the real site TKPHs at different ambient temperatures ranging from -30 to 40 °C, a cycle length of 5 km, and a $Q_m \times V_m$ of 3154 tonne×km/h. The average cycle speed ($V_m$) is the average speed of the OTR tire within one complete cycle of a hauling trip and a return trip. The average vertical tire load $Q_m$ refers to the load vertically applied to one OTR tire on average within this cycle; it reaches about 83 tonnes when the truck is under the fully loaded condition (i.e., a payload of 363 tonnes (Ma et al., 2022d)) during the hauling trip.
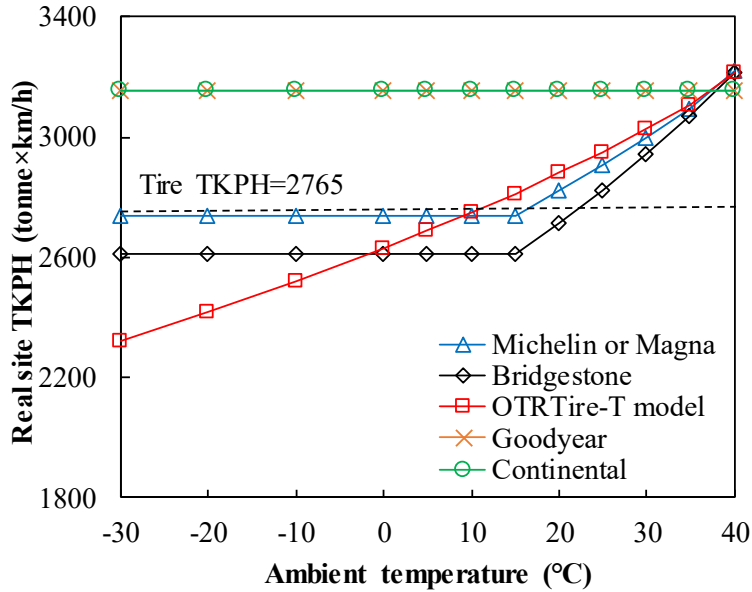
Figure 6.5. Variations of the real site TKPHs at different ambient temperatures ranging from -30 to 40 °C, a cycle length of 5 km, and a $Q_m \times V_m$ of 3154 tonne×km/h

In Figure 6.5, the Goodyear TKPH (TKPH$_G$) and Continental TKPH (TKPH$_C$) did not vary with ambient temperatures, showing two overlapping flat lines (green and yellow) at 3154 tonne×km/h. This indicates that the TKPH$_G$ and TKPH$_C$ did not take the effects of ambient temperatures into consideration. In other words, it indicates that the TKPH$_G$ and TKPH$_C$ neglected the significant role of ambient temperatures on real site TKPHs. This is opposed to site observations. At mine sites, when the ambient temperature rose from 20 to 40 °C, the maximum rubber temperature in a Bridgestone 24.00R35 OTR tire increased from 54.1 to 69.1 °C (Li et al., 2012), leading to a rise in the real site TKPH by 10.8%. This issue also existed in the Michelin or Magna TKPH (TKPH$_M$), and Bridgestone TKPH (TKPH$_B$) when the ambient temperature ranged from -30 to 15 °C. In Figure 6.5, when the ambient temperature increased from 15 to 40 °C, the TKPH$_M$, TKPH$_B$, and the real site TKPH derived from the OTRTire-T model (TKPH$_T$) increased

177

with a rise in ambient temperatures. For instance, at rising ambient temperatures from 15 to 40 °C, the $TKPH_T$ increased from 2813 to 3213 tonne×km/h, and the $TKPH_M$ and $TKPH_B$ went up by 483 and 599 tonne×km/h, respectively. These increasing real site TKPHs were related to the elevation in OTR tire temperature (SAE, 2012). As per site observation (Alberta Agriculture and Forestry, 2018; Ta, 2018), the tire temperature increased with a rise in ambient temperatures. For example, at an average cycle speed of 25.6 km/h and an average vertical tire load of 83 tonnes, the maximum temperature inside a Michelin 56/80R63 OTR tire increased from 34 to 68 °C as the ambient temperature rose from -29.0 to 6.2 °C (Ta, 2018).

In Figure 6.5, compared with other existing TKPHs, the $TKPH_T$ was the only one that was able to identify the variations of real site TKPHs when the ambient temperature ranged from -30 to 15 °C and give new insights into OTR tire management at these low ambient temperatures. This is important because low ambient temperatures from -30 to 15 °C are common at local mine sites in Alberta (Alberta Agriculture and Forestry, 2018). For instance, at an ambient temperature of 5 °C, the $TKPH_T$ was 2687 tonne×km/h. This $TKPH_T$ was lower than the tire TKPH (2765 tonne×km/h), thus the tire was not suffering from overheating. However, when the $TKPH_T$ was lower than the tire TKPH, the working capacity of the OTR tire was not fully utilized (Kravchenko and Sakno, 2011; Xu et al., 2022). In other words, the tire was recommended to be used at a larger $Q_m \times V_m$ (i.e., 3245 tonne×km/h derived from the back calculation as per Equation (6.1)). At the $Q_m$ $\times V_m$ of 3245 tonne×km/h, when the $V_m$ was 38 km/h, the $Q_m$ was calculated as 85.4 tonnes. This indicates that the truck may be overloaded by 8.2% (i.e., leading to a recommended payload of 393 tonnes) during the hauling trip. Some similar insights can also be given into OTR tire management at other low ambient temperatures below 15 °C. At these low ambient temperatures,

the TKPH$_T$ recommended the truck to be overloaded (compared with its rating payload of 363 tonnes) at mine sites. For example, when the ambient temperature was 0 °C, the $Q_m$ was calculated as 87.3 tonnes, which indicates that the truck may carry an extra 53 tonnes of materials beyond its rating payload (363 tonnes). As the ambient temperature decreased to -5 °C, the $Q_m$ was 89 tonnes. This $Q_m$ (89 tonnes) indicates that the truck can be considered to be overloaded by 20.1% (i.e., having a recommended payload of 436 tonnes) during the haulage operations.

As per Figure 6.5, it is noted that when the ambient temperature decreased to extreme lows such as -30 °C, it was calculated that the $Q_m$ reached about 98.8 tonnes, corresponding to a truck payload of up to 554 tonnes during the hauling trip. However, the payload of 554 tonnes has not been found in practical operating conditions at mine sites. As per mine site data (Ta, 2018), the maximum truck payload rarely exceeded 456 tonnes. Thus, it is important for mining engineers to be cautious in using the payload of 554 tonnes because there may be other restrictions for the truck payload, such as the loading capacity of the OTR tire and the truck loading frame (Caterpillar, 2018).

### 6.3.3. Relationship between the real site TKPHs and average cycle speeds

Figure 6.6 shows the relationship between the real site TKPHs and average cycle speeds at an average vertical tire load ($Q_m$) of 83 tonnes and a cycle length of 5 km. The average cycle speed can be calculated as a ratio of cycle length to the total traveling hours within one cycle of haulage operation (hauling and return) (Krzyzanowska, 2007; Thompson et al., 2019). At mine sites, the average cycle speeds usually range from 10 to 45 km/h (Ma et al., 2022d).
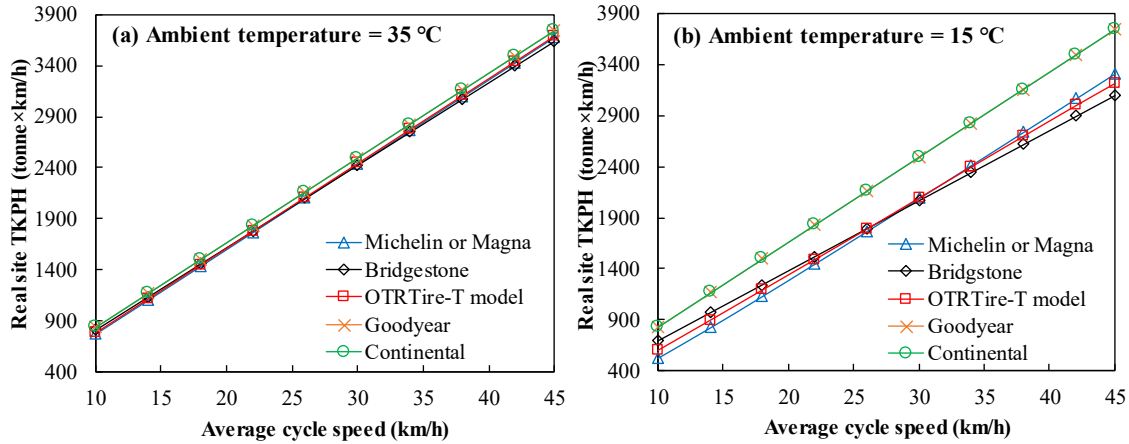
Figure 6.6. Relationship between the real site TKPHs and average cycle speeds at a $Q_m$ of 83 tonnes and a cycle length of 5 km when the ambient temperature is (a) 35 ℃; (b) 15 ℃

Figure 6.6(a) shows the correlation of the real site TKPHs with average cycle speeds at an ambient temperature of 35 ℃. Note that 35 ℃ is the highest ambient temperature at Alberta's mine sites in the past 10 years (Alberta Agriculture and Forestry, 2018). In Figure 6.6(a), the TKPHT increased at rising average cycle speeds ($V_m$). For instance, the TKPHT grew from 783 to 3686 tonne×km/h when the $V_m$ was raised from 10 to 45 km/h. These $TKPH_T$ matched well with the $TKPH_M$, $TKPH_B$, $TKPH_G$, and $TKPH_C$, showing a deviation in values with an average MAPE of only 1.8%.

Figure 6.6(b) presents the results of the real site TKPHs when the ambient temperature was 15 ℃; all of them increased with a rise in the average cycle speeds ($V_m$). For example, at the $V_m$ rising from 10 to 45 km/h, the $TKPH_T$ went up from 597 to 3219 tonne×km/h; there was a growth in the $TKPH_M$ from 527 to 3312 tonne×km/h and an increase in the $TKPH_B$ of 2411 tonne×km/h. However, unlike at 35 ℃, the deviations among the $TKPH_T$, $TKPH_M$, and $TKPH_B$ at 15 ℃ were

180

relatively large. For instance, the TKPHT deviated from the $TKPH_M$ with a maximum MAPE of up to 11.7%; there was still a deviation between the $TKPH_T$ and $TKPH_B$ with an average MAPE of 4.4%. These deviations were mainly derived from the differences in the values of the $K_2$ coefficients (i.e., OTRTire-T model-based $K_2$ coefficients, Michelin or Magna $K_2$ coefficients, and Bridgestone K2 coefficients) at the $V_m$ in the ranges of 10~25 km/h and 35~45 km/h. In Figure 6.4(c), when the $V_m$ ranged from 10 to 25 km/h or from 35 to 45 km/h, the three sets of the $K_2$ coefficients deviated from each other significantly with an average MAPE of 6.3%. These coefficients can result in deviations in the $TKPH_T$, $TKPH_M$, and $TKPH_B$ when the coefficients are used to calculate the $TKPH_T$, $TKPH_M$, and $TKPH_B$ as per Equation (6.1).

In addition to $TKPH_M$ and $TKPH_B$, the $TKPH_T$ showed differences in values with $TKPH_G$ and $TKPH_C$. For instance, the $TKPH_G$ (or $TKPH_C$) was greater than $TKPH_T$ by 338 tonne×km/h at the $V_m$ of 22 km/h and by 423 tonne×km/h at the $V_m$ of 34 km/h. There were differences because the $K_2$ coefficients were not included in the $TKPH_G$ and $TKPH_C$. Without these coefficients, the effects of average cycle speeds cannot be considered in the $TKPH_G$ and $TKPH_C$, resulting in overestimations in their values at rising average cycle speeds ($V_m$). In Figure 6.6(b), compared with the $TKPH_T$, $TKPH_M$, and $TKPH_B$ that included the $K_2$ coefficients, the $TKPH_G$ (or $TKPH_C$) overestimated its value by 342 tonne×km/h on average at the $V_m$ of 22 km/h; the overestimations increased and rose to 437 and 525 tonne×km/h, respectively, as the $V_m$ was further raised to 34 and 45 km/h.

## 6.3.4. Effects of cycle lengths on the real site TKPHs

The effects of cycle lengths on the real site TKPHs are critical to haulage management because cycle length increases with time when mine working faces are extended during the mine's life. At mine sites, the cycle length can be as short as 5 km; it can also be increased to long distances, reaching up to 50 km when mine working faces are extended (Meech and Parreira, 2013; Parreira, 2013). Figure 6.7 shows the results of real site TKPHs at an average vertical tire load ($Q_m$) of 83 tonnes, an average cycle speed ($V_m$) of 30 km/h, an ambient temperature of 38 °C, and increasing cycle lengths from 5 to 50 km.
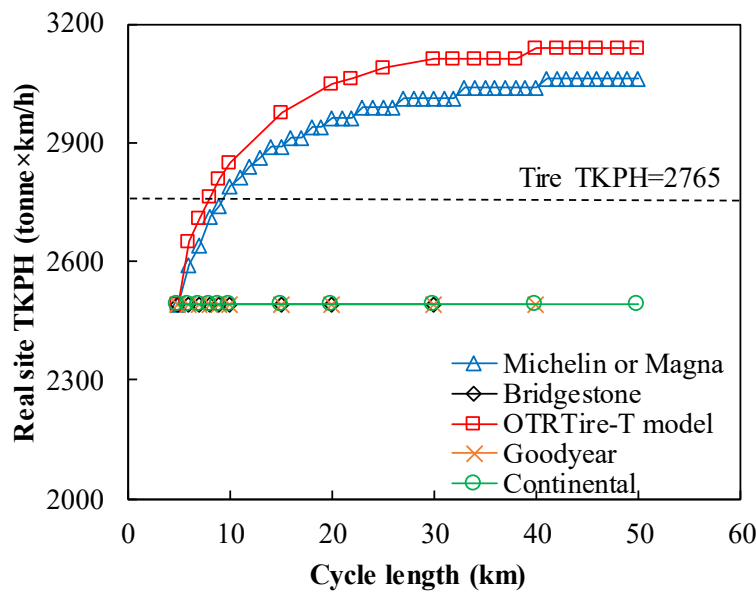


Figure 6.7. Real site TKPHs at a $Q_m$ of 83 tonnes, a $V_m$ of 30 km/h, an ambient temperature of 38 °C, and increasing cycle lengths from 5 to 50 km

In Figure 6.7, the TKPH$_T$ increased logarithmically at rising cycle lengths. This indicates that the TKPH$_T$ increased relatively rapidly when the cycle lengths were short but rose slowly, or

even leveled off, with a further increase in cycle lengths. For instance, as the cycle length was raised from 5 to 20 km, the $TKPH_T$ grew from 2490 to 3049 tonne×km/h; however, when the cycle length was further raised from 20 to 40 km, there was a relatively slow growth in the $TKPH_T$, from 3049 to 3137 tonne×km/h. At cycle lengths rising from 40 to 50 km, the $TKPH_T$ leveled off at 3137 tonne×km/h. The increase of the $TKPH_T$ was in accordance with the increase in the $TKPH_M$. The $TKPH_M$ grew with a rise in cycle lengths in a similar logarithmic manner. For example, the $TKPH_M$ increased steeply from 2490 to 2963 tonne×km/h at rising cycle lengths from 5 to 20 km, but it grew only slightly from 2963 to 3063 tonne×km/h when the cycle length varied from 20 to 50 km. In comparison to $TKPH_T$ and $TKPH_M$, the $TKPH_B$, $TKPH_G$, and $TKPH_C$ showed as flat lines at rising cycle lengths, which indicates that the effects of cycle lengths were not reflected in the $TKPH_B$, $TKPH_G$, and $TKPH_C$.

In Figure 6.7, when the cycle length was raised from 5 to 20 km, the $TKPH_T$ and $TKPH_M$ increased steeply since the effects of long cycle lengths (i.e., 5~20 km) on OTR tire temperatures were significant. The tire temperatures were affected significantly because heat generation and heat build-up occurred within the tire rubbers as the cycle length increased up to 20 km (Le Saux et al., 2010; Li et al., 2016; Ma et al., 2022c). For instance, at a vertical tire load of 104 tonnes and a truck speed of 30 km/h, as the cycle length increased to 20 km, there was a total of 1080 MW/m$^3$ of heat generated within a one-unit volume of tread rubbers in a Michelin 56/80R63 OTR tire (Ma et al., 2022c). The heat was then trapped in tire rubbers, which led to a heat build-up in the OTR tire (Ghoreishy et al., 2013; Ma et al., 2022b). In Figure 6.7, when the cycle length further increased to extreme long distance exceeding 20 km, the growth of $TKPH_T$ and $TKPH_M$ slowed down. This may be related to the high temperatures within the OTR tire. OTR tire temperature can increase at rising cycle lengths due to the heat build-up (Ghoreishy et al., 2013; Ma et al., 2022b;

Marais, 2017; Marais and Venter, 2018). High tire temperatures of even up to 95 °C have been found before at mine sites (Kerr, 2017). At high tire temperatures, the heat within the tire was lost to the ambient environment more dramatically due to larger temperature differences (Li et al., 2012). This heat loss retarded the further growth in tire temperatures (Jayme and Al-Qadi, 2021) and, as a result, mitigated the rise in the $TKPH_T$ and $TKPH_M$.

As shown in Figure 6.7, there were similar plateaus in the variations of both $TKPH_T$ and $TKPH_M$—the $TKPH_T$ and $TKPH_M$ did not vary with rising cycle lengths. For example, the $TKPH_T$ plateaued at 3112 tonne×km/h when the cycle length was longer than 30 km; the $TKPH_M$ leveled off at 2988 tonne×km/h as the cycle length exceeded 23 km. These plateaus were related to the tire temperatures that stabilized at rising cycle lengths when an equilibrium was reached between the heat generation and heat loss within the OTR tire. Stabilized OTR tire temperatures were common during long-distance haulage operations as per previous studies (Meech and Parreira, 2013; Parreira, 2013). For example, at an average vertical tire load of 48 tonnes and an average cycle speed of 16 km/h, the internal air temperature in a Bridgestone 40.00R57 OTR tire became stable (~81.0 °C) when the cycle length was longer than 18 km (Meech and Parreira, 2013).

Despite the similarities, the plateau in the $TKPH_T$ appeared later than that in the $TKPH_M$. For instance, the $TKPH_M$ started to plateau when the cycle length was 23 km; however, the $TKPH_T$ did not level off until the cycle length reached 30 km. In Figure 6.7, as the cycle length rose from 23 to 30 km, the $TKPH_T$ continued to increase from 3063 to 3112 tonne×km/h. This increment in the $TKPH_T$ is not negligible in mine transport. Based on the back calculation as per Equation (6.1), when the real site TKPH increased from 3063 to 3112 tonne×km/h, the $Q_m$ reduced from 78.5 to 76.3 tonnes at a $V_m$ of 30 km/h and an ambient temperature of 38 °C. This indicates that the truck

payload was recommended to decrease by 13 tonnes when the cycle length was extended from 23 to 30 km.

## 6.4. Conclusion

This study investigated the effects of site operating conditions on the real site TKPH (tonne-kilometer-per-hour) of ultra-large off-the-road (OTR) tires. The main conclusions are enumerated as follows:

1. The cycle length coefficient $K_1$ and the site ambient temperature coefficient $K_2$ derived from the OTR tire thermal (OTRTire-T) model have been cross-verified by the existing coefficients from different OTR tire manufacturers (i.e., Michelin, Magna, and Bridgestone). Their values matched each other with a maximum mean absolute percentage error (MAPE) of only 2.1% at cycle lengths ranging from 5 to 10 km, ambient temperatures from 30 to 40 °C, and average cycle speeds of 25 to 30 km/h.

2. The real site TKPH increased with a rise in ambient temperatures and average cycle speeds. For instance, the real site TKPH increased from 2813 to 3213 tonne×km/h when the ambient temperature rose from 15 to 40 °C; it also grew from 783 to 3686 tonne×km/h at rising average cycle speeds from 10 to 45 km/h.

3. At low ambient temperatures of below 15 °C, as per the real site TKPH with refined K1 and K2 coefficients, the loading capacity of the truck increased (compared with its rating payload of 363 tonnes) at mine sites. For example, at an ambient temperature of -5 °C and an average cycle speed of 38 km/h, the average vertical tire load was 89 tonnes, which indicates that the truck payload can be considered to be increased by 20.1% (i.e., having a

recommended payload of 436 tonnes) during the haulage operations.

4. The real site TKPH increased relatively rapidly when the cycle lengths were short but rose slowly, or even leveled off, with a further increase in cycle lengths. For instance, as the cycle length was raised from 5 to 20 km, the real site TKPH grew from 2490 to 3049 tonne×km/h; however, when the cycle length was further raised from 20 to 40 km., there was a relatively slow growth in the real site TKPH, from 3049 to 3137 tonne×km/h. When cycle lengths rose from 40 to 50 km, the real site TKPH leveled off at 3137 tonne×km/h.

5. At an ambient temperature of 38 °C and an average cycle speed of 30 km/h, the real site TKPH increased from 2849 to 3049 tonne×km/h at rising cycle lengths from 10 to 20 km. Due to this increment in the real site TKPH, the truck payload was recommended to decrease by 31.8 tonnes when the cycle length was extended from 10 to 20 km.

## Appendix 6A. Procedures for finding the $K_1$ and $K_2$ coefficients

According to the results from the OTRTire-T model, the curves showing the relationship between the air temperatures inside the tire and the product of the average vertical tire load ($Q_m$; in tonnes) and the average cycle speed ($V_m$; in km/h) were derived. The internal air temperature was the focus because it is the one that can be monitored by temperature sensors in OTR tires at real mine sites. Figure 6A.1 shows the relation curve at a reference cycle length of 5 km and a reference ambient temperature of 38 °C.
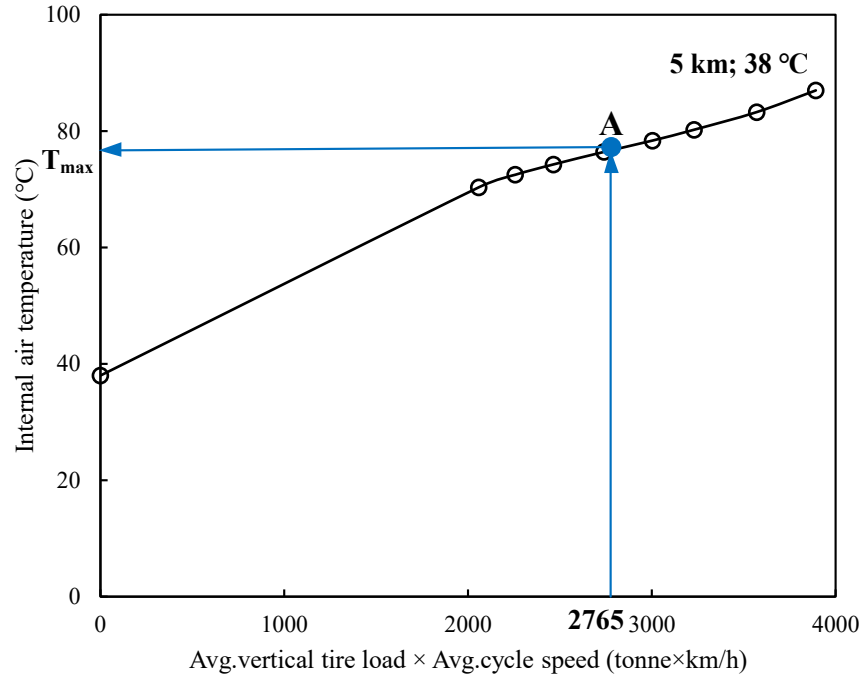
Figure 6A.1. Relation curve between the internal air temperature and the $Q_m \times V_m$ at a reference cycle length of 5 km and a reference ambient temperature of 38 °C

As per the Michelin Technical Data Book (Michelin, 2016), when the cycle length is 5 km and the ambient temperature is 38 °C, there is a $K_1 = K_2 = 1$ in the real site TKPH. Then Equation (6.1) can be simplified as in Equation (6A.1).

$$\text{Tire TKPH} \geq \text{Real site TKPH} = Q_m \times V_m \times 1 \times 1 \tag{6A.1}$$

Based on Equation (6A.1) and Figure 6A.1, when the real site TKPH is selected as a value that is equal to the tire TKPH (2765 tonne×km/h (Michelin, 2016)), the maximum recommended air temperature $T_{max}$ (75.7 °C) can be found within the OTR tire via Point A on the curve. Herein,

the air temperature refers to the temperature of the air inflated in the tire at a location close to the inner layer of the lower sidewall (the same location as the MEMS temperature sensors).

## 6A.1. The $K_1$ coefficient

At the ambient temperature of 38 °C, when the cycle length increased, the relation curve varied. By evaluating the variations of the curves at increasing cycle lengths, the $K_1$ coefficient in the real site TKPH was found. An example of finding the $K_1$ coefficient at a cycle length of 10 km is shown in Figure 6A.2.
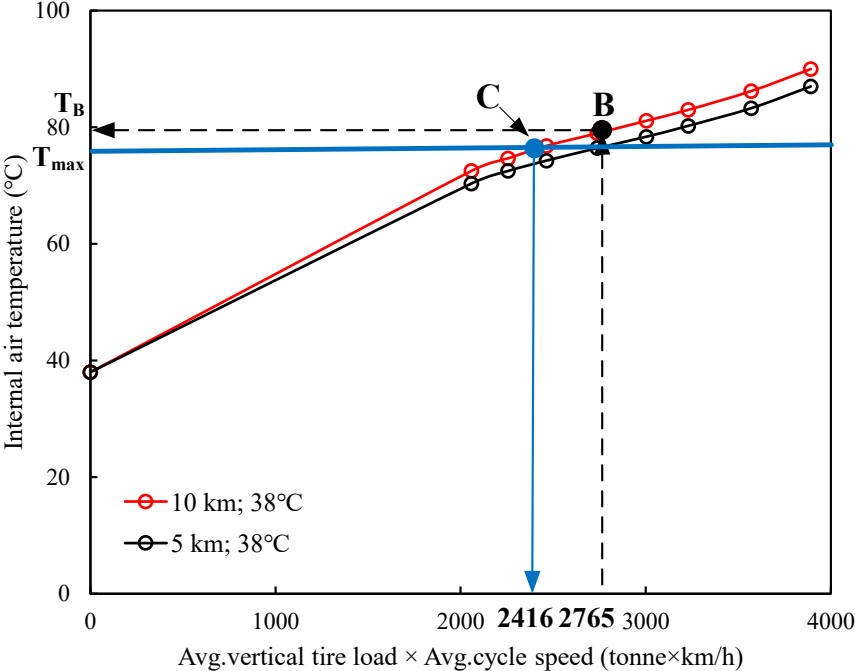


Figure 6A.2. An example of finding the $K_1$ coefficient at a cycle length of 10 km

As per the results from the OTRTire-T model, when the cycle length is 10 km, the relationship between the internal air temperature and the $Q_m \times V_m$ was derived and represented as the red curve in Figure 6A.2. Based on this curve, an air temperature $T_B$ (79.8 °C) is found inside

the tire corresponding to the real site TKPH of 2765 tonne×km/h (also the tire TKPH) via Point B. However, this air temperature is at a value greater than the maximum recommended air temperature ($T_B > T_{max}$), which leads to overheating in the tire (Behnke and Kaliske, 2018; Dubinkin et al., 2020). To reduce the air temperature and avoid tire overheating, the $T_{max}$ (75.7 °C) is used to find the value of $Q_m \times V_m$ (2416 tonne×km/h) via Point C on the red curve. Then the ratio of the real site TKPH (2765 tonne×km/h) to this $Q_m \times V_m$ (2416 tonne×km/h) is used to find the K₁ coefficient as per Equation (6A.2), which is equal to 1.144.

$$\text{Tire TKPH} \geq \text{Real site TKPH} = Q_m \times V_m \times K_1 \times 1 \qquad (6A.2)$$

where $K_1 \neq 1$ when the cycle length is 10 km; $K_2 = 1$ at the ambient temperature of 38 °C.

The above procedures can also be used to find other K₁ coefficients when the cycle length varies. This cycle length can increase from 5 to 50 km at mine sites (Michelin, 2016; Parreira, 2013).

## 6A.2. The K₂ coefficient

When the cycle length was kept at 5 km, the relation curve (showing the relationship between the internal air temperature and the $Q_m \times V_m$) varied with ambient temperatures. As the ambient temperature increased or decreased, the variations of the curves were investigated to find the K₂ coefficient in the real site TKPH. Two examples of finding the K₂ coefficients at the ambient temperatures of 40 and 35 °C are shown in Figure 6A.3.
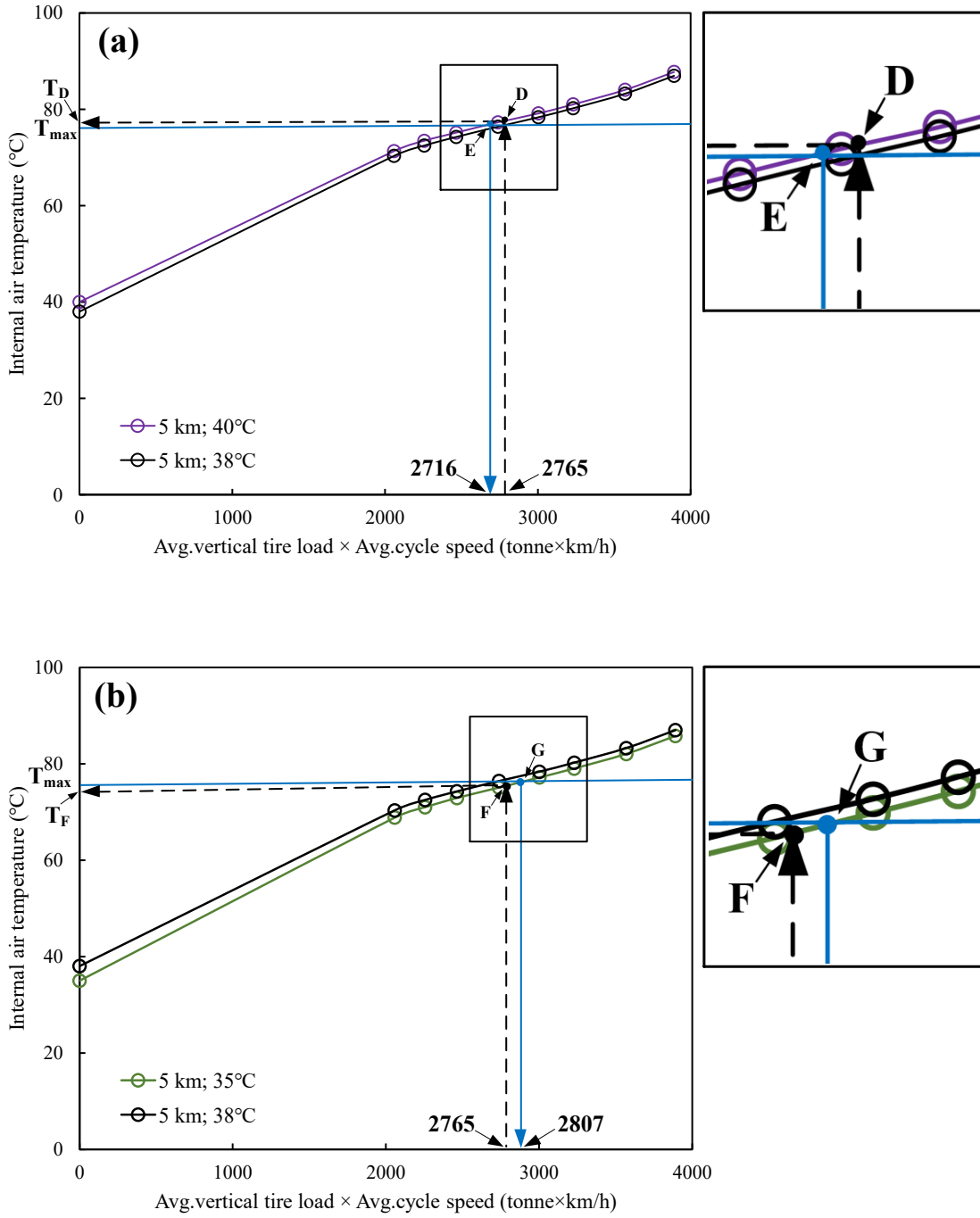
Figure 6A.3. Two examples of finding the $K_2$ coefficients at ambient temperatures of (a) 40 °C; (b) 35 °C

From the OTRTire-T model, at the cycle length of 5 km, when the ambient temperature increases up to 40 °C, the relationship between the internal air temperature and the $Q_m \times V_m$ was derived and represented as the purple curve in Figure 6A.3(a). Based on this curve, an internal air temperature $T_D$ (76.6 °C) is found corresponding to the real site TKPH of 2765 tonne×km/h (also the tire TKPH) via Point D. This air temperature is greater than the $T_{max}$ (75.7 °C) and the tire suffers from overheating. Thus, like the procedure for finding the $K_1$ coefficients, the value of $Q_m$ $\times V_m$ is found as 2716 tonne×km/h via Point E on the purple curve. This $Q_m \times V_m$ ensures that the internal air temperature does not exceed the maximum recommended air temperature $T_{max}$, and subsequently avoids overheating in the tire. Then the ratio of the real site TKPH (2765 tonne×km/h) to this $Q_m \times V_m$ (2716 tonne×km/h) is used to find the $K_2$ coefficient as per Equation (6A.3), which is equal to 1.018.

$$\text{Tire TKPH} \geq \text{Real site TKPH} = Q_m \times V_m \times 1 \times K_2 \tag{6A.3}$$

where $K_1 = 1$ at the cycle length of 5 km; $K_2 \neq 1$ when the ambient temperature increases or decreases from 38 °C.

When the ambient temperature decreased to 35 °C, Figure 6A.3(b) shows the relationship between the internal air temperature and the $Q_m \times V_m$ using the green curve. Based on this curve, an air temperature $T_F$ (73.5 °C) is found inside the tire corresponding to the real site TKPH of 2765 tonne×km/h (also tire TKPH) via Point F. This air temperature is below the maximum recommended air temperature $T_{max}$ (75.7 °C), and thus the tire is not suffering from overheating.

However, $T_F < T_{max}$ indicates that the working capacity of the tire is not fully utilized (Kravchenko and Sakno, 2011; Xu et al., 2022). In other words, the tire can be used under a larger vertical tire load or a higher cycle speed—a larger $Q_m \times V_m$ is recommended. This $Q_m \times V_m$ is found via the Point G on the green curve. Then the ratio of the real site TKPH (2765 tonne×km/h) to this $Q_m \times V_m$ (2807 tonne×km/h) is used to find the $K_2$ coefficient according to Equation (6A.3).

The method shown in Appendix 6A.2 can also be used to find other $K_2$ coefficients when the ambient temperature increases or decreases from 38 °C. The ambient temperatures range from -30 to 40 °C at local mine sites in Alberta (Alberta Agriculture and Forestry, 2018; Li et al., 2012).

# Chapter 7. Conclusion and future work

## 7.1. Conclusions

Overall, this thesis refined the real site TKPH (tonne-kilometer-per-hour) of ultra-large off-the-road (OTR) tires by investigating the hysteresis loss, heat generation, and tire temperatures under operating conditions at mine sites. The main concluding remarks of this thesis are enumerated as follows:

1. The hysteresis loss of OTR tire rubbers was affected by strain levels and strain rates. For instance, a large strain level (e.g., 100%) increased the hysteresis loss considerably. Rubber hysteresis loss increased with a rise in strain rates, and the increasing rates became greater at larger strain levels (e.g., 100%).

2. A rise of rubber temperatures caused a decrease in hysteresis loss; however, the decrease became less significant when the rubber temperatures were above 10 °C. For example, at 500% s$^{-1}$ and the 100% strain level, the hysteresis loss reduced by approximately 15% as the rubber temperature was raised from -30 to 10 °C, yet it decreased by only 8% in total with further increases in rubber temperatures from 10 to 100 °C.

3. The HLSRT model (a Hysteresis Loss model considering Strain levels, strain Rates, and rubber Temperatures) can predict the hysteresis loss of OTR tire rubbers with average and maximum mean absolute percent errors (MAPEs) of 11.2% and 18.6%, respectively, at strain levels ranging from 10% to 100%, strain rates from 10% to 500% s$^{-1}$, and rubber temperatures from -30 to 100 °C. These MAPEs were relatively low when compared with previous studies, showing that the HLSRT model has higher prediction accuracy.

4. The HLSRT model characterized the exponential increase of hysteresis loss at rising strain levels and identified the linear growth of hysteresis loss as the strain rate increased. The

193

HLSRT model also predicted the inverse proportional variation of hysteresis loss with rubber temperatures that was consistent with the laboratory recording. The predicted hysteresis loss reduced sharply at the beginning of the rubber temperature rise (e.g., -30 ~ 10 °C), but the hysteresis loss decreased slightly as the rubber temperature further increased (e.g., 10 ~ 100 °C).

5. The temperatures of OTR tires were affected by vertical tire load (having the conversion from payload) and truck speeds. For instance, a large vertical tire load (e.g., 1.04 MN) increased the tire temperatures considerably. At 30 km/h and 20 °C, when the vertical tire load increased from 0.34 to 1.04 MN, the rubber temperature in the tread region of the tire increased from 54.4 to 82.2 °C. In addition, the tire temperature increased with a rise in truck speeds, and the increase became more significant at larger vertical loads (e.g., 1.04 MN). At 20 °C and a vertical tire load of 1.04 MN, the maximum rubber temperature in the tire tread region increased from 29.5 to 82.2 °C with a rise in truck speeds from 5 to 30 km/h.

6. The OTR tire thermal (OTRTire-T) model identified an inverse proportional relationship between the rubber temperature increments in OTR tires and the ambient temperatures from -30 to 40 °C. This indicates that the rubber temperature increment reduced relatively sharply at low ambient temperatures from -30 to 0 °C but decreased slightly as the ambient temperature increased above 0 °C. Despite the decreasing trend in rubber temperature increments, the rubber temperature in the OTR tire increased relatively rapidly with a rise of ambient temperatures. For example, at a vertical tire load of 1.04 MN and a truck speed of 30 km/h. the maximum rubber temperature in the sidewall region grew from 19.2 to 82.7 °C at increasing ambient temperatures from -30 to 40 °C.

7. As per the results from the OTRTire-T model, the cycle length coefficient $K_1$ and the site ambient temperature coefficient $K_2$ were refined. These refined coefficients matched the existing coefficients from other OTR tire manufacturers (i.e., Michelin, Magna, and Bridgestone) with a maximum MAPE of only 2.1% at cycle lengths ranging from 5 to 10 km, ambient temperatures from 30 to 40 °C, and average cycle speeds of 25 to 30 km/h.

8. The real site TKPH increased relatively rapidly when the cycle lengths were short but went up slowly or even leveled off with a further increase in cycle lengths. For instance, as the cycle length was raised from 5 to 20 km, the real site TKPH grew from 2490 to 3049 tonne×km/h; however, when the cycle length was further raised from 20 to 40 km., there was a relatively slow growth in the real site TKPH, from 3049 to 3137 tonne×km/h. At cycle lengths rising from 40 to 50 km, the real site TKPH leveled off at 3137 tonne×km/h.

9. As per the refined cycle length coefficient $K_1$, at an ambient temperature of 38 °C and an average cycle speed of 30 km/h, the real site TKPH increased from 2849 to 3049 tonne×km/h at rising cycle lengths from 10 to 20 km. Due to this increment in the real site TKPH, the truck payload was recommended to decrease by 31.8 tonnes when the cycle length was extended from 10 to 20 km.

10. At cold ambient temperatures of below 0 °C, as per the real site TKPH with refined site ambient temperature coefficient $K_2$, the loading capacity of the truck increased (compared with its rating payload of 363 tonnes) at mine sites. For example, at an ambient temperature of -5 °C and an average cycle speed of 38 km/h, the average vertical tire load was 89 tonnes, which indicates that the truck payload can be considered to be increased by 20.1% (i.e., having a recommended payload of 436 tonnes) during the haulage operations.

## 7.2. Key contributions

The findings from this thesis are significant for academia and industry. The key contributions of this thesis are listed as follows:

1. Novelly, hysteresis loss of OTR tire rubbers was investigated under a dynamic and broad range of testing conditions (i.e., strain levels, strain rates, and rubber temperatures). These testing conditions were converted from real operating conditions (i.e., payloads, truck speeds, and ambient temperatures) at mine sites. This can help to estimate the heat generation of tire rubbers during daily haulage operations.

2. A novel phenomenological model was developed—the HLSRT model. This HLSRT model can provide a new approach to predicting the hysteresis loss of OTR tire rubbers based on operating conditions at mine sites.

3. Innovatively, this research developed a mathematical equation for determining the internal heat generation rates in OTR tire rubbers. This equation was originally generated based on a modified Mooney-Rivlin (MR) strain energy function, the pseudo-elasticity theory, and the inverse analysis method.

4. The OTRTire-T model is the first one in the literature that can predict both surface and internal temperatures of OTR tires under different site operating conditions, especially at long cycle lengths (e.g., > 10 km) and at cold ambient temperatures (e.g., < 0 °C).

5. The research leads to the novelty that the cycle length coefficient $K_1$ and site ambient temperature coefficient $K_2$ in real site TKPHs were refined at long cycle lengths (e.g., > 10 km) and at cold ambient temperatures (e.g., < 0 °C). The refined coefficients innovate the TKPH system and provide guidance to current mining operations and future mine planning.

## 7.3. Limitations and future work

Although this thesis has refined the real site TKPH of ultra-large OTR tires at mine sites, there are still some limitations in this thesis. Further work is needed in the future.

1. OTR tire temperatures are affected by operating conditions at mine sites. The site operating conditions are very complex, not only including payloads, cycle speeds, cycle lengths, and ambient temperatures as indicated in the TKPH method. In other words, more operating conditions (e.g., precipitation and snow, and haul road surface conditions) should be taken into consideration. In the future, the effects of these conditions will be included into research when investigating OTR tire temperatures at mine sites.

2. The OTRTire-T model was developed with some limitations. For example, the model was developed using the one-way coupling method, and during tire rolling, the effects of temperature rise on tire stresses and strains were not considered. In addition, the model did not consider the compressibility of the air inside the tire and the heat generation in the air. All of these will be improved in future research.

3. When refining real site TKPHs, the bulk material handling operations did not consider the loading/dumping time and loading dynamics (loading impacts). The loading/dumping time and loading dynamics may lead to variations in tire temperatures within a cycle of handling operation, affecting the accuracy of the refined TKPHs. In the future, the material loading/dumping time and loading dynamics will be included into the handling operations at mine sites.

4. This research was conducted based on real rubber samples cut from used OTR tire. These rubber samples may have some aging issues that may affect their properties. In the future, research will be considered to be conducted based on new OTR tire rubbers.

# Bibliography

Alberta Agriculture and Forestry, 2018. Current and Historical Alberta Weather Station Data Viewer [WWW Document]. URL https://acis.alberta.ca/weather-data-viewer.jsp (accessed 12.16.22).

Allouis, C., Farroni, F., Sakhnevych, A., Timpone, F., 2016. Tire thermal characterization: test procedure and model parameters evaluation, in: Proceedings of the World Congress on Engineering.

Amin, A., Lion, A., Sekita, S., Okui, Y., 2006. Nonlinear dependence of viscosity in modeling the rate-dependent response of natural and high damping rubbers in compression and shear: Experimental identification and numerical verification. Int. J. Plast. 22, 1610–1657.

Anzabi, R.V., 2015. Haul Truck Tire Reliability and Condition Monitoring. PhD Thesis, University of Alberta, Canada.

Anzabi, R.V., Nobes, D.S., Lipsett, M.G., 2012. Haul truck tire dynamics due to tire condition, in: Journal of Physics: Conference Series. London: Institute of Physics, Huddersfield, United Kingdom, 18 - 20 June 2012, p. 12005.

ASTM D412-16: 2016, 2016. Standard test methods for vulcanized rubber and thermoplastic elastomers – Tension. https://doi.org/10.1520/D0412-16

ASTM D6370-99: 2019, n.d. Standard test method for rubber – Compositional analysis by thermogravimetric (TGA).

Azuma, K., Naito, M., Tomita, Y., 2007. Strain rate dependent constitutive equation of rubber and simulation of deformation behavior of carbon-black-filled rubber. Nippon Kikai Gakkai Ronbunshu A Hen(Transactions Japan Soc. Mech. Eng. Part A)(Japan) 19, 558–566.

Baker, C.R., Cohanier, B., Gibassier, D., 2018. Environmental Management Controls at Michelin– how do they link to sustainability? Soc. Environ. Account. J. 38, 75–96.

Banić, M.S., Stamenković, D.S., Miltenović, V., Milošević, M.S., Miltenović, A. V, Đekić, P.S., Rackov, M.J., 2012. Prediction of heat generation in rubber or rubber-metal springs. Therm. Sci. 16, 527–539.

Bazkiaei, A.K., Shirazi, K.H., Shishesaz, M., 2021. Thermo-hyper-viscoelastic analysis of a rubber cylinder under cyclic deformation. J. Rubber Res. 24, 13–26. https://doi.org/10.1007/s42464-020-00068-2

Beda, T., 2014. An approach for hyperelastic model-building and parameters estimation a review of constitutive models. Eur. Polym. J. 50, 97–108.

Behnke, R., Kaliske, M., 2018. Numerical modeling of thermal aging in steady state rolling tires. Int. J. Non. Linear. Mech. 103, 145–153.

Behnke, R., Kaliske, M., Klüppel, M., 2016. Thermo-mechanical analysis of cyclically loaded

particle-reinforced elastomer components: experiment and finite element simulation. Rubber Chem. Technol. 89, 154–176. https://doi.org/10.5254/rct.15.84852

Bengtson, H.H., 2010. Convection heat transfer coefficient estimation [WWW Document]. URL https://s3.amazonaws.com/suncam/docs/119.pdf (accessed 5.12.21).

Benkahla, J., Baranger, T.N., Issartel, J., 2013. Fatigue life estimation for an NBR rubber and an expanded polyurethane. Exp. Mech. 53, 1383–1393. https://doi.org/10.1007/s11340-013-9749-y

Benoit, R., Lafrance, L., Malo, D., Baron, J., 2009. Heavy vehicles tire blowout and explosion. IRSST Montr. QC, Canada.

Bergman, T.L., Lavine, A.S., Incropera, F.P., DeWitt, D.P., 2011. Introduction to heat transfer. John Wiley & Sons, Hoboken, New Jersey.

Besdo, D., Gvozdovskaya, N., Oehmen, K.H., 2010. Thermal Effects and Dissipation in a Model of Rubber Phenomenology, in: Elastomere Friction. Springer, pp. 95–121.

Beyer, W.H., 1991. CRC standard mathematical tables and formulae. CRC Press, Boca Raton, Florida, USA.

Brancati, R., Strano, S., Timpone, F., 2011. An analytical model of dissipated viscous and hysteretic energy due to interaction forces in a pneumatic tire: Theory and experiments. Mech. Syst. Signal Process. 25, 2785–2795.

Bridgestone, 2020. Data Book for Bridgestone Off-the-Road Tires.

Brieu, M., Diani, J., Mignot, C., Moriceau, C., 2010. Response of a carbon-black filled SBR under large strain cyclic uniaxial tension. Int. J. Fatigue 32, 1921–1927.

Carleo, F., Barbieri, E., Whear, R., Busfield, J.J.C., 2018. Limitations of viscoelastic constitutive models for carbon-black reinforced rubber in medium dynamic strains and medium strain rates. Polymers (Basel). 10, 988.

Carter, R.A., 2020. Data and Design Drive OTR Tire Improvements. Eng. Min. J. 221, 38–41.

Carter, R.A., 2016. Tools to Tackle Tire Life Challenges. Eng. Min. J. 217, 62.

Carter, R.A., 2011. OTR tire supply comes under pressure. Eng. Min. J. 212, 40.

Caterpillar, 2018. Caterpillar performance handbook [WWW Document]. URL https://wheelercat.com/wp-content/uploads/2018/07/SEBD0351_ED48.pdf (accessed 9.25.20).

Caterpillar, 2009. Caterpillar 797F mining truck product brochure (AEHQ6029) [WWW Document]. URL https://www.webcitation.org/5khS1wxbr?url=http://www.cat.com/cda/files/1882082/7/797F %2C AEHQ6039.pdf?m=264225&x=7 (accessed 10.1.20).

Cebeci, T., Bradshaw, P., 2012. Physical and computational aspects of convective heat transfer.

Springer Science & Business Media, Berlin/Heidelberg, Germany.

Cheheb, Z., Mousseau, P., Sarda, A., Deterre, R., 2012. Thermal conductivity of rubber compounds versus the state of cure. Macromol. Mater. Eng. 297, 228–236. https://doi.org/10.1002/mame.201100127

Cho, J.R., Lee, H.W., Jeong, W.B., Jeong, K.M., Kim, K.W., 2013. Numerical estimation of rolling resistance and temperature distribution of 3-D periodic patterned tire. Int. J. Solids Struct. 50, 86–96. https://doi.org/10.1016/j.ijsolstr.2012.09.004

Cole, K., Beck, J., Haji-Sheikh, A., Litkouhi, B., 2010. Heat conduction using Greens functions. CRC Press, Boca Raton, Florida.

Disk, H., 2018. Hot disk thermal constants analyser instruction manual [WWW Document]. URL https://www.hotdiskinstruments.com/content/uploads/2017/04/TPS-500-S.pdf (accessed 8.1.21).

Dodge, Y., 2008. The concise encyclopedia of statistics. Springer Science & Business Media, Berlin/Heidelberg, Germany.

Dolez, P.I., Nohile, C., Anh, T.H., Vu-Khanh, T., Benoit, R., Bellavigna-Ladoux, O., 2008. Exploring the chemical aspects of truck tire blowouts and explosions. Saf. Sci. 46, 1334–1344.

Dorfmann, A., Ogden, R.W., 2004. A constitutive model for the Mullins effect with permanent set in particle-reinforced rubber. Int. J. Solids Struct. 41, 1855–1878. https://doi.org/10.1016/j.ijsolstr.2003.11.014

Dorfmann, A., Ogden, R.W., 2003. A pseudo-elastic model for loading, partial unloading and reloading of particle-reinforced rubber. Int. J. Solids Struct. 40, 2699–2714.

Dubinkin, D., Kulpin, A., Stenin, D., 2020. Justification of the Number and Type of Tire Size for a Dump Truck with a Lifting Capacity from 90 to 130 Tons, in: E3S Web of Conferences. EDP Sciences, p. 3015.

Duffy, D.G., 2015. Green's functions with applications. Chapman and Hall/CRC, Boca Raton, Florida.

Duffy, O.C., Wright, G., 2015. Fundamentals of Medium/Heavy Duty Commercial Vehicle Systems: 2014 NATEF Edition. Jones & Bartlett Publishers, Burlington, Massachusetts.

El-Zomor, H.M., 2019. Real-time estimation of pneumatic tyre hysteresis loss. Int. J. Heavy Veh. Syst. 26, 175–187.

Farroni, F., Sakhnevych, A., Timpone, F., 2017. Physical modelling of tire wear for the analysis of the influence of thermal and frictional effects on vehicle performance. Proc. Inst. Mech. Eng. Part L J. Mater. Des. Appl. 231, 151–161.

Feng, C., 2017. Analysis on temperature rise characteristic and mechanics of load vehicle radial tire. Master's Thesis, Xi'an University of Science and Technology, China.

Fernandes, A.P., Sousa, P.F.B., Borges, V.L., Guimaraes, G., 2010. Use of 3D-transient analytical solution based on Green's function to reduce computational time in inverse heat conduction problems. Appl. Math. Model. 34, 4040–4049. https://doi.org/10.1016/j.apm.2010.04.006

Flint, T.F., Francis, J.A., Smith, M.C., Vasileiou, A.N., 2018. Semi-analytical solutions for the transient temperature fields induced by a moving heat source in an orthogonal domain. Int. J. Therm. Sci. 123, 140–150. https://doi.org/10.1016/j.ijthermalsci.2017.09.012

FLIR, 2018. FLIR Exx-Series building brochure [WWW Document]. URL https://www.testequipmentdepot.com/flir/pdf/exx-series-building_brochure.pdf (accessed 7.10.21).

Fowles, R., Williams, R.F., 1970. Plane stress wave propagation in solids. J. Appl. Phys. 41, 360–363.

Gent, A.N., Walter, J.D., 2006. Pneumatic tire. Dept. of Transportation, National Highway Traffic Safety Administration, Washington, DC.

Ghoreishy, M.H.R., 2012. Determination of the parameters of the Prony series in hyper-viscoelastic material models using the finite element method. Mater. Des. 35, 791–797.

Ghoreishy, M.H.R., Alimardani, M., Mehrabian, R.Z., Gangali, S.T., 2013. Modeling the hyperviscoelastic behavior of a tire tread compound reinforced by silica and carbon black. J. Appl. Polym. Sci. 128, 1725–1731. https://doi.org/10.1002/app.38242

Golbakhshi, H., Namjoo, M., 2014. Finite element analysis for estimating the effect of various working conditions on the temperature gradients created inside a rolling tire. Int. J. Eng. 27, 1920–1927.

Golbakhshi, H., Namjoo, M., Mohammadi, M., 2014. Evaluating the effect of dissipated viscous energy of a rolling tire on stress, strain and deformation fields using an efficient 2D FE analysis. Int. J. Automot. Eng. 16, 3–7.

Goyanes, S., Lopez, C.C., Rubiolo, G.H., Quasso, F., Marzocca, A.J., 2008. Thermal properties in cured natural rubber/styrene butadiene rubber blends. Eur. Polym. J. 44, 1525–1534. https://doi.org/10.1016/j.eurpolymj.2008.02.016

Greenberg, M.D., 2015. Applications of Green's functions in science and engineering. Courier Dover Publications, Mineola, New York.

Gschwandl, M., Kerschbaumer, R.C., Schrittesser, B., Fuchs, P.F., Stieger, S., Meinhart, L., 2019. Thermal conductivity measurement of industrial rubber compounds using laser flash analysis: Applicability, comparison and evaluation, in: AIP Conference Proceedings. AIP Publishing LLC, College Park, Maryland, p. 30041.

Guo, Q., Zaïri, F., Ovalle Rodas, C., Guo, X., 2018. Constitutive modeling of the cyclic dissipation in thin and thick rubber specimens. ZAMM-Journal Appl. Math. Mech. für Angew. Math. und Mech. 98, 1878–1899. https://doi.org/10.1002/zamm.201800087

Guo, Z., Sluys, L.J., 2017. Application and comparison of constitutive models for description of

rubber-like materials under cyclic loading, in: Constitutive Models for Rubber IV: Proceedings of the Fourth European Conference on Constitutive Models for Rubber, ECCMR 2005, Stockholm, Sweden, 27-29 June 2005. Routledge, p. 263.

Haghpanahi, M., Salimi, S., Bahemmat, P., Sima, S., 2013. 3-D transient analytical solution based on Green's function to temperature field in friction stir welding. Appl. Math. Model. 37, 9865–9884. https://doi.org/10.1016/j.apm.2013.05.034

Harwood, J.A.C., Mullins, L., Payne, A.R., 1965. Stress softening in natural rubber vulcanizates. Part II. Stress softening effects in pure gum and filler loaded rubbers. J. Appl. Polym. Sci. 9, 3011–3021.

He, Y., 2005. Study of the unsteady temperature field of tire. PhD Thesis, Huazhong University of Science and Technology, China.

He, Y., Liu, L., Ma, L., Sun, X., 2006. Dependence of heat build-up of tire on temperature and frequency. Tire Ind. 2006 6.

He, Z., 2008. Temperature virtual experimental field technology research for radial type. PhD Thesis, Jiangsu University, China.

Hu, X., 2013. Micro-and macro-viscohyperelastic behavior of carbon black filled rubbers. PhD Thesis, Xiangtan University, China.

Hu, X., He, R., Huang, Y., Yin, B., Luo, W., 2019. A method to predict the dynamical behaviors of carbon black filled natural rubber at different temperatures. Polym. Test. 79, 106067. https://doi.org/10.1016/j.polymertesting.2019.106067

Hu, X., Liu, X., Shan, Y., He, T., 2021. Simulation and Experimental Validation of Sound Field in a Rotating Tire Cavity Arising from Acoustic Cavity Resonance. Appl. Sci. 11, 1121.

Huang, J., 2016. Study of thermomechanical coupling issue of radial truck tire. Dissertation, Qingdao University of Science and Technology, China.

Huang, L., Yang, X., Gao, J., 2019. Pseudo-elastic analysis with permanent set in carbon-filled rubber. Adv. Polym. Technol. 2019. https://doi.org/10.1155/2019/2369329

Hurtado, J., Lapczyk, I., Govindarajan, S., 2013. Parallel rheological framework to model non-linear viscoelasticity, permanent set, and Mullins effect in elastomers. Const. Model. Rubber 8, 95–100.

Isotemp, 2005. Isotemp bath circulators [WWW Document]. URL https://fscimage.fishersci.com/webimages _FSC/downloads/IsotempCatv.5RM5-18.pdf (accessed 10.5.20).

Jamshidi, M., Afshar, F., Mohammadi, N., Pourmahdian, S., 2005. Study on cord/rubber interface at elevated temperatures by H-pull test method. Appl. Surf. Sci. 249, 208–215.

Jamshidi, M., Afshar, F., Shamayeli, B., 2006. Evaluation of cord/rubber adhesion by a new fatigue test method. J. Appl. Polym. Sci. 101, 2488–2494.

Jamshidi, M., Taromi, F.A., 2007. Study on temperature dependence of loss function in a model cord–adhesive–rubber system. J. Adhes. Sci. Technol. 21, 169–177.

Jayme, A., Al-Qadi, I.L., 2021. Thermomechanical coupling of a hyper-viscoelastic truck tire and a pavement layer and its impact on three-dimensional contact stresses. Transp. Res. Rec. 2675, 359–372.

Jiji, L.M., 2009. Heat convection. Springer Science & Business Media, Berlin/Heidelberg, Germany.

Jin, Z., Cui, Z., 2010. Investigation on strain dependence of dynamic recrystallization behavior using an inverse analysis method. Mater. Sci. Eng. A 527, 3111–3119. https://doi.org/10.1016/j.msea.2010.01.062

Joseph, A., 2014. Off-road tire tread. U.S. Patent Application No. 14/343,313.

Kagogo, T.S., 2014. A critical evaluation of haul truck tyre performance and management system at Rössing Uranium Mine. J. South. African Inst. Min. Metall. 114, 293–298.

Kerr, C.L., 2017. Load G-level as a Truck-Ground KPI. Master's Thesis, University of Alberta, Canada.

Kerschbaumer, R.C., Stieger, S., Gschwandl, M., Hutterer, T., Fasching, M., Lechner, B., Meinhart, L., Hildenbrandt, J., Schrittesser, B., Fuchs, P.F., 2019. Comparison of steady-state and transient thermal conductivity testing methods using different industrial rubber compounds. Polym. Test. 80, 106121. https://doi.org/10.1016/j.polymertesting.2019.106121

Kießling, R., Landgraf, R., Scherzer, R., Ihlemann, J., 2016. Introducing the concept of directly connected rheological elements by reviewing rheological models at large strains. Int. J. Solids Struct. 97, 650–667.

Kim, B., Lee, S.B., Lee, J., Cho, S., Park, H., Yeom, S., Park, S.H., 2012. A comparison among Neo-Hookean model, Mooney-Rivlin model, and Ogden model for chloroprene rubber. Int. J. Precis. Eng. Manuf. 13, 759–764. https://doi.org/10.1007/s12541-012-0099-y

Kocjan, T., Nagode, M., Klemenc, J., Oman, S., 2022. Prediction of actual fatigue test temperature and isothermal fatigue life curves for non-crystallising rubber under fully relaxing uni-axial loading conditions. Int. J. Fatigue 157, 106622.

Kravchenko, A., Sakno, O., 2011. Tire life adjustment on the coefficients of operational and road conditions. Teka Kom. Motoryz. i Energ. Rol. 11.

Krmela, J., Krmelová, V., 2017. Dynamic experiment of parts of car tyres. Procedia Eng. 187, 763–768.

Krzyzanowska, J., 2007. The impact of mixed fleet hauling on mining operations at Venetia mine. J. South. African Inst. Min. Metall. 107, 215–224.

Kumar, N., Rao, V.V., 2016. Hyperelastic Mooney-Rivlin model: determination and physical interpretation of material constants. Parameters 2(10), 1.

LBB, 2011. LBB series oven owner's manual [WWW Document]. URL https://www.despatch.com/pdfs/ 336979LBBSeriesOwnersManualC188V18.pdf (accessed 10.4.20).

Le Cam, J.-B., 2017. Energy storage due to strain-induced crystallization in natural rubber: the physical origin of the mechanical hysteresis. Polymer (Guildf). 127, 166–173.

Le Saux, V., Marco, Y., Calloch, S., Doudard, C., Charrier, P., 2010. Fast evaluation of the fatigue lifetime of rubber-like materials based on a heat build-up protocol and micro-tomography measurements. Int. J. Fatigue 32, 1582–1590.

Lee, H.W., Cho, J.R., Jeong, W.B., Jeong, K.M., Kim, K.W., 2014. Mesh generation and hysteretic loss prediction of 3-D periodic patterned tire. Int. J. Automot. Technol. 15, 411–417.

Lei, F., Szeri, A.Z., 2007. Inverse analysis of constitutive models: biological soft tissues. J. Biomech. 40, 936–940. https://doi.org/10.1016/j.jbiomech.2006.03.014

Li, F., Liu, F., Liu, J., Gao, Y., Lu, Y., Chen, J., Yang, H., Zhang, L., 2018. Thermo-mechanical coupling analysis of transient temperature and rolling resistance for solid rubber tire: Numerical simulation and experimental verification. Compos. Sci. Technol. 167, 404–410. https://doi.org/10.1016/j.compscitech.2018.08.034

Li, F., Liu, J., Lu, Y., Zhang, L., Yang, H., 2017. Modeling on Constitutive Behaviors of Filled Rubber Compounds for Cyclic Loading Path. China Rubber Ind. 64, 79–83.

Li, F., Liu, J., Yang, H., Lu, Y., Zhang, L., 2016. Numerical simulation and experimental verification of heat build-up for rubber compounds. Polymer (Guildf). 101, 199–207. https://doi.org/10.1016/j.polymer.2016.08.065

Li, X., 2012. Study on the reinforcement and blend dependence of hyperelasticity of tire rubbers under the moderate finite deformation. PhD Thesis, University of Science and Technology of China, China.

Li, X., Dong, Y., Li, Z., Xia, Y., 2011. Experimental study on the temperature dependence of hyperelastic behavior of tire rubbers under moderate finite deformation. Rubber Chem. Technol. 84, 215–228.

Li, Y., Liu, W.Y., Frimpong, S., 2012. Effect of ambient temperature on stress, deformation and temperature of dump truck tire. Eng. Fail. Anal. 23, 55–62. https://doi.org/10.1016/j.engfailanal.2012.02.004

Liang, C., Ji, L., Mousavi, H., Sandu, C., 2019. Evaluation of tire traction performance on dry surface based on tire-road contact stress, in: SIAR International Congress of Automotive and Transport Engineering: Science and Management of Automotive and Transportation Engineering. Springer, pp. 138–152.

Lin, Y.J., Hwang, S.J., 2004. Temperature prediction of rolling tires by computer simulation. Math. Comput. Simul. 67, 235–249.

Lindeque, G.C., 2016. A critical investigation into tyre life on an iron ore haulage system. J. South.

African Inst. Min. Metall. 116, 317–322.

Lion, A., 1997. A physically based method to represent the thermo-mechanical behaviour of elastomers. Acta Mech. 123, 1–25.

Liu, M., 2010. Constitutive equations for the dynamic response of rubber. PhD Thesis, University of Akron, USA.

Liu, M., 2007. A three-dimensional hyper-viscoelasticity constitutive model for the dynamic response of rubber. PhD Thesis, University of Akron, USA.

Liu, M., Fatt, M.S.H., 2011. A constitutive equation for filled rubber under cyclic loading. Int. J. Non. Linear. Mech. 46, 446–456.

Luo, W., Hu, X., Wang, C., Li, Q., 2010. Frequency-and strain-amplitude-dependent dynamical mechanical properties and hysteresis loss of CB-filled vulcanized natural rubber. Int. J. Mech. Sci. 52, 168–174.

Luo, W., Huang, Y., Yin, B., Jiang, X., Hu, X., 2020. Fatigue life assessment of filled rubber by hysteresis induced self-heating temperature. Polymers (Basel). 12, 846.

Luo, W., Li, M., Huang, Y., Yin, B., Hu, X., 2019. Effect of temperature on the tear fracture and fatigue life of carbon-black-filled rubber. Polymers (Basel). 11, 768.

Luo, W., Yin, B., Hu, X., Zhou, Z., Deng, Y., Song, K., 2018. Modeling of the heat build-up of carbon black filled rubber. Polym. Test. 69, 116–124. https://doi.org/10.1016/j.polymertesting.2018.05.017

Lv, X., 2005. Study of rubber used in tire with low rolling resistance. PhD Thesis, Qingdao University of Science and Technology, China.

Ma, S., Guo, Y., Liu, W.V., 2022a. An analytical solution to predict temperatures of dumbbell-shaped rubber specimens under cyclic deformation. J. Test. Eval.

Ma, S., Huang, G., Obaia, K., Moon, S., WV, & L., 2021a. Hysteresis loss of ultra-large off-the-road tire rubber compounds under testing conditions simulated from mine sites. Proc Inst Mech Eng Part D J Automob Eng (Accepted).

Ma, S., Huang, G., Obaia, K., Moon, S., WV, & L., 2021b. A novel phenomenological model for predicting hysteresis loss of rubber compounds obtained from ultra-large off-the-road tires. Proc. Inst. Mech. Eng. Part D J. Automob. Eng.

Ma, S., Huang, G., Obaia, K., Moon, S.W., Liu, W.V., 2022b. Hysteresis loss of ultra-large off-the-road tire rubber compounds based on operating conditions at mine sites. Proc. Inst. Mech. Eng. Part D J. Automob. Eng. 236, 439–450.

Ma, S., Huang, G., Obaia, K., Won Moon, S., Victor Liu, W., 2022c. A novel phenomenological model for predicting hysteresis loss of rubber compounds obtained from ultra-large off-the-road tires. Proc. Inst. Mech. Eng. Part D J. Automob. Eng. 09544070211072494.

Ma, S., Wu, L., Liu, W.V., 2022d. Numerical investigation of temperatures in ultra-large off-the-

road tires under operating conditions at mine sites. J. Therm. Sci. Eng. Appl. 1–51.

Magna, 2014. Magna Technical Book.

Marais, J., 2017. Numerical modelling and evaluation of the temperature distribution in an Earthmover Tyre: establishing a safe operating envelope. Dissertation, Stellenbosch University, South Africa.

Marais, J., Venter, G., 2018. Numerical modelling of the temperature distribution in the cross-section of an earthmover tyre. Appl. Math. Model. 57, 360–375. https://doi.org/10.1016/j.apm.2018.01.018

Maritz, J.C., 2015. Numerical modelling and experimental measurement of the temperature distribution in a rolling tire. Master's Thesis, Stellenbosch University, South Africa.

Marlow, R.S., 2003. A general first-invariant hyperelastic constitutive model. Const. Model. Rubber 157–160.

Mars, W. V, Fatemi, A., 2003. Fatigue crack nucleation and growth in filled natural rubber. Fatigue Fract. Eng. Mater. Struct. 26, 779–789. https://doi.org/10.1046/j.1460-2695.2003.00678.x

Mars, W. V, Fatemi, A., 2002. A literature survey on fatigue analysis approaches for rubber. Int. J. Fatigue 24, 949–961. https://doi.org/10.1016/S0142-1123(02)00008-7

Martinez, J.R.S., Le Cam, J.-B., Balandraud, X., Toussaint, E., Caillard, J., 2013. Mechanisms of deformation in crystallizable natural rubber. Part 1: thermal characterization. Polymer (Guildf). 54, 2717–2726. https://doi.org/10.1016/j.polymer.2013.03.011

Meech, J., Parreira, J., 2013. Predicting wear and temperature of autonomous haulage truck tires. IFAC Proc. Vol. 46, 142–147.

Michelin, 2016. Technical data – Earthmover tires [WWW Document]. URL https://www.otrusa.com/wp-content/uploads/2017/07/Michelin-Technical-Data-6.pdf (accessed 12.20.22).

Minaei, A., Safikhani, H., 2021. A new transient analytical model for heat transfer of earth-to-air heat exchangers. J. Build. Eng. 33, 101560. https://doi.org/10.1016/j.jobe.2020.101560

Mohotti, D., Ali, M., Ngo, T., Lu, J., Mendis, P., 2014. Strain rate dependent constitutive model for predicting the material behaviour of polyurea under high strain rate tensile loading. Mater. Des. 53, 830–837.

Mooney, M., 1940. A theory of large elastic deformation. J. Appl. Phys. 11, 582–592. https://doi.org/10.1063/1.1712836

Morton, J., 2017. New OTR Tires to Run Cooler, Longer as Suppliers Crunch Data From Afar. Eng. Min. J. 218, 40.

MTS, 2006. MTS 810 & 858 material testing systems [WWW Document]. URL https://www.upc.edu/sct/ documents_equipament/d_77_id-412.pdf (accessed 10.15.20).

Mu, Q., Feng, S., Diao, G., 2007. Thermal conductivity of silicone rubber filled with ZnO. Polym. Compos. 28, 125–130. https://doi.org/10.1002/pc.20276

Mullins, L., 1969. Softening of rubber by deformation. Rubber Chem. Technol. 42, 339–362.

Narasimha Rao, K. V, Kumar, R.K., Bohara, P.C., 2006. A sensitivity analysis of design attributes and operating conditions on tyre operating temperatures and rolling resistance using finite element analysis. Proc. Inst. Mech. Eng. Part D J. Automob. Eng. 220, 501–517.

Neves, R.R. V, Micheli, G.B., Alves, M., 2010. An experimental and numerical investigation on tyre impact. Int. J. Impact Eng. 37, 685–693.

Nyaaba, W., 2017. Thermomechanical fatigue life investigation of an ultra-large mining dump truck tire. Dissertation, Missouri University of Science and Technology, USA.

Nyaaba, W., Bolarinwa, E.O., Frimpong, S., 2019a. Durability prediction of an ultra-large mining truck tire using an enhanced finite element method. Proc. Inst. Mech. Eng. Part D J. Automob. Eng. 233, 161–169. https://doi.org/10.1016/j.ijfatigue.2018.07.009

Nyaaba, W., Frimpong, S., Anani, A., 2019b. Fatigue damage investigation of ultra-large tire components. Int. J. Fatigue 119, 247–260.

Ogden, R.W., Roxburgh, D.G., 1999. A pseudo–elastic model for the Mullins effect in filled rubber. Proc. R. Soc. London. Ser. A Math. Phys. Eng. Sci. 455, 2861–2877. https://doi.org/10.1098/rspa.1999.0431

Oil Sands Discovery Center, 2016. Facts about Alberta's oil sands and its industry [WWW Document]. URL https://open.alberta.ca/publications/facts-about-alberta-s-oil-sands-and-its-industry (accessed 10.12.20).

Österlöf, R., Kari, L., Wentzel, H., 2015. Temperature dependency of a viscoplastic constitutive model for rubber with reinforcing fillers, in: 9th European Conference on Constitutive Models for Rubbers, ECCMR 2015, 1 September 2015 through 4 September 2015. CRC Press/Balkema, pp. 149–156.

Österlöf, R., Wentzel, H., Kari, L., 2016. A finite strain viscoplastic constitutive model for rubber with reinforcing fillers. Int. J. Plast. 87, 1–14.

Pang, B.-J., Yang, Z.-Q., Wang, L.-W., CHI, R.-Q., 2011. Dynamic compression properties and constitutive model with strain rate effect of rubber material. Chinese J. High Press. Phys. 25, 407–415.

Park, D.M., Hong, W.H., Kim, S.G., Kim, H.J., 2000. Heat generation of filled rubber vulcanizates and its relationship with vulcanizate network structures. Eur. Polym. J. 36, 2429–2436.

Parreira, J., 2013. An interactive simulation model to compare an autonomous haulage truck system with a manually-operated system. PhD Thesis, University of British Columbia, Canada.

Pascual, R., Román, M., López-Campos, M., Hitch, M., Rodovalho, E., 2019. Reducing mining

footprint by matching haul fleet demand and route-oriented tire types. J. Clean. Prod. 227, 645–651.

Ramazani, S., Morshed, M., Ghane, M., 2011. Effect of service temperature on structure and mechanical properties of polyamide 6 & 66 tyre cords. J. Polym. Res. 18, 781–792.

Rangarajan, S.E., Ramarathnam, K.K., 2021. Viscoelastic properties of natural rubber with fatigue damage. Int. J. Fatigue 150, 106344.

Raut, P., Swanson, N., Kulkarni, A., Pugh, C., Jana, S.C., 2018. Exploiting arene-perfluoroarene interactions for dispersion of carbon black in rubber compounds. Polymer (Guildf). 148, 247–258.

Rivlin, Rs., 1948. Large elastic deformations of isotropic materials. I. Fundamental concepts. Philos. Trans. R. Soc. London. Ser. A, Math. Phys. Sci. 240, 459–490. https://doi.org/10.1098/rsta.1948.0002

Rodas, C.O., Zaïri, F., Naït-Abdelaziz, M., Charrier, P., 2016. A thermo-visco-hyperelastic model for the heat build-up during low-cycle fatigue of filled rubbers: formulation, implementation and experimental verification. Int. J. Plast. 79, 217–236. https://doi.org/10.1016/j.ijplas.2015.01.001

Rodrigues, M.K., da Silva Brum, R., Vaz, J., Rocha, L.A.O., dos Santos, E.D., Isoldi, L.A., 2015. Numerical investigation about the improvement of the thermal potential of an Earth-Air Heat Exchanger (EAHE) employing the Constructal Design method. Renew. Energy 80, 538–551. https://doi.org/10.1016/j.renene.2015.02.041

SAE, 2012. Tonne Kilometer Per Hour Application.

Sahoo, L.K., Bandyopadhyay, S., Banerjee, R., 2018. Benchmarking energy consumption of truck haulage, in: Energy Efficiency in the Minerals Industry. Springer, 1st ed. New York, NY, pp. 159–180.

Schieppati, J., Schrittesser, B., Wondracek, A., Robin, A.H.S., Pinter, G., 2019. Heat build-up of rubbers during cyclic loading, in: Proceeding of 2019 European Conference on Constitutive Models for Rubber-ECCMR. Nantes, France.

Smith, R.E., Tang, T., Johnson, D., Ledbury, E., Goddette, T., Felicelli, S.D., 2012. Simulation of thermal signature of tires and tracks. Report, Mississippi State Univ Mississippi State Center for Advanced Vehicular Systems, USA.

Sokolov, S.L., 2009. Analysis of the heat state of pneumatic tires by the finite element method. J. Mach. Manuf. Reliab. 38, 310–314. https://doi.org/10.3103/S1052618809030182

Stringham, G., 2012. Energy developments in Canada's oil sands. Dev. Environ. Sci. 11, 19–34.

Su, B., Wu, J., Cui, Z., Wang, Y., 2015. Modeling of truck tire curing process by an experimental and numerical method. Iran. Polym. J. 24, 583–593. https://doi.org/10.1007/s13726-015-0349-9

Suwannachit, A., Nackenhorst, U., 2010. On the constitutive modeling of reinforced rubber in a broad frequency domain. ZAMM-Journal Appl. Math. Mech. für Angew. Math. und Mech. Appl. Math. Mech. 90, 418–435.

Syncrude, 2018. Syncrude mine site report - 2018. Report, Syncrude Canada Ltd., Canada.

Ta, C., 2018. Operation truck data. Report, Syncrude Canada Ltd., Canada.

Tang, T., Johnson, D., Smith, R.E., Felicelli, S.D., 2014. Numerical evaluation of the temperature field of steady-state rolling tires. Appl. Math. Model. 38, 1622–1637. https://doi.org/10.1016/j.apm.2013.08.033

Terrill, E.R., Centea, M., Evans, L.R., MacIsaac Jr, J.D., 2010. Dynamic mechanical properties of passenger and light truck tire treads. Report, Akron Rubber Dev. Lab. Inc., USA, Febr. 2010.

Thompson, R., Peroni, R., Visser, A., 2019. Mining haul roads: theory and practice. CRC Press.

Tomita, Y., Azuma, K., Naito, M., 2007. Strain-rate-dependent deformation behavior of carbon-black-filled rubber under monotonic and cyclic straining. Key Eng. Mater. 340, 1017–1024.

Tye-Gingras, M., Gosselin, L., 2014. Generic ground response functions for ground exchangers in the presence of groundwater flow. Renew. energy 72, 354–366. https://doi.org/10.1016/j.renene.2014.07.026

Van Blommestein, W.B., 2016. Experimentally determined material parameters for temperature prediction of an automobile tire using finite element analysis. Dissertation, Stellenbosch University, South Africa.

Wang, G., Xu, H., Liang, C., Zhou, H., Sun, Y., 2017. Research on the influence of thermophysical parameters of tire compound on temperature field. Rubber Ind. 435–440.

Wang, M., Liao, Y., Chen, D., 2013. Study on the thermal effects of rubbers during loading–unloading cycles by infrared thermography. Polym. Bull. 70, 171–180. https://doi.org/10.1007/s00289-012-0795-x

Wang, W., Yan, S., Zhao, S., 2013. Experimental verification and finite element modeling of radial truck tire under static loading. J. Reinf. Plast. Compos. 32, 490–498.

Wang, X., Wang, W., 2021. Numerical Simulation and Experimental Study on Dynamic Heat Build-up of Rubber. ACTA Polym. Sin. 52, 787–795.

Wang, Z.P., Yu, Z., Li, K., 2013. Research of automobile tire vertical stiffness optimization method on the basis of ADAMS/Car. Key Eng. Mater. 561, 527–532. https://doi.org/10.4028/www.scientific.net/KEM.561.527

Weng, G., Huang, G., Lei, H., Qu, L., Nie, Y., Wu, J., 2011. Crack initiation and evolution in vulcanized natural rubber under high temperature fatigue. Polym. Degrad. Stab. 96, 2221–2228. https://doi.org/10.1016/j.polymdegradstab.2011.09.004

Wineman, A., 2005. Some results for generalized neo-Hookean elastic materials. Int. J. Non. Linear. Mech. 40, 271–279. https://doi.org/10.1016/j.ijnonlinmec.2004.05.007

Wrubleski, E.G.M., Marczak, R.J., 2013. A modification of hyperelastic incompressible constitutive models to include non-conservative effects, in: Proceedings of the 22nd International Congress of Mechanical Engineering (COBEM 2013). pp. 2176–5480.

Wu, F., 2009. Finite element analysis of temperature distribution in steady rolling tire. PhD Thesis, University of Science and Technology of China, China.

Wu, W., 2017. Simulation analysis of tire temperature field. Master's Thesis, Jilin University, China.

Xia, K., 2011. Finite element modeling of tire/terrain interaction: Application to predicting soil compaction and tire mobility. J. Terramechanics 48, 113–123.

Xia, Yong, Li, W., Xia, Yuanming, 2004. Test and characterization for the incompressible hyperelastic properties of conditioned rubbers under moderate finite deformation. Acta Mech. Solida Sin. 4, 307–314. https://doi.org/10.1007/s10338-004-0437-4

Xu, N., Hashemi, E., Tang, Z., Khajepour, A., 2022. Data-Driven Tire Capacity Estimation With Experimental Verification. IEEE Trans. Intell. Transp. Syst.

Xu, Y., 2011. The simulation analysis of tire's stiffness characteristics and rolling resistance. PhD Thesis, South China University of Technology, China.

Yang, X., Olatunbosun, O., Ramos, D.G.-P., Bolarinwa, E., 2013. Experimental investigation of tire dynamic strain characteristics for developing strain-based intelligent tire system. SAE Int. J. Passeng. Cars-Mechanical Syst. 6, 97–108.

Yang, Y.L., Qiao, L., Wang, C., Lu, F., Kang, X.H., 2014. Effect Analysis of Temperature on the Rubber Material Stress-strain Relationship, in: Advanced Materials Research. Trans Tech Publ, pp. 116–119.

Yeoh, O.H., 1993. Some forms of the strain energy function for rubber. Rubber Chem. Technol. 66, 754–771.

Yoo, S., Ju, J., Choi, S.-J., Kim, D., 2016. Non Linear Viscoelastic Constitutive Relation of Elastomers for Hysteresis Behavior. Trans. Korean Soc. Mech. Eng. A 40, 353–362.

Yoo, S., Uddin, M.S., Heo, H., Ju, J., Choi, S.-J., 2017. Thermoviscoelastic modeling of a nonpneumatic tire with a lattice spoke. Proc. Inst. Mech. Eng. Part D J. Automob. Eng. 231, 241–252.

Yu, H., Cai, C., Bobet, A., Zhao, X., Yuan, Y., 2019. Analytical solution for longitudinal bending stiffness of shield tunnels. Tunn. Undergr. Sp. Technol. 83, 27–34. https://doi.org/10.1016/j.tust.2018.09.011

Yu, H., Li, F., Yang, H., Zhang, L., 2017. A nonlinear hyper-viscoelastic constitutive model for rubber material with finite strain. China Rubber Ind. 11.

Yu, H., Zhang, Z., Chen, J., Bobet, A., Zhao, M., Yuan, Y., 2018. Analytical solution for longitudinal seismic response of tunnel liners with sharp stiffness transition. Tunn. Undergr.

Sp. Technol. 77, 103–114. https://doi.org/10.1016/j.tust.2018.04.001

Zhang, J., Xue, F., Wang, Y., Zhang, X., Han, S., 2018. Strain energy-based rubber fatigue life prediction under the influence of temperature. R. Soc. open Sci. 5, 180951. https://doi.org/10.1098/rsos.180951

Zhao, Z., Wang, Q., Li, J., Li, Y., Chu, L., 2001. Steady state thermal analysis on temperature field of tire based on rolling state. Chinese J. Mech. Eng. 37, 30–34.

Zhi, J., Lu, H., Wang, H., Wang, S., Lin, W., Qiao, C., Jia, Y., 2016. Analysis on dynamic compression performance of tire rubber based on generalized Maxwell model. Acta Polym. Sin. 887–894.

Zhi, J., Wang, S., Wang, H., Lu, H., Lin, W., Qiao, C., Hu, C., Jia, Y., 2017. Analysis on energy loss of rubber under dynamic load. ACTA Polym. Sin. 708–715.

Zhi, J., Wang, S., Zhang, M., Wang, H., Lu, H., Lin, W., Qiao, C., Hu, C., Jia, Y., 2019. Numerical analysis of the dependence of rubber hysteresis loss and heat generation on temperature and frequency. Mech. Time-Dependent Mater. 23, 427–442. https://doi.org/10.1007/s11043-018-9398-8

Zhou, H., Wang, G., Ding, Y., Yang, J., Liang, C., Fu, J., 2015. Effect of friction model and tire maneuvering on tire-pavement contact stress. Adv. Mater. Sci. Eng. 2015.

Zhou, J., Hall, R.A., Huntingford, K., Fowler, G., 2008. Effect of off-the-road tyre rotation practices on tyre life: a case study. Min. Technol. 117, 101–110.

Zine, A., Benseddiq, N., Abdelaziz, M.N., 2011. Rubber fatigue life under multiaxial loading: Numerical and experimental investigations. Int. J. Fatigue 33, 1360–1368. https://doi.org/10.1016/j.ijfatigue.2011.05.005

Zwillinger, D., 2018. CRC standard mathematical tables and formulas. chapman and hall/CRC, Boca Raton, Florida.

# Appendix X. Code and charts

## X.1. MATLAB code for predicting temperatures in dumbbell-shaped tire rubber specimen

```
syms n

t=1000;

x=0.003;

y=0.001;

m=0.000000165;

B=0.0877;

L=0.002;

k=0.282;

Q=453250;

a=0;

b=0;

beta1=[0.42 3.195 6.31 9.445 12.58 15.715 18.855 21.995 25.14 28.285];

beta2=[0.715 3.3 6.365 9.48 12.605 15.745 18.875 22.015 25.155 28.295];
```

```
for i=1:1:10

    a=(2/(3*L))*exp((-beta1(i)^2*m*(t-
n))/(9*(L^2)))*(beta1(i)*cos(beta1(i)*x/(3*L))+3*B*sin(beta1(i)*x/(3*L)))*(3*L*sin(beta1(i))+
3*B*3*L*(1/beta1(i))*(1-
cos(beta1(i))))/((beta1(i)^2+9*(B^2))*(1+(3*B)/(beta1(i)^2+9*(B^2)))+3*B)+a;

    b=(2/L)*exp((-beta2(i)^2*m*(t-
n))/(L^2))*(beta2(i)*cos(beta2(i)*y/L)+B*sin(beta2(i)*y/L))*(L*sin(beta2(i))+B*L*(1/beta2(i))
*(1-cos(beta2(i))))/((beta2(i)^2+(B^2))*(1+B/(beta2(i)^2+(B^2)))+B)+b;

end



a*b

int(a*b,n,0,t)

(m/k)*Q*int(a*b,n,0,t)
```

```
syms n

t=1000;

x=0.003;

y=0.001;

m=0.000000165;

k=0.282;

h=12.37;

L=0.002;

B=0.0877;

T=20;

a=0;

b=0;

c=0;

d=0;

beta1=[0.42 3.195 6.31 9.445 12.58 15.715 18.855 21.995 25.14 28.285];

beta2=[0.715 3.3 6.365 9.48 12.605 15.745 18.875 22.015 25.155 28.295];
```

```
for i=1:1:10

    a=-(2/(3*L))*exp((-beta1(i)^2*m*(t-
n))/(9*(L^2)))*(beta1(i)*cos(beta1(i)*x/(3*L))+3*B*sin(beta1(i)*x/(3*L)))*(beta1(i))/((beta1(i)
^2+9*(B^2))*(1+(3*B)/(beta1(i)^2+9*(B^2)))+3*B)*(2/L)*exp((-beta2(i)^2*m*(t-
n))/(L^2))*(beta2(i)*cos(beta2(i)*y/L)+B*sin(beta2(i)*y/L))*(L*sin(beta2(i))+B*L*(1/beta2(i))
*(1-cos(beta2(i))))/((beta2(i)^2+(B^2))*(1+B/(beta2(i)^2+(B^2)))+B)+a;

    b=(2/(3*L))*exp((-beta1(i)^2*m*(t-
n))/(9*(L^2)))*(beta1(i)*cos(beta1(i)*x/(3*L))+3*B*sin(beta1(i)*x/(3*L)))*(beta1(i)*cos(beta1(
i))+3*B*sin(beta1(i)))/((beta1(i)^2+9*(B^2))*(1+(3*B)/(beta1(i)^2+9*(B^2)))+3*B)*(2/L)*exp
((-beta2(i)^2*m*(t-
n))/(L^2))*(beta2(i)*cos(beta2(i)*y/L)+B*sin(beta2(i)*y/L))*(L*sin(beta2(i))+B*L*(1/beta2(i))
*(1-cos(beta2(i))))/((beta2(i)^2+(B^2))*(1+B/(beta2(i)^2+(B^2)))+B)+b;

    c=-(2/L)*exp((-beta2(i)^2*m*(t-
n))/(L^2))*(beta2(i)*cos(beta2(i)*y/L)+B*sin(beta2(i)*y/L))*(beta2(i))/((beta2(i)^2+(B^2))*(1+
B/(beta2(i)^2+(B^2)))+B)*(2/(3*L))*exp((-beta1(i)^2*m*(t-
n))/(9*(L^2)))*(beta1(i)*cos(beta1(i)*x/(3*L))+3*B*sin(beta1(i)*x/(3*L)))*(3*L*sin(beta1(i))+
3*B*3*L*(1/beta1(i))*(1-
cos(beta1(i))))/((beta1(i)^2+9*(B^2))*(1+(3*B)/(beta1(i)^2+9*(B^2)))+3*B)+c;

    d=(2/L)*exp((-beta2(i)^2*m*(t-
n))/(L^2))*(beta2(i)*cos(beta2(i)*y/L)+B*sin(beta2(i)*y/L))*(beta2(i)*cos(beta2(i))+B*sin(beta
2(i)))/((beta2(i)^2+(B^2))*(1+B/(beta2(i)^2+(B^2)))+B)*(2/(3*L))*exp((-beta1(i)^2*m*(t-
n))/(9*(L^2)))*(beta1(i)*cos(beta1(i)*x/(3*L))+3*B*sin(beta1(i)*x/(3*L)))*(3*L*sin(beta1(i))+
3*B*3*L*(1/beta1(i))*(1-
cos(beta1(i))))/((beta1(i)^2+9*(B^2))*(1+(3*B)/(beta1(i)^2+9*(B^2)))+3*B)+d;

end
```

a+b+c+d

int(a+b+c+d,n,0,t)

(m*h*T/k)*int(a+b+c+d,n,0,t)

## X.2. ABAQUS code for OTRTire-T model

Note that the following code hides the node and element numbers.

```
*HEADING

Written using Tire Wizard version 1.1-2 at  time :  Sun Nov 21 21:29:42 2021

*PREPRINT, MODEL=NO

*RESTART,WRITE,FREQ=100

*NODE,NSET=ROAD

10001,   0.0,   0.0, 0

*SYMMETRIC MODEL GENERATION,PERIODIC

 0.0, 0.0, 0.0,    0.0, 1.0, 0.0

9,40

*SYMMETRIC RESULTS TRANSFER,STEP=2

*SURFACE,NAME=ROAD_SURF, TYPE=CYLINDER

0.0,0.0,-2000,  0.0,1.0,-2000

-1.0,0.0,-2000

START, -1000,0.0

LINE,  1000,0.0

*RIGID BODY,REF NODE=ROAD,ANALYTICAL SURFACE=ROAD_SURF

*CONTACT PAIR,INTERACTION=SRIGID

 SURF-TIRE-ROAD, ROAD_SURF
```

*SURFACE INTERACTION,NAME=SRIGID

*FRICTION

0.1

*************************************************

*STEP,INC=100,NLGEOM=YES

 1:  BRING TRANSFERRED RESULTS TO EQUILIBRIUM

*STATIC

 1.0, 1.0

*BOUNDARY

** Enter appropriate boundary conditions from axi analysis

SET-RIM,3,3,0.0

SET-RIM,1,1,0.0

SET-RIM,2,2,0.0

SET-RIM,6,6,0.0

SET-RIM,5,5,0.0

SET-RIM,4,4,0.0

PART-RIM-1_SET-RIM,3,3,0.0

PART-RIM-1_SET-RIM,1,1,0.0

PART-RIM-1_SET-RIM,2,2,0.0

PART-RIM-1_SET-RIM,6,6,0.0

PART-RIM-1_SET-RIM,5,5,0.0

PART-RIM-1_SET-RIM,4,4,0.0

ROAD,1,6

*DSLOAD,OP=NEW

** The plugin takes care of uniform pressure loads

**

Surf-P,P,0.7585

** Enter appropriate loads from axi analysis

** Here add all other history information so as

** to get the model in the same state as the

** end of the axi-symmetric analysis

*OUTPUT,FIELD,FREQ=1

*ELEMENT OUTPUT

 S,LE,TEMP,CENER,SENER,VENER

**ELEMENT OUTPUT,REBAR

** S,LE,RBANG,RBFOR,RBROT

*NODE OUTPUT

 U,NT

*CONTACT OUTPUT, VAR=PRESELECT

*OUTPUT,HISTORY, VAR=PRESELECT

*OUTPUT,HISTORY

*NODE OUTPUT, NSET=ROAD

U,TF

*END STEP

*************************************************

*STEP,INC=100,NLGEOM=YES

2: FOOTPRINT (Displacement controlled)

*STATIC

0.2, 1.0

*BOUNDARY,OP=NEW

SET-RIM,3,3,0.0

SET-RIM,1,1,0.0

SET-RIM,2,2,0.0

SET-RIM,6,6,0.0

SET-RIM,5,5,0.0

SET-RIM,4,4,0.0

PART-RIM-1_SET-RIM,3,3,0.0

PART-RIM-1_SET-RIM,1,1,0.0

PART-RIM-1_SET-RIM,2,2,0.0

PART-RIM-1_SET-RIM,6,6,0.0

PART-RIM-1_SET-RIM,5,5,0.0

PART-RIM-1_SET-RIM,4,4,0.0

ROAD, 1,2 ,0.0

ROAD, 4,6 ,0.0

ROAD, 3,3 ,10.0

*OUTPUT,FIELD,FREQ=1

*ELEMENT OUTPUT

 S,LE,TEMP,CENER,SENER,VENER

**ELEMENT OUTPUT,REBAR

** S,LE,RBANG,RBFOR,RBROT

*NODE OUTPUT

 U,NT

*CONTACT OUTPUT, VAR=PRESELECT

*OUTPUT,HISTORY, VAR=PRESELECT

*OUTPUT,HISTORY

*NODE OUTPUT, NSET=ROAD

U,TF

*END STEP

**************************************************

*STEP,INC=100,NLGEOM=YES

 3: FOOTPRINT (Load controlled)

*STATIC

 0.1, 1.0

*BOUNDARY,OP=NEW

** Enter appropriate boundary conditions from axi analysis

SET-RIM,3,3,0.0

SET-RIM,1,1,0.0

SET-RIM,2,2,0.0

SET-RIM,6,6,0.0

SET-RIM,5,5,0.0

SET-RIM,4,4,0.0

PART-RIM-1_SET-RIM,3,3,0.0

PART-RIM-1_SET-RIM,1,1,0.0

PART-RIM-1_SET-RIM,2,2,0.0

PART-RIM-1_SET-RIM,6,6,0.0

PART-RIM-1_SET-RIM,5,5,0.0

PART-RIM-1_SET-RIM,4,4,0.0

ROAD,1,2

ROAD,4,6

*CLOAD,OP=NEW

 ROAD, 3, 1120000

** Here add all other history information so as

** to get the model in the same state as the

** end of the axi-symmetric analysis, possibly

** modified as per requirements of this analyis

*OUTPUT,FIELD,FREQ=1

*ELEMENT OUTPUT

 S,LE,TEMP,CENER,SENER,VENER

**ELEMENT OUTPUT,REBAR

** S,LE,RBANG,RBFOR,RBROT

*NODE OUTPUT

 U,NT

*CONTACT OUTPUT, VAR=PRESELECT

*OUTPUT,HISTORY, VAR=PRESELECT

*OUTPUT,HISTORY

*NODE OUTPUT, NSET=ROAD

U,TF

*END STEP


```
      SUBROUTINE HETVAL(CMNAME,TEMP,TIME,DTIME,STATEV,FLUX,
     1 PREDEF,DPRED)
C
      INCLUDE 'ABA_PARAM.INC'
C
      CHARACTER*80 CMNAME
C
```

```fortran
      DIMENSION TEMP(2),STATEV(*),PREDEF(*),TIME(2),FLUX(2),
     1 DPRED(*)


      IF(TIME(2).GE.1.) flux = STATEV(1)




      RETURN

      END




      SUBROUTINE USDFLD(FIELD,STATEV,PNEWDT,DIRECT,T,CELENT,
     1 TIME,DTIME,CMNAME,ORNAME,NFIELD,NSTATV,NOEL,NPT,LAYER,
     2 KSPT,KSTEP,KINC,NDI,NSHR,COORD,JMAC,JMATYP,MATLAYO,LACCFLA)
C
      INCLUDE 'ABA_PARAM.INC'
C
      CHARACTER*80 CMNAME,ORNAME
      CHARACTER*3  FLGRAY(15)
      DIMENSION FIELD(NFIELD),STATEV(NSTATV),DIRECT(3,3),
     1 T(3,3),TIME(2)
```

```fortran
      DIMENSION ARRAY(15),JARRAY(15),JMAC(*),JMATYP(*),COORD(*)

      DIMENSION S1(50000,3),S2(50000,3),SE(50000)

      DIMENSION NOELE(50000)

      SAVE S1,S2,NOELE,SE

      SAVE KFLAG

      DATA KFLAG/0/
C


      IF(KSTEP.NE.1) GOTO 2000


        IF(KFLAG.EQ.0)THEN

          !OPEN(1001,FILE='s1.txt',STATUS='OLD')

          !OPEN(1002,FILE='s2.txt',STATUS='OLD')

          OPEN(1001,FILE='e:\se.txt',STATUS='OLD')

          OPEN(1003,FILE='e:\element.txt',STATUS='OLD')

        COUNT=1


        DO WHILE(.TRUE.)


          READ(1001,*,IOSTAT=ISTAT) SE(COUNT)
```

```fortran
        IF(ISTAT.NE.0) goto 500

        COUNT = COUNT+1

      ENDDO

500   continue


      !COUNT=1

      !DO WHILE(.TRUE.)

      !   READ(1002,*,IOSTAT=ISTAT) S2(COUNT,:)

      !   IF(ISTAT.NE.0)EXIT

      !   COUNT = COUNT+1

      !ENDDO

      COUNT=1

      DO WHILE(.TRUE.)

         READ(1003,*,IOSTAT=ISTAT) NOELE(COUNT)


         IF(ISTAT.NE.0) goto 600

         COUNT = COUNT+1

      ENDDO

600   continue

      CLOSE(1001)

      !CLOSE(1002)
```

```
      CLOSE(1003)

      KFLAG=1

   ENDIF


C


   SELECT CASE(CMNAME(1:1))

   CASE('S')

      TAND = 0.2

   CASE('C')

      TAND = 0.12

   CASE('T')

      TAND = 0.2

   CASE('A')

      TAND = 0.2

   CASE('I')

      TAND = 0.35

   ENDSELECT


   W=3.4767

   DO I =1,50000
```

```
         IF(NOEL.EQ.NOELE(I))THEN


         STATEV(1) = SE(I)

         STATEV(1) = W/2.*TAND*STATEV(1)

         EXIT

         ENDIF

      ENDDO

2000  CONTINUE



      RETURN

      END
```

*Surface, type=NODE, name=s_Set-99_CNS_, internal

s_Set-99, 1.

*Nset, nset="_T-Transform__T-Datum csys-1", internal

SET-AIR,

SET-R,

*Transform, nset="_T-Transform__T-Datum csys-1", type=C

    0.,      0.,      0.,      0.,      1.,      0.

** Constraint: CONSTRAINT-5-1

*Tie, name=CONSTRAINT-5-1, adjust=yes

SURF-4, SURF-3

** Constraint: Embed-1

*Embedded Element, host elset=SET-BASE

_M139

** Constraint: RigidBody-1

*Rigid Body, ref node=_PickedSet138, elset=PART-RIM-1

** Constraint: RigidBody-2

*Rigid Body, ref node=_PickedSet141, tie nset=SET-5

*End Assembly

**

** ELEMENT CONTROLS

**

*Section Controls, name=EC-1, hourglass=ENHANCED

1., 1., 1.

*Amplitude, name=Amp-1

     0.,      0.,     0.5,     1.,     1.,     0.

**

** MATERIALS

**

*Material, name=AIR

*Acoustic Medium

 0.45,

*Conductivity

 0.0255,

*Damping, alpha=0.1

*Density

 1.146e-12,

*Specific Heat

 1.013e+09,

*Material, name=APEX

*Conductivity

 0.438,

*Density

 1.1e-09,

*Depvar

   20,

*Hyperelastic, mooney-rivlin, moduli=LONG TERM

 1.00493, 0.41652,     0.

*Specific Heat

 1.19e+09,

*User Defined Field

*Viscoelastic, time=PRONY

 0.1447,    0., 17.162

*Trs

20.,  50.,1000.

*Material, name=CASING

*Conductivity

 0.438,

*Density

 1.1e-09,

*Hyperelastic, mooney-rivlin, moduli=LONG TERM

 0.44445, 0.13319,     0.

*Specific Heat

 1.19e+09,

*Viscoelastic, time=PRONY

 0.1144,    0., 17.722

*Trs

20.,  50.,1000.

*Material, name=INNERLINER

*Conductivity

 0.438,

*Density

1.1e-09,

*Hyperelastic, mooney-rivlin, moduli=LONG TERM

 0.17405, 0.07494,     0.

*Specific Heat

 1.19e+09,

*Viscoelastic, time=PRONY

 -0.0129,   0., 0.32

*Trs

20.,  50.,1000.

*Material, name=RABER

*Conductivity

 0.1,

*Density

 7.8e-09,

*Elastic

100000., 0.3

*Specific Heat

 1e+06,

*Material, name=RUBBER

*Damping, alpha=0.1, beta=1e-07

*Density

1.1e-09,

*Hyperelastic, neo hooke

 0.6, 0.03

*Material, name=SIDEWALL

*Conductivity

 0.438,

*Density

 1.1e-09,

*Hyperelastic, mooney-rivlin, moduli=LONG TERM

 0.38186, 0.12143,     0.

*Specific Heat

 1.19e+09,

*Viscoelastic, time=PRONY

 0.124,    0., 16.679

*Trs

20.,  50.,1000.

*Material, name=TREAD

*Conductivity

 0.438,

*Density

 1.1e-09,

*Hyperelastic, mooney-rivlin, moduli=LONG TERM

 0.46841, 0.12057,     0.

*Specific Heat

 1.19e+09,

*Viscoelastic, time=PRONY

 0.0656,    0., 16.061

*Trs

20.,  50.,1000.

**

** INTERACTION PROPERTIES

**

*Surface Interaction, name=INTPROP-1

1.,

*Friction, slip tolerance=0.005

 0.3,

*Surface Interaction, name=_INTPROP-1-1-Prop

1.,

*Friction, slip tolerance=0.005

 0.3,

**

** BOUNDARY CONDITIONS

**

** Name: Disp-BC-1 Type: Displacement/Rotation

*Boundary

SET-AIR, 1, 1

** Name: Disp-BC-2 Type: Displacement/Rotation

*Boundary

SET-R, 2, 2

** Name: Disp-BC-3 Type: Symmetry/Antisymmetry/Encastre

*Boundary

SET-RIM, ENCASTRE

** Name: Disp-BC-4 Type: Symmetry/Antisymmetry/Encastre

*Boundary

PART-RIM-1_SET-RIM, ENCASTRE

**

** PREDEFINED FIELDS

**

** Name: Predefined Field-1   Type: Temperature

*Initial Conditions, type=TEMPERATURE

Set-102, 30.

**

** INTERACTIONS

**

** Interaction: INTPROP-1-1

*Contact Pair, interaction=_INTPROP-1-1-Prop, type=SURFACE TO SURFACE

SURF-BASE, SURF-RIM

** Interaction: Int-2

*Contact Pair, interaction=INTPROP-1, small sliding, type=SURFACE TO SURFACE

s_Set-99_CNS_, Part-3-1.m_Surf-29

** ----------------------------------------------------------------

**

** STEP: Step-1

**

*Step, name=Step-1, nlgeom=YES

*Static

1., 1., 1e-05, 1.

**

** BOUNDARY CONDITIONS

**

** Name: BC-5 Type: Displacement/Rotation

*Boundary

Set-100, 1, 1

Set-100, 2, 2

Set-100, 3, 3

Set-100, 4, 4

Set-100, 5, 5

Set-100, 6, 6

**

** INTERACTIONS

**

** Interaction: INTPROP-1-1

*Change Friction, interaction=_INTPROP-1-1-Prop

*Friction, slip tolerance=0.005

 0.3,

*Contact Interference, shrink

SURF-BASE, SURF-RIM

**

** OUTPUT REQUESTS

**

*Restart, write, frequency=0

**

** FIELD OUTPUT: F-Output-3

**

*Output, field

*Contact Output

CDISP, CSTRESS

**

** FIELD OUTPUT: F-Output-1

**

*Node Output

CF, NT, RF, U

**

** FIELD OUTPUT: F-Output-2

**

*Element Output, directions=YES

LE, PE, PEEQ, PEMAG, S, TEMP

**

** HISTORY OUTPUT: H-Output-1

**

*Output, history

*Energy Output

ALLAE, ALLCD, ALLIE, ALLSD, ALLVD, ALLWK, ETOTAL

*End Step

** ----------------------------------------------------------------

**

** STEP: Step-2

**

*Step, name=Step-2, nlgeom=YES, inc=10000

*Static, stabilize, factor=0.0002, allsdtol=0., continue=NO

0.1, 1., 1e-05, 1.

**

** LOADS

**

** Name: SURFFORCE-1   Type: Pressure

*Dsload

SURF-P, P, 0.7585

**

** OUTPUT REQUESTS

**

*Restart, write, overlay, frequency=1

**

** FIELD OUTPUT: F-Output-6

**

*Output, field

*Element Output, directions=YES

S,

*Contact Output

CDISP, CSTRESS

**

** FIELD OUTPUT: F-Output-4

**

*Node Output

CF, NT, RF, U

*Element Output, directions=YES

E,

**

** HISTORY OUTPUT: H-Output-2

**

*Output, history

*Energy Output

ALLAE, ALLCD, ALLIE, ALLSD, ALLVD, ALLWK, ETOTAL

*End Step

** ----------------------------------------------------------------

**

** STEP: Step-3

**

** STEP: Step-3

**

*Step, name=Step-3, nlgeom=YES

*Static

0.01, 1., 1e-05, 0.1

**

** BOUNDARY CONDITIONS

**

** Name: BC-5 Type: Displacement/Rotation

*Boundary, op=NEW

Set-100, 2, 2

Set-100, 3, 3

Set-100, 4, 4

Set-100, 5, 5

Set-100, 6, 6

** Name: Disp-BC-1 Type: Displacement/Rotation

*Boundary, op=NEW

SET-AIR, 1, 1

** Name: Disp-BC-2 Type: Displacement/Rotation

*Boundary, op=NEW

SET-R, 2, 2

** Name: Disp-BC-3 Type: Symmetry/Antisymmetry/Encastre

*Boundary, op=NEW

SET-RIM, ENCASTRE

** Name: Disp-BC-4 Type: Symmetry/Antisymmetry/Encastre

*Boundary, op=NEW

PART-RIM-1_SET-RIM, ENCASTRE

**

** LOADS

**

** Name: Load-2   Type: Concentrated force

*Cload

Set-101, 1, -100000.

**

** OUTPUT REQUESTS

**

*Restart, write, frequency=0

**

** FIELD OUTPUT: F-Output-6

**

*Output, field

*Element Output, directions=YES

S,

*Contact Output

CDISP, CSTRESS

**

** FIELD OUTPUT: F-Output-4

**

*Node Output

CF, NT, RF, U

*Element Output, directions=YES

E,

**

** HISTORY OUTPUT: H-Output-2

**

*Output, history

*Energy Output

ALLAE, ALLCD, ALLIE, ALLSD, ALLVD, ALLWK, ETOTAL

*End Step

## X.3. Refined $K_1$ and $K_2$ charts in real site TKPHs

Table X1. Refined $K_1$ coefficients in real site TKPHs

| K₁ coefficients | | | | | | | | | |
|---|---|---|---|---|---|---|---|---|---|
| L (km) | OTRTire-T model | L (km) | OTRTire-T model | L (km) | OTRTire-T model | L (km) | OTRTire-T model | L (km) | OTRTire-T model |
| | | 11 | 1.15 | 21 | 1.22 | 31 | 1.25 | 41 | 1.26 |
| | | 12 | 1.17 | 22 | 1.23 | 32 | 1.25 | 42 | 1.26 |
| | | 13 | 1.18 | 23 | 1.23 | 33 | 1.25 | 43 | 1.26 |
| | | 14 | 1.19 | 24 | 1.23 | 34 | 1.25 | 44 | 1.26 |
| 5 | 1.00 | 15 | 1.20 | 25 | 1.24 | 35 | 1.25 | 45 | 1.26 |
| 6 | 1.06 | 16 | 1.20 | 26 | 1.24 | 36 | 1.25 | 46 | 1.26 |
| 7 | 1.09 | 17 | 1.21 | 27 | 1.24 | 37 | 1.25 | 47 | 1.26 |
| 8 | 1.11 | 18 | 1.21 | 28 | 1.24 | 38 | 1.25 | 48 | 1.26 |
| 9 | 1.13 | 19 | 1.22 | 29 | 1.24 | 39 | 1.25 | 49 | 1.26 |
| 10 | 1.14 | 20 | 1.22 | 30 | 1.25 | 40 | 1.26 | 50 | 1.26 |

Table X2. Refined $K_2$ coefficients in in real site TKPHs (from -40 to -12.5 °C)

| Vm (km/h) | K₂ coefficients | | | | | | | | | | | |
|---|---|---|---|---|---|---|---|---|---|---|---|---|
| | Ambient temperature (°C) | | | | | | | | | | | |
| | -40 | -37.5 | -35 | -32.5 | -30 | -27.5 | -25 | -22.5 | -20 | -17.5 | -15 | -12.5 |
| 10 | 0.391 | 0.398 | 0.407 | 0.415 | 0.424 | 0.433 | 0.442 | 0.452 | 0.463 | 0.474 | 0.485 | 0.498 |
| 12 | 0.435 | 0.443 | 0.451 | 0.460 | 0.469 | 0.478 | 0.488 | 0.498 | 0.508 | 0.519 | 0.531 | 0.543 |
| 14 | 0.473 | 0.481 | 0.490 | 0.498 | 0.507 | 0.517 | 0.526 | 0.536 | 0.547 | 0.558 | 0.569 | 0.581 |
| 16 | 0.506 | 0.514 | 0.523 | 0.532 | 0.541 | 0.550 | 0.559 | 0.569 | 0.580 | 0.590 | 0.602 | 0.613 |
| 18 | 0.536 | 0.544 | 0.552 | 0.561 | 0.570 | 0.579 | 0.588 | 0.598 | 0.608 | 0.619 | 0.629 | 0.641 |
| 20 | 0.562 | 0.570 | 0.578 | 0.587 | 0.595 | 0.604 | 0.613 | 0.623 | 0.633 | 0.643 | 0.654 | 0.664 |
| 21 | 0.574 | 0.582 | 0.590 | 0.598 | 0.607 | 0.616 | 0.625 | 0.634 | 0.644 | 0.654 | 0.665 | 0.675 |
| 22 | 0.585 | 0.593 | 0.601 | 0.609 | 0.618 | 0.627 | 0.636 | 0.645 | 0.655 | 0.665 | 0.675 | 0.685 |
| 24 | 0.606 | 0.614 | 0.622 | 0.630 | 0.638 | 0.647 | 0.656 | 0.665 | 0.674 | 0.684 | 0.694 | 0.704 |
| 26 | 0.625 | 0.633 | 0.640 | 0.648 | 0.657 | 0.665 | 0.674 | 0.682 | 0.691 | 0.701 | 0.710 | 0.720 |
| 28 | 0.642 | 0.650 | 0.657 | 0.665 | 0.673 | 0.681 | 0.690 | 0.698 | 0.707 | 0.716 | 0.725 | 0.735 |
| 30 | 0.658 | 0.665 | 0.673 | 0.680 | 0.688 | 0.696 | 0.704 | 0.713 | 0.721 | 0.730 | 0.739 | 0.748 |
| 32 | 0.672 | 0.679 | 0.687 | 0.694 | 0.702 | 0.710 | 0.717 | 0.726 | 0.734 | 0.742 | 0.751 | 0.760 |
| 34 | 0.685 | 0.692 | 0.700 | 0.707 | 0.714 | 0.722 | 0.730 | 0.738 | 0.746 | 0.754 | 0.762 | 0.771 |
| 36 | 0.698 | 0.705 | 0.711 | 0.719 | 0.726 | 0.733 | 0.741 | 0.748 | 0.756 | 0.764 | 0.773 | 0.781 |
| 38 | 0.709 | 0.716 | 0.722 | 0.729 | 0.736 | 0.744 | 0.751 | 0.758 | 0.766 | 0.774 | 0.782 | 0.790 |
| 40 | 0.719 | 0.726 | 0.733 | 0.739 | 0.746 | 0.753 | 0.760 | 0.768 | 0.775 | 0.783 | 0.791 | 0.798 |
| 42 | 0.729 | 0.736 | 0.742 | 0.749 | 0.755 | 0.762 | 0.769 | 0.776 | 0.784 | 0.791 | 0.798 | 0.806 |
| 44 | 0.738 | 0.745 | 0.751 | 0.757 | 0.764 | 0.771 | 0.777 | 0.784 | 0.791 | 0.799 | 0.806 | 0.813 |
| 46 | 0.747 | 0.753 | 0.759 | 0.765 | 0.772 | 0.778 | 0.785 | 0.792 | 0.799 | 0.806 | 0.813 | 0.820 |
| 48 | 0.755 | 0.761 | 0.767 | 0.773 | 0.779 | 0.786 | 0.792 | 0.799 | 0.805 | 0.812 | 0.819 | 0.826 |
| 50 | 0.762 | 0.768 | 0.774 | 0.780 | 0.786 | 0.792 | 0.799 | 0.805 | 0.812 | 0.818 | 0.825 | 0.832 |

Table X3. Refined K$_2$ coefficients in in real site TKPHs (from -10 to 20 ℃)

| Vm (km/h) | K$_2$ coefficients | | | | | | | | | | | | |
|---|---|---|---|---|---|---|---|---|---|---|---|---|---|
| | Ambient temperature (℃) | | | | | | | | | | | | |
| | -10 | -7.5 | -5 | -2.5 | 0 | 2.5 | 5 | 7.5 | 10 | 12.5 | 15 | 17.5 | 20 |
| 10 | 0.510 | 0.524 | 0.538 | 0.552 | 0.568 | 0.585 | 0.602 | 0.621 | 0.641 | 0.662 | 0.685 | 0.709 | 0.735 |
| 12 | 0.556 | 0.569 | 0.583 | 0.597 | 0.612 | 0.628 | 0.645 | 0.663 | 0.682 | 0.702 | 0.723 | 0.745 | 0.769 |
| 14 | 0.593 | 0.606 | 0.619 | 0.633 | 0.648 | 0.664 | 0.680 | 0.697 | 0.714 | 0.733 | 0.753 | 0.773 | 0.795 |
| 16 | 0.625 | 0.637 | 0.650 | 0.664 | 0.678 | 0.693 | 0.708 | 0.724 | 0.741 | 0.758 | 0.777 | 0.796 | 0.816 |
| 18 | 0.652 | 0.664 | 0.677 | 0.690 | 0.703 | 0.717 | 0.732 | 0.747 | 0.763 | 0.779 | 0.796 | 0.814 | 0.833 |
| 20 | 0.676 | 0.687 | 0.699 | 0.712 | 0.725 | 0.738 | 0.752 | 0.766 | 0.781 | 0.797 | 0.813 | 0.830 | 0.847 |
| 21 | 0.686 | 0.698 | 0.709 | 0.722 | 0.734 | 0.747 | 0.761 | 0.775 | 0.789 | 0.805 | 0.820 | 0.837 | 0.854 |
| 22 | 0.696 | 0.707 | 0.719 | 0.731 | 0.743 | 0.756 | 0.769 | 0.783 | 0.797 | 0.812 | 0.827 | 0.843 | 0.859 |
| 24 | 0.714 | 0.725 | 0.736 | 0.748 | 0.759 | 0.772 | 0.784 | 0.797 | 0.811 | 0.825 | 0.839 | 0.854 | 0.870 |
| 26 | 0.730 | 0.741 | 0.751 | 0.762 | 0.774 | 0.785 | 0.798 | 0.810 | 0.823 | 0.836 | 0.850 | 0.864 | 0.878 |
| 28 | 0.745 | 0.755 | 0.765 | 0.776 | 0.787 | 0.798 | 0.809 | 0.821 | 0.833 | 0.846 | 0.859 | 0.872 | 0.886 |
| 30 | 0.758 | 0.767 | 0.777 | 0.787 | 0.798 | 0.809 | 0.820 | 0.831 | 0.843 | 0.855 | 0.867 | 0.880 | 0.893 |
| 32 | 0.769 | 0.779 | 0.788 | 0.798 | 0.808 | 0.818 | 0.829 | 0.840 | 0.851 | 0.863 | 0.874 | 0.886 | 0.899 |
| 34 | 0.780 | 0.789 | 0.798 | 0.808 | 0.817 | 0.827 | 0.837 | 0.848 | 0.859 | 0.870 | 0.881 | 0.892 | 0.904 |
| 36 | 0.789 | 0.798 | 0.807 | 0.816 | 0.826 | 0.835 | 0.845 | 0.855 | 0.865 | 0.876 | 0.887 | 0.898 | 0.909 |
| 38 | 0.798 | 0.807 | 0.815 | 0.824 | 0.833 | 0.843 | 0.852 | 0.862 | 0.872 | 0.882 | 0.892 | 0.903 | 0.913 |
| 40 | 0.806 | 0.815 | 0.823 | 0.832 | 0.840 | 0.849 | 0.858 | 0.868 | 0.877 | 0.887 | 0.897 | 0.907 | 0.917 |
| 42 | 0.814 | 0.822 | 0.830 | 0.838 | 0.847 | 0.855 | 0.864 | 0.873 | 0.882 | 0.892 | 0.901 | 0.911 | 0.921 |
| 44 | 0.821 | 0.829 | 0.837 | 0.845 | 0.853 | 0.861 | 0.870 | 0.878 | 0.887 | 0.896 | 0.905 | 0.915 | 0.924 |
| 46 | 0.827 | 0.835 | 0.842 | 0.850 | 0.858 | 0.866 | 0.875 | 0.883 | 0.891 | 0.900 | 0.909 | 0.918 | 0.927 |
| 48 | 0.833 | 0.841 | 0.848 | 0.856 | 0.863 | 0.871 | 0.879 | 0.887 | 0.896 | 0.904 | 0.913 | 0.921 | 0.930 |
| 50 | 0.839 | 0.846 | 0.853 | 0.861 | 0.868 | 0.876 | 0.883 | 0.891 | 0.899 | 0.907 | 0.916 | 0.924 | 0.933 |

Table X4. Refined $K_2$ coefficients in in real site TKPHs (from 22.5 to 50 ℃)

| Vm (km/h) | K₂ coefficients | | | | | | | | | | | |
|---|---|---|---|---|---|---|---|---|---|---|---|---|
| | Ambient temperature (℃) | | | | | | | | | | | |
| | 22.5 | 25 | 27.5 | 30 | 32.5 | 35 | 37.5 | 40 | 42.5 | 45 | 47.5 | 50 |
| 10 | 0.763 | 0.794 | 0.826 | 0.862 | 0.901 | 0.943 | 0.990 | 1.075 | 1.187 | 1.325 | 1.498 | 1.724 |
| 12 | 0.795 | 0.822 | 0.851 | 0.882 | 0.916 | 0.952 | 0.992 | 1.062 | 1.151 | 1.257 | 1.383 | 1.538 |
| 14 | 0.819 | 0.843 | 0.870 | 0.897 | 0.927 | 0.959 | 0.993 | 1.053 | 1.127 | 1.212 | 1.311 | 1.429 |
| 16 | 0.838 | 0.860 | 0.884 | 0.909 | 0.936 | 0.964 | 0.994 | 1.046 | 1.109 | 1.181 | 1.262 | 1.356 |
| 18 | 0.853 | 0.874 | 0.896 | 0.918 | 0.942 | 0.968 | 0.994 | 1.040 | 1.096 | 1.158 | 1.227 | 1.304 |
| 20 | 0.866 | 0.885 | 0.905 | 0.926 | 0.948 | 0.971 | 0.995 | 1.036 | 1.085 | 1.140 | 1.199 | 1.266 |
| 21 | 0.871 | 0.890 | 0.909 | 0.929 | 0.950 | 0.972 | 0.995 | 1.034 | 1.081 | 1.132 | 1.188 | 1.250 |
| 22 | 0.876 | 0.894 | 0.913 | 0.932 | 0.952 | 0.973 | 0.995 | 1.033 | 1.077 | 1.125 | 1.178 | 1.236 |
| 24 | 0.886 | 0.902 | 0.920 | 0.938 | 0.956 | 0.976 | 0.996 | 1.030 | 1.070 | 1.114 | 1.161 | 1.212 |
| 26 | 0.893 | 0.909 | 0.925 | 0.942 | 0.959 | 0.977 | 0.996 | 1.028 | 1.064 | 1.104 | 1.147 | 1.193 |
| 28 | 0.900 | 0.915 | 0.930 | 0.946 | 0.962 | 0.979 | 0.996 | 1.026 | 1.060 | 1.096 | 1.135 | 1.176 |
| 30 | 0.906 | 0.920 | 0.935 | 0.949 | 0.965 | 0.980 | 0.997 | 1.024 | 1.055 | 1.089 | 1.125 | 1.163 |
| 32 | 0.912 | 0.925 | 0.938 | 0.952 | 0.967 | 0.982 | 0.997 | 1.022 | 1.052 | 1.083 | 1.116 | 1.151 |
| 34 | 0.916 | 0.929 | 0.942 | 0.955 | 0.969 | 0.983 | 0.997 | 1.021 | 1.049 | 1.078 | 1.108 | 1.141 |
| 36 | 0.921 | 0.933 | 0.945 | 0.957 | 0.970 | 0.984 | 0.997 | 1.020 | 1.046 | 1.073 | 1.102 | 1.132 |
| 38 | 0.925 | 0.936 | 0.948 | 0.960 | 0.972 | 0.984 | 0.997 | 1.019 | 1.043 | 1.069 | 1.096 | 1.124 |
| 40 | 0.928 | 0.939 | 0.950 | 0.962 | 0.973 | 0.985 | 0.998 | 1.018 | 1.041 | 1.065 | 1.091 | 1.117 |
| 42 | 0.931 | 0.942 | 0.952 | 0.963 | 0.974 | 0.986 | 0.998 | 1.017 | 1.039 | 1.062 | 1.086 | 1.111 |
| 44 | 0.934 | 0.944 | 0.954 | 0.965 | 0.976 | 0.987 | 0.998 | 1.016 | 1.037 | 1.059 | 1.082 | 1.106 |
| 46 | 0.937 | 0.947 | 0.956 | 0.966 | 0.977 | 0.987 | 0.998 | 1.015 | 1.035 | 1.056 | 1.078 | 1.100 |
| 48 | 0.939 | 0.949 | 0.958 | 0.968 | 0.978 | 0.988 | 0.998 | 1.015 | 1.034 | 1.054 | 1.074 | 1.096 |
| 50 | 0.942 | 0.951 | 0.960 | 0.969 | 0.978 | 0.988 | 0.998 | 1.014 | 1.033 | 1.052 | 1.071 | 1.092 |